University of Nevada, Reno

GPS Studies of Subtle Deformation Signals in the Western United States

A dissertation submitted in partial fulfillment of the requirements for the degree of
Doctor of Philosophy in Geophysics

by

Zachary Michael Young

Dr. Corné Kreemer
Dissertation Advisor

August, 2022

THE GRADUATE SCHOOL

We recommend that the dissertation
prepared under our supervision by

ZACHARY M. YOUNG

entitled

**GPS Studies of Subtle Deformation Signals
in the Western United States**

be accepted in partial fulfillment of the
requirements for the degree of

DOCTOR OF PHILOSPHY

Corné Kreemer, Ph.D.
Advisor

William C. Hammond, Ph.D.
Committee Member

Geoffrey Blewitt, Ph.D.
Committee Member

John Louie, Ph.D.
Committee Member

Ilya Zaliapin, Ph.D.
Graduate School Representative

Markus Kemmelmeier, Ph.D., Dean
Graduate School

August, 2022

Abstract of the Dissertation

In the past fifteen years, the network of Global Positioning System (GPS) stations in the western United States has dramatically expanded, greatly improving the spatial resolution at which we can resolve geophysical signals. This is particularly important for areas such as the Basin and Range, where data limitations prevented substantial analysis in the past. In addition to improved network geometries, many robust data analysis techniques have been produced, and revised reference frames and data processing strategies have greatly improved data quality. While these advancements have expanded our understanding of long term tectonics in the western United States, they also provide the opportunity to robustly investigate temporally variable, subtle deformation signals. Many of these signals were previously below uncertainty levels of the data, or station coverage was too sparse. The research presented in this dissertation takes advantage of this progress, to advance our understanding of the interaction of subtle deformation signals within the western United States, across a range of spatio-temporal scales.

The first study investigates drought induced deformation observed at GPS stations near the Great Salt Lake (GSL), in Utah, between 2012 and 2016. During this time, GPS timeseries show a subtle, but distinct, three-dimensional change in trend, with horizontal motion away from the lake and vertical uplift centered upon it. Concurrently, GSL lost a total of 1.89 m of surface elevation. Previous hydrologic studies have typically only used vertical GPS displacements to quantify load variation over broad, regional scales. Here, we find that at small spatial scales, three-dimensional GPS is sensitive to not just the

unloading of the lake, but the nearby groundwater as well. In our preferred model, the volume lost by GSL is equivalent to that observed, at 5.5 ± 1.0 km^3, and the inferred groundwater is substantial at 10.9 ± 2.8 km^3. Seismicity is modulated by the hydrologic cycle within the inferred load region, revealing increased earthquake rates during drier periods as stresses on faults under the loads are reduced. This study highlights the impact of subtle, multi-year, drought signals on GPS time series, and indicates, that for robust regional analyses, small scale hydrologic loading must be accounted for.

In the second study, we focus on correcting subtle deformation signals within the central Basin and Range, and produce the most robust interseismic velocity field of the region to date. Since deformation rates are low, the combined corrections produced in this study for postseismic deformation, hydrologic loading, and regional common mode error, substantially alter the velocity field and resulting strain rates. Station uncertainties reduce by 62.1% and 53.8% in the east and north components, compared to the original velocity field. The Pahranagat Shear Zone is strongly affected by postseismic relaxation, which accounts for as much as half the shear along its western extent. We find that east–west extension across the Las Vegas Valley is substantially larger than previously estimated at 0.5 – 0.6 mm/yr and our preferred strain rates within the Las Vegas Valley are 8.5 ± 2.4 $\text{x}10^{-9}\text{yr}^{-1}$, supporting that crustal deformation is active within the urban area of Las Vegas. These results show in detail the significant impact that subtle deformation signals impart on regional analyses and their interpretation.

Positioning errors present in five-minute GPS time series propagate subtly into the daily position of the station. In the final study, we produce a sensitivity analysis of the

zenith tropospheric delay (ZTD) random walk constraint, and show that station vertical scatter can be greatly improved by loosening its value. We find that large wavelike displacements of ~100 mm, which occurred along the coast of California during Winter Storm Ezekiel in 2019, are suppressed when using a random walk constraint of 24 mm/√(hr) (i.e., eight times looser than the default value). Global station RMS and repeatability shows improvements of 4% – 9% and 10% – 21% respectively, when using uniform random walk constraints of 6 – 12 mm/√(hr). Further improvement is attained when defining characteristic random walk constraints to the stations, with a 10% improvement in repeatability globally. A daily optimal random walk approach reveals 24% improvement in global station repeatability. These findings reveal an opportunity to greatly improve five-minute vertical positioning, not just for stations in the western United States during storms, but for the global GPS network as a whole, by loosening the ZTD random walk constraint at least to a value of 6 mm/√(hr).

To my wife and son, Tiandra and Dean Young

Acknowledgments

First and foremost, I would like to thank my advisor Dr. Corné Kreemer. Corné has been a fantastic mentor, providing excellent guidance and freedom within my research. I began my graduate career as a masters student with Corné in the Nevada Geodetic Laboratory. At the time, my experience was largely on the seismicity side of geophysics and I only had a vague understanding of geodesy. After the first year under Corné's mentorship, however, I knew that I had found a field I could truly enjoy, and Corné graciously accepted my transfer into the PhD program. Thank you for your patience in the early years as I was building my coding skills and general knowledge. In the time since, Corné instilled a passion for figure preparation and taught me the importance of letting the data speak for itself. I am extremely grateful for everything Corné has taught me. I would not be the scientist I am today without his mentorship. Thank you for everything.

My committee members are Drs. Bill Hammond, Geoff Blewitt, John Louie, and Ilia Zaliapin. Thank you all for the time and wisdom you have provided, both inside and outside of the classroom, to teach and guide me. The unique skills I have learned from each of you has greatly broadened my toolbox and made me a better scientist, thank you.

I would like to thank Dr. Ileana Tibuleac, who gave me my first experience with field work and took me on as an undergraduate research assistant in the Nevada Seismological Laboratory. I will always remember the seismic deployment in Dixie

Valley. Ileana brought me into the world of coding and recommended that I speak with Corné regarding pursuing a graduate degree.

To my wife Tiandra, I could write a whole dissertation on how much I appreciate you, but I doubt that would cover it. Words are not enough. Thank you for your constant support, and for always believing in me. You are a fantastic mother to Dean. Thank you for taking so much more on your plate while I have been finishing this up. I could not have done this without you. Oh, and thank you for refusing to date me if I didn’t go back to school to get my associates at TMCC nine years ago. Apparently I didn’t hear the word “associates” because here we are today. Thank you. “To infinity and beyond!”

Table of Contents

List of Tables

List of Figures

List of Videos

1

Introduction

1.1 Robust Identification of Subtle Deformation Signals in the Western United States

The western United States is one of the most tectonically active and complex regions in the world, not only due to the presence of the Pacific – North American plate boundary, but the diverse inland deformation observed far from its margins (Hammond et al., 2009; Hammond & Thatcher, 2004; Kreemer et al., 2010). Since its initiation in the early 1990's to monitor crustal processes, the network of Global Positioning System (GPS) stations has become crucial to enhancing our understanding of the region. This has driven a flourishing field of study, with a consistent flow of new applications and insights produced. Not only does the GPS network provide a direct view of crustal deformation in the western United States, it allows comparison of modern deformation with geologic observations. Validating results when in agreement, and providing a view into the temporal variability exhibited in recent years when results differ. Processing strategies are continuously evolving to produce improved positioning [e.g., revised reference frames (Altamimi et al., 2016) and positioning software (Bertiger et al., 2020)], driving down uncertainties and increasing station repeatability.

Additionally, in the past fifteen years, the GPS network in the western United States has seen a dramatic increase in the number of stations and available data (Blewitt et al., 2018), with more than double the number of stations present in 2007. This has been driven by the installation of the Plate Boundary Observatory (PBO) and Mobile Array of

GPS for Nevada Transtension (MAGNET) networks (Blewitt et al., 2009), as well as the expansion of existing networks. The PBO stations greatly improved the distribution of stations across the entire western United States, while the MAGNET network improved coverage within sparsely populated areas of the Basin and Range. Furthermore, many robust processing techniques have been produced in this time, which improve velocity [i.e., the Median Interannual Difference Adjusted for Skewness algorithm (Blewitt et al., 2016)], strain rate [i.e., the Median Estimation of Local Deformation Algorithm (Kreemer et al., 2018), and common mode [i.e., Common Mode Component Imaging (Kreemer & Blewitt, 2021)] estimates, as well as improved modeling software for postseismic deformation [i.e. PSGRN/PSCMP (Wang et al., 2006)] and elastic deformation [i.e., LoadDef (Martens et al., 2019)]. The progress made toward improving data quality, and increasing the resolution of the GPS network in the western United States, has greatly furthered our understanding of long term tectonic processes. However, in combination with robust analysis techniques, it additionally provides the opportunity to investigate temporally variable subtle deformation signals present in the GPS timeseries. Previously, sparse data often left studies with open-ended interpretations (Kreemer et al., 2010), and hydrologic loading investigations were limited to broad regions with typically only the vertical GPS component used (Amos et al., 2014; Borsa et al., 2014). Additionally, postseismic deformation, and displacements due to regional common mode error (i.e., timeseries noise which is correlated across hundreds of kilometers), have been shown to alter velocity fields (Broermann et al., 2021; Freed et al., 2007; Hammond et al., 2009;

Kreemer & Blewitt, 2021; Márquez-Azúa & DeMets, 2003; Serpelloni et al., 2013), raising questions over their impact to the interpretation of the velocity field in the western United States. While much of the focus in geodesy relies on the use of daily positions, these positions are derived from five-minute solutions, and the expansion of the network provides to opportunity to better investigate deformation signals which occur over hourly time frames. This dissertation is comprised of three unique studies of subtle deformation signals, observed in the western United States, across daily, multi-year, and sub-daily time frames, to improve our understanding of their effects on regional analyses. Summaries of each study are provided in the following section.

1.2 Summary of Dissertation Chapters

1.2.1 Using GPS to Quantify Hydrologic Load Variation at Small Spatial Scales

In Chapter 2, the sensitivity of GPS stations near Great Salt Lake (GSL), Utah, to hydrologic load variation during the 2012-2016 drought is investigated. During this time, the lake lost 1.89 m of surface elevation, and GPS stations nearby show a subtle, but clear thee-dimensional change in trend. The pattern of these displacements is characteristic of an unloading signal, however, calculations for the displacements attributed to the observed lake unloading, indicate that additional mass loss is required to explain the GPS observations. This suggests that the signal is the combination of both the unloading of the lake, and nearby groundwater. A suite of loading models are tested, allowing a range of distributions of groundwater loads, to identify the model which best accounts for the observed displacements and to test the maximum resolvability of the current GPS network. In our preferred solution, we find that the model accurately estimates the volume of water lost by GSL, at 5.5 ± 1.0 km^3, and that GPS is sensitive to groundwater loss up to 64 km from the edge of the lake. The total mass loss for the inferred groundwater is substantial, at 10.9 ± 2.8 km^3, and wells within its distribution observe significant decline. Further support of the model is present in the seismicity analysis, which finds that within the inferred load region, earthquakes are modulated by the seismic cycle. Outside of the load, no relationship is observed. The findings presented in this study indicate that, at small spatial scales, GPS data is sensitive to, and their velocities affected by, subtle deformation due to hydrologic variation.

The material presented here was published in: Young, Z. M., C. Kreemer, and G. Blewitt, (2021). GPS Constraints on Drought-Induced Groundwater Loss Around Great Salt Lake, Utah, With Implications for Seismicity Modulation. *Journal of Geophysical Research: Solid Earth, 126*(10), e2021JB022020. https://doi.org/10.1029/2021JB022020. In this project, I identified the unloading signal at GPS stations near GSL and performed the time series analysis. Hilary Martens provided guidance on using the LoadDef software and assisted with benchmark testing my results. I then designed and applied the sensitivity test for the load models. Ilya Zaliapin declustered the earthquake catalog, after which I produced the seismicity analysis. Throughout the entire process, Corné Kreemer provided substantial guidance and insight, greatly improving the project. I produced all of the figures and authored the text. Both Corné Kreemer and Geoff Blewitt assisted with several rounds of edits to prepare the manuscript for final submission.

1.2.2 Central Basin and Range Interseismic Strain Accumulation

Since deformation rates within the central Basin and Range are low, the presence of subtle deformation signals within the GPS time series, can significantly alter the velocity field and its associated hazard. In Chapter 2, we present the most robust interseismic velocity field to date for the region, and investigate its implications for the seismic hazard near Las Vegas. Results of this study, corroborate many of the findings of Kreemer et al. (2010), when using our original velocity data set, and improve upon them by producing robust corrections for postseismic deformation, hydrologic loading, and regional common mode error. Results are greatly improved by the expansion of the GPS network in recent years, and after corrections, our final velocity uncertainties are reduced by 62.1% and 53.8% in the east and north components. Large strain rate differences are observed when using the original versus the final corrected velocities, and we find the values to be significantly larger within the Las Vegas Valley than previously estimated and compared to the original velocity model, at $8.5 \pm 2.4 \text{ x}10^{-9} \text{ yr}^{-1}$. East to west extension within the valley is much larger as well, at 0.5 – 0.6 mm/yr, indicating that deformation is active within the Las Vegas Valley. These results highlight the significant impact subtle deformation signals have on regional analyses, particularly where deformation rates are low.

These materials have been submitted for consideration to the *Bulletin of the Seismological Society of America*: Young, Z. M., C. Kreemer, W. C. Hammond, and G. Blewitt (in review), Interseismic Strain Accumulation Between the Colorado Plateau and the Eastern California Shear Zone: Implications for the Seismic Hazard Near Las Vegas, Nevada. This project was designed by Corné Kreemer and myself. I conducted the time series analysis and produced the postseismic model. Corné provided the codes and guidance for the MELD, Haines and Holt, and CMC Imaging programs. Bill Hammond provided the codes and guidance for the scripts used in the block modeling. I applied theses codes to produce the common mode correction and to calculate strain rates and block models for the CBR. All of the results and figures were produced by myself and I authored the text. All co-authors assisted with many rounds of revisions which greatly improved the text.

1.2.3 Improved Tropospheric Path Delay Estimation

While Chapters 2 and 3, analyzed the effects of subtle deformation signals on daily GPS time series, Chapter 4 investigates a spurious deformation signal observed within five-minute timeseries. During Winter Storm Ezekiel in 2019, sub-daily GPS vertical time series along the coast of California, show significant wavelike displacements. These displacements are large, at ±100 mm, and travel from northern California to Los Angeles by the end of the day. The spatio-temporal distribution of the displacements is highly correlated with radar reflectivity, suggesting they are a result of the satellite signal interacting with moisture in the atmosphere. To investigate this, we produce a sensitivity analysis of the zenith tropospheric delay (ZTD) random walk constraint. Since Bar-Sever et al. (1998), the majority of GPS processing centers have adopted their recommended value of 3 mm/√(hr) as the default value to constrain the random walk. We show that increasing the constraint to 24 mm/√(hr) allows the ZTD enough freedom to more accurately account for atmospheric variability, without introducing substantial noise into the time series. This adjustment improves station repeatability by 21% during the storm. To investigate the effect of loosening the random walk during more typical atmospheric conditions, we expand our study to the global GPS network, and find substantial improvements when loosening its value to 6 – 12 mm/√(hr). Regionally we find that vertical RMS and repeatability, for all but the polar regions, are improved by 4% – 9% and 10% – 21% respectively. We show that there is large regional variability, dependent on climactic, temporal, and geographic factors, suggesting that determining variable random walk constraints, per station, is more appropriate. For our data sets, we find a global improvement of station repeatability of 10% when a characteristic random walk per station is identified, and of 24% when determining daily optimal, station specific, random walks. This study identifies a prevalent source of vertical positioning error in the five-minute GPS time series, which propagates subtly into the daily positions, and we present recommended approaches which will substantially improve data quality.

These results are being prepared for publication with the *Journal of Geodesy* in: Young, Z. M., G. Blewitt, and C. Kreemer (in prep), Improved GPS Tropospheric Path Delay Estimation Using Variable Random Walk Process Noise. In this project, I identified that large displacements present in the 5-minute GPS time series were associated with weather systems. Geoffrey Blewitt and I designed the project. All GPS data presented in this study were produced by Geoff using the Nevada Geodetic Laboratory processing strategy. I performed all of the analysis with guidance from both Geoff and Corne Kreemer. All figures and videos were produced by myself and I authored the text. Geoff provided insight into the methodologies applied in this project and his edits substantially improved the text.

1.2.4 References

Altamimi, Z., Rebischung, P., Métivier, L., & Collilieux, X. (2016). ITRF2014: A new release of the International Terrestrial Reference Frame modeling nonlinear station motions. *Journal of Geophysical Research: Solid Earth*, *121*(8), 6109–6131. https://doi.org/10.1002/2016JB013098

Amos, C. B., Audet, P., Hammond, W. C., Bürgmann, R., Johanson, I. A., & Blewitt, G. (2014). Uplift and seismicity driven by groundwater depletion in central California. *Nature*, *509*(7501), 483–486. https://doi.org/10.1038/nature13275

Bar-Sever, Y. E., Kroger, P. M., & Borjesson, J. A. (1998). Estimating horizontal gradients of tropospheric path delay with a single GPS receiver. *Journal of Geophysical Research: Solid Earth*, *103*(B3), 5019–5035. https://doi.org/10.1029/97JB03534

Bertiger, W., Bar-Sever, Y., Dorsey, A., Haines, B., Harvey, N., Hemberger, D., et al. (2020). GipsyX/RTGx, a new tool set for space geodetic operations and research. *Advances in Space Research*, *66*(3), 469–489. https://doi.org/10.1016/j.asr.2020.04.015

Blewitt, G., Hammond, W. C., & Kreemer, C. (2009). Geodetic observation of contemporary deformation in the northern Walker Lane: 1. Semipermanent GPS strategy. In J. S. Oldow & P. H. Cashman, *Late Cenozoic Structure and Evolution of the Great Basin-Sierra Nevada Transition*. Geological Society of America. https://doi.org/10.1130/2009.2447(01)

Blewitt, G., Kreemer, C., Hammond, W. C., & Gazeaux, J. (2016). MIDAS robust trend estimator for accurate GPS station velocities without step detection. *Journal of Geophysical Research: Solid Earth*, *121*(3), 2054–2068. https://doi.org/10.1002/2015JB012552

Blewitt, G., Hammond, W., & Kreemer, C. (2018). Harnessing the GPS Data Explosion for Interdisciplinary Science. *Eos*, *99*. https://doi.org/10.1029/2018EO104623

Borsa, A. A., Agnew, D. C., & Cayan, D. R. (2014). Ongoing drought-induced uplift in the western United States. *Science*, *345*(6204), 1587–1590. https://doi.org/10.1126/science.1260279

Broermann, J., Bennett, R. A., Kreemer, C., Blewitt, G., & Pearthree, P. A. (2021). Geodetic Extension Across the Southern Basin and Range and Colorado Plateau. *Journal of Geophysical Research: Solid Earth*, *126*(6), e2020JB021355. https://doi.org/10.1029/2020JB021355

Freed, A. M., Ali, S. T., & Bürgmann, R. (2007). Evolution of stress in Southern California for the past 200 years from coseismic, postseismic and interseismic stress changes. *Geophysical Journal International*, *169*(3), 1164–1179. https://doi.org/10.1111/j.1365-246X.2007.03391.x

Hammond, W. C., Kreemer, C., & Blewitt, G. (2009). Geodetic constraints on contemporary deformation in the northern Walker Lane: 3. Central Nevada seismic belt postseismic relaxation. In J. S. Oldow & P. H. Cashman, *Late Cenozoic Structure and Evolution of the Great Basin-Sierra Nevada Transition*. Geological Society of America. https://doi.org/10.1130/2009.2447(03)

Hammond, William C., & Thatcher, W. (2004). Contemporary tectonic deformation of the Basin and Range province, western United States: 10 years of observation with the Global Positioning System. *Journal of Geophysical Research: Solid Earth*, *109*(B8). https://doi.org/10.1029/2003JB002746

Kreemer, C., & Blewitt, G. (2021). Robust estimation of spatially varying common-mode components in GPS time-series. *Journal of Geodesy*, *95*(1), 13. https://doi.org/10.1007/s00190-020-01466-5

Kreemer, C., Blewitt, G., & Hammond, W. C. (2010). Evidence for an active shear zone in southern Nevada linking the Wasatch fault to the Eastern California shear zone. *Geology*, *38*(5), 475–478. https://doi.org/10.1130/G30477.1

Kreemer, C., Hammond, W. C., & Blewitt, G. (2018). A Robust Estimation of the 3-D Intraplate Deformation of the North American Plate From GPS. *Journal of Geophysical Research: Solid Earth*, *123*(5), 4388–4412. https://doi.org/10.1029/2017JB015257

Márquez-Azúa, B., & DeMets, C. (2003). Crustal velocity field of Mexico from continuous GPS measurements, 1993 to June 2001: Implications for the neotectonics of Mexico. *Journal of Geophysical Research: Solid Earth*, *108*(B9). https://doi.org/10.1029/2002JB002241

Martens, H. R., Rivera, L., & Simons, M. (2019). LoadDef: A Python-Based Toolkit to Model Elastic Deformation Caused by Surface Mass Loading on Spherically Symmetric Bodies. *Earth and Space Science*, *6*(2), 311–323. https://doi.org/10.1029/2018EA000462

Serpelloni, E., Faccenna, C., Spada, G., Dong, D., & Williams, S. D. P. (2013). Vertical GPS ground motion rates in the Euro-Mediterranean region: New evidence of velocity gradients at different spatial scales along the Nubia-Eurasia plate boundary. *Journal of Geophysical Research: Solid Earth*, *118*(11), 6003–6024. https://doi.org/10.1002/2013JB010102

Wang, R., Lorenzo-Martín, F., & Roth, F. (2006). PSGRN/PSCMP—a new code for calculating co- and post-seismic deformation, geoid and gravity changes based on the viscoelastic-gravitational dislocation theory. *Computers & Geosciences*, *32*(4), 527–541. https://doi.org/10.1016/j.cageo.2005.08.006

2

GPS Constraints on Drought-Induced Groundwater Loss Around Great Salt Lake, Utah, with Implications for Seismicity Modulation

2.1 Publication Status

The material presented in this chapter was published in: Young, Z. M., C. Kreemer, and G. Blewitt, (2021). GPS Constraints on Drought-Induced Groundwater Loss Around Great Salt Lake, Utah, With Implications for Seismicity Modulation. *Journal of Geophysical Research: Solid Earth*, *126*(10), e2021JB022020. https://doi.org/10.1029/2021JB022020. The dissertation author led the research and authored the text. The co-authors provided guidance and revisions which assisted the production of the presented research.

2.2 Key Points:

- 3D time-series of local GPS stations are sensitive to mass loss in Great Salt Lake and additional groundwater contributions nearby.
- During the 2012 – 2016 drought, the Great Salt Lake basin lost 10.9 ± 2.8 km^3 of groundwater while the lake itself lost 5.5 ± 1.0 km^3.
- Seismicity near Great Salt Lake is modulated throughout the drought cycle with significantly more events occurring during drought periods.

2.3 Abstract

Great Salt Lake (GSL), Utah, lost 1.89 ± 0.04 meters of water during the 2012 to 2016 drought. During this timeframe, data from the GRACE mission underestimates this mass loss, while nearby Global Positioning System (GPS) stations exhibit significant shifts in position. We find that crustal deformation, from unloading the Earth’s crust consistent with the observed GSL water loss alone, does not explain the GPS displacements, suggesting contributions from additional water storage loss surrounding GSL. This study applies a damped least squares inversion to the 3D GPS displacements to test a range of distributions of groundwater loads to fit the observations. When considering the horizontal and vertical displacements simultaneously, we find a realistic distribution of water loss while also resolving the observed water loss of the lake. Our preferred model identifies mass loss up to 64 km from the lake via two radial rings. The contribution of exterior groundwater loss is substantial (10.9 ± 2.8 km^3 vs. 5.5 ± 1.0 km^3 on the lake), and greatly improves the fit to the observations. Nearby groundwater wells exhibit significant water loss during the drought, which substantiates the presence of significant water loss outside of the lake, but also highlights greater spatial variation than our model can resolve. We observe seismicity modulation within the inferred load region, while the region outside the (un)loading reveals no significant modulation. Drier periods exhibit higher quantities of events than wetter periods and changes in trend of the earthquake rate are correlated with regional mass trends.

2.4 Plain Language Summary

During the 2012 – 2016 drought, GPS stations near Great Salt Lake (GSL), UT, showed a distinct shift in position. The GSL lost nearly two meters of water. As water mass is lost from a lake, the crust uplifts and extends from the center of the source; however, the amount of water loss observed on the GSL is not enough to explain the displacements observed by nearby GPS stations. To address this, water loss in the form of additional rings of groundwater surrounding the GSL are estimated and we find the model that best fits the GPS displacements. We find that water loss up to 64 km from the edge of the lake contributes to the observed signal, at a volume substantially larger than lost on the lake itself. Our results show that GPS data can be used to infer localized water loss and discriminate between loss of surface water versus ground water. Furthermore, we see evidence that changes in mass in the region result in changes in the quantity and rate of seismicity; significantly more events occur in the crust underneath the area with water fluctuations when there is a reduced water load.

2.5 Introduction

Decline in fresh water availability is one of many societal challenges resulting from the compounding effects of climate change and population growth (Famiglietti, 2014; Gleeson et al., 2012; Vörösmarty et al., 2000). Most groundwater loss can be attributed to the increase of pumping for irrigation and other anthropogenic use, particularly during times of drought (Castle et al., 2014; Famiglietti et al., 2011; Ojha et al., 2019; Matthew Rodell et al., 2009; Russo & Lall, 2017; Scanlon et al., 2012; Tiwari et al., 2009), with depletion rates often highest in land-locked basins within (semi-)arid regions (Wang, 2018). Commensurate with the groundwater loss, significant global surface water loss has also been recorded (Pekel et al., 2016), which is likewise most dramatic for (saline) lakes in (semi-)arid areas (Wurtsbaugh et al., 2017). Regional water loss due to the recent drought in the Western United States has provided insight into the balance between surface (i.e., lakes and reservoirs) and groundwater loss. The ratio of ground to surface water loss has been reported to be 1.89 for the Upper Colorado River basin (Castle et al., 2014), and 4.79 for California's San Joaquin Valley (Ojha et al., 2019).

The Gravity Recovery and Climate Experiment (GRACE) satellite mission has brought invaluable insight into changes in terrestrial water storage (TWS) (e.g., Famiglietti & Rodell, 2013; Rodell et al., 2018). GRACE's wide spatial resolution of ~300 km (Wahr et al., 2013), limits the observations of TWS changes to large regional scales. Even significant deviations localized on relatively small basins, such as Great Salt Lake (GSL), Utah, are virtually undetectable (Rodell & Famiglietti, 1999). Many studies have found Global Positioning System (GPS) data sensitive to mass variation associated with extreme drought conditions (Amos et al., 2014; Argus et al., 2017; Borsa et al., 2014). Changes in load result in elastic deformation, in which the crust is displaced in both the vertical and horizontal components, thus deforming the crust as the load changes. These elastic displacements are dependent on the magnitude and distribution of the load variation, and return to their original position when equilibrium is re-attained. While many studies rely primarily on vertical GPS observations to identify and quantify TWS variation, some studies have shown that horizontal motion is a useful indicator of mass localization when regional trends are well accounted for (Fu et al., 2013; Kreemer & Zaliapin, 2018; Wahr et al., 2013).

In this study, we investigate a three-dimensional (3D) transient deformation signal observed at GPS sites near GSL between 2012 and 2016. Onset of this signal correlates well with the beginning of severe drought conditions in the region. During this period, GSL surface elevation decreased by 1.89 ± 0.04 m. Concurrently, GRACE only observes 1.18 ± 0.08 m of equivalent water loss, if the full 300 km resolution is consolidated on the lake, corroborating the findings of Rodell & Famiglietti (1999). While GRACE is unable to quantify the load on the lake for this timeframe, a previous study showed that GPS sites near GSL exhibited load-induced deformation correlated with lake level variation between 1997 and 2003 (Elósegui et al., 2003). Only two long-running GPS sites were available at the time of that study, but results identified the signal in all three components and suggested the need for more complex load geometries. Currently, long-running GPS sites are well distributed around the lake and provide an opportunity to further investigate the sensitivity of 3D GPS near GSL to small spatial scale mass variation (Figure 2.1). During the recent drought, GPS timeseries reflect horizontal extension and vertical uplift at pairs of stations located on opposite sides of GSL, indicating the presence of an unloading signal (Figure 2.2). As we will show below, the data cannot be explained solely by the unloading of the lake. Considering the observed ratios of groundwater to surface water shown in previous studies, as well as observed well water level changes during this drought, it is likely that additional groundwater unloading has contributed to the observed GPS transients. To address this, we estimate displacements due to GSL unloading combined with distributions of groundwater loss and explore a range of models to identify the spatial distribution of mass loss in this region which best explains the 3D GPS signal.

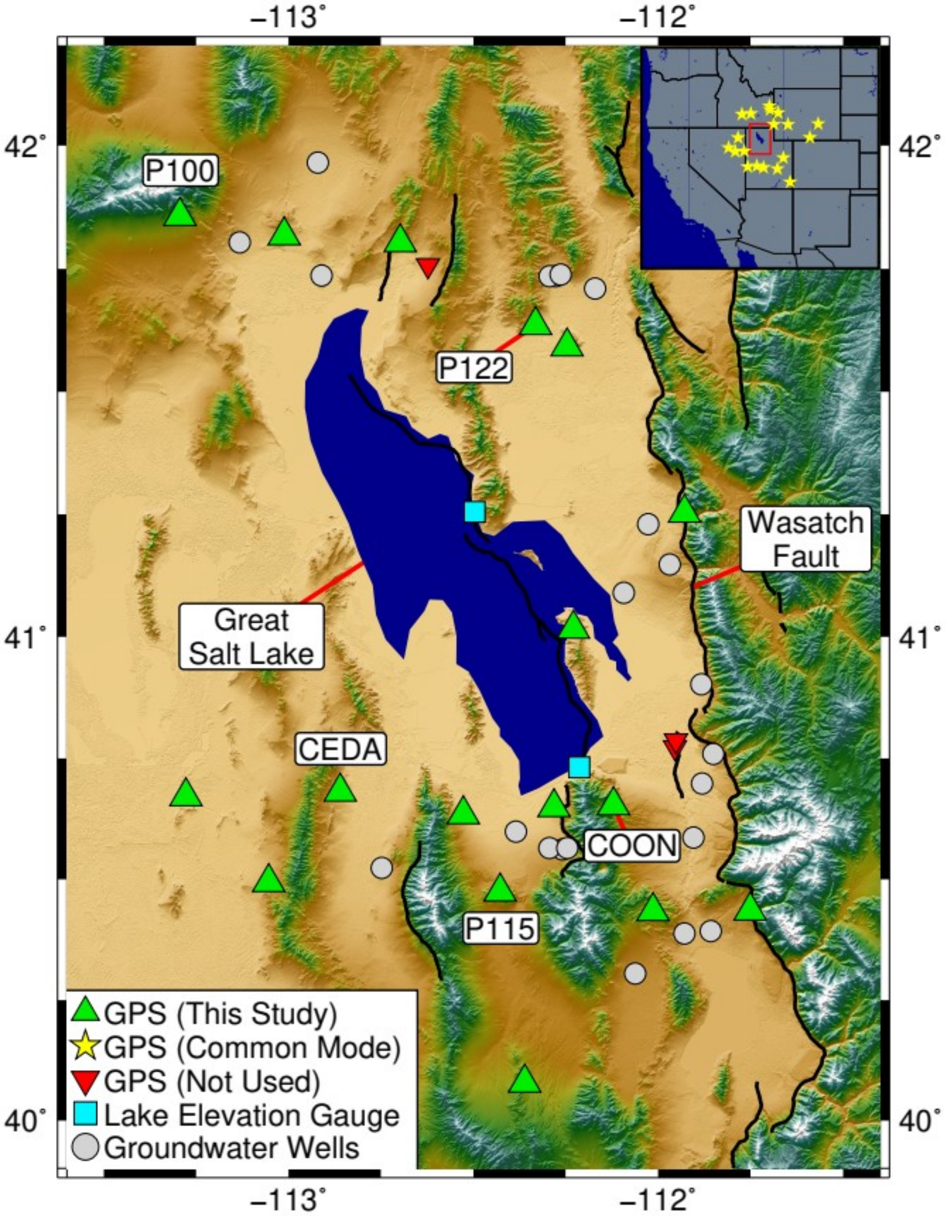

Figure 2.1: Location map of the study area. Green triangles represent GPS stations included in this study. Red triangles represent GPS stations not included. Turquoise rectangles represent USGS water surface elevation gauges and grey circles represent USGS groundwater well locations. The red box in the inset identifies the bounds of the figure with yellow stars showing the location of stations used to calculate the common mode in the GPS time-series. Labeled stations identify locations of GPS timeseries shown in Figure 2.2. Black lines represent significant faults in the region, including the Wasatch fault. No data east of the Wasatch fault are included in this study.

2.6 Observations

Great Salt Lake sits in close proximity to the Wasatch fault to the east (Figure 2.1). For this study, we only include data within the GSL basin and west of the Wasatch fault. GPS displacements and seismicity on opposing sides of the fault are expected to behave independently and reflect unique dynamics respectively.

2.6.1 Water Level Variation

Historically, GSL has experienced large fluctuations in lake surface elevation, and the lake level has been in decline since the 1850’s (Elósegui et al., 2003; Wurtsbaugh et al., 2017). To investigate the modern trends, we inspect two long running lake level gauges (USGS Water Resources, 2020). These gauges are labeled 10010100, located on the northeastern side of GSL, and 10010000, located on the southeastern side of GSL. Deviations in lake level compare well with the Palmer Drought Severity Index (PDSI), which provides an index for the intensity of dryness in a region (Abatzoglou et al., 2017) (Figure 2.2a). In Figure 2.2, PDSI for the study area is reflected as the background shading and is used to indicate drier and wetter periods in comparison to the lake level deviations. The period of 2004 – 2012 (henceforth referred to as our base period), reveals variable drought conditions and minor net change in lake elevation. Between 2012 and 2016 (i.e., the drought period), the PDSI indicates consistent drought conditions and GSL exhibits steady lake level decline, totaling 1.89 ± 0.04 m of surface elevation lost. This value is calculated with the MIDAS algorithm, which provides a robust trend estimation with realistic uncertainty while being insensitive to seasonality (Blewitt et al., 2016).

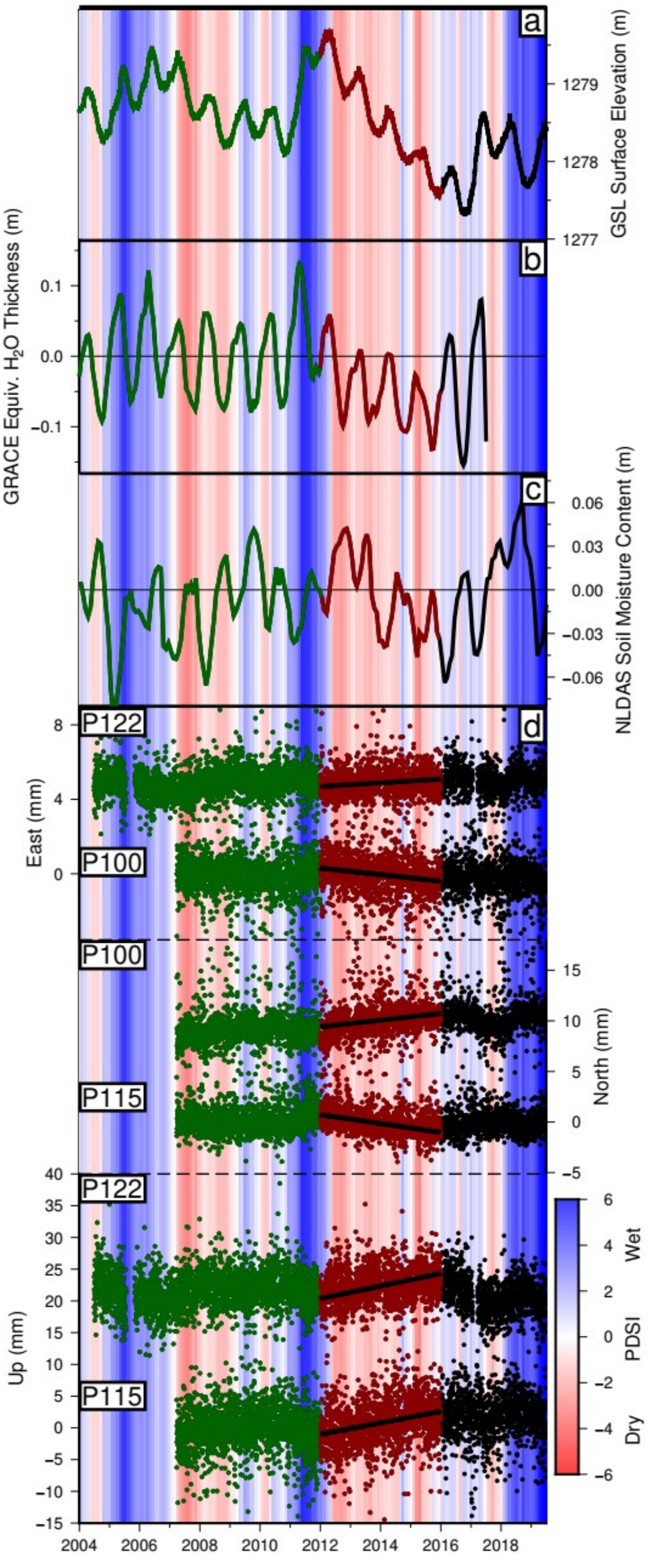
a
GSL Surface Elevation (m)
1279
1278
1277
b
GRACE Equiv. H_2O Thickness (m)
0.1
0.0
−0.1
c
NLDAS Soil Moisture Content (m)
0.06
0.03
0.00
−0.03
−0.06
d
P122
P100
East (mm)
8
4
0
P100
P115
North (mm)
15
10
5
0
−5
P122
P115
Up (mm)
40
35
30
25
20
15
10
5
0
−5
−10
−15
PDSI
Wet
Dry
6
4
2
0
−2
−4
−6
2004
2006
2008
2010
2012
2014
2016
2018

Figure 2.2: Comparison of GPS, GRACE, PDSI, and GSL surface elevation data. Background shading indicates the Palmer Drought Severity Index averaged over the study area. Green data represent the base period of 2004 – 2012, red data represent the drought period of 2012 – 2016, and black data represents later data not included in this study. **a)** Average of the two GSL water level gauges. **b)** Averaged GRACE TWS data covering a range of 300 km centered on GSL, detrended relative to the base period. **c)** Average NLDAS soil moisture content within the study area. **d)** GPS timeseries detrended relative to the base period. Regional common mode and annual/semi-annual signals have been removed. Station pairs in each component are located on opposite sides of the lake. Black lines represent the trends during the drought period calculated with MIDAS. Stations P122 and P100 show East – West extension, while stations P100 and P115 show North – South extension during the test period. Stations P122 and P115 both show vertical uplift. Station locations are shown in Figure 2.1.

The increase in lake level observed at the end of 2016 reveals the combined effects of increased precipitation and anthropogenic modifications. GSL is split by a railroad causeway which separates the lake into northern and southern portions and was retrofitted to improve flow in December of 2016 (Hassibe & Keck, 1991). This has historically caused a difference in water level across the causeway. For the period of 2004 – 2015, the lake elevation in the northern portion showed a consistent ~20-cm lower level than that of the southern half. Between 2015 and 2016, the halves of the lake diverge slightly with the southern portion retaining more water than the northern half. This deviation is not readily distinguishable in the GPS data and is unlikely to influence loading results due to the magnitude and localization of the deviation. For the purpose of this study, we refer to the average of the two lake level gauges.

Groundwater well observations reveal a similar pattern of water level decline, with the majority of wells reflecting a distinct trend of water loss during the drought period. Well data are obtained from the National Groundwater Monitoring Network, with sites distributed around the majority of GSL (Figure 2.1) (NGWMN, 2020). Since many wells have poor temporal resolution or inconsistent sampling, three interpretations of the groundwater variation during the drought are provided (Table S2.1). First, we calculate the Theil-Sen median slope and apply it to the duration of the drought (Sen, 1968; Theil, 1950). All wells exhibit water loss during this period and cover a range of water variation between -0.28 and -9.34 meters. For 22 out of 39 available wells, the decline is significant at the 2-standard deviation level, where the standard deviation is calculated as 1.4826 times the median absolute deviation (Huber, 1981). Similar results are observed when applying the MIDAS algorithm, however, only nine stations had enough data points required for this method. Many wells provide data near the start and end times of the drought and investigation of the net difference reveals similar observed ranges to those produced by MIDAS. While these changes in water level cannot be directly compared to the lake level change, as they are a function of the characteristics of the host rock and aquifer dynamics, these observations highlight substantial mass variation exterior to the bounds of GSL and exhibit the largest water level deviations at wells closest to the lake.

2.6.2 GRACE and NLDAS

GRACE data are able to identify spatio-temporal variation of TWS (e.g., Castle et al., 2014; Ojha et al., 2019; Tiwari et al., 2009). Although our study area is below the spatial resolution of GRACE, we inspect the temporal variability of the GRACE signal. Here we use the Release 06 version of the TELLUS GRACE TWS anomaly data and select the grid points which span 300 km, centered on GSL (Landerer & Swenson, 2012). The unique JPL, GFZ, and CSR solutions produce extremely similar results and minimal spatial variability is observed across grid points. Considering these similarities and to minimize potential errors in the solutions, we average the three unique solutions for each grid point and present the average of these timeseries in this study (Figure 2.2b). We observe that the TWS anomaly remains fairly stable across the duration of the base period, followed by a distinct change in trend, beginning in 2012, which exhibits a 4-year net loss of water mass of 41.1 mm across the drought period. This is equivalent to only 3.48 ± 0.21 km^3 of water loss and is comparable to only -1.18 ± 0.08 m if the load was entirely constrained to the bounds of the lake. Although the timing of the deviation matches well with the onset of the drought, the volume is significantly smaller than the 5.58 ± 0.11 km^3 implied from the observed lake level decline itself. This indicates that for the small spatial scale of this study, GRACE identifies the regional onset of water loss but does not accurately estimate the magnitude of the loss, supporting the findings of Rodell & Famiglietti (1999).

The North American Land Data Assimilation System Phase 2 (NLDAS-2), provides unique land surface parameters which distinguish surface process variation over time (Xia et al., 2012). Here we use the NLDAS-2 monthly Noah model to observe variation in soil moisture content within the top two meters of soil near GSL (Mocko, 2012). While a slight trend change is observable during the drought, this trend, and that of the base period, are below their respective significance levels (Figure 2.2c), indicating that the source of the deviation observed in both the GRACE data and GPS displacements, is not primarily confined to the uppermost soil layers.

2.6.3 GPS Displacement Fields

The ability of GPS to resolve load variations is highly dependent on the removal of extraneous signals, particularly within the horizontal components (Wahr et al., 2013). To better distinguish the signal attributed to the drought period, contributions of local and regional signals must be taken into account. We address this issue by first identifying well-behaved, long-running, GPS sites in the region. We analyze GPS station coordinate time-series data that are publicly available at the Nevada Geodetic Laboratory in the IGS14 reference frame (Blewitt et al., 2018). Stations are limited to those which recorded data for the entirety of the drought period as well as at least four years of data spanning the base period. Three stations, SLCU, ZLC1, and P057, meet the time requirements but exhibit unmodeled transients associated with local aquifer deformation (Hu & Bürgmann, 2020), and/or questionable monumentation. Consequentially, we consider 17 stations in our study area (Figure 2.1), including stations CEDA and COON, whose response to lake load variation was previously investigated by Elósegui et al. (2003). The considered stations provide good spatial coverage around the lake, with the exception of the western side of GSL where there are currently no stations installed.

Regional common mode variation in the GPS positions can alter the inferred displacement field and is a source of error for our study (Kreemer & Blewitt, 2021; Li et al., 2020; Márquez-Azúa & DeMets, 2003; Serpelloni et al., 2013). We are interested uniquely in how the GSL area affects the GPS positions and not how the positions may be affected by large-scale signals. We therefore use nineteen long-running regional stations outside our study area with limited data gaps (see inset of Figure 2.1, Table S2.2), to calculate the regional common mode component (CMC). Station timeseries are detrended, and the CMC is defined as the median position at each epoch and removed from our study timeseries. A comparison of GPS observations is shown in Figure 2.2d. These timeseries are detrended relative to the base period, with the common mode, annual, and semi-annual components removed. A consistent change in trend is present for the duration of the drought period in all three components. Each pair of stations are positioned on opposite sides of the lake, as identified in Figure 2.1, revealing east-west and north-south extension with vertical uplift.

To distinguish the unique displacements attributed to the drought period, long term trends, due to both tectonic and non-tectonic sources, must be removed from each timeseries. To achieve this goal we must identify a period which exhibits stable, consistent positions across its duration, hence our base period of 2004-2012. Across this period, GPS stations reveal only minor changes in trend as drought conditions vary, resulting in a consistent long term trend. Furthermore, GRACE TWS estimates remain very consistent during the base period and GSL exhibits low surface level variability. The combination of these factors provide the best opportunity to isolate the long term, steady rate attributed to external factors present across both the base and drought periods, thus isolating our specific drought signal.

Individual velocities of the cleaned timeseries, for both the base and drought periods, are calculated using MIDAS, and then differenced. The MIDAS algorithm is robust to outliers, steps, and annual signals in the timeseries. The extended duration of our base period, as well as the minimum requirement of four years of data, assists in ensuring the resulting rate is not affected by short term variations in drought conditions. The drought relative to base-period velocities are then multiplied by the duration of the drought period, identifying the net displacements unique to this timeframe.

The resulting GPS drought-specific displacement field shows motion consistent with an unloading signal centered on/near GSL (Figure 2.3, Table S2.3). Horizontal displacements exhibit extension across the lake. All stations exhibit vertical uplift, with the largest displacements at stations located closest to the lake. We note that stations to the south of the GSL exhibit more scatter than their counterparts to the north.

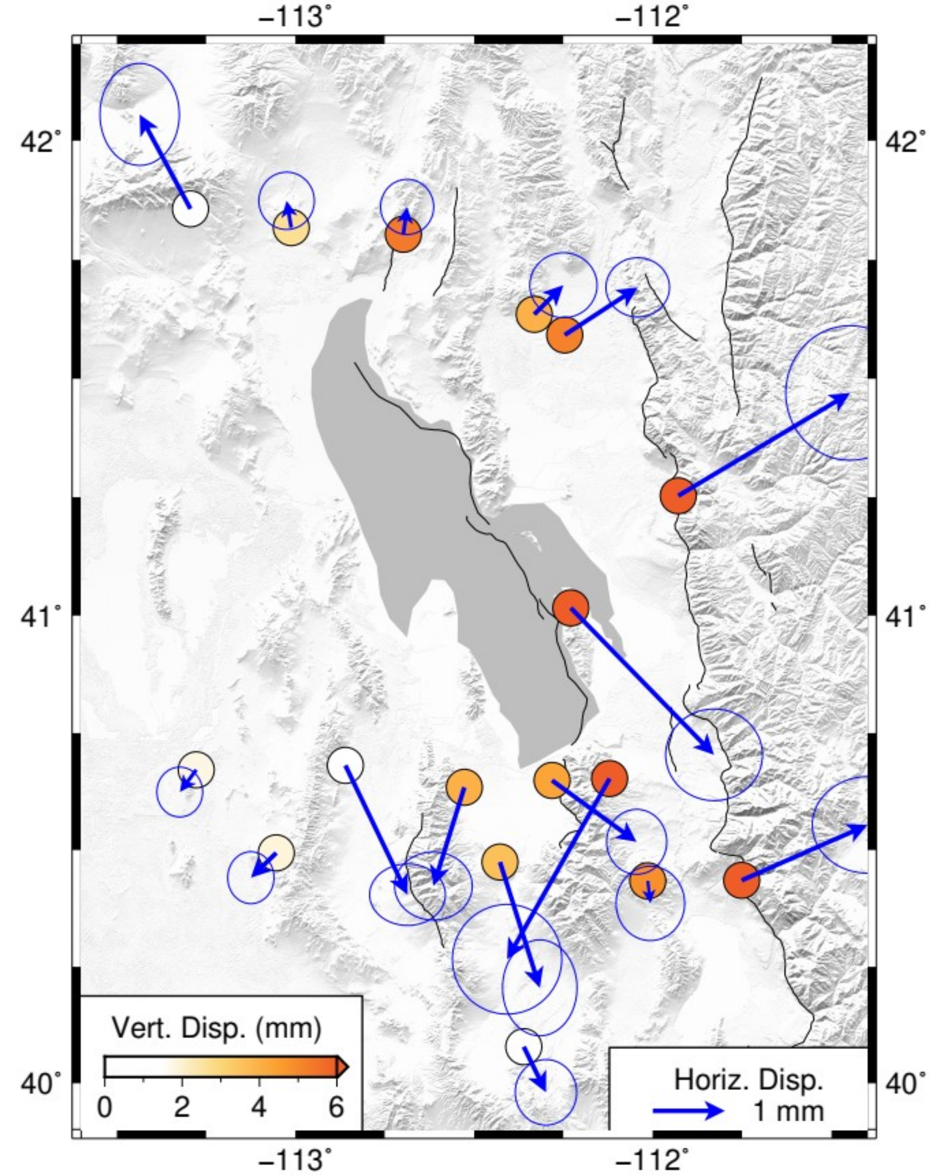

Figure 2.3: Observed GPS displacements for the drought period (2012 – 2016) relative to the base period (2004 – 2012). Blue arrows represent horizontal displacements with 95% confidence ellipses. Circles represent vertical displacements. Note that horizontal displacements exhibit extension centered on/near GSL, while the largest vertical displacements are located at stations nearest the lake.

2.7 Loading Models

2.7.1 Elastic Loading Model

To establish the relationship between observed GPS displacements and the signal attributed to load variations, we apply an elastic loading model. Homogeneous half-space models are often used for this goal (Amos et al., 2014; D’Urso & Marmo, 2013); however, Argus et al. (2017) showed that these models overestimate the displacements in the vertical component by a factor of ~2.5. This also affects the horizontal distribution of the uplift signal. Accurately calculating the vertical displacement field is key to the inversion as it can lead to underestimation of the net loading and poor interpretation of the distribution of mass. For this goal, we use the LoadDef software suite (Martens et al., 2019). LoadDef calculates displacements on a self-gravitating stratified sphere for a given Earth model and allows for complex geometries of the load distributions through the use of a user-defined template grid. This template grid calculates the response at a defined point to the users applied load model and allows the user to define the resolution in both the near and far fields. To ensure well defined edges of the applied load geometry, we supply LoadDef with applied load models on a regular grid at the spatial resolution of 0.005°x0.005° and the near field of the template grid is also defined at a resolution of 0.005°x0.005°. For our Earth model, we use the Preliminary Reference Earth Model (PREM) (Dziewonski & Anderson, 1981). While more detailed Earth models exist [e.g., CRUST 1.0 and CSEM (Fichtner et al., 2018; Laske et al., 2013)], the resulting GPS displacements differ by only fractions of a millimeter between the different Earth models, and estimated loads differ by only a few centimeters. We therefore retain PREM as our Earth model. A thorough description of the methods applied in LoadDef can be found in Martens et al. (2019).

2.7.2 Observed and Inferred GSL Load Models

Our first goal is to determine whether the unloading of GSL alone is able to produce the observed displacements at nearby GPS stations. We produce a load model in which all points within the bounds of the lake exhibit a uniform load of -1.89 m and calculate the resulting displacements at the GPS positions with LoadDef. The results indicate that the observed unloading significantly underestimates the observed GPS displacements (Figure S2.1, Table S2.4). While the orientation of the horizontal components compares well with the observations, the magnitude of the vertical component is severely underestimated. In order to determine the amount of load required to best explain both horizontal and vertical components, we invert for the load on the lake. To do so, Green’s functions are produced at the GPS sites by applying a uniform load of -1.00 m to the bounds of GSL to determine the respective 3D response vectors. These are then used in the inversion to estimate the load on GSL. The results obtain a significantly improved fit to the vertical component, however, the estimated load on GSL is -5.01 ± 0.26 m (Figure S2.2, Table S2.4). This is substantially larger than the -1.89 ± 0.04 m observed on the surface of the lake and unrealistic. While the orientation of the horizontal components are promising, we find that we cannot explain the observed GPS displacements with GSL loading alone. This, combined with the fact that substantially higher loads are required to fit the vertical component, suggests that additional mass loss exterior to GSL likely plays a significant factor in producing the observed unloading signal at the GPS stations.

2.7.3 Groundwater Model Setup

Because the effect of the drought does not end at the edge of the lake, our goal is to determine whether additional water loss around GSL contributes to the observed GPS displacements during the drought period. In the following two sections, we present two suites of groundwater models. The first investigates segmented load sections surrounding GSL, and in the second a range of radial load rings are tested which expand from the bounds of GSL. Both suites follow the same methodology described here.

Two constraints are applied to the distribution of loads within individual rings. First, contributions of load variation within bedrock units are assumed to be negligible, so loads are constrained to alluvial units, as identified by the Utah Geologic Unit Map (Hintze et al., 2000). Second, since the basement footwall side of the Wasatch fault to the east sits adjacent to sedimentary layers on the GSL side to the west, it therefore acts as a natural barrier to groundwater. Thus, we prevent loads from crossing the fault to the east.

For each unique distribution, individual load Green’s functions are calculated by supplying LoadDef with high resolution applied load grids. The resulting response vectors for each load are then used as individual parameters in the inversion to estimate the loads on GSL and surrounding groundwater regions. Finally, these estimated loads are used to produce a single high resolution load model, which is then passed to LoadDef to calculate the estimated displacements at the GPS sites.

Since we do not expect loads in adjacent segments or rings to differ wildly and because some load regions may contain too many or too few GPS observations, we include a Tikhonov regularization term in our inversion (e.g., Aster et al., 2013). The regularized least squares equation is shown in Equation 1 and our individual load solutions are shown in Equation 2.

$$min\ \|Gm - d\|_2^2 + \alpha\|Lm\|_2^2 \tag{1}$$

$$\mathrm{m}_\alpha = (G^T W G + \alpha L^T L)^{-1} G^T W d \tag{2}$$

Here *G* is our matrix of Green’s functions, *m* contains the loads we are inferring (as equivalent water thickness), *d* contains our observed GPS displacements, *W* is the weighting matrix built from the GPS observation uncertainties, *L* is the roughening matrix for the regularization, and *α* is the regularization parameter. To find the optimal balance between the regularization and the fit to the data, a range of *α* values are tested. We choose the best solution from the L-curve for each load distribution, which identifies the regularization parameter which minimizes the solution and residual norms.

2.7.4 Segmented Groundwater Models

Considering the non-uniform distribution of GPS stations around GSL, we first test groundwater distributions which take this into account. To do so, we investigate four distributions of groundwater loads (V1 through V4) in which we divide the area surrounding the lake based on the locations of the GPS observations (Figures S2.3-S2.6, Tables S2.5-S2.6). These segments are prepared with the goal to account for the distribution of the GPS stations as evenly as possible, with the number of segments ranging between nine, for segmented model V1, and three for V4. Since no data exist to the west of GSL, this region is omitted from these models.

We find that none of these models are able to estimate the load on GSL, with estimated loads well below the two sigma range. Furthermore, models V1-V3 each suggest positive loads to the southwest of GSL are necessary and exhibit the largest water loss in the eastern and southeastern segments where GPS data exhibit the largest vertical signal. Considering the severity of the drought, and the fact that decline in well water levels is observed throughout the entirety of the study area, we do not expect substantial positive loads at these scales to be realistic. While it is likely more water is lost within the eastern segments, as wells show generally higher deviations in these areas, the high estimated loads introduce large displacements in the east component, resulting in a poor fit to the horizontal components regionally. This indicates that at the resolution of these models, the vertical component dominates the inversion, resulting in positive loads in the western sections to balance the fit to the data. Estimation of groundwater loss at these resolutions is distinctly affected by the quantity and distribution of available GPS data. In order to fit both the horizontal and vertical components accurately, a lower resolution load distribution is necessary.

2.7.5 Parallel Load Ring Groundwater Model

Because of the aforementioned shortcoming of the segmented load models, we considered an alternative set of models which use parallel load rings surrounding the bounds of GSL. These rings benefit from the station distribution and receive information from all sides of the lake. This provides more insight into the regional trends in groundwater than the segmented models could provide. To determine to best distribution of ring loads, a suite of solutions is produced, in which up to three parallel load ring are tested with varying widths between 10 and 45 km. This randomization of ring distributions results in 1,889 unique ring load models tested in this study.

Our primary goal is to minimize the misfit to the displacements, but this does not guarantee the most realistic model, so a few considerations are taken into account to identify the preferred model. First, we omit solutions which exhibit ring loads greater than the inferred load on the lake. The individual loads represent an average load, applied evenly across the surface of each region. Although the average decline in water levels in the wells is higher than the load on the lake, these values indicate the presence of groundwater loss and are not directly comparable to the estimated loads since they are a function of the porosity in the host rock. Considering this, GSL is likely to exhibit the highest average rate of load variation due to direct evaporation from the surface of GSL itself. Groundwater observations reveal spatial variability in the distribution of loads, indicating non-uniform load variation exterior to the lake. The average load across the surface of each ring is likely to be lower than localized well observations and lower than the uniform load change on the lake. Similarly, due to the intensity of the drought and well observations, we do not expect rings to exhibit average net positive loads. Non-positivity is not enforced in the inversion, but solutions with positive loads are simply removed from these results. Of the remaining solutions, we identify those that best minimize the data misfit and also have a GSL load comparable to that observed during the drought (i.e. within the range of -1.89 ± 0.15 m).

We find that our preferred model estimates a load of -1.85 ± 0.33 m on the GSL and provides a good fit to both the horizontal and vertical GPS displacements observed, with a 3D RMS misfit of 1.73 mm (Figure 2.4, Table S2.7). This model exhibits two radial load rings. An inner ring of 24 km width with a load of -1.16 ± 0.20 m, and an outer ring of 40 km width with a load of -0.32 ± 0.14 m. The load inferred on the lake itself is very close to the observed -1.89 ± 0.04 m. Inclusion of the groundwater loads provide a more disperse vertical uplift signal and significantly improves the fit to the vertical displacements. This results in a net improvement in the 3D GPS misfit of 30.5%, compared to the model that fixed the observed lake level decline solely to the bounds of the lake. The regularization parameter for our preferred model is 1.75, with the solution sitting well on the corner of the trade-off curve. A comparison of the preferred ring model to the observed and inferred lake only models is shown in Table 2.1. While the volume inferred on the lake is comparable to that observed (i.e., 5.5 ± 1.0 km^3 versus the observed 5.58 ± 0.11 km^3), the combined volume attributed to groundwater loss surrounding the GSL is twice the lake loss at 10.9 ± 2.8 km^3, spread over an area nearly six times larger than GSL, resulting in a combined model volume of -16.5 ± 3.8 km^3. This is nearly five times the volume observed within the spatial resolution of GRACE. The volume we find is consistent across the full set of ring model solutions with a median volume of -15.92 ± 0.71 km^3, at 95% confidence.

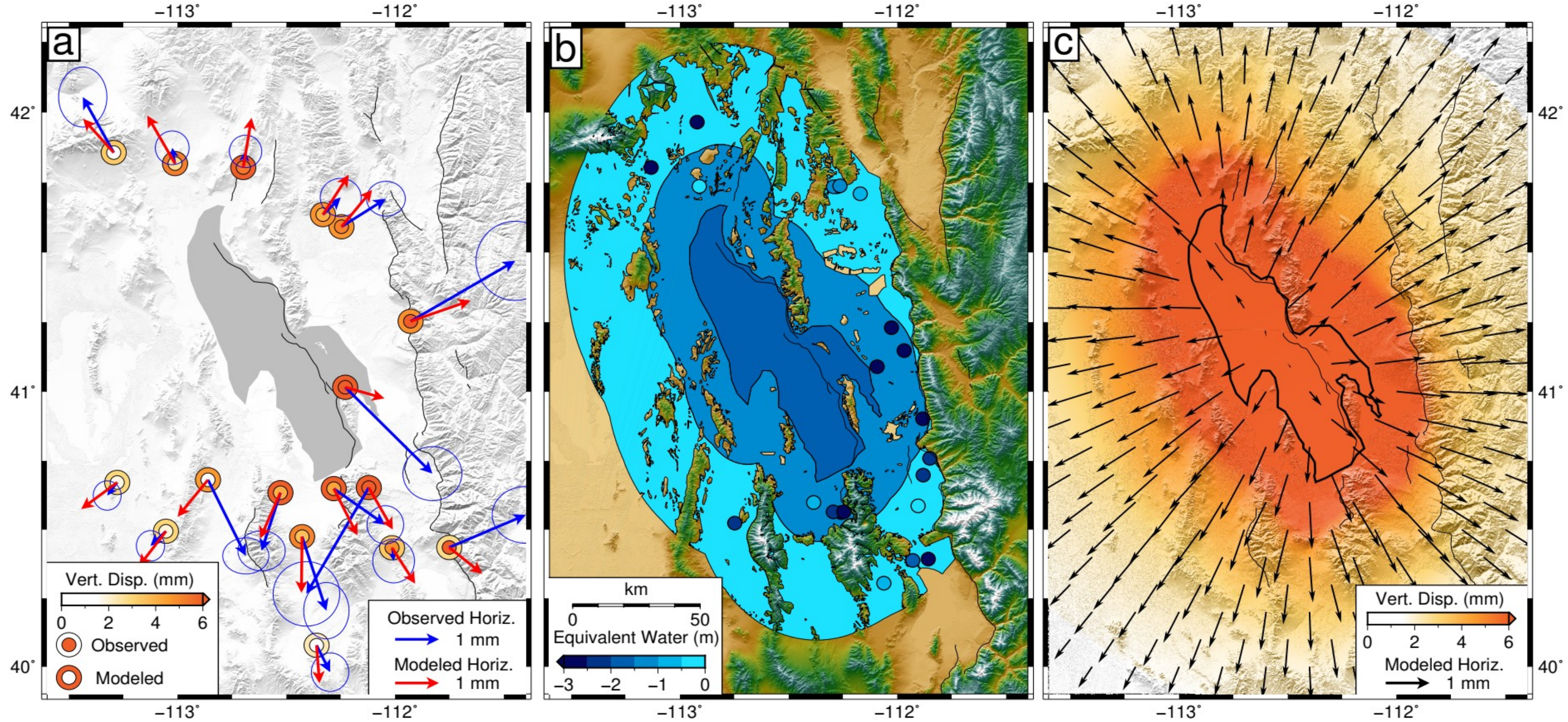

Figure 2.4: Displacements and distribution of the preferred load model. This model includes the load on GSL and two rings of groundwater at widths of 24 km (inner ring) and 40 km (outer ring). **a)** Comparison of observed and modeled displacements at GPS stations. Blue arrows represent observed horizontal displacements with 95% confidence ellipses. Red arrows represent modeled horizontal displacements. Inner circles represent the observed GPS displacements, while outer circles represent modeled displacements. Faults are represented as thin black lines. The data misfit for this model is 1.73 mm. **b)** Inferred load distribution. Polygon shading represents the load inferred for GSL and two additional rings. GSL load is inferred at -1.85 ± 0.33 m, the inner ring at -1.16 ± 0.20 m, and the outer ring at -0.32 ± 0.14 m. Circles represent changes in groundwater levels observed at wells, with the same color scale as the ring loads. **c)** Modeled displacement field on a grid. Black arrows show horizontal displacements while the background shading shows vertical displacements. The bounds of GSL are shown as the thick black line.

Table 2.1: Comparisons between the observed GSL load model (fixed to -1.89 m), the solved GSL load model (inferred at -5.01 m), and the preferred ring model.

Model	Region	Load (m)	Volume (km^3)	3D RMS (mm)
Observed GSL	GSL	-1.89 ± 0.04	-5.58 ± 0.11	2.49
Solved GSL	GSL	-5.01 ± 0.26	-14.8 ± 0.8	1.85
Preferred Ring Model	GSL	-1.85 ± 0.33	-5.5 ± 1.0	1.73
	Ring 1 – 24 km	-1.16 ± 0.20	-7.5 ± 1.3	
	Ring 2 – 40 km	-0.32 ± 0.14	-3.5 ± 1.5	
		Total Volume	-16.5 ± 3.8	

2.8 Regional Seismicity Modulation

We next assess whether the drought-modulated load variations on the Earth's surface is reflected in spatio-temporal variations in seismicity in our study area. We use the Utah Authoritative Region earthquake catalog for 1981 – 2020. Prior to our analysis, the catalog was declustered following Zaliapin & Ben-Zion (2020). Events are limited to only mainshocks that occur to the west of the Wasatch fault. While studies have identified strong correlations between seasonal water level variation and seismicity (Amos et al., 2014; Craig et al., 2017; Kreemer & Zaliapin, 2018), we find no evidence of annual seismicity modulation, in agreement with the findings of Hu & Bürgmann (2020), so we inspect the catalog for evidence of temporally variable, drought-cycle induced seismicity modulation. To allow for an equal assessment of seismicity during wet and dry periods, we cut the catalog to the period of 1987.1 – 2020, in which there are equal timeframes where the PDSI indicates either wet or dry periods. The distribution of earthquakes is shown in Figure 2.5. Earthquakes are primarily located to the northeast of the lake near the Hansel Valley, Hansel Mountain, and North Promontory faults, and to the south of the lake along the Wasatch fault. Events occurring within the bounds of the lake occur near the ends of the Great Salt Lake fault zone, which runs NW–SE along the eastern edge of the lake and dips to the west.

The trimmed catalog is separated into two sets. The first are those events which occur within the load of the preferred model, shown in light blue. The second reflects the events occurring outside the load region. For an objective comparison of earthquakes occurring inside and outside of the load, the area of the outside region is constrained to be equivalent to that of the load region. Due to the sparsity of events to the west of GSL, the outside region is mostly limited to the area north of the GSL (i.e., up to 42.5°) and south of the GSL. Finally, we set a conservative magnitude cutoff of 1.3, inferred from an inspection of the cumulative and non-cumulative distribution of events within our region. This cutoff magnitude is comparable the findings of Pankow (2004), who found a cutoff magnitude of 1.2 for the GSL basin for the period of 2000 – 2003.

Following these criteria, the cumulative number of events in the study area (i.e., the defined inside and outside areas) between 1987.1 and 2020 is 1,345. We then separate these events depending on whether they occurred during dry and wet periods and whether they are in the area inside or outside the load. This reveals that inside the load area, earthquakes occur ~20% more frequently when the region is experiencing drier conditions, while outside the load area there only being ~2% more events during drier periods (Table 2.2). While the number of events in this catalog is fairly small, we find that the observed ratio of events during dry over wet periods for the load region is well above the 95%, 1-sided confidence level, following 100,000 temporal randomizations of the catalog. The same ratio outside of the load is not statistically significant. The prevalence of earthquakes during dry time periods identifies modulation of seismicity likely associated with fault unloading due to the reduced mass on the Earth’s surface within the load region during dry periods.

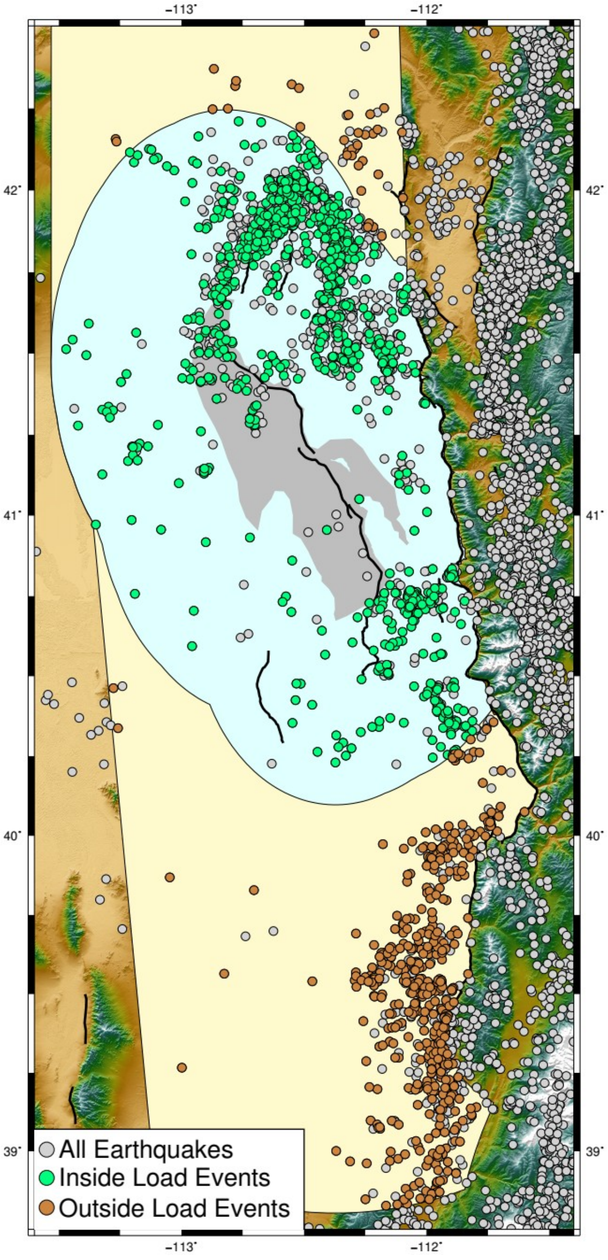

Figure 2.5: Distribution of regional earthquakes for 1987.1 – 2020. Light blue polygon shows the preferred model load distribution. Light yellow polygon defines the region used to identify earthquakes outside of the load region. The area of this region is equivalent to the area of the modeled load and the northern section ends at 42.5° N. All regional earthquakes are shown as grey circles, those inside of the load and greater than M_W 1.3 are shown as green circles, and those chosen outside of the load and greater than M_W 1.3 are shown as brown circles.

Table 2.2: Regional earthquakes for the timeframe of 1987.1 – 2020. Dry and wet periods are defined by the PDSI value at the time of the events. Expected median and confidence ratio are calculated from 100,000 randomizations of the catalog. The inside load exhibits significantly more events during dry periods than during wet periods.

Earthquake Counts by Region	Dry Periods	Wet Periods	Expected Median	Observed Ratio	95% Confid. in expected Ratio
Inside Load	444	369	406	1.20	1.15
Outside Load	269	263	266	1.02	1.19
Combined	713	632	672	1.13	1.12

To further investigate the temporal aspect of the seismicity near the GSL, we compare the relationship between the surface elevation rate of the lake and the seismicity rate, shown in Figure 2.6. Each dataset is smoothed with a 3-year moving window to identify long term trends. Regional PDSI is shown in the background, indicating periods of relative dryness and wetness in the study area. Periods which exhibit drier conditions see an increase in seismicity rate as the lake level recedes, and the inverse occurs as the lake fills. Notably, the earthquake rate exhibits periods of distinct trends which are consistent and unique for each individual period. The relationship between the timing of these rate changes is illuminated when compared to the rate of GSL surface elevation change. We see a temporal relationship between changes in the trend of seismicity rate and the inflection of the GSL surface elevation rate. As the surface elevation rate changes sign, a change in the trend of the rate of earthquakes is closely observed. Increasing seismicity trend changes are tied to periods when the lake exhibits negative rates and decreasing seismicity trends relate to periods when the lake is filling. These results further indicate a close relationship between the trends of mass fluctuation within the GSL basin and seismicity.

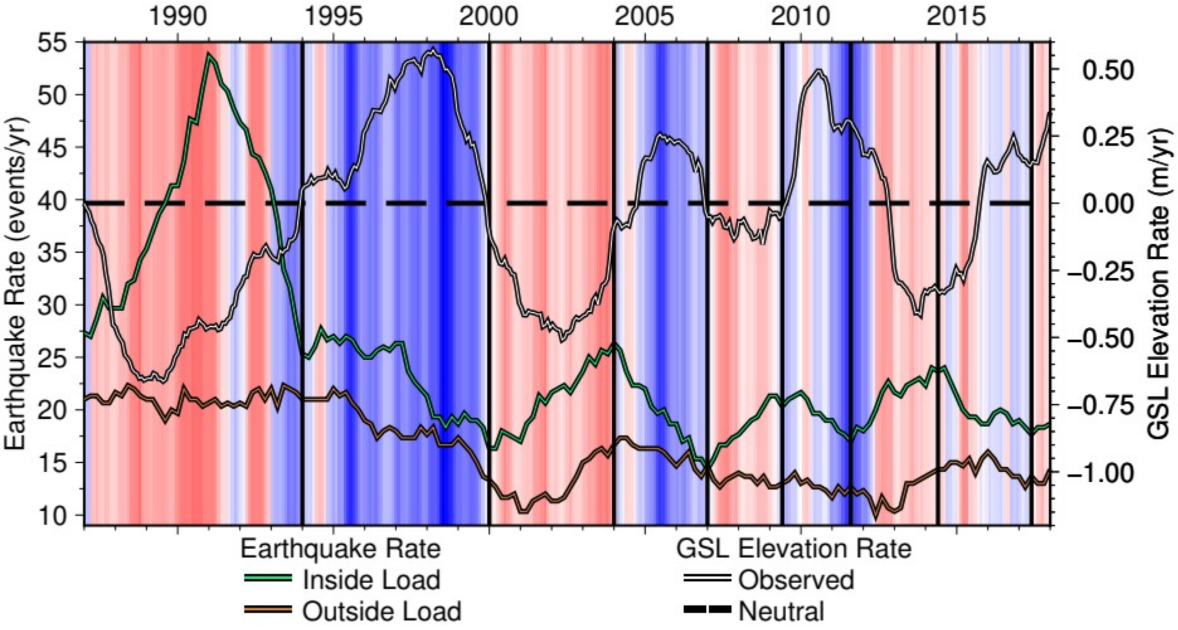

Figure 2.6: Comparison of earthquake rates for the inside (green) and outside (brown) load regions with the rate of lake elevation change over time (white). Each dataset has been smoothed with a 3-year moving window. Background shading shows PDSI values, scale as shown in Figure 2.2. Black dashed line represents the neutral line of the GSL elevation rate. Vertical black lines indicate breakpoints for periods of unique trends in the earthquake rate in the inside load area. Note that the timing of the GSL elevation rate inflection often closely matches the timing of changes in the trends of the earthquake rate for the inside load region. Those periods which do not match the inflection better match switches in the PDSI. The outside load region shows minimal variation with the exception of the 1999 – 2004 period.

2.9 Discussion

We find that the observed drought-induced GPS displacements can best be described by the presence of additional groundwater mass loss surrounding the GSL. When inverting only for the load on GSL itself, we find an unrealistic load on the GSL that is 2.65 times higher than what is observed from the lake level decline. In our preferred ring model, which includes mass loss outside the GSL, we resolve the observed unloading of GSL between 2012 and 2016. It is possible to produce a ring model which estimates the load on the lake from the vertical component only, but the 3D inversion produces more consistent estimates. The median GSL load estimate is -1.87 ± 0.15 m compared to -1.75 ± 0.22 m for the vertical only ring models. Furthermore, the vertical-only inversion produces higher ring estimates. The balance between reduced GSL load estimates and increased ring load estimates, indicates a bias due to the distribution of GPS sites, which is addressed by the inclusion of the horizontal components. An over-emphasis on fitting the vertical data is also observed in the segmented models and none of the segmented models could resolve the lake load. We see that the full 3D inversion better localizes the mass to the lake and produces more consistent results.

The estimated volume of water loss is substantial, at 16.4 ± 3.8 km^3, with a ratio of groundwater to surface water volume of 2:1. Differences between the GRACE estimated volume of 3.48 ± 0.21 km^3 and the observed lake volume loss of 5.58 ± 0.11 km^3 can be explained by the spatial resolution of GRACE; however, this still leaves significant additional water level variation observed at nearby wells unaccounted for, resulting in a possibly even larger discrepancy between the GRACE estimate and the true change. All three interpretations of the well data find an average water level change within Ring 1 near -3 m and less water loss in Ring 2 (Table 2.3). Without knowledge of the storativity of the aquifers, direct comparison to the load estimates is not possible, however, we note that the ratio of well water loss between the two rings is comparable to the ratio inferred by our model (with 3 – 4 times higher change in water level within the inner ring compared to the outer ring) when the well change is estimated by MIDAS or net difference approaches. While the well observations show that some localized areas exhibit large changes in groundwater levels, they also show a wide range of observed water displacement. Considering that wells are primarily located where water levels are most observable or intriguing, it is likely that water levels in wells reflect above average loss of water compared to the entire surface area of the inferred rings. Furthermore, our inferred rings reflect area averaged loads, which provides insight into the net magnitude of water loss required to explain the GPS displacements, but underestimates the complexity of the real mass distribution. While we refer to our loads as groundwater, we make no distinction to the specific location of the mass and the estimated loads reflect net mass loss in the column below the surface of the load from any source. Although the soil moisture data does not reflect statistically significant trends during the drought, it is likely to play a minor role and is combined with our estimated loads. We note that GPS uplift is significantly less to the west of the GSL than east of the GSL (Figure 2.3), which may reflect greater water loss closer to the Wasatch fault and our inferred load rings provide a more regionally averaged estimate. The segmented models estimate larger loads in this region, but due to network configuration, were unable to produce regionally realistic results as positive loads were required to balance the fit to the data. To better infer the complexity of the true load distribution in future studies, a significantly higher density of long running GPS stations is required than are currently installed to resolve complex load distributions.

Table 2.3: Comparison of observed groundwater level changes with respect to location within the inferred load rings. Three methods are tested to quantify the observed water deviation during the drought: the Theil-Sen slope estimate, the MIDAS algorithm, and a net difference between the start and end of the drought. For the Theil-Sen and MIDAS solutions, only wells with water level differences greater than two sigma are presented. The net difference solutions take the difference in the average position of 2012 ± 0.1 and 2016 ± 0.1. Each method finds a higher average water loss within the bounds of Ring 1 compared to Ring 2. The ring ratios for both MIDAS and net difference approaches is comparable to the ratio of the ring loads inferred in our model.

Method	Location	Number of Wells	Mean Water Level Change (m)	Median Water Level Change (m)	Water Level Range (m)	
Theil-Sen	Ring 1	9	-3.25	-2.98	-6.21	-0.28
	Ring 2	13	-2.39	-1.77	-9.34	-0.45
MIDAS	Ring 1	4	-3.04	-3.78	-4.37	-0.25
	Ring 2	5	-0.77	-0.11	-3.16	0.32
Net Difference 2012 - 2016	Ring 1	9	-2.98	-2.47	-7.34	-0.24
	Ring 2	13	-1.00	-1.00	-3.87	0.61

Vertical displacements associated with loading signals are largest near the center of the load, while horizontal displacements reach their maximum at the edges of the load (e.g., Becker & Bevis, 2004). Consequently, extension or contraction is expected within the load bounds, depending on the sign of the signal, with the largest change in vertical stresses directly under the load. In the presence of listric normal faults [e.g., the Wasatch fault zone as suggested by Pang et al. (2020) and Savage et al. (1992)], the role of vertical stresses on faults is increased at depth when the fault dip becomes shallower (i.e., less than 45°). Since the majority of events within the catalog are at depths deeper than 2 km below sea level (i.e. the depth at which Pang et al. (2020) suggests the fault becomes shallower than 45°), we expect higher quantities of events during drier periods, due to the reduction of vertical stresses on the faults cutting underneath the load at depth. This matches well with our findings (Table 2.2), and we observe the strongest distinction between the inside and outside regions with this load distribution. If the actual load were constrained closer to the bounds of the lake, or to a much wider region around GSL, such a distinction between dry and wet events would not be clear at this specific radial distance. The observed seismicity modulation may therefore corroborate the spatial extent of the load implied by our model. While a cutoff magnitude of 1.3 is used in this study, observed seismicity trends are also found when using magnitudes above 0.8, but they are only significant (at the 95% confidence level) when considering events with magnitudes above 1.2 (Figure S2.7). In fact, the higher the cutoff magnitudes we consider, the higher the difference between dry and wet events within the load region, while the events outside the load continue to reflect no significant trends.

Comparison of the earthquake rates to lake elevation rates highlights long-term seismicity modulation in the region (Figure 2.6). A clear distinction exists between inside and outside load events, with those inside exhibiting significant levels of anti-correlation, at a value of -0.49 ± 0.23, and those outside showing no relationship, at a value of -0.14 ± 0.23, following 100,000 randomizations of the catalog. Changes in the trend of earthquake rate in the region alter when the rate of GSL surface elevation changes sign. That is, as the lake shifts from losing water to gaining water, the seismicity rate changes from negative to positive. These trends are consistent between inversions of the lake elevation rate and are unique for each time period, supporting an inverse relationship between load variation and seismicity.

This study advances the findings of Elósegui et al., 2003, and further distinguishes the contribution the GSL and surrounding groundwater make to regional water loss during droughts. As noted in their study, load geometry plays a significant role in best explaining the GPS observations and the placement of loads determines which signals will be constructive or deconstructive at each site. Significantly higher complexity of load distribution is applied in this study than their two disk model; however, the real distribution of groundwater loads is undoubtedly still more complex. This likely explains some of the residuals exhibited at GPS sites to the south of the GSL where wells exhibit increased spatial variability of water level change and localized aquifers have been shown to alter the deformation field (Hu & Bürgmann, 2020). Nevertheless, the simple distribution of surface averaged groundwater loss in addition to the unloading of the GSL, provides significant improvement to the interpretation of GPS data near the GSL. The results of this study highlight that mass variability on local scales have a significant impact on GPS timeseries and must be accounted for when, for example, using those data to infer secular loading rates on nearby faults.

2.10 Conclusions

The results presented in this study find that GPS data are able to detect and localize mass loss within the GSL basin and that the regional extent of inferred water loss during the drought period is supported by both regional seismicity variations and well observations. Inclusion of two surface averaged groundwater rings in the inversion, covering a radial distance of 64 km from the lake, significantly improves the fit to the 3D GPS observations. We find the inferred groundwater loss to be substantial (10.9 ± 2.8 km^3), at twice the volume observed on the lake (5.58 ± 0.11 km^3), and are able to recover the lake observation with an inferred lake volume loss of 5.5 ± 1.0 km^3. The modeled ratio of groundwater to surface water estimates is comparable to the findings of Castle et al. (2014) and Ojha et al. (2019) in which groundwater loss exceeded surface water loss at a rate 1.89 – 4.79 times higher, during the same drought. Additionally, wells within our inferred load region corroborate the presence of significant water level decline, and the ratio between average well water levels and inferred loads, between the inner and outer rings, are comparable.

We find that earthquakes within the load region occur during dry versus wet periods ~20% more frequently, and that the earthquake rate is anti-correlated with the lake elevation rate, with a coefficient of -0.49 ± 0.23. Events outside the load show no significant relationships. These results reveal a long-term relationship between the distribution and variation of loads with stresses on faults, resulting in drought-cycle influenced seismicity modulation within the loaded region.

Our study benefits greatly from the distribution of long running GPS stations near the GSL, which directly improved the performance of the inversion and advances the finding of Elósegui et al., 2003; however, we also present limitations for the maximum resolvability of the network during this time. Future modeling of load variation on and near GSL will be significantly improved by the quantity of GPS stations which have been installed in the past 10 years, although there remains no nearby GPS sites to the west of the lake. Additionally, expansion of the GPS network will reduce uncertainty in load estimates, allowing for more complex load geometries. Our case study for the GSL highlights how regional GPS networks are particularly well suited to identify water loss in similarly sized lakes and reservoirs during drought periods. Continued expansion of GPS networks will further allow water management authorities to identify and quantify regional variation in water storage and its redistribution.

2.11 Acknowledgments

We thank H. Martens for her help with the LoadDef software and I. Zaliapin for declustering the earthquake catalog. Our manuscript was greatly improved by comments from M. Shirzaei and an anonymous reviewer. We are grateful for UNAVCO for the maintenance of the NOTA GPS stations and making the data freely available. This work was supported by NSF grant EAR1615253 and NASA Earth Surface and Interior grant 80NSSC19K1044 to CK and GB. All figures were produced using Generic Mapping Tools (Wessel et al., 2013).

2.12 Data Availability Statement

GPS timeseries are available from the Nevada Geodetic Laboratory at geodesy.unr.edu/gps_timeseries/ (Blewitt et al., 2018). GSL surface elevation data can be found courtesy of the USGS at https://waterdata.usgs.gov/nwis/sw, and groundwater well data from the National Ground-Water Monitoring Network through the data portal at https://cida.usgs.gov/ngwmn/. NLDAS solutions are available through the GES DISC at https://disc.gsfc.nasa.gov/datasets/NLDAS_NOAH0125_M_002/summary. PDSI data from the West Wide Drought Tracker can be downloaded at https://wrcc.dri.edu/wwdt/batchdownload.php. CSR, GFZ, and JPL GRACE RL06 solutions are available through the PODAAC archive (NASA Jet Propulsion Laboratory (JPL), 2019a, 2019b, 2019c). The earthquake catalog can be found through the University of Utah at https://quake.utah.edu/earthquake-information-products/earthquake-catalogs.

MIDAS software is available at http://geodesy.unr.edu/ (Blewitt et al., 2016), and the LoadDef software is available at https://github.com/hrmartens/LoadDef (Martens et al., 2019).

2.13 References

Abatzoglou, J. T., McEvoy, D. J., & Redmond, K. T. (2017). The West Wide Drought Tracker: Drought Monitoring at Fine Spatial Scales. *Bulletin of the American Meteorological Society*, *98*(9), 1815–1820. https://doi.org/10.1175/BAMS-D-16-0193.1

Amos, C. B., Audet, P., Hammond, W. C., Bürgmann, R., Johanson, I. A., & Blewitt, G. (2014). Uplift and seismicity driven by groundwater depletion in central California. *Nature*, *509*(7501), 483–486. https://doi.org/10.1038/nature13275

Argus, D. F., Landerer, F. W., Wiese, D. N., Martens, H. R., Fu, Y., Famiglietti, J. S., et al. (2017). Sustained Water Loss in California's Mountain Ranges During Severe Drought From 2012 to 2015 Inferred From GPS. *Journal of Geophysical Research: Solid Earth*, *122*(12), 10,559-10,585. https://doi.org/10.1002/2017JB014424

Aster, R., Borchers, B., & Thurber, C. (2013). Chapter Four - Tikhonov Regularization. In *Parameter Estimation and Inverse Problems* (Second Edition, p. Pages 93-127). Academic Press.

Becker, J. M., & Bevis, M. (2004). Love's problem. *Geophysical Journal International*, *156*(2), 171–178. https://doi.org/10.1111/j.1365-246X.2003.02150.x

Blewitt, G., Kreemer, C., Hammond, W. C., & Gazeaux, J. (2016). MIDAS robust trend estimator for accurate GPS station velocities without step detection. *Journal of Geophysical Research: Solid Earth*, *121*(3), 2054–2068. https://doi.org/10.1002/2015JB012552

Blewitt, G., Hammond, W., & Kreemer, C. (2018). Harnessing the GPS Data Explosion for Interdisciplinary Science. *Eos*, *99*. https://doi.org/10.1029/2018EO104623

Borsa, A. A., Agnew, D. C., & Cayan, D. R. (2014). Ongoing drought-induced uplift in the western United States. *Science*, *345*(6204), 1587–1590. https://doi.org/10.1126/science.1260279

Castle, S. L., Thomas, B. F., Reager, J. T., Rodell, M., Swenson, S. C., & Famiglietti, J. S. (2014). Groundwater depletion during drought threatens future water security of the Colorado River Basin. *Geophysical Research Letters*, *41*(16), 5904–5911. https://doi.org/10.1002/2014GL061055

Craig, T. J., Chanard, K., & Calais, E. (2017). Hydrologically-driven crustal stresses and seismicity in the New Madrid Seismic Zone. *Nature Communications*, *8*(1), 2143. https://doi.org/10.1038/s41467-017-01696-w

D'Urso, M. G., & Marmo, F. (2013). On a generalized Love's problem. *Computers & Geosciences*, *61*, 144–151. https://doi.org/10.1016/j.cageo.2013.09.002

Dziewonski, A. M., & Anderson, D. L. (1981). Preliminary reference Earth model. *Physics of the Earth and Planetary Interiors*, *25*(4), 297–356. https://doi.org/10.1016/0031-9201(81)90046-7

Elósegui, P., Davis, J. L., Mitrovica, J. X., Bennett, R. A., & Wernicke, B. P. (2003). Crustal loading near Great Salt Lake, Utah. *Geophysical Research Letters*, *30*(3). https://doi.org/10.1029/2002GL016579

Famiglietti, J. S. (2014). The global groundwater crisis. *Nature Climate Change*, *4*(11), 945–948. https://doi.org/10.1038/nclimate2425

Famiglietti, J. S., Lo, M., Ho, S. L., Bethune, J., Anderson, K. J., Syed, T. H., et al. (2011). Satellites measure recent rates of groundwater depletion in California's Central Valley. *Geophysical Research Letters*, *38*(3). https://doi.org/10.1029/2010GL046442

Famiglietti, James S., & Rodell, M. (2013). Water in the Balance. *Science*, *340*(6138), 1300–1301. https://doi.org/10.1126/science.1236460

Fichtner, A., van Herwaarden, D.-P., Afanasiev, M., Simutė, S., Krischer, L., Çubuk-Sabuncu, Y., et al. (2018). The Collaborative Seismic Earth Model: Generation 1. *Geophysical Research Letters*, *45*(9), 4007–4016. https://doi.org/10.1029/2018GL077338

Fu, Y., Argus, D. F., Freymueller, J. T., & Heflin, M. B. (2013). Horizontal motion in elastic response to seasonal loading of rain water in the Amazon Basin and monsoon water in Southeast Asia observed by GPS and inferred from GRACE: HORIZONTAL SEASONAL MOTIONS BY GPS/GRACE. *Geophysical Research Letters*, *40*(23), 6048–6053. https://doi.org/10.1002/2013GL058093

Gleeson, T., Wada, Y., Bierkens, M. F. P., & van Beek, L. P. H. (2012). Water balance of global aquifers revealed by groundwater footprint. *Nature*, *488*(7410), 197–200. https://doi.org/10.1038/nature11295

Hassibe, W. R., & Keck, W. G. (1991). *The Great Salt Lake*. U.S Department of the Interior, U.S. Geological Survey. Retrieved from https://books.google.com/books?id=F13LpLqW-EwC

Hintze, L., Willis, G., Laes, D., Sprinkel, D., & Brown, K. (2000). DIGITAL GEOLOGIC MAP OF UTAH Compiled by.

Hu, X., & Bürgmann, R. (2020). Aquifer deformation and active faulting in Salt Lake Valley, Utah, USA. *Earth and Planetary Science Letters*, *547*, 116471. https://doi.org/10.1016/j.epsl.2020.116471

Huber, P. (1981). *Robust statistics*. Wiley, New York.

Kreemer, C., & Blewitt, G. (2021). Robust estimation of spatially varying common-mode components in GPS time-series. *Journal of Geodesy*, *95*(1), 13. https://doi.org/10.1007/s00190-020-01466-5

Kreemer, C., & Zaliapin, I. (2018). Spatiotemporal Correlation Between Seasonal Variations in Seismicity and Horizontal Dilatational Strain in California. *Geophysical Research Letters*, *45*(18), 9559–9568. https://doi.org/10.1029/2018GL079536

Landerer, F. W., & Swenson, S. C. (2012). Accuracy of scaled GRACE terrestrial water storage estimates. *Water Resources Research*, *48*(4). https://doi.org/10.1029/2011WR011453

Laske, G., Masters, G., Ma, Z., & Pasyanos, M. (2013). Update on CRUST1.0 - A 1-degree global model of Earth's crust. *Abstract EGU2013-2658 Presented at 2013 Geophys. Res. Abstracts 15*, *15*, 2658.

Li, W., Jiang, W., Li, Z., Chen, H., Chen, Q., Wang, J., & Zhu, G. (2020). Extracting Common Mode Errors of Regional GNSS Position Time Series in the Presence of Missing Data by Variational Bayesian Principal Component Analysis. *Sensors*, *20*(8), 2298. https://doi.org/10.3390/s20082298

Márquez-Azúa, B., & DeMets, C. (2003). Crustal velocity field of Mexico from continuous GPS measurements, 1993 to June 2001: Implications for the neotectonics of Mexico. *Journal of Geophysical Research: Solid Earth*, *108*(B9). https://doi.org/10.1029/2002JB002241

Martens, H. R., Rivera, L., & Simons, M. (2019). LoadDef: A Python-Based Toolkit to Model Elastic Deformation Caused by Surface Mass Loading on Spherically Symmetric Bodies. *Earth and Space Science*, *6*(2), 311–323. https://doi.org/10.1029/2018EA000462

Mocko, D. (2012). NLDAS Noah Land Surface Model L4 Monthly 0.125 x 0.125 degree, Version 002 [Data set]. NASA Goddard Earth Sciences Data and Information Services Center. https://doi.org/10.5067/NOXZSD0Z6JGD

NASA Jet Propulsion Laboratory (JPL). (2019a). CSR TELLUS GRACE Level-3 Monthly LAND Water-Equivalent-Thickness Surface-Mass Anomaly Release 6.0 in netCDF/ASCII/Geotiff Formats [Data set]. NASA Physical Oceanography DAAC. https://doi.org/10.5067/TELND-3AC06

NASA Jet Propulsion Laboratory (JPL). (2019b). GFZ TELLUS GRACE Level-3 Monthly LAND Water-Equivalent-Thickness Surface-Mass Anomaly Release 6.0 in netCDF/ASCII/Geotiff Formats [Data set]. NASA Physical Oceanography DAAC. https://doi.org/10.5067/TELND-3AG06

NASA Jet Propulsion Laboratory (JPL). (2019c). JPL TELLUS GRACE Level-3 Monthly LAND Water-Equivalent-Thickness Surface-Mass Anomaly Release 6.0 in netCDF/ASCII/Geotiff Formats [Data set]. NASA Physical Oceanography DAAC. https://doi.org/10.5067/TELND-3AJ06

NGWMN. (2020). National Ground-Water Monitoring Network. Retrieved January 19, 2021, from https://cida.usgs.gov/ngwmn/

Ojha, C., Werth, S., & Shirzaei, M. (2019). Groundwater Loss and Aquifer System Compaction in San Joaquin Valley During 2012–2015 Drought. *Journal of Geophysical Research: Solid Earth*, *124*(3), 3127–3143. https://doi.org/10.1029/2018JB016083

Pang, G., Koper, K. D., Mesimeri, M., Pankow, K. L., Baker, B., Farrell, J., et al. (2020). Seismic Analysis of the 2020 Magna, Utah, Earthquake Sequence: Evidence for a

Listric Wasatch Fault. *Geophysical Research Letters*, *47*(18), e2020GL089798. https://doi.org/10.1029/2020GL089798

Pankow, K. L. (2004). Triggered Seismicity in Utah from the 3 November 2002 Denali Fault Earthquake. *Bulletin of the Seismological Society of America*, *94*(6B), S332–S347. https://doi.org/10.1785/0120040609

Pekel, J.-F., Cottam, A., Gorelick, N., & Belward, A. S. (2016). High-resolution mapping of global surface water and its long-term changes. *Nature*, *540*(7633), 418–422. https://doi.org/10.1038/nature20584

Rodell, M., & Famiglietti, J. S. (1999). Detectability of variations in continental water storage from satellite observations of the time dependent gravity field. *Water Resources Research*, *35*(9), 2705–2723. https://doi.org/10.1029/1999WR900141

Rodell, M., Famiglietti, J. S., Wiese, D. N., Reager, J. T., Beaudoing, H. K., Landerer, F. W., & Lo, M.-H. (2018). Emerging trends in global freshwater availability. *Nature*, *557*(7707), 651–659. https://doi.org/10.1038/s41586-018-0123-1

Rodell, Matthew, Velicogna, I., & Famiglietti, J. S. (2009). Satellite-based estimates of groundwater depletion in India. *Nature*, *460*(7258), 999–1002. https://doi.org/10.1038/nature08238

Russo, T. A., & Lall, U. (2017). Depletion and response of deep groundwater to climate-induced pumping variability. *Nature Geoscience*, *10*(2), 105–108. https://doi.org/10.1038/ngeo2883

Sakumura, C., Bettadpur, S., & Bruinsma, S. (2014). Ensemble prediction and intercomparison analysis of GRACE time-variable gravity field models. *Geophysical Research Letters*, *41*(5), 1389–1397. https://doi.org/10.1002/2013GL058632

Savage, J. C., Lisowski, M., & Prescott, W. H. (1992). Strain accumulation across the Wasatch Fault near Ogden, Utah. *Journal of Geophysical Research: Solid Earth*, *97*(B2), 2071–2083. https://doi.org/10.1029/91JB02798

Scanlon, B. R., Faunt, C. C., Longuevergne, L., Reedy, R. C., Alley, W. M., McGuire, V. L., & McMahon, P. B. (2012). Groundwater depletion and sustainability of irrigation in the US High Plains and Central Valley. *Proceedings of the National*

Academy of Sciences, *109*(24), 9320–9325. https://doi.org/10.1073/pnas.1200311109

Sen, P. K. (1968). Estimates of the Regression Coefficient Based on Kendall's Tau. *Journal of the American Statistical Association*, *63*(324), 1379–1389. https://doi.org/10.1080/01621459.1968.10480934

Serpelloni, E., Faccenna, C., Spada, G., Dong, D., & Williams, S. D. P. (2013). Vertical GPS ground motion rates in the Euro-Mediterranean region: New evidence of velocity gradients at different spatial scales along the Nubia-Eurasia plate boundary. *Journal of Geophysical Research: Solid Earth*, *118*(11), 6003–6024. https://doi.org/10.1002/2013JB010102

Theil, H. (1950). A rank-invariant method of linear and polynomial regression analysis, 1-2; confidence regions for the parameters of linear regression equations in two, three and more variables. *Indagationes Mathematicae*, *1*(2). Retrieved from https://ir.cwi.nl/pub/18446

Tiwari, V. M., Wahr, J., & Swenson, S. (2009). Dwindling groundwater resources in northern India, from satellite gravity observations. *Geophysical Research Letters*, *36*(18). https://doi.org/10.1029/2009GL039401

USGS Water Resources. (2020). USGS Surface-Water Daily Data for the Nation. Retrieved January 25, 2021, from https://waterdata.usgs.gov/nwis/dv/?referred_module=sw

Vörösmarty, C. J., Green, P., Salisbury, J., & Lammers, R. B. (2000). Global Water Resources: Vulnerability from Climate Change and Population Growth. *Science*, *289*(5477), 284–288. https://doi.org/10.1126/science.289.5477.284

Wahr, J., Khan, S. A., Dam, T. van, Liu, L., Angelen, J. H. van, Broeke, M. R. van den, & Meertens, C. M. (2013). The use of GPS horizontals for loading studies, with applications to northern California and southeast Greenland. *Journal of Geophysical Research: Solid Earth*, *118*(4), 1795–1806. https://doi.org/10.1002/jgrb.50104

Wang, J. (2018). Recent global decline in endorheic basin water storages. *Nature Geoscience*, *11*, 10.

Wessel, P., Smith, W. H. F., Scharroo, R., Luis, J., & Wobbe, F. (2013). Generic Mapping Tools: Improved Version Released. *Eos, Transactions American Geophysical Union*, *94*(45), 409–410. https://doi.org/10.1002/2013EO450001

Wurtsbaugh, W. A., Miller, C., Null, S. E., DeRose, R. J., Wilcock, P., Hahnenberger, M., et al. (2017). Decline of the world’s saline lakes. *Nature Geoscience*, *10*(11), 816–821. https://doi.org/10.1038/ngeo3052

Xia, Y., Mitchell, K., Ek, M., Sheffield, J., Cosgrove, B., Wood, E., et al. (2012). Continental-scale water and energy flux analysis and validation for the North American Land Data Assimilation System project phase 2 (NLDAS-2): 1. Intercomparison and application of model products. *Journal of Geophysical Research: Atmospheres*, *117*(D3). https://doi.org/10.1029/2011JD016048

Zaliapin, I., & Ben-Zion, Y. (2020). Earthquake Declustering Using the Nearest-Neighbor Approach in Space-Time-Magnitude Domain. *Journal of Geophysical Research: Solid Earth*, *125*(4), e2018JB017120. https://doi.org/10.1029/2018JB017120

2.14 Supplemental Material

2.14.1 Description

This supplemental material consists of Figures S2.1 to S2.7 and Tables S2.1 to S2.7

2.14.2 Supplemental Figures

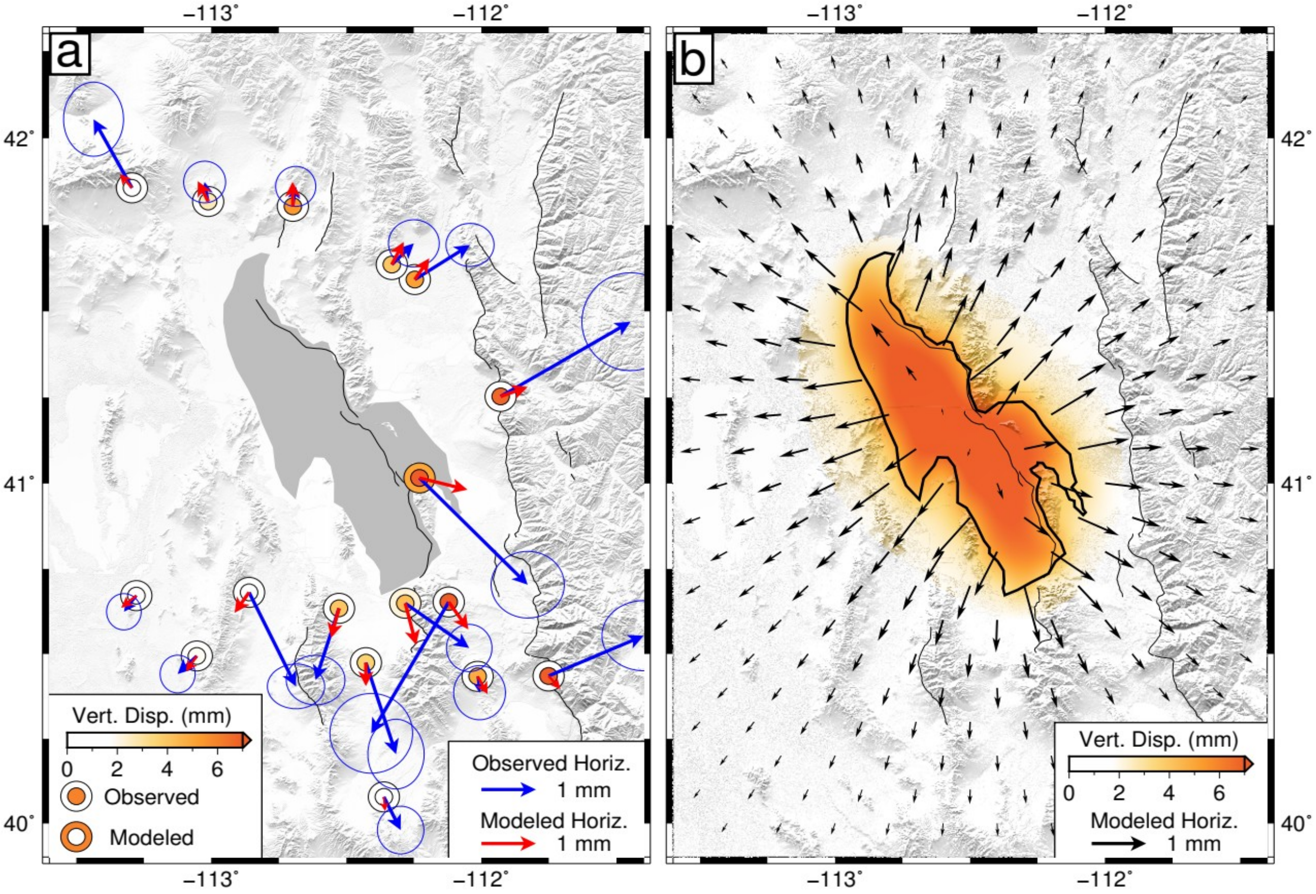

Figure S2.1: Modeled displacements for a load equivalent to the observed lake level change between 2012 and 2016 (-1.89 m). Displacements are calculated with LoadDef. Applied load is constrained to the bounds of GSL. **a)** Comparison of observed and modeled displacements at GPS stations. Blue arrows represent observed horizontal displacements with 95% confidence ellipses. Red arrows represent modeled horizontal displacements. Inner circles represent the observed GPS displacements while outer circles represent modeled displacements. Faults are represented as thin black lines. The 3D data misfit for this model is 2.49 mm. **b)** Modeled displacement field on a grid. Black arrows show horizontal displacements, while the background shading shows vertical displacements. The bounds of the region where the load is applied is shown by the thick black line. Note the poor fit to the vertical component.

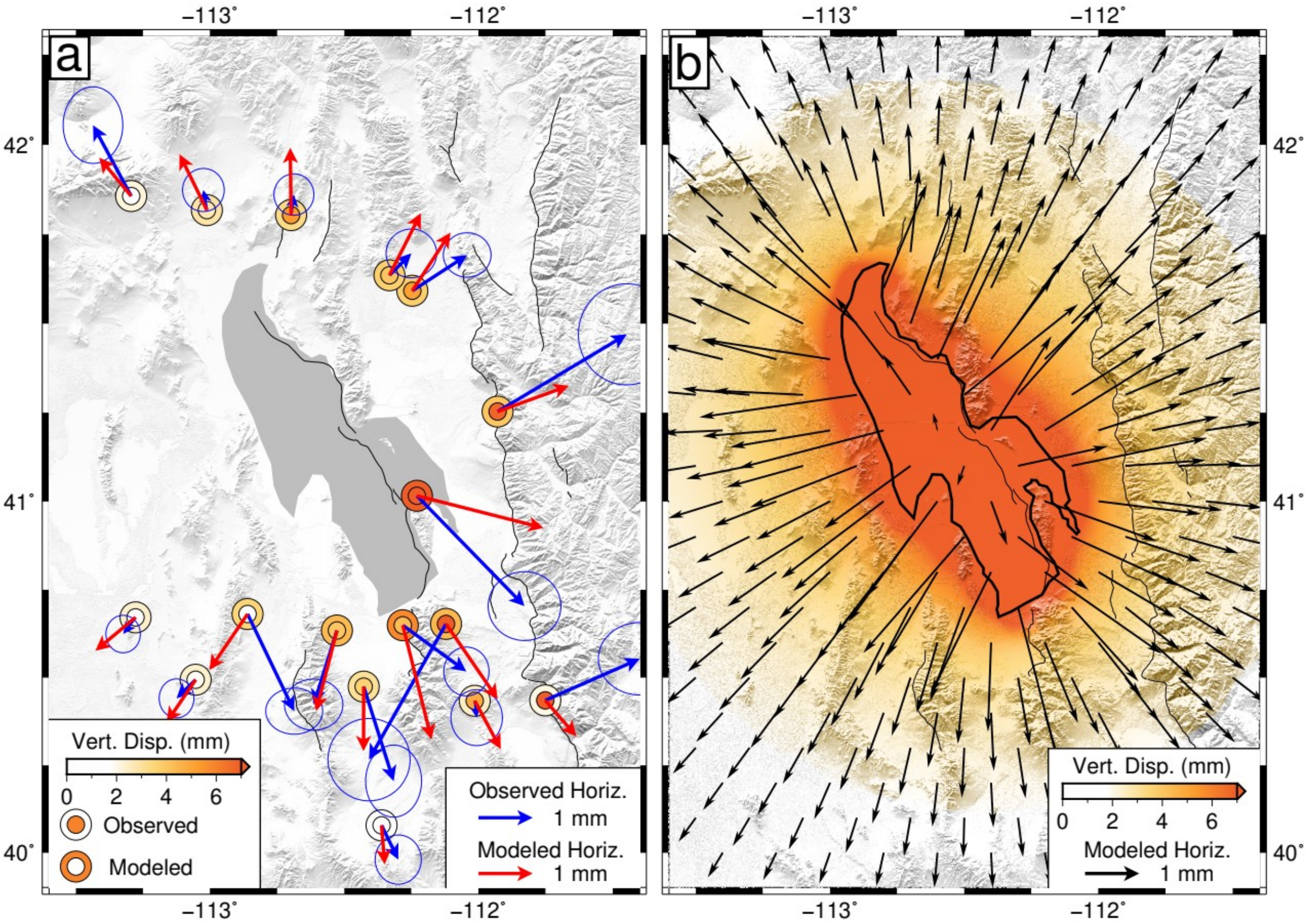

Figure S2.2: Modeled displacements for the inferred load on GSL. The distribution of load is constrained to the bounds of GSL and applied equally. Key as described in Figure S2.1. The inferred load is 5.01 ± 0.26 m with a data misfit of 1.85 mm. Note that the fit improves but the load is significantly higher than the observed GSL water loss and unrealistic.

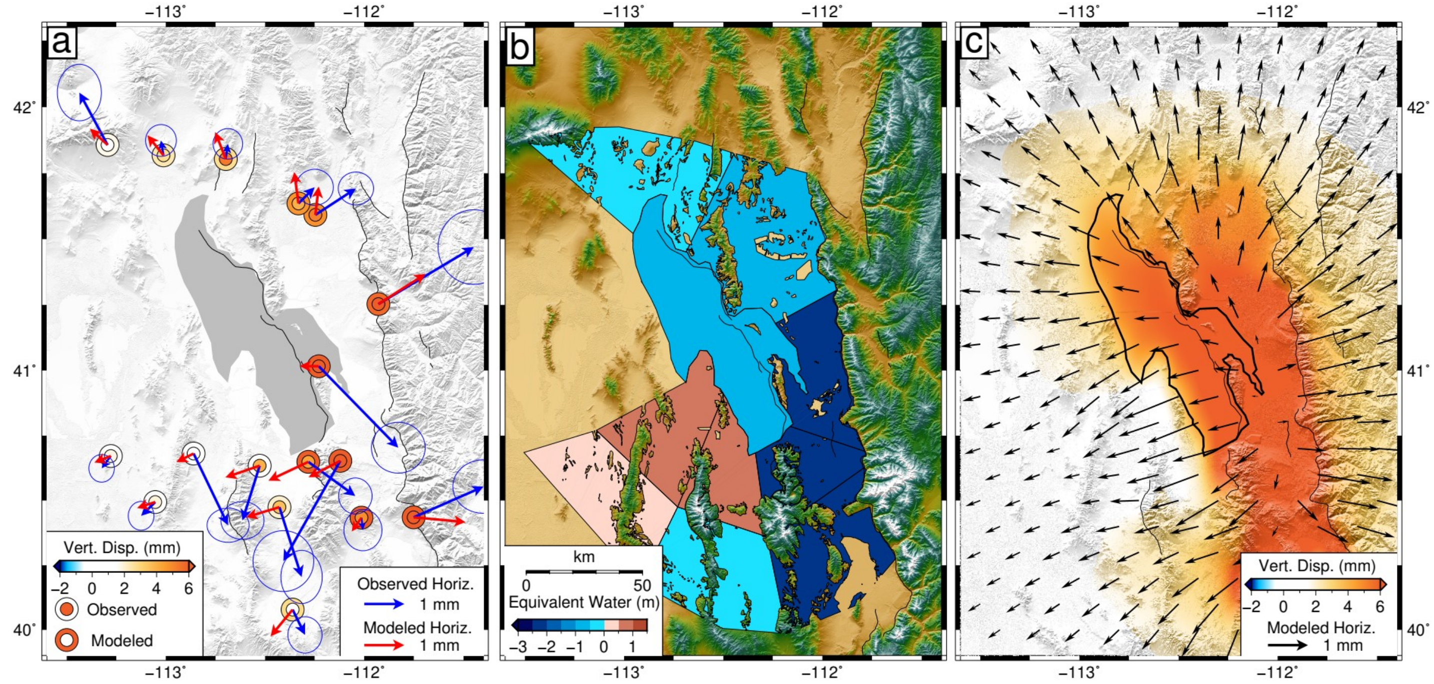

Figure S2.3: Displacements and distribution of segmented load model V1. This model includes nine segments in addition to GSL. **a)** Comparison of observed and modeled displacements at GPS stations. Blue arrows represent observed horizontal displacements with 95% confidence ellipses. Red arrows represent modeled horizontal displacements. Inner circles represent the observed GPS displacements, while outer circles represent modeled displacements. Faults are represented as thin black lines. The data misfit for this model is 1.40 mm. **b)** Inferred load distribution. Polygon shading represents the load inferred for GSL and groundwater load segments. GSL load is inferred at -0.98 ± 0.26 m, with segment loads ranging between -2.43 ± 0.35 m and 0.87 ± 0.36 m. The alpha value is 1.55. Individual segment loads are identified in Table S5. **c)** Modeled displacement field on a grid. Black arrows show horizontal displacements while the background shading shows vertical displacements. The bounds of GSL are shown as the thick black line. Note the presence of positive loads to the southwest of GSL, and the poor fit to the horizontal GPS displacements.

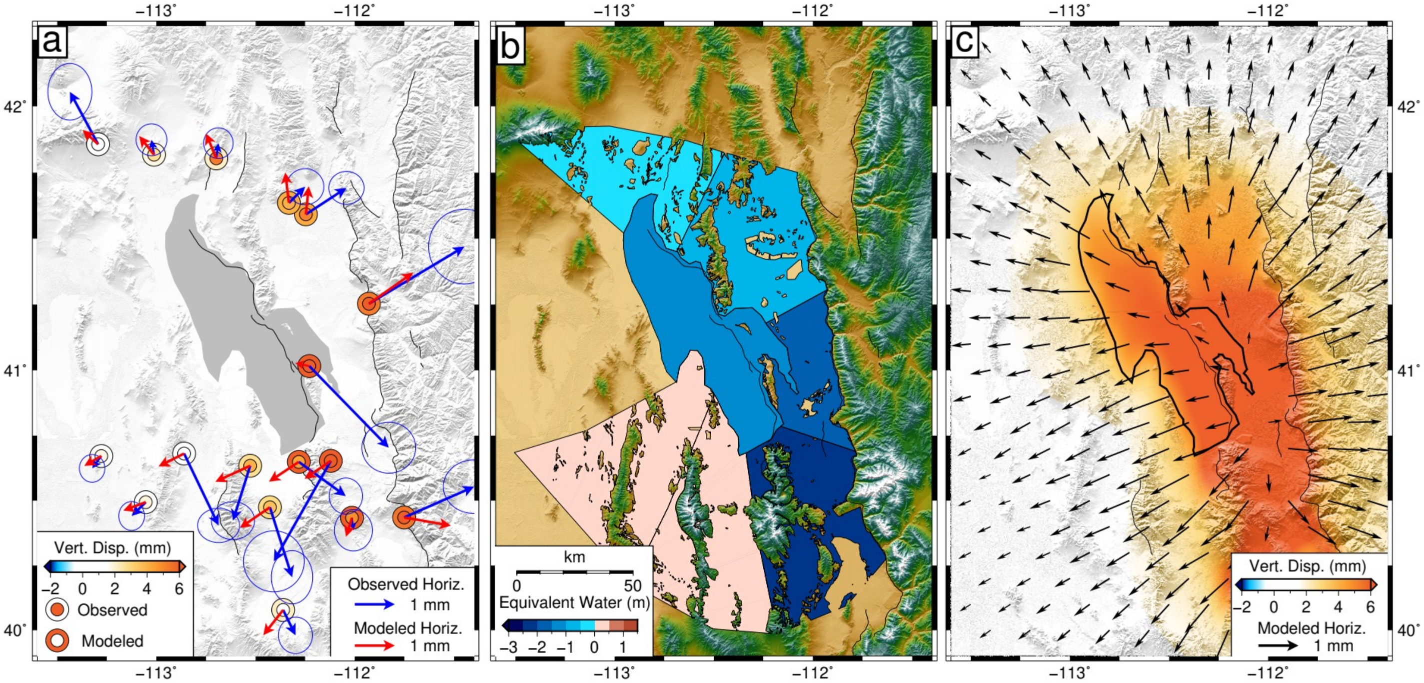

Figure S2.4: Displacements and distribution of segmented load model V2. This model includes six segments in addition to GSL. Key as described in Figure S2.3. GSL load is inferred at -1.02 ± 0.21 m, with segment loads ranging between -2.04 ± 0.21 m and 0.32 ± 0.20 m. The alpha value is 2.25 with a data misfit of 1.42 mm.

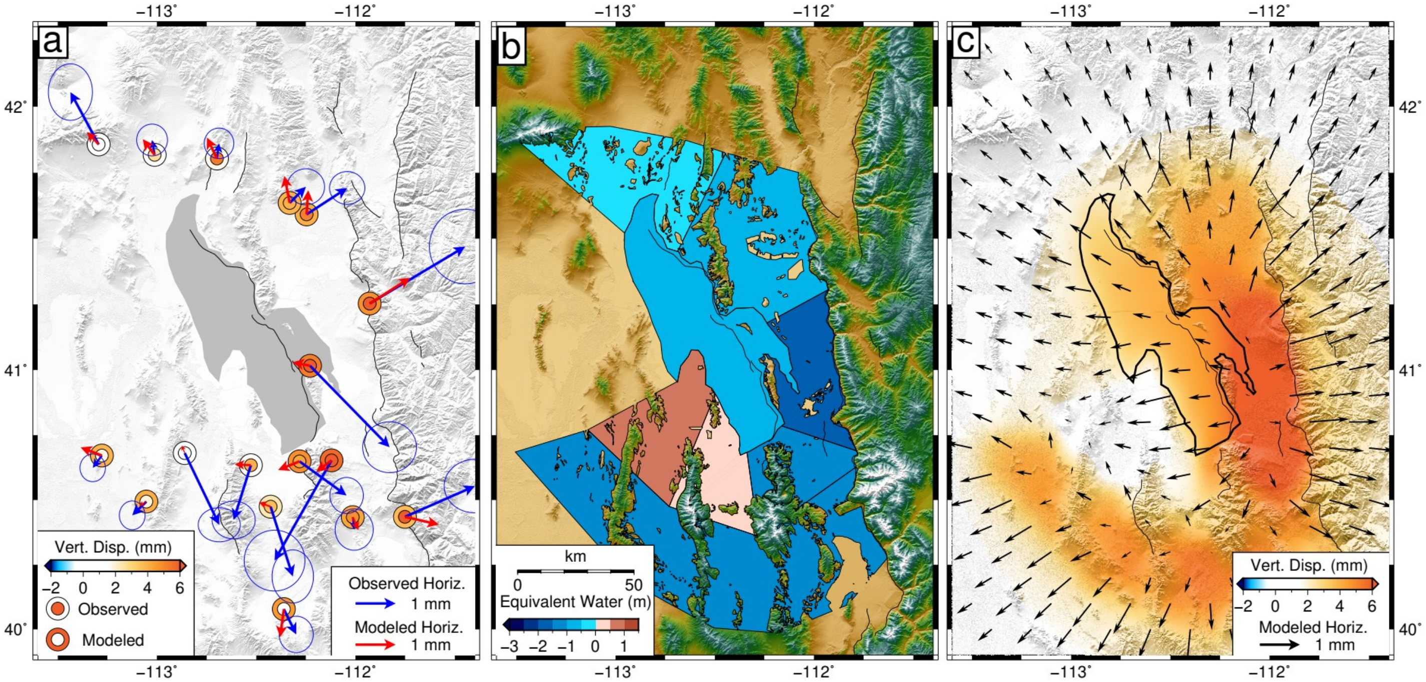

Figure S2.5: Displacements and distribution of segmented load model V3. This model includes seven segments in addition to GSL. Key as described in Figure S2.3. GSL load is inferred at -0.52 ± 0.16 m, with segment loads ranging between -1.84 ± 0.27 m and 0.75 ± 0.28 m. The alpha value is 5.00 with a data misfit of 1.86 mm.

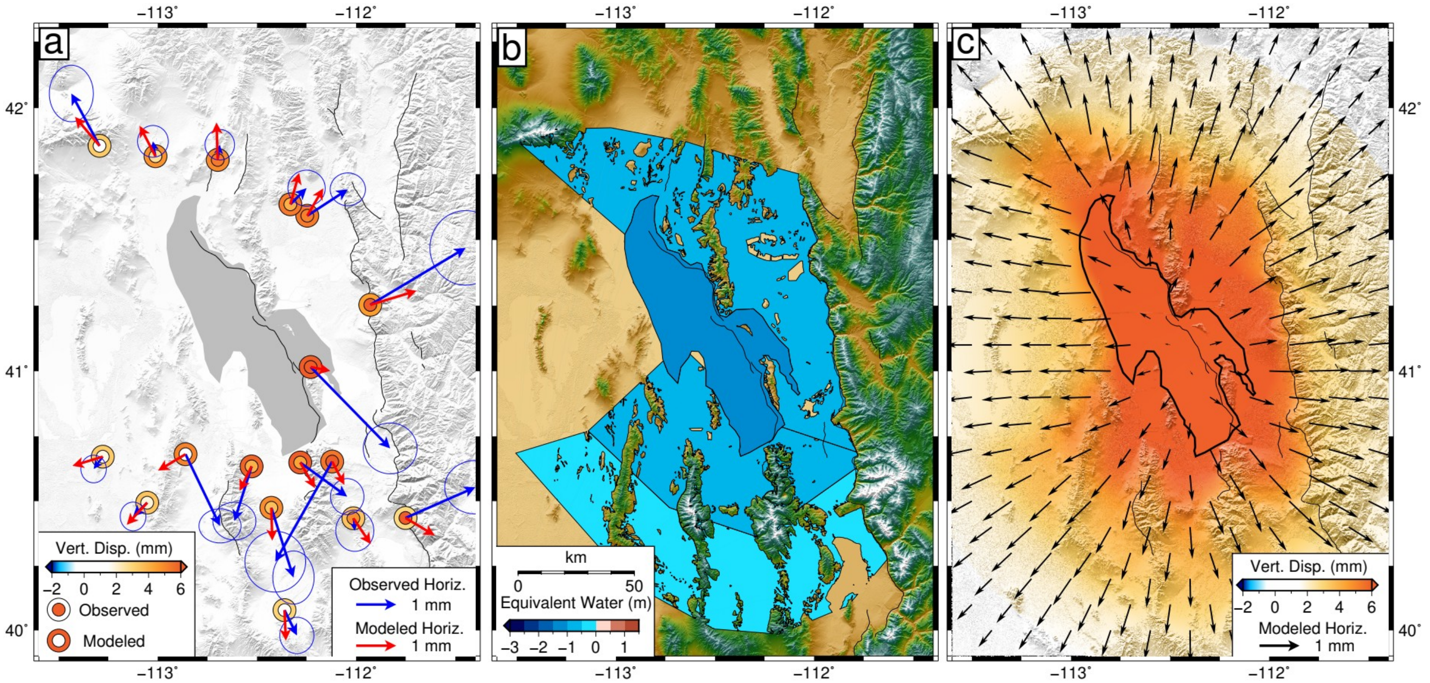

Figure S2.6: Displacements and distribution of segmented load model V4. This model includes three segments in addition to GSL. Key as described in Figure S2.3. GSL load is inferred at -1.18 ± 0.21 m. The northern segment has a load of -0.95 ± 0.11 m, the inner southern segment has a load of -0.92 ± 0.13 m, and the outer southern segment has a load of -0.42 ± 0.15 m. The alpha value is 5.50 with a data misfit of 1.86 mm.

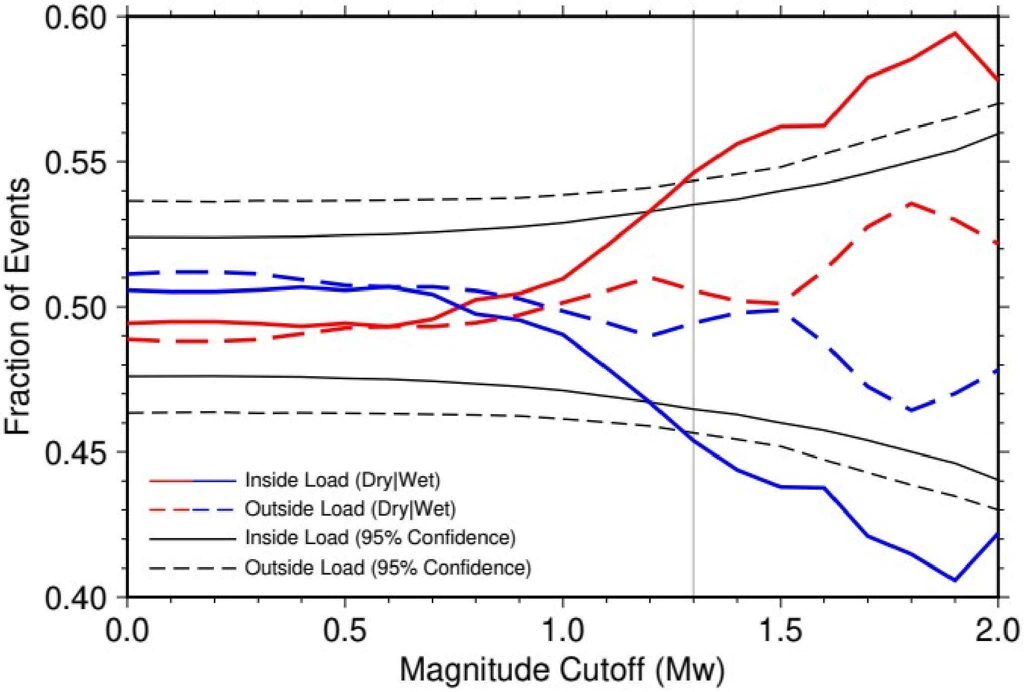

Figure S2.7: Confidence level plot comparing dry and wet period events, for the inside and outside load regions, across a range of cutoff magnitudes of the earthquake catalog. Reds indicate events which occur during dry periods as identified by the PDSI. Blues indicate events which occur during wet periods. Solid colored lines reflect events within the inside load region. Dashed colored lines reflect events within the outside load region. Black lines show two sigma confidence bounds for the inside region (solid) and outside region (dashed) following 100,000 randomizations of the catalog at each magnitude. Grey vertical bar reflects the chosen cutoff magnitude of 1.3. Note that for the inside load region, the number of dry events is above the significance level for all magnitudes above 1.2.

2.14.3 Supplemental Tables

Table S2.1: Observed groundwater level change for wells within the inferred load rings by three methods. Water level trends are calculated with Theil-Sen slope estimation method and the MIDAS algorithm and applied to the duration of the drought. The net difference results indicate the difference in the average well water level positions at the start (2012 ± 0.1 yr) and end (2016 ± 0.1 yr) of the drought. Bold Theil-Sen data reflect accepted wells which exhibit water level changes greater than two sigma. All MIDAS values are greater than two sigma.

				Drought Displacement Calculation Method				
				Theil-Sen		MIDAS		Net Diff.
Well ID	Location	Longitude	Latitude	Water Level Disp. (m)	σ (m)	Water Level Disp. (m)	σ (m)	Water Level Disp. (m)
403339112152501	Ring 1	-112.2588	40.5619	**-3.79**	**0.452**	-4.37	1.06	-3.27
403355112173601	Ring 1	-112.2947	40.5647	**-2.14**	**0.112**	~	~	~
403400112144001	Ring 1	-112.2461	40.5647	**-4.95**	**0.613**	-4.25	0.323	-7.34
403555112230303	Ring 1	-112.3850	40.5986	**-0.84**	**0.102**	~	~	~
403949112043301	Ring 1	-112.0766	40.6636	0.28	0.294	~	~	-0.61
405412111525701	Ring 1	-111.8833	40.9019	**-6.21**	**0.707**	~	~	-6.40
410523112053301	Ring 1	-112.0933	41.0897	**-2.91**	**0.404**	~	~	-2.47
410852111580501	Ring 1	-111.9688	41.1477	**-5.16**	**0.699**	~	~	-3.46
411035111594501	Ring 1	-111.9966	41.1763	-0.22	1.147	~	~	-0.77
411348112013601	Ring 1	-112.0274	41.2299	**-2.98**	**0.931**	-3.30	0.130	-2.24
414411112543701	Ring 1	-112.9111	41.7363	**-0.29**	**0.094**	-0.26	0.002	-0.24
401818112014501	Ring 2	-112.0299	40.3049	0.01	0.065	0.02	0.004	0.02
401818112034201	Ring 2	-112.0624	40.3049	**-0.51**	**0.174**	~	~	~
402317111554401	Ring 2	-111.9292	40.3881	**-1.54**	**0.135**	~	~	~
402333111513401	Ring 2	-111.8579	40.3930	**-3.27**	**1.546**	-3.16	0.075	-3.87

403126112444501	Ring 2	-112.7480	40.5236	**-2.14**	**0.233**	~	~	~
403511111541501	Ring 2	-111.9049	40.5863	**-0.45**	**0.127**	~	~	0.14
403916111575901	Ring 2	-111.9672	40.6544	0.08	0.162	0.32	0.021	0.13
404152111525101	Ring 2	-111.8816	40.6977	**-2.18**	**0.220**	~	~	-1.25
404531111510101	Ring 2	-111.8510	40.7586	**-2.01**	**0.248**	~	~	-1.59
405735112593001	Ring 2	-112.9925	40.9597	-0.06	0.046	~	~	~
411928111581001	Ring 2	-111.9702	41.3244	-0.80	0.548	~	~	0.61
414236112101201	Ring 2	-112.1708	41.7099	**-0.90**	**0.202**	-0.93	0.018	-0.85
414406112163601	Ring 2	-112.2775	41.7349	**-1.77**	**0.060**	~	~	-1.55
414406112173601	Ring 2	-112.2941	41.7349	**-1.16**	**0.159**	~	~	-1.29
414418112154801	Ring 2	-112.2641	41.7383	**-1.27**	**0.269**	~	~	-1.00
414813113075401	Ring 2	-113.1325	41.8035	**-4.55**	**1.072**	~	~	~
415703112514501	Ring 2	-112.8633	41.9508	-0.39	2.343	-0.11	0.022	-0.17
415754112551301	Ring 2	-112.9211	41.9649	**-9.34**	**4.196**	~	~	-2.36

Table S2.2: GPS stations included in the regional common mode calculation.

Station	Longitude	Latitude
AHID	-111.0637	42.2731
BBID	-111.5261	43.6850
BLW2	-109.5578	42.2671
CASP	-106.3841	42.3192
CAST	-110.6773	38.6910
ELKO	-115.8172	40.4147
FOOT	-113.8054	38.8694
GOSH	-114.1797	40.1402
HLID	-114.4140	43.0626
MYT5	-110.0482	39.6027
P007	-114.8197	41.2242
P012	-109.3338	37.5974
P032	-107.2559	41.2417
P684	-111.4505	43.4191
RUBY	-115.1228	40.1172
SMEL	-112.8449	38.9256
SPIC	-112.1275	38.8062
TCSG	-113.4782	43.1192
TSWY	-110.5975	43.1741

Table S2.3: Observed GPS relative displacements during the drought period. Values are calculated from the difference of the MIDAS velocities for the drought and base periods then applied to the duration of the drought (four years).

Observed Displacements at GPS Stations

			Drought Disp. (mm)			Uncertainty (mm)		
Station	Longitude	Latitude	E	N	U	σ_E	σ_N	σ_U
CEDA	-112.8605	40.6807	0.86	-1.79	0.47	0.21	0.17	0.64
COON	-112.1210	40.6526	-1.42	-2.50	10.34	0.31	0.31	1.25
EOUT	-111.9289	41.2532	2.38	1.42	6.78	0.36	0.38	1.28
LTUT	-112.2468	41.5921	1.01	0.66	5.17	0.18	0.17	0.78
NAIU	-112.2296	41.0157	1.98	-2.04	9.67	0.27	0.26	1.18
P016	-112.3614	40.0781	0.31	-0.63	0.30	0.17	0.19	0.67
P057	-112.6231	41.7566	1.15	0.03	4.88	0.16	0.19	0.68
P084	-113.0540	40.4940	-0.35	-0.34	1.90	0.13	0.15	0.61
P086	-112.2821	40.6488	1.17	-0.85	4.30	0.17	0.18	0.79
P100	-113.2942	41.8568	-0.70	1.31	0.47	0.22	0.29	0.96
P111	-113.0122	41.8173	-0.06	0.37	2.69	0.16	0.16	0.73
P113	-113.2780	40.6713	-0.23	-0.31	1.80	0.13	0.14	0.57
P114	-112.5276	40.6340	-0.43	-1.37	4.00	0.22	0.19	0.78
P115	-112.4280	40.4744	0.55	-1.74	3.59	0.21	0.27	0.89
P116	-112.0142	40.4340	0.04	-0.31	4.84	0.19	0.21	0.73
P117	-111.7514	40.4352	1.74	0.77	10.12	0.31	0.27	1.09
P121	-112.6983	41.8034	0.05	0.38	5.36	0.15	0.16	0.60
P122	-112.3319	41.6354	0.40	0.40	3.99	0.19	0.18	0.79
SLCU	-111.9550	40.7722	4.77	0.93	3.84	0.49	0.33	1.47
ZLC1	-111.9522	40.7860	8.33	-0.78	11.79	0.38	0.25	1.02

Table S2.4: Displacements at GPS sites, calculated with LoadDef, for the observed fixed GSL load model, and the solved (inferred) GSL load model. The fixed load model only applies the observed load of -1.89 m to the bounds of the lake while the solved GSL model applies the inferred load of -5.01 m.

Modeled Displacements at GPS Stations

			Observed GSL Only (-1.89 m)			Solve For GSL Only (-5.01m)		
Station	Longitude	Latitude	E	N	U	E	N	U
CEDA	-112.8605	40.6807	-0.27	-0.39	1.33	-0.70	-1.03	3.52
COON	-112.1210	40.6526	0.36	-0.52	1.68	0.95	-1.39	4.44
EOUT	-111.9289	41.2532	0.50	0.18	1.51	1.31	0.48	4.01
LTUT	-112.2468	41.5921	0.27	0.40	1.40	0.70	1.07	3.71
NAIU	-112.2296	41.0157	0.88	-0.22	5.01	2.34	-0.59	13.29
P016	-112.3614	40.0781	0.02	-0.27	0.63	0.06	-0.72	1.67
P084	-113.0540	40.4940	-0.20	-0.30	0.89	-0.54	-0.79	2.36
P086	-112.2821	40.6488	0.20	-0.79	2.20	0.53	-2.11	5.84
P100	-113.2942	41.8568	-0.22	0.27	0.83	-0.59	0.71	2.21
P111	-113.0122	41.8173	-0.19	0.39	1.09	-0.50	1.03	2.88
P113	-113.2780	40.6713	-0.28	-0.23	0.91	-0.74	-0.62	2.41
P114	-112.5276	40.6340	-0.15	-0.56	1.67	-0.39	-1.49	4.42
P115	-112.4280	40.4744	0.00	-0.45	1.16	0.00	-1.19	3.09
P116	-112.0142	40.4340	0.18	-0.34	0.94	0.48	-0.89	2.49
P117	-111.7514	40.4352	0.22	-0.25	0.79	0.57	-0.67	2.09
P121	-112.6983	41.8034	-0.01	0.47	1.24	-0.02	1.24	3.29
P122	-112.3319	41.6354	0.22	0.43	1.40	0.58	1.14	3.71

Table S2.5: Inferred loads and model uncertainties for segmented models V1-V4 shown in Figures S3-S6. Segments with their location noting “in”, indicate those closest to the southern side of the lake. Those identified as “out”, indicate segments that are farthest from the southern side of the lake.

Load ID	Location	Load (m)	σ (m)
Segmented Model V1			
GSL	~	-0.98	0.26
P1	N	-0.28	0.22
P2	NE	-0.93	0.22
P3	E	-2.10	0.35
P4	SE – in	-2.03	0.28
P5	S – in	0.55	0.29
P6	SW – in	0.87	0.36
P7	SW – out	0.03	0.29
P8	S – out	-0.17	0.32
P9	SE – out	-2.43	0.35
Segmented Model V2			
GSL	~	-1.02	0.21
P1	N	-0.12	0.22
P2	NE	-0.75	0.20
P3	E	-1.96	0.31
P4	SE	-2.04	0.21
P5	S	0.02	0.19
P6	SW	0.32	0.20
Segmented Model V3			
GSL	~	-0.52	0.16
P1	N	-0.05	0.20
P2	NE	-0.84	0.17
P3	E	-1.84	0.27
P4	SE – in	-1.37	0.24
P5	S – in	0.45	0.20
P6	SW – in	0.75	0.28
P7	S – out	-1.05	0.15
Segmented Model V4			
GSL	~	-1.18	0.21
P1	N	-0.95	0.11
P2	S – in	-0.92	0.13
P3	S – out	-0.42	0.16

Table S2.6: Displacements at GPS sites, calculated with LoadDef, for segmented models V1-V4.

Modeled Displacements at GPS Stations

			Segmented Model V1			Segmented Model V2		
Station	Longitude	Latitude	E	N	U	E	N	U
CEDA	-112.8605	40.6807	-0.43	-0.21	0.01	-0.64	-0.32	1.10
COON	-112.1210	40.6526	-0.79	-0.41	7.71	-0.65	-0.45	7.68
EOUT	-111.9289	41.2532	1.18	0.75	5.75	1.11	0.77	5.36
LTUT	-112.2468	41.5921	0.08	0.71	4.82	0.07	0.70	4.17
NAIU	-112.2296	41.0157	-0.48	0.01	6.96	-0.35	0.07	6.86
P016	-112.3614	40.0781	-0.55	-0.67	2.80	-0.50	-0.63	2.12
P084	-113.0540	40.4940	-0.45	-0.15	1.18	-0.56	-0.21	0.56
P086	-112.2821	40.6488	-1.00	-0.47	6.46	-0.75	-0.49	6.83
P100	-113.2942	41.8568	-0.44	0.41	1.72	-0.38	0.36	1.36
P111	-113.0122	41.8173	-0.40	0.50	2.37	-0.37	0.47	1.81
P113	-113.2780	40.6713	-0.41	-0.16	1.09	-0.43	-0.25	0.42
P114	-112.5276	40.6340	-0.86	-0.29	1.37	-0.87	-0.40	2.70
P115	-112.4280	40.4744	-0.83	-0.25	2.03	-0.75	-0.51	2.82
P116	-112.0142	40.4340	-0.24	-0.35	6.63	-0.15	-0.47	6.02
P117	-111.7514	40.4352	1.29	-0.12	6.18	1.17	-0.20	5.50
P121	-112.6983	41.8034	-0.26	0.68	2.72	-0.26	0.62	2.15
P122	-112.3319	41.6354	-0.11	0.79	4.73	-0.09	0.76	4.07

			Segmented Model V3			Segmented Model V4		
Station	Longitude	Latitude	E	N	U	E	N	U
CEDA	-112.8605	40.6807	-0.07	0.19	0.89	-0.69	-0.41	5.14
COON	-112.1210	40.6526	-0.38	-0.29	5.69	0.30	-0.58	5.42
EOUT	-111.9289	41.2532	1.01	0.64	4.82	1.16	0.35	4.54
LTUT	-112.2468	41.5921	0.04	0.60	4.05	0.40	0.68	5.34
NAIU	-112.2296	41.0157	-0.44	0.09	5.29	0.49	-0.10	6.62
P016	-112.3614	40.0781	-0.09	-0.70	4.62	0.03	-0.76	3.05
P084	-113.0540	40.4940	-0.18	-0.10	4.10	-0.51	-0.55	3.52
P086	-112.2821	40.6488	-0.53	-0.22	4.86	0.37	-0.64	6.00
P100	-113.2942	41.8568	-0.29	0.31	1.08	-0.61	0.72	3.32
P111	-113.0122	41.8173	-0.30	0.39	1.38	-0.40	0.76	4.78
P113	-113.2780	40.6713	-0.53	0.20	3.94	-0.76	-0.23	3.32
P114	-112.5276	40.6340	-0.40	0.02	1.52	-0.30	-0.61	5.85
P115	-112.4280	40.4744	-0.29	0.11	2.36	0.02	-0.82	4.94
P116	-112.0142	40.4340	0.14	-0.32	4.28	0.44	-0.65	3.50
P117	-111.7514	40.4352	0.84	-0.19	3.71	0.73	-0.44	2.85
P121	-112.6983	41.8034	-0.25	0.52	1.70	-0.03	0.94	4.97
P122	-112.3319	41.6354	-0.13	0.67	3.94	0.22	0.79	5.36

Table S2.7: Displacements at GPS sites, calculated with LoadDef, for the preferred ring load model. The preferred ring model estimates a GSL load of -1.85 m, a 24 km inner ring at -1.16 m, and a 40 km outer ring at -0.32 m.

Modeled Displacements at GPS Stations

			Preferred Ring		
Station	Longitude	Latitude	E	N	U
CEDA	-112.8605	40.6807	-0.69	-0.87	4.66
COON	-112.1210	40.6526	0.55	-0.99	6.24
EOUT	-111.9289	41.2532	1.36	0.48	4.84
LTUT	-112.2468	41.5921	0.68	0.87	4.73
NAIU	-112.2296	41.0157	0.89	-0.27	8.82
P016	-112.3614	40.0781	0.07	-0.90	2.32
P084	-113.0540	40.4940	-0.62	-0.83	3.00
P086	-112.2821	40.6488	0.54	-1.11	7.25
P100	-113.2942	41.8568	-0.70	0.79	3.36
P111	-113.0122	41.8173	-0.64	1.13	5.26
P113	-113.2780	40.6713	-0.82	-0.63	2.94
P114	-112.5276	40.6340	-0.46	-1.08	6.75
P115	-112.4280	40.4744	-0.02	-1.33	5.11
P116	-112.0142	40.4340	0.53	-0.85	3.45
P117	-111.7514	40.4352	0.75	-0.62	2.79
P121	-112.6983	41.8034	0.18	1.17	6.10
P122	-112.3319	41.6354	0.58	0.94	4.80

3

Interseismic Strain Accumulation Between the Colorado Plateau and the Eastern California Shear Zone: Implications for the Seismic Hazard Near Las Vegas, Nevada

3.1 Publication Status

The material presented in this chapter has been submitted for consideration to the *Bulletin of the Seismological Society of America*: Young, Z. M., C. Kreemer, W. C. Hammond, and G. Blewitt (in review), Interseismic Strain Accumulation Between the Colorado Plateau and the Eastern California Shear Zone: Implications for the Seismic Hazard Near Las Vegas, Nevada. The dissertation author led the research and authored the text. The co-authors provided guidance and revisions which assisted the production of the presented research.

3.2 Key Points

- Active deformation across the central Basin and Range and Las Vegas, NV is determined from GPS data.
- The extension rate across Las Vegas Valley is larger than previously reported, at 0.5 – 0.6 mm/yr.
- Postseismic relaxation substantially alters the deformation field within the central Basin and Range.

3.3 Abstract

Crustal deformation in the central Basin and Range between the Colorado Plateau and the Eastern California Shear Zone is active but slow, making it a challenge to assess how strain is distributed and crustal motion transferred. However, knowledge of strain rates is very important, particularly for addressing the seismic hazard for both the Las Vegas urban area and the site of the proposed Yucca Mountain nuclear waste repository, in southern Nevada. Global Positioning System (GPS) data provide important constraints, particularly now that the GPS network in the area has substantially expanded in recent years. However, because deformation is slow, it is important to mitigate any transient tectonic and non-tectonic signals to obtain the most accurate long-term interseismic motion and use robust estimation of strain rates. We use data from all GPS stations in the region, including both long-running continuous and semi-continuous stations. We model and remove postseismic displacements at these stations using source parameters for 41 events, dating back to the 1700 Cascadia megathrust earthquake, which contribute significantly to the deformation field within the central Basin and Range. We also remove correlated noise from the time series with the Common Mode Component Imaging technique. We find that removal of both the postseismic transients and common-mode noise substantially reduces the uncertainties and spatial variation in the velocities. We find east–west extension across the Las Vegas Valley of 0.5 – 0.6 mm/yr. The interseismic strain rate field, calculated with the final velocities, reveals higher strain rates through southern Nevada than in previous studies, with rates within Las Vegas Valley of 8.5 ± 2.4

$x10^{-9}$ yr^{-1}. Our results confirm shear along the Pahranagat Shear Zone but the estimated amplitude is strongly affected by postseismic relaxation.

3.4 Introduction

The American Southwest is tectonically complex, exhibiting a broad range of deformation regimes which are driven in part by inland accommodation of deformation due to the Pacific – North American plate motion. The eastward transfer of deformation is facilitated by shear along the Eastern California Shear Zone (ECSZ) and Pahranagat Shear Zone, and extension throughout the Basin and Range, including the Central Nevada Seismic Belt (CNSB) and Wasatch Fault Zone (Figure 3.1) (e.g., Dixon & Xie, 2018; Flesch et al., 2007; Frankel et al., 2008; Hammond & Thatcher, 2004; Kreemer et al., 2010). Throughout this region, a number of large earthquakes have occurred over the years, e.g., Owens Valley (1872), Sonora (1887), Pleasant Valley (1915), Dixie Valley (1954), Hebgen Lake (1959), Landers (1992), Hector Mine (1999). The 2008 M_w 6.0 Wells earthquake showed that significant earthquakes can occur in very low strain rate areas, and cause considerable damage (dePolo & Pecoraro, 2011). Because deformation rates are particularly low, but not zero, within the central Basin and Range (Hammond et al., 2014; Kreemer et al., 2010), any lingering transient postseismic deformation from these earthquakes, could be significant compared to the steady component of interseismic strain accumulation. Because proper constraints on the interseismic strain rate are essential for seismic hazard assessment, postseismic transients must be accounted for.

In the most recent investigation of strain rates across the central Basin and Range, which included the Las Vegas Valley, Kreemer et al., (2010) used GPS data, in conjunction with seismicity, to provide constraints on deformation and identify the

Pahranagat Shear Zone. That study, however, was severely limited by the sparsity of data at the time, with only 105 GPS stations across the entirety of their study area. Consequently, this led to some open-ended interpretations of their results. Since then, the GPS network has experienced rapid growth, and the density of stations in the central Basin and Range has been greatly improved (Blewitt et al., 2018), in part by the installation of the semi-continuous MAGNET network (Blewitt et al., 2009). The addition of these stations provides the opportunity to significantly improve the resolution of the deformation field.

In addition, Kreemer et al., (2010) did not account for transient signals or regional common mode in their time series. One of the strongest sources of transient motion in GPS time series is postseismic deformation, which has been shown to produce signals hundreds of kilometers from the source that can last decades to hundreds of years (Broermann et al., 2021; Freed et al., 2007; Hammond et al., 2009; Hearn, 2003). Considering the proximity of the central Basin and Range to the large earthquakes produced in neighboring regions, it is likely that GPS velocities are strongly affected. Additionally, hydrologic loading has been shown to be prevalent in GPS time series (Amos et al., 2014; Argus et al., 2017; Young et al., 2021), and regional common mode noise plays a key role in station time series scatter (Kreemer & Blewitt, 2021; Tian & Shen, 2016; Wdowinski et al., 1997), and can affect velocity estimation (Kreemer & Blewitt, 2021; Márquez-Azúa & DeMets, 2003; Santamaría-Gómez & Mémin, 2015; Serpelloni et al., 2013).

In this study, we produce the most robust interseismic strain rate field for the central Basin and Range to date. We calculate corrections for postseismic deformation, hydrologic loading, and common mode for all stations within the study area and produce maps of our revised velocity and strain rate fields. These results are compared to those of the uncorrected field and we investigate their implications for fault slip rates within the Las Vegas Valley through a GPS derived velocity budget and block modeling. Our results improve constraints on interseismic deformation throughout the central Basin and Range and provide insight into the associated seismic hazard of the region, with special attention to the Las Vegas urban area.

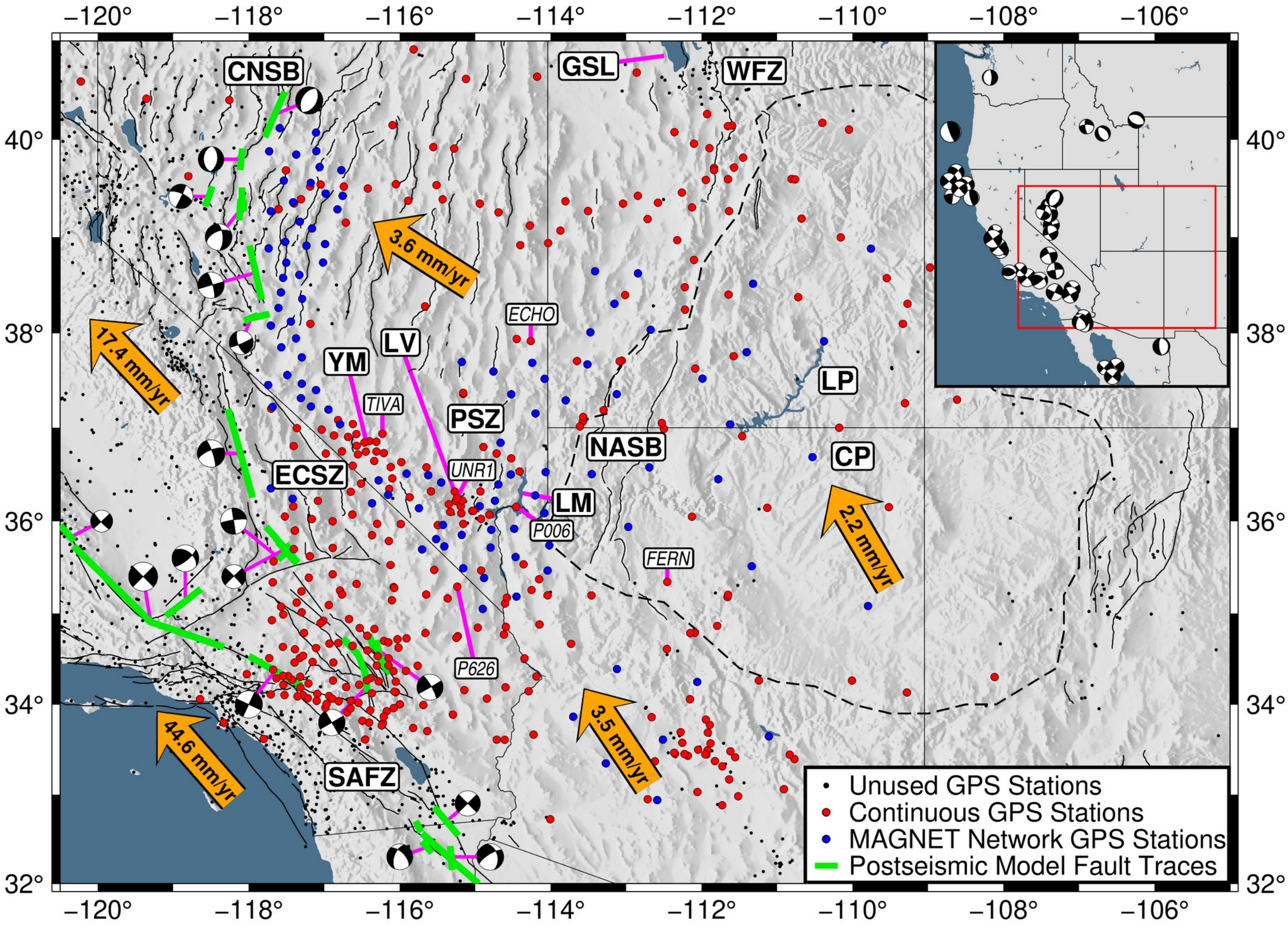

Figure 3.1: Location map of our study area within the American Southwest. Black dots show the location of all available GPS stations in the region. Blue and red dots represent GPS stations considered in this study, with blue dots showing the location of semi-continuous MAGNET stations and red dots showing continuous stations. Green lines, and their respective focal mechanisms, represent the location of fault traces for the earthquake models used to calculate postseismic deformation at GPS stations. Bold labels are as follows: SAFZ – San Andreas Fault Zone, ECSZ – Eastern California Shear Zone, CNSB – Central Nevada Seismic Belt, YM – Yucca Mountain Nuclear Waste Repository, LV – Las Vegas, PSZ – Pahranagat Shear Zone, LM – Lake Mead, NASB – Northern Arizona Seismic Belt, GSL – Great Salt Lake, WFZ – Wasatch Fault Zone, LP – Lake Powell, and CP – Colorado Plateau. Italicized labels show GPS station locations whose time series are shown in Figures 4 and S3.3 – S3.7. Orange arrow labels reflect general regional velocity

trends and orientation with respect to the NA reference frame of Kreemer et al., (2014). Thin black lines represent regional faults and the dashed black line indicates the bounds of the Colorado Plateau. Inset shows the location of the study area compared to the western United States with focal mechanisms for all earthquake models. Pink lines are used as pointers.

3.5 Methods And Data Preparation

3.5.1 GPS Data

We use GPS data from the Nevada Geodetic Laboratory (NGL), where solutions are produced in the IGS14 reference frame using the GipsyX software (Altamimi et al., 2016; Bertiger et al., 2020; Blewitt et al., 2018, see the Data and Resources section). We use 445 stations, which span the region between the SAFZ, the CNSB, the Wasatch Fault Zone, and the Colorado Plateau (Figure 3.1), and were measured during the timeframe of our study, 1999 – 2021.5 (further description in the Removing Common Mode Components section below). These stations represent a combination of long-running continuous stations from the NSF supported Network of the Americas, semi-continuous Mobile Array of GPS for Nevada Transtension (MAGNET) (Blewitt et al., 2009), and commercial and regional networks. The MAGNET network was installed and observed by the NGL over the last decade to complement and densify the continuous GPS network. The presence of the 107 MAGNET stations used in this study improves the median distance to the ten nearest stations by 24.4%, from 50.3 km to 38.0 km, across the central and southern Basin and Range. This is particularly important for refining our understanding of deformation across the Pahranagat Shear Zone and Las Vegas Valley, for which the Kreemer et al., (2010) study was limited to only a few stations.

Prior to the corrections described below, each station undergoes inspection for steps and problem data in the time series. Velocities are then calculated with MIDAS (Blewitt et al., 2016), producing our “original” velocity data set. These velocities still include effects from postseismic deformation, hydrologic loading, and common mode errors.

3.5.2 Removing Postseismic Relaxation

Many large earthquakes have occurred throughout the western United States, with historical events along the plate boundary (San Francisco 1938/1906, Fort Tejon, Cascadia, etc.), CNSB earthquakes (Dixie Valley, Pleasant Valley, etc.), modern events (Hector Mine, Ridgecrest, El Mayor Cucapah, etc.), and others (Hebgen Lake, Sonoran, etc.). Considering the central location of our study area within the greater plate boundary zone, it is likely that large earthquakes throughout the entire western United States may have affected, to some degree, the deformation field of our study area. To properly assess the interseismic velocity field, it is necessary to consider all significant earthquakes in the western United States and produce, and ultimately remove, a cumulative postseismic deformation model. In total, we identify 41 events to consider as potential contributors to the postseismic deformation field of our study area (Table 3.1). We consider most events greater than M_w 6.0 since 1989, events above M_w 6.8 since the 1812 Wrightwood event, and include the 1700 M_w 9.1 Cascadia megathrust event.

To calculate the postseismic displacements attributed to these events, we use the PSGRN/PSCMP software, which applies a layered viscosity model and accounts for gravitational effects (Wang et al., 2006). For the majority of the events, displacement time series are produced using previously published earthquake source slip models acquired from the SRCMOD database (see the Data and Resources section), or obtained from the literature (Table 3.1). Adopted slip models are input with their original geometries, with some simple models only using 1 – 3 fault slip planes and other, more complex models, using tens to hundreds to define each event. For the remaining events, we produce our own models based on a combination of published literature, moment tensors, and expected magnitudes. Fault traces and focal mechanisms of the considered events are shown in Figure 3.1. For the viscosity structure, we adopt the model of Broermann et al., (2021), which was derived for the Southern Basin and Range and the Colorado Plateau, and used for all earthquake models (Broermann et al., 2021) (Table 3.2). As shown by Guns & Bennett (2020), this viscosity structure is quite similar to those produced for several studies throughout Southern California and the Basin and Range where the majority of our earthquakes occurred. However, Hammond et al. (2009) and Dickinson et al. (2016) estimate that viscosities are higher than those of Broermann et al. (2021) for the CNSB. Variability in viscosity structures throughout the western United States is indeed expected, especially when comparing viscosity of the Southern Basin and

Range to Cascadia. A three-dimensional viscosity structure of the entire western United States would therefore need to be derived. We leave this task, however, to future studies, and emphasize that we find that Broerman et al. (2021) provides a reasonable viscosity structure for the majority of our events since most fall within regions where similar viscosities have been identified.

Model postseismic time series are produced for each event at each GPS station which we sum to create composite time series. This composite postseismic correction is then removed from all GPS time series in the study area. While PSCMP provides co-seismic offsets in the solution, we limit our model to the postseismic component and allow steps for modern events to be accounted for in the MIDAS velocity calculation.

Table 3.1: List of earthquake models used to calculate postseismic deformation at GPS stations with expected and modeled magnitudes. Model complexity is indicated by N Subfaults. Further details are provided in Table S3.1.

Event	Date	Author	Expected M_w	Modeled M_w	N Subfaults
Borah Peak	1983OCT28	Mendoza & Hartzell (1988)	6.82	6.77	128
Cascadia	1700JAN26	Pollitz et al. (2008)	9.1	9.07	16
Cedar Mountain	1932OCT21	Hammond et al. (2009)	7.1	7.13	1
Central Idaho	2020MAR31	USGS (2020)	6.46	6.45	500
Dixie Valley	1954DEC16	Hodgkinson et al. (1996)	6.9	6.94	1
El Mayor–Cucapah	2010APR04	Wei et al. (2011)	7.2	7.24	386
Fairview Peak Complex	1954DEC16	Hodgkinson et al. (1996)	7.3	7.25	3
Fort Tejon	1857JAN09	This study	7.9	7.87	2
Gulf of California 1	2009AUG03	Hayes (2009)	6.9	6.85	144
Gulf of California 2	2009AUG03	Broermann et al. (2021)	6.2	6.24	1
Gulf of California 3	2012APR12	Broermann et al. (2021)	6	5.99	1
Gulf of California 4	2012APR12	Broermann et al. (2021)	7	7.03	1
Hebgen Lake	1959AUG18	Barrientos et al. (1987)	7.3	7.26	1
Hector Mine	1999OCT16	Salichon et al. (2004)	7.14	7.1	144
Imperial Valley	1940MAY18	Broermann et al. (2021)	6.9	6.86	1
Kern County	1952JUL21	Bawden, (2001)	7.3	7.28	2
Laguna Salada	1892FEB23	Broermann et al. (2021)	7.05	7.05	1

Landers	1992JUN28	Hernandez et al. (1999)	7.22	7.18	48
Loma Prieta	1989OCT18	Emolo & Zollo (2005)	6.91	6.87	7840
Mendocino Triple Junction 1	1980NOV08	Rollins & Stein (2010)	7.3	7.34	1
Mendocino Triple Junction 2	1991AUG17	Rollins & Stein (2010)	7.1	7.1	1
Mendocino Triple Junction 3	1992APR25	Rollins & Stein (2010)	6.9	6.92	1
Mendocino Triple Junction 4	1994SEP01	Rollins & Stein (2010)	7	7.02	1
Mendocino Triple Junction 5	2005JUN15	Shao & Ji (2005)	7.2	7.22	119
Mendocino Triple Junction 6	2014MAR10	USGS (2017)	6.8	6.83	1
Masset	2012OCT28	S. Wei (2012)	7.83	7.67	189
Monte Cristo	2020MAY15	Zheng et al. (2020)	6.5	6.5	2
Napa	2014AUG24	Gallovič (2015)	6.07	6.2	320
Nisqually	2001FEB28	USGS (2015)	6.8	6.8	1
Northridge	1994JAN17	Zeng & Anderson (2000)	6.71	6.64	1728
Owens Valley	1872MAR26	Haddon et al. (2016)	7.4	7.47	1
Parkfield	2004SEP28	Ji (2004)	5.9	5.99	200
Pleasant Valley	1915OCT03	Hammond et al. (2009)	7.4	7.43	1
Ridgecrest 1	2019JUL04	Jin & Fialko (2020)	6.4	6.5	108
Ridgecrest 2	2019JUL06	Jin & Fialko (2020)	7.1	7.12	420
San Francisco 1838	1838JUN25	Smith & Sandwell (2006)	7.4	7.42	1
San Francisco 1906	1906APR18	Song et al. (2008)	7.91	7.89	48
San Simeon	2003DEC22	Johanson & Bürgmann (2010)	6.5	6.52	250

Sonoran	1887MAY03	Broermann et al. (2021)	7.5	7.49	1
Stillwater	1954AUG24	Hodgkinson et al. (1996)	6.6	6.62	1
Wrightwood	1812DEC08	Wang et al. (2009)	7.5	7.5	1

Table 3.2: Postseismic viscosity structure adopted from Broermann et al., (2021). Here, ρ is density, η_1 is the transient viscosity, η_2 is the steady-state viscosity, and α is the ratio between the effective and unrelaxed shear modulus.

Layer	**Depth (km)**	**Vp (km/s)**	**Vs (km/s)**	**ρ (kg/m^3)**	**η_1 (Pa – s)**	**η_2 (Pa – s)**	**α**
1	0 – 15	6.17	3.58	2760	0	0	1
2	15 – 30	6.44	3.66	2820	0	8.32E+19	1
3	30 – 60	7.93	4.41	3270	3.55E+18	3.55E+19	0.5
4	60+	7.93	4.41	3270	6.03E+17	6.03E+18	0.5

3.5.3 Removing Hydrologic Loading

The recent drought in the western United States has increased the impact of surface mass load variation on the modern deformation field. Both horizontal and vertical GPS data have been shown to be particularly sensitive to hydrologic variation (Amos et al., 2014; Argus et al., 2017; van Dam et al., 2001; Fu et al., 2013; W. C. Hammond et al., 2019; Kreemer & Zaliapin, 2018; Young et al., 2021). While the hydrologic cycle imparts load variation throughout the entire region, three distinct sources of surface loading are present within the study area. These are Lake Mead to the east of Las Vegas, Lake Powell in southern Utah, and Great Salt Lake in northern Utah (Figure 3.1). Each of which have well documented historical water levels and defined shorelines allowing load induced displacements to be calculated. While the surface levels of Lake Mead and Lake Powell show significant decline in recent years, the narrow widths of the lakes suggests only GPS stations in the near field are likely to be significantly affected. The regional impact of these loads is likely to be minor; however, for the best inference of the interseismic velocity field, it is necessary to account for all known signals.

We obtain surface water level time series from the Bureau of Reclamation for Lake Mead and Lake Powell, and through the National Water Information System for Great Salt Lake (see Data and Resources section). Time series of load induced surface displacements at nearby GPS stations are then calculated with the software LoadDef (Martens et al., 2019), using deviations in the historical surface water levels as loads applied to shoreline geometries and the Preliminary Reference Earth Model as the solid earth model (Dziewonski & Anderson, 1981). While (Young et al., 2021) showed that GPS stations near Great Salt Lake were affected by both surface and groundwater load variation, in this study we make no attempt to model water variation beyond the edges of the lakes and leave additional hydrologic signals throughout the study area to be addressed through common mode filtering. We remove the predictions of the load displacement models from the postseismic corrected time series of each GPS station. Velocities estimated from these time series are referred to as our "corrected" data set.

3.5.4 Removing Common Mode Components

Scatter in GPS time series influences uncertainty in velocities. Some of scatter is noise caused by multipath, monumentation issues, and processing errors; however, a portion of it can be attributed to regional common mode noise [see He et al. (2017) for an overview]. This is where time series exhibit scatter that is spatially correlated over multiple adjacent stations, separated by up to hundreds of kilometers, and can be caused by atmospheric effects, unmodeled hydrologic load changes, and other un/under-modeled signals (Bogusz et al., 2015; van Dam et al., 2007; Kreemer & Blewitt, 2021; Springer et al., 2019; vanDam et al., 1994). It has been shown that regional common mode can alter station velocities (Kreemer & Blewitt, 2021; Márquez-Azúa & DeMets, 2003; Santamaría-Gómez & Mémin, 2015; Serpelloni et al., 2013). While this is often a small effect, the low levels of deformation within the central Basin and Range require all potential biases to be addressed. To account for this, we follow Kreemer and Blewitt,

(2021) to produce common mode component filtered time series for all GPS stations in the study area. While some common mode identification methods rely only on the longest running stations in a region, Kreemer and Blewitt (2021) relies on robust statistics, allowing all but the most sparsely observed (i.e., semi-continuous) stations to be used. In order to take advantage of this method, it is necessary to include a set of core, long term stations which span the duration of the study period. This provides the baseline upon which the common mode of shorter duration stations may be evaluated. To best define the broad, long term common mode across the central Basin and Range, our study area is expanded to include additional stations beyond its extent which contain >95% data across the timeframe of 1999 – 2021.5, totaling 20 core stations. This timeframe provided the best trade-off between the number and distribution of core stations, while retaining as much data as possible, and we use it as our study period. Following calculation of the common mode for each station, it is removed from the corrected time series and new velocities are calculated, producing our corrected and filtered “final” data set.

3.5.5 Strain Rate Calculations

We opt to produce two sets of strain rate estimates using two methods, using the results of the first method as an a priori constraint of the second. Our first method is the MELD algorithm, which provides robust strain rate estimates, realistic uncertainties, and relies on median statistics (Kreemer et al., 2018, 2020). The use of medians in this method helps to account for poor data but also tends to provide smoother results than other methods. The second method is the Haines and Holt method, which calculates strain rates using bi-cubic spline interpolation (Beavan & Haines, 2001; Holt & Haines, 1993; Holt et al., 2000). A key benefit of the Haines and Holt method is the ability to input a priori uncertainties. This allows the model to be adjusted according to expected variation in the deformation field. In the case of our study, strong gradients extending from the ECSZ to the central Basin and Range would likely result in ECSZ strain leaking eastward if uniform uncertainty was applied. To address this, and to take advantage of the robust nature of the MELD solution, we use the second invariant of the MELD solution to adjust the input a priori uncertainties of Haines and Holt. This allows the model to better account for the expected variation in strain rate across the region. We determine our preferred model by scaling the uncertainties until we reach a χ^2 misfit equal to 4, thus setting the misfit equivalent to 2σ of the data. While Kreemer et al. (2010), used seismologic data in conjunction with GPS data to produce their strain rate estimates, we rely purely on GPS data. Solutions are produced for the final velocities as well as the original velocities, allowing for comparison between the observed modern field and our corrected interseismic field.

3.5.6 Las Vegas Block Modeling

Block modeling is an analysis framework for using geodetic and geologic data to estimate fault slip rates. In these models the GPS data constrain the motion of blocks whose boundaries are faults that are locked at the surface. Because the motion is measured during the interseismic period with GPS, the strain accumulation near the faults associated with locking is taken into account (Mccaffrey, 2002; Meade & Hager, 2005). Gradients in the GPS velocity field are thus separated analytically into components of Euler rotation of blocks and strain accumulation on faults. To derive our block model, we follow Hammond et al., (2011). Block boundaries are defined using fault traces obtained from the USGS Quaternary Fault and Fold database (U.S. Geological Survey et al., 2022). Individual segments are aligned with the traces of significant faults and are extrapolated and simplified as needed to produce a set of contiguous representative blocks. In some places it is necessary to assign a boundary where no faults are known to complete a block. For these locations, relative block motion is allowed so blocks can move as required by the GPS velocity data, but no shallow locking is assumed or slip rate estimated. We represent the tectonics of southern Nevada with 19 distinct blocks, that are bounded on their perimeters by 119 fault segments. The solutions produced by this method use prior uncertainty thresholds to provide balanced damping to the vertical axis spin rates and fault slip rates. To identify a model that finds a balance between the need to fit the GPS data, and also to be kinematically parsimonious, we test a range of solutions varying these parameters and identify the solution which has both a low data misfit and low slip rate model norm. For this data set, we identify the optimal a priori uncertainty in rotation rate as 3 x10^{-9} rad/yr and the uncertainty in slip rates as 0.2 mm/yr. With these values, we produce models using both the final and original velocity fields and compare estimated slip rates for the Eglington/Decatur and Frenchman Mountain sections with the observed GPS velocity budget for Las Vegas.

3.6 Results

3.6.1 Postseismic Correction within the CBR

Because central Basin and Range deformation rates are very low, the recurrence time between large earthquakes on a specific fault is generally longer than the time needed for most of the postseismic relaxation to occur. Thus, each fault is for most of its cycle, experiencing a strain rate near its long term average interseismic rate. So, when we subtract our modeled postseismic relaxation field, which represents deformation associated with a few specific recent earthquakes, from the observed GPS velocity field, the result is an approximation of the long term average interseismic deformation field. Thus, the composite postseismic model gives an indication of the difference between the long term average interseismic motion and the field that is detected now with contemporary GPS measurements. Figure 3.2 shows the postseismic relaxation field predicted by our model and shows that the crust throughout the entire region is substantially affected by postseismic transients. Here, velocities are calculated for each composite model across the study period (1999 – 2021.5), and the background color reflects the associated dilatational strain rate, calculated with MELD. While the strongest, and most variable, relaxation occurs along the SAFZ, broad regional relaxation extends well beyond the ECSZ into the central Basin and Range, with a rotational pattern driven by the Cascadia and SAFZ events. Within the Central Basin and Range itself, the relaxation field exhibits southeasterly movement, with the area around Las Vegas moving at ~2 mm/yr. The shear associated with this model is focused along the SAFZ and to a lesser extent the CNSB; however, we find that shear is also observed to span the region between Las Vegas and the Owens Valley Fault Zone (Figure S3.1).

We find that the majority of postseismic deformation is primarily driven by a few large events; however, the cumulative effect of smaller events is significant. Figure S3.2 shows the postseismic response to individual events for station UNR1, which is located inside the city limits of Las Vegas. The largest trends are found in the east component due to Fort Tejon (1857), San Francisco (1906), and Cascadia (1700), which amounts to 1.05, 0.64, and −0.48 mm/yr respectively over the duration of observation at UNR1 (Table S2). The north component is most affected by Hector Mine (1999), Landers (1992), and Fort Tejon with trends of −0.39, −0.37, and 0.28 mm/yr respectively. When considering low displacement events (i.e., those whose induced trends within the Las Vegas Valley are under 0.10 mm/yr), we find that the cumulative effect of these events is comparable to that of Cascadia and El Mayor–Cucapah in the north component, and San Francisco (1938) in the east (black lines in Figure S3.3).

While the modeled trends for each event reveal a strong influence on the velocities of the stations, it is important to assess the influence of individual events on the strain rate field within Las Vegas Valley. We produce strain rate models for each event and present the second invariant, dilatation, and shear strain rates in Table S3.2. The largest postseismic strain rates within the Las Vegas Valley are produced by the Fort Tejon, Ridgecrest, Owens Valley, and Landers earthquakes, with rates of 2.94, 1.59, 1.49, and 1.28 $x10^{-9}\,yr^{-1}$ respectively. We find that strain rates for the combined model of events which exhibited trends lower than 0.10 mm/yr in both components, is comparable in magnitude to that of Cascadia, with second invariant and dilatational strain rates of 0.79 $x10^{-9}\,yr^{-1}$ and -0.51 $x10^{-9}\,yr^{-1}$ respectively. Considering the values for the full composite model within Las Vegas Valley are 4.36 $x10^{-9}\,yr^{-1}$ and -1.40 $x10^{-9}\,yr^{-1}$, these results indicate the cumulative impact of low impact events plays an important role on the strain rate field and justifies our consideration of them.

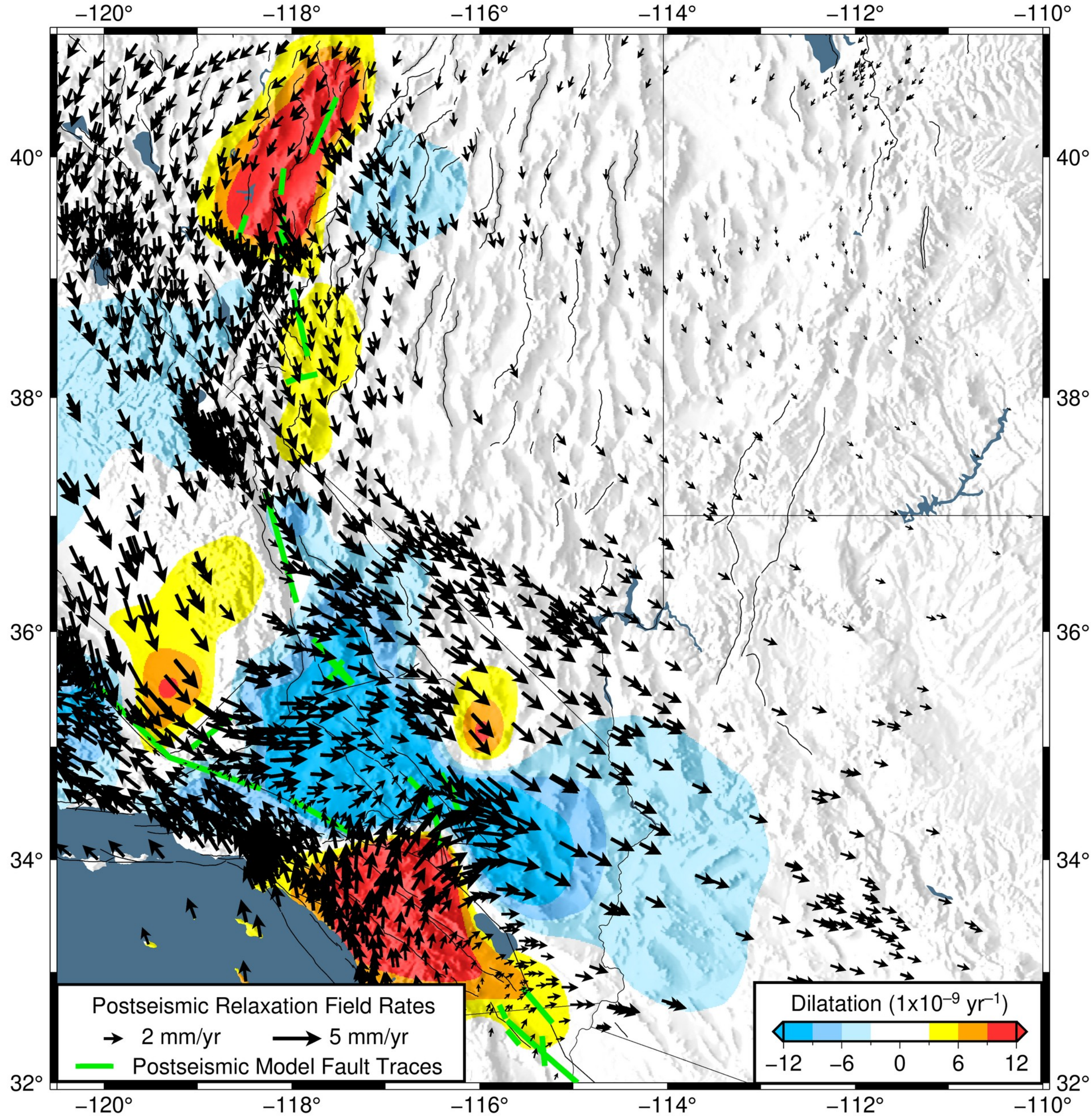

Figure 3.2: Modeled postseismic relaxation field. Black arrows represent relaxation velocities at the GPS stations. Modeled velocities are calculated with MIDAS over the study period of 1999-2021.5. Green lines indicate the location of fault traces of the earthquake models. Background shading indicates the dilatation component of the strain rates attributed to this model, calculated with MELD. Here, reds indicate extension and blues indicate contraction.

3.6.2 Corrected GPS Timeseries

Time series are noticeably improved following our corrections. A comparison of the east and north components of station UNR1 is shown in Figure 3.3, as well as their respective residuals following a fit for trend, annual/semi-annual terms, and steps. Here, time series for each data set are shown relative to the final solution and are plotted alongside the postseismic model which estimates a net displacement of 38 mm in the east and 25 mm in the north over ~17 years. The largest earthquakes during duration of this station’s time series are El Mayor–Cucapah in 2010 and the Ridgecrest events in 2019, shown by vertical red lines on the figure. We note that El Mayor–Cucapah introduces curvature in the north component while Ridgecrest affects the east component. For both cases, the postseismic models straighten the time series and improve the residual fit. Following filtering, a strong annual signal is present in the east component and becomes clearer in the north. The residual scatter in both components is greatly reduced with most deviations observed in the original data are removed.

Additional plots for stations ECHO, FERN, P626, TIVA, and P006, whose locations are distributed around the study area (Figure 3.1), are provided in the Supplemental Material (Figures S3.3 – S3.6). These plots highlight not only consistent data improvements but also the variability of the magnitude of the postseismic field across the study area. Figure S3.7 shows a comparison for station P006, which is located near the center of mass of Lake Mead on the Middle Point Islands, and includes the hydrologic model and all three components. We find the vertical displacements due to load changes on Lake Mead are substantial and dominate the vertical signal for this station. The horizontals are less substantial, with the east component showing minimal variability due to its location relative to the center of the load. The north component shows more displacement and its removal improves the residuals slightly.

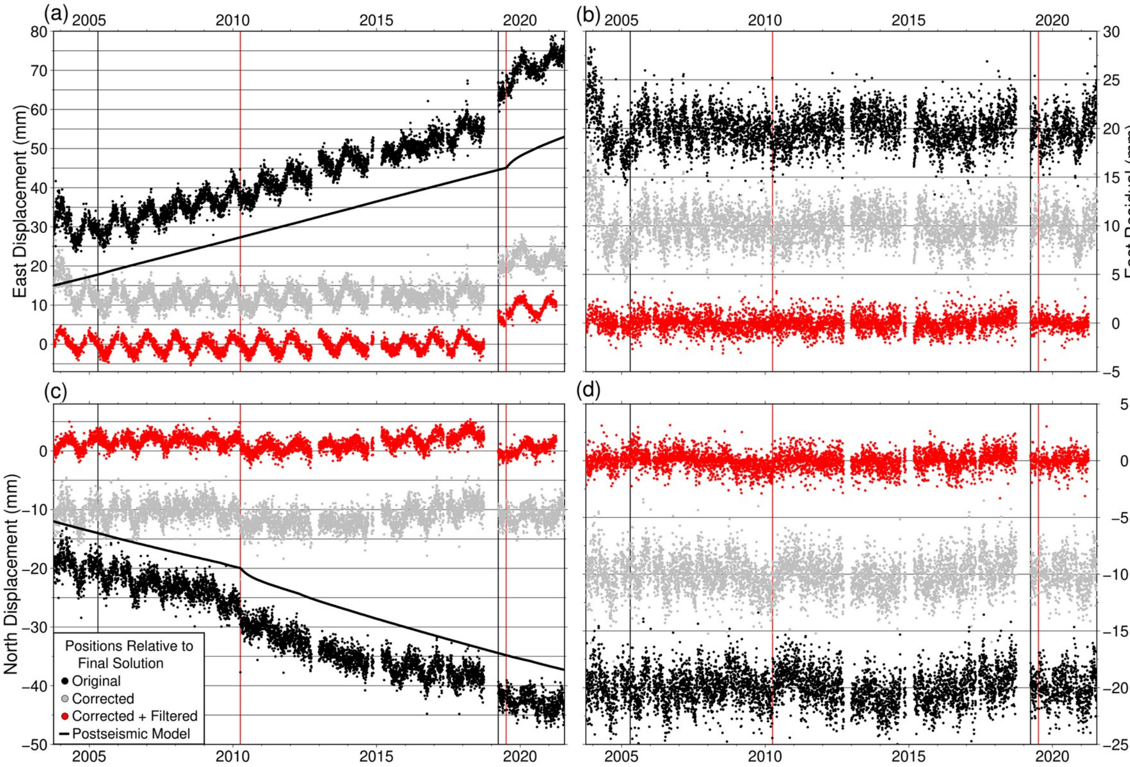

Figure 3.3: Time series comparison for station UNR1, located within Las Vegas. **(a)** East component. Black dots represent original positions. The thick black line is the postseismic deformation model for this station. Grey dots are the positions following postseismic and hydrologic model corrections. Red dots represent the positions after corrections and common mode filtering. All time series are detrended relative to the corrected and filtered final solution. **(b)** East residuals. **(c)** North component. **(d)** North residuals. Vertical black lines indicate the times of equipment related steps in the time series and the red vertical lines represent the El Mayor–Cucahpah (2010) and Ridgecrest (2019) earthquakes.

3.6.3 Velocity Uncertainty Reduction

The combination of postseismic and hydrological loading corrections with common mode filtering, substantially reduces station velocity uncertainties. Figure 4 shows a comparison between the uncertainties of the original, corrected, and final velocity fields calculated with MIDAS. While traditional least squares uncertainties are based on formal propagation of assumed levels of noise of the data, MIDAS derives its uncertainties from the scatter of inter-annual coordinate differences, and will result in improved uncertainties when accurate models are applied (Blewitt et al., 2016). The scatter plot shows that both the original and corrected solutions exhibit slightly higher uncertainties in the east component compared to the north, and that this is reversed following filtering. Median uncertainties per data set are shown in Table 3.3. We find that the postseismic correction reduces time series residual scatter, thus lowering velocity uncertainties on those stations affected by postseismic curvature. This improvement is significant with a median uncertainty reduction of 17.7% in the east and 14.5% in the north compared to the base uncertainties. Following filtering, the final velocity uncertainties are again substantially improved, resulting in a decrease of 62.1% and 53.8% in the east and north components relative to the original velocity uncertainties.

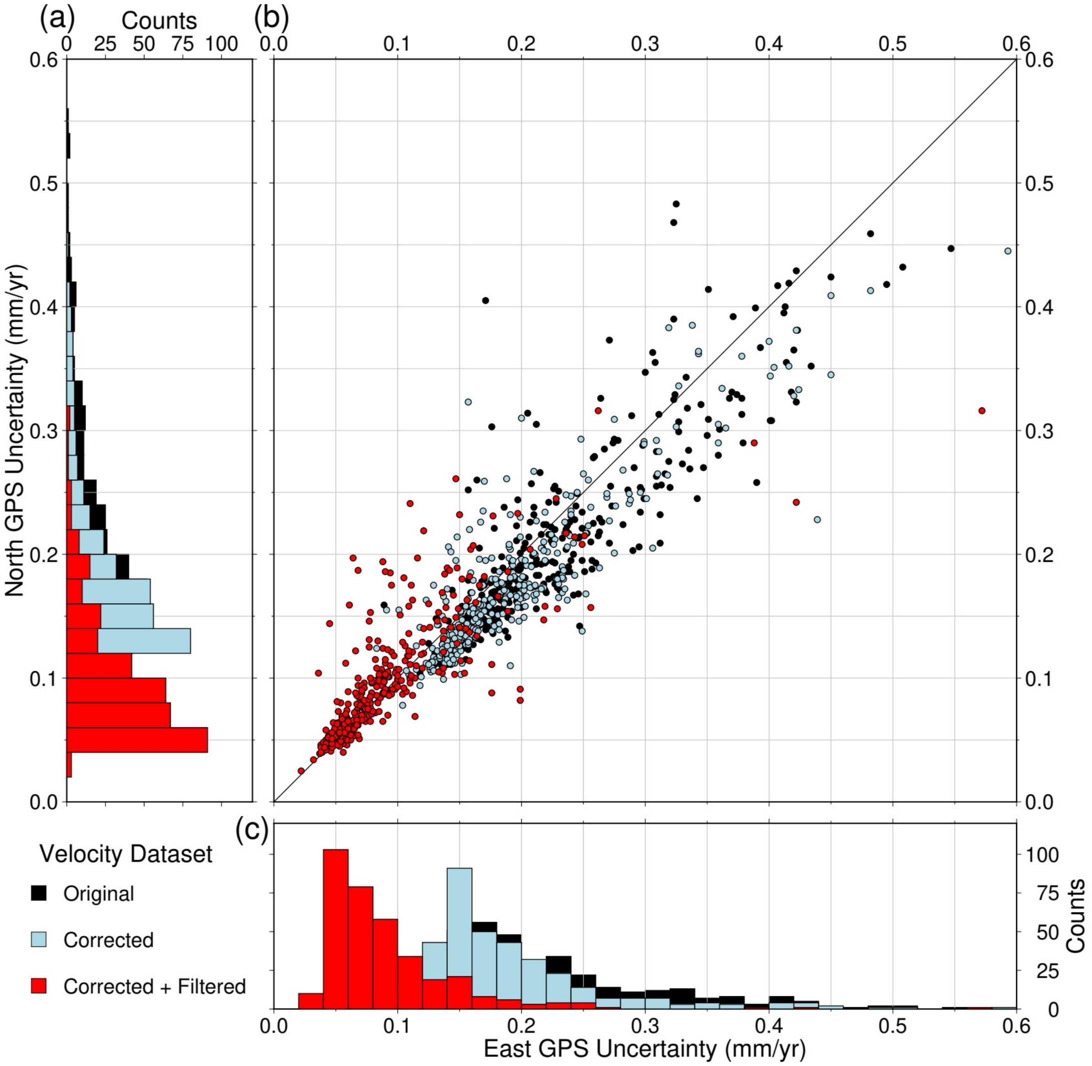

Figure 3.4: (a) Histogram of GPS station MIDAS velocity uncertainties in the north component. (**b**) Scatter plot of east and north uncertainties with a thin black equivalency line. **(c)** Histogram of GPS station MIDAS velocity uncertainties in the east component. Black bars (dots) represent the uncertainties of the original data, blue bars (dots) represent corrected uncertainties (i.e., following removal of the postseismic and hydrologic loading models), and red bars (dots) represent the corrected and filtered final uncertainties (i.e. corrections for both postseismic and hydrologic loading with common-mode filtering).

Table 3.3: Median MIDAS horizontal velocity uncertainties with error bounds relative to their trend, for the data sets shown in Figure 3.4. Error bounds for the uncertainties are defined as 1.4826*MAD, where MAD is the median absolute deviation of the residual scatter after removal of the estimated trend between the two components (Huber, 1981). Note that the median uncertainties are substantially reduced in the corrected and filtered solution, and that the scatter about their trend is equivalent.

Velocity Data Set	**Component**	$\widetilde{\sigma}$ **(mm/yr)**
Original	East	0.203 ± 0.057
	North	0.186 ± 0.067
Corrected	East	0.167 ± 0.039
	North	0.159 ± 0.041
Corrected + Filtered	East	0.077 ± 0.044
	North	0.086 ± 0.044

3.6.4 Corrected Velocity Field

A comparison of our original and final velocity field is shown in Figure 3.5. Here velocities are presented relative to the stable Colorado Plateau with the original velocities as black vectors and the corrected and filtered final velocities in red. To produce velocities relative to the Colorado Plateau, we identify the Euler rotation vector for all stations within its bounds, and then use it to rotate all velocities. Outliers (blue arrows) are identified as those whose magnitude differ by more than 0.9 mm/yr relative to a predicted velocity based on neighboring stations, using the technique of Kreemer et al. (2018). This threshold allows for variability in the field while quantitatively identifying distinct problem stations.

Station velocities increase rapidly beyond the border of the Colorado Plateau, introducing westward motion and shear along the eastern Pahranagat Shear Zone and southern Wasatch Fault. Velocities continue to steadily increase until reaching the ECSZ, where stations begin to exhibit more northward trends. We find that the final velocities produce significantly higher westward motions than observed in the original data set. This feature is driven strongly by corrections for the Fort Tejon and San Francisco 1906 events and is particularly apparent across Las Vegas where velocities are nearly purely westward and along the Mojave Desert where velocities are doubled for most stations. The strong postseismic effect on the east component of the velocities for stations in Arizona, has been discussed by Broermann et al. (2021). Station uncertainties, shown by 95% confidence ellipses, are significantly improved and are uniform across the region following CMC filtering.

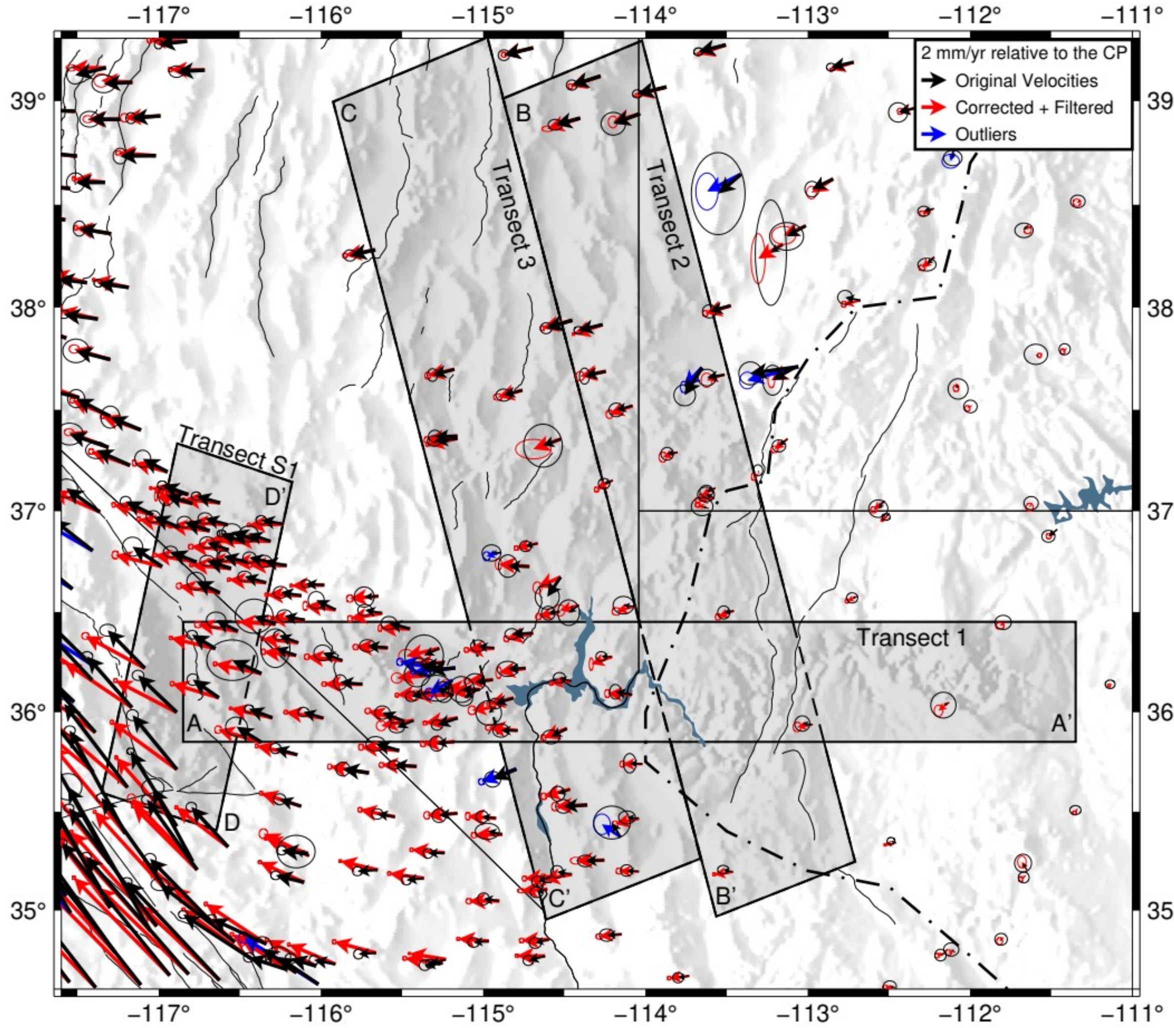

Figure 3.5: GPS velocity field comparison. Velocities are shown relative to the Colorado Plateau with 95% confidence ellipses. Black arrows represent velocities of the original time series and red arrows represent the corrected and filtered final velocities. Blue arrows identify outliers following corrections and filtering. Shaded rectangles identify the bounds of Transects 1 – 3 (Figures 3.6 – 3.7) and Transect S1 (Figure S3.12). Faults are shown as thin black lines and the dash-dotted black line represents the western edge of the Colorado Plateau. Dashed lines indicate transect overlap.

3.6.5 Las Vegas Velocity Budget

Closer inspection of the velocity field is provided through Transects 1 – 3 and S1 (Figure 3.5). Transect 1 is oriented east–west and runs between the easternmost edge of the ECSZ, crosses Las Vegas and Lake Mead, and ends on the Colorado Plateau (Figure 3.6). For all three data sets, the east component reveals a consistent velocity trend. Westward motion is increased by 2.5 mm/yr along the length of the transect. The north component, however, shows two distinct trends. We find that the area to the east of Las Vegas marks a transition zone between stable, near zero velocities to the east, and increasing northward velocities to the west. This transition occurs between the city limits of Las Vegas and the western edge of Lake Mead near the Frenchman Mountain fault.

To examine the amount of extension observed across the faults of the Las Vegas Valley, we determine a GPS derived velocity budget. Trendlines are fit to each velocity data set between the eastern edge of Las Vegas and the ECSZ and their values are presented in Table 3.4. We find that the eastward velocity trend is more than twice as fast in the final solution compared to that of the original data, at a rate of 0.84 ± 0.29 (mm/yr)/100 km versus 0.35 ± 0.23 (mm/yr)/100 km. The trend of the north component is reduced slightly to a rate of -0.69 ± 0.26 from -0.90 ± 0.35 (mm/yr)/100 km in the original data. The significance level of the east component trend is substantially improved while the north component retains a similar level of significance following filtering.

The two normal faults which bound the Las Vegas Valley are the Eglington/Decatur faults to the west and the Frenchman Mountain fault to the east. Since the elastic deformation due to these locked normal faults extends away from the faults (Freund & Barnett, 1976), we define our velocity budget as the region between these faults plus an additional 20 km to the west and east, totaling 62.4 km. Applying the observed trends across our preferred budget zone, produces 0.52 ± 0.18 mm/yr (0.22 ± 0.14 mm/yr) of eastward motion and 0.43 ± 0.16 mm/yr (0.56 ± 0.22 mm/yr) of southward motion for the final (original) data sets (Table 3.5). The final solutions are our preferred rates. Those of the original data set are clearly incorrect due to the strong impact of postseismic relaxation within the Las Vegas Valley. While a more fine-tuned viscosity model may change the corrected rates, this difference would likely be slight in comparison to the difference between our final and original rates.

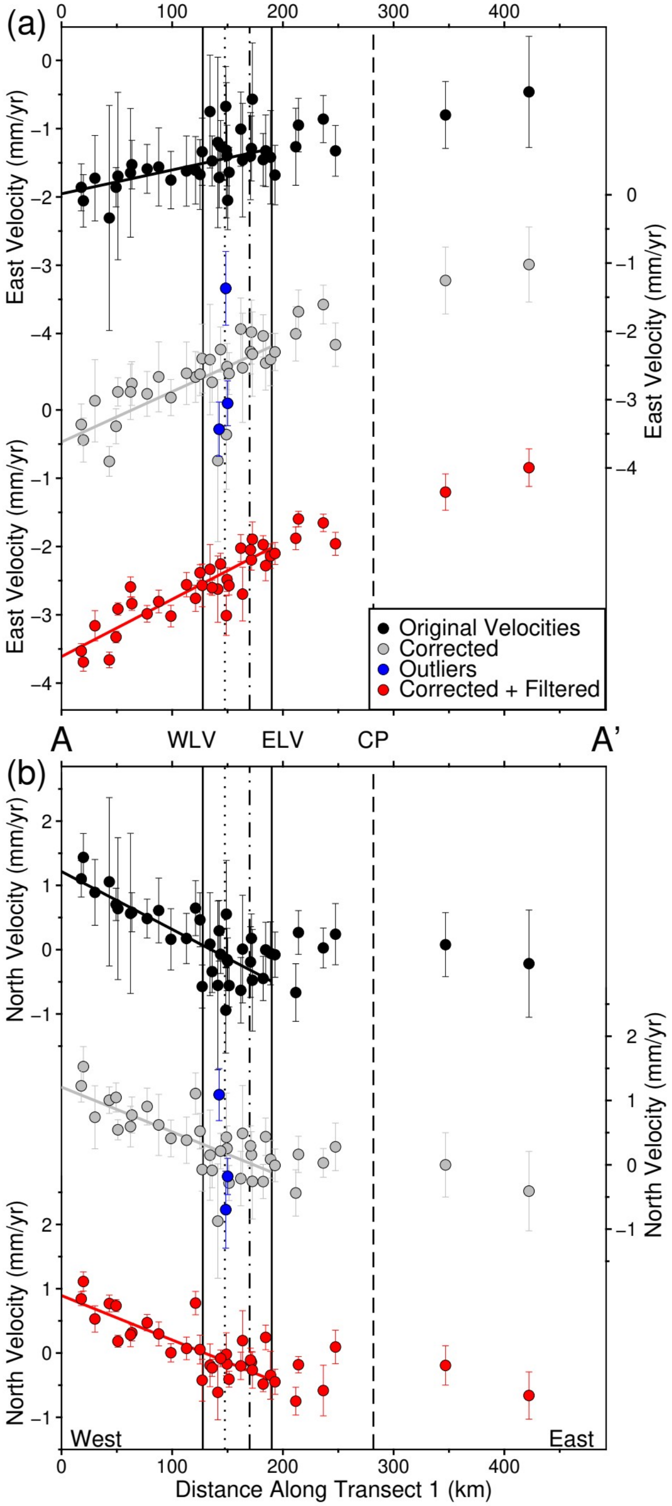
(a)
0
100
200
300
400
East Velocity (mm/yr)
0
−1
−2
−3
−4
East Velocity (mm/yr)
0
−1
−2
−3
−4
Original Velocities
Corrected
Outliers
Corrected + Filtered
A
WLV
ELV
CP
A'
(b)
North Velocity (mm/yr)
2
1
0
−1
North Velocity (mm/yr)
2
1
0
−1
West
East
Distance Along Transect 1 (km)

Figure 3.6: GPS velocities in the east **(a)** and north **(b)** components along Transect 1 (see Figure 3.5), with two sigma error bars. Transect is oriented east–west. Black dots represent velocities of the original data, grey dots represent the corrected velocities, blue dots represent outliers following corrections and filtering, and red dots represent the corrected and filtered final velocities. Solid lines represent the trends for each data set in their respective colors. The black dotted (dash-dotted) lines represent the location of the Eglington (Frenchman Mountain) faults and the dashed vertical line is the western edge of the Colorado Plateau. The solid black vertical lines represent the western and eastern edges of the Las Vegas Valley used to calculate the velocity budget. This accounts for an additional 20 km to capture the zone of strain accumulation associated with the Eglington and Frenchman Mountain faults.

Table 3.4: Velocity trends and their significance ratios, for the trendlines shown in Figure 3.6, along Transect 1.

Velocity Trends	**ΔV_E [(mm/yr)/100 km]**	**Significance Ratio**	**ΔV_N [(mm/yr)/100 km]**	**Significance Ratio**
Original	0.35 ± 0.23	1.51	−0.90 ± 0.35	2.59
Corrected	0.74 ± 0.35	2.10	−0.70 ± 0.41	1.69
Corrected + Filtered	0.84 ± 0.29	2.89	−0.69 ± 0.26	2.63

Table 3.5: Las Vegas Valley velocity budget and reflective strain rates, per data set. The velocity budget is calculated as the trend (see Table 3.4), over the distance between the Eglington and Frenchman Mountain faults, plus an additional 20 km to both the west and east to account for off-fault deformation (62.4 km in total).

LV Valley Velocity Budget	**ΔV_E (mm/yr)**	**Velocity Gradient ($1\text{x}10^{-9}\text{yr}^{-1}$)**	**ΔV_N (mm/yr)**	**Velocity Gradient ($1\text{x}10^{-9}\text{yr}^{-1}$)**
Original	0.22 ± 0.14	3.5 ± 2.3	−0.56 ± 0.22	8.9 ± 3.5
Corrected	0.46 ± 0.22	7.4 ± 3.5	−0.43 ± 0.26	7.0 ± 4.1
Corrected + Filtered	0.52 ± 0.18	8.4 ± 2.9	−0.43 ± 0.16	6.9 ± 2.6

3.6.6 Pahranagat Shear Zone Transects

Transects 2 and 3 run parallel to each other and are orthogonal to the Pahranagat Shear Zone (Figure 3.7). The eastern Pahranagat Shear Zone is shown in Transect 2 and reveals a clear velocity gradient between GPS station ECHO and the Colorado Plateau. This zone accommodates a velocity trend of 1.46 ± 0.19 (mm/yr)/100 km (Table 3.6), with velocities on either side being stable. Along the western Pahranagat, shown by Transect 3, a much slower trend of 0.31 ± 0.25 (mm/yr)/100 km is observed. Notably, the trend across Transect 3 is substantially affected by the postseismic model with a corrected trend that is half that of the original rate. This level of reduction is not observed in the eastern Pahranagat where the final velocities only indicate a slight reduction in the velocity trend.

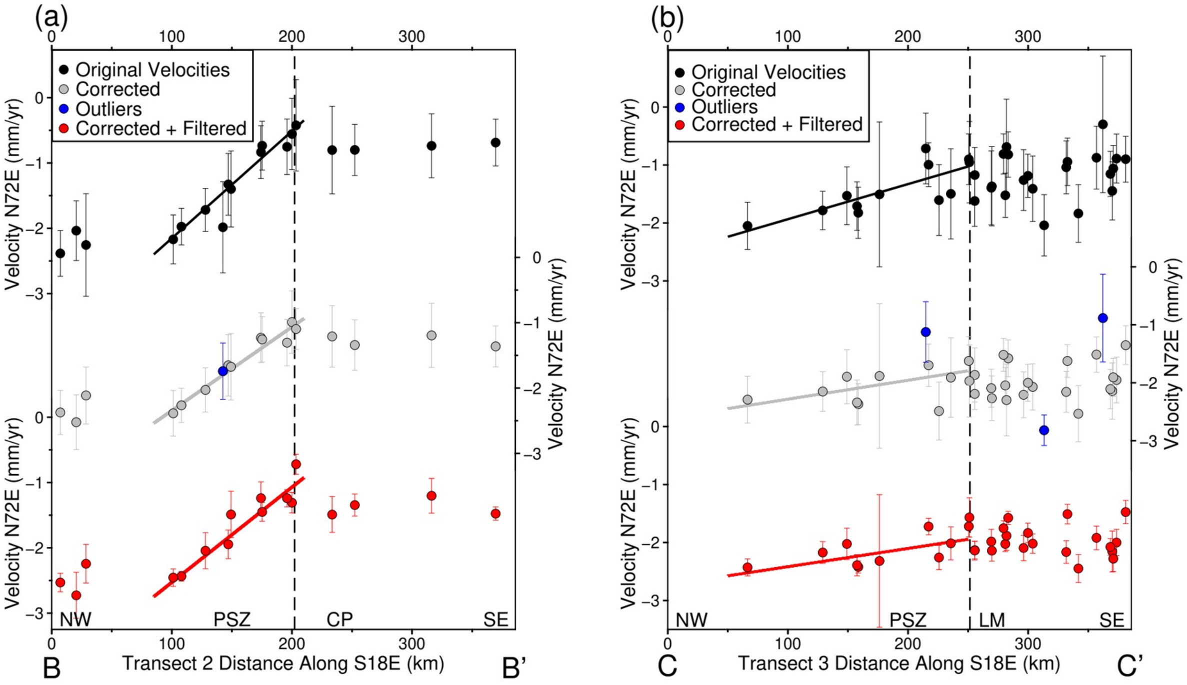

Figure 3.7: (a) GPS velocities perpendicular to Transect 2 (Figure 3.5). Transect is oriented S18E and runs from eastern Nevada, crosses the eastern Pahranagat Shear Zone, and the western Colorado Plateau. Key as described in Figure 3.6. Dashed line indicates the western edge of the Colorado Plateau. (**b)** Velocities perpendicular to Transect 3. This transect runs parallel to Transect 2 and crosses the western Pahranagat and Lake Mead. Dashed line indicates the northern edge of Lake Mead.

Table 3.6: Perpendicular velocities per 100 km and their implied strain rates, by velocity data set, for the trend lines shown on Transect 2 and 3 (Figure 3.7).

	Transect 2		**Transect 3**	
	ΔV [(mm/yr)/100 km]	**Velocity Gradient ($1x10^{-9}yr^{-1}$)**	**ΔV [(mm/yr)/100 km]**	**Velocity Gradient ($1x10^{-9}yr^{-1}$)**
Original Velocities	1.64 ± 0.11	16.41 ± 1.07	0.61 ± 0.26	6.06 ± 2.60
Corrected	1.28 ± 0.12	12.81 ± 1.21	0.33 ± 0.22	3.26 ± 2.20
Corrected + Filtered	1.46 ± 0.19	14.57 ± 1.86	0.31 ± 0.25	3.15 ± 2.45

3.6.7 Central Basin and Range Strain Rates

Strain rate estimates based on the final velocities, for both the MELD solution and Haines and Holt solution, are shown in Figure 3.8. Here we present all strain rates that exceed 1σ. The strain rate patterns for both solutions are quite similar, with the Haines and Holt solution providing a more variable depiction of the deformation field. Both solutions observe the largest second invariant strain rates along the ECSZ and the Wasatch Fault Zone. Between these two features, a band of elevated strain rate (6 – 12 $\times10^{-9}$ yr^{-1}) is present, which crosses from the ECSZ near the Mojave Desert, runs through Las Vegas and the western edge of Lake Mead, and connects into the eastern Pahranagat Shear Zone and the southern Wasatch Fault. The largest dilatation values are observed along the Wasatch Fault Zone with elevated levels near Las Vegas. Low level dilatation (3 – 6 $\times10^{-9}$ yr^{-1}) is found in the area connecting the southern Wasatch Fault to southern Nevada and western Arizona. Shear is primarily concentrated along the ECSZ and the eastern Pahranagat Shear Zone. Nearly pure east–west extension is shown by the principal axis across the majority of the study area with the exception of the ECSZ and the region between the Pahranagat Shear Zone and the CNSB. The latter is likely driven by GPS network geometry due to the sparsity of stations beyond the northern flank of the Pahranagat Shear Zone. This would lead to shear seemingly spreading across central Nevada and explains east–west extension within the Pahranagat Shear Zone, even though our profiles clearly highlight shear there. The average second invariant strain rates for the Las Vegas Valley are 8.5 ± 2.4 $\times10^{-9}$ yr^{-1} for the Haines and Holt solution, and 7.6 ± 2.7

$x10^{-9}\,yr^{-1}$ for MELD. These values are higher than those estimated with the original velocities, which were 4.7 ± 1.4 $x10^{-9}\,yr^{-1}$ for the Haines and Holt solution, and 5.1 ± 3.5 $x10^{-9}\,yr^{-1}$ for MELD.

Comparison of these solutions to the strain rate solutions for the original velocities, reveals several distinct differences (Figure S3.8). Primarily, the band of higher strain rates that is observed to extend across Las Vegas, does not connect the ECSZ to the Wasatch Fault Zone. Instead, the southern portion terminates to the southwest of Las Vegas and the northern arm continues westward along the Pahranagat Shear Zone rather than turning south toward Las Vegas. The original velocity solutions also suggest substantially higher shear across the Pahranagat Shear Zone with a clear connection between the southern Wasatch Fault and the ECSZ, at a latitude of ~37°. Notably, dilatation is much lower across the entirety of the study area in this solution.

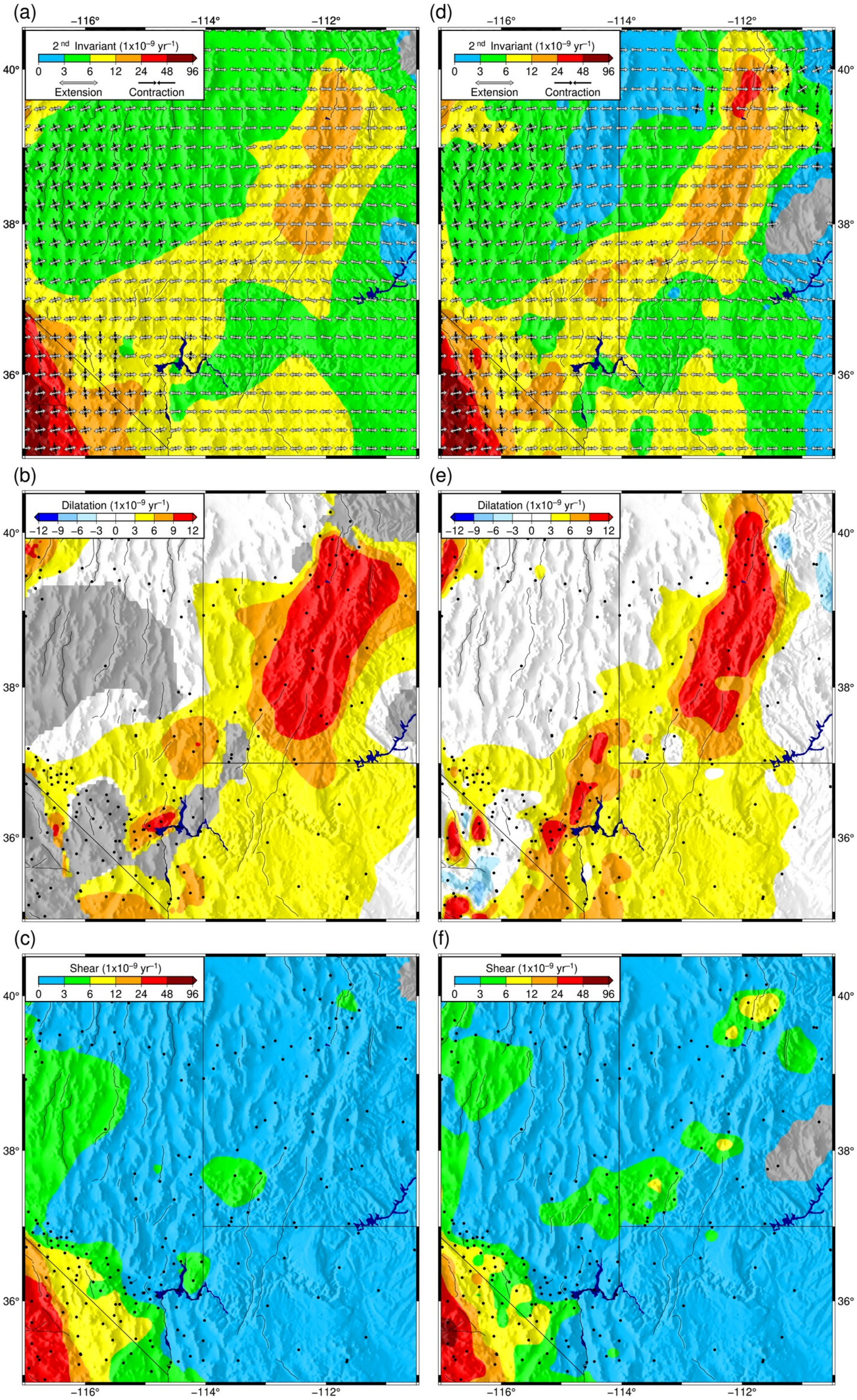
(a)
(b)
(c)
(d)
(e)
(f)
2nd Invariant (1x10⁻⁹ yr⁻¹)
0 3 6 12 24 48 96
Extension
Contraction
Dilatation (1x10⁻⁹ yr⁻¹)
−12 −9 −6 −3 0 3 6 9 12
Shear (1x10⁻⁹ yr⁻¹)
0 3 6 12 24 48 96
−116°
−114°
−112°
40°
38°
36°

Figure 3.8: Solutions for the MELD **(a – c)** and Haines and Holt **(d – f)** strain rate models for the final velocities. **(a and d)** Plots of second invariant strain rates overlain with normalized strain rate axis. Grey arrows indicate extension and black arrows indicate contraction. **(b and e)** Plots of the dilatational component of the strain rate. **(c and f)** Plot of the shear component of the strain rate. All plots are limited to strain rates greater than one sigma.

3.6.8 Block Models

Our preferred block model, using the final velocities, is shown in Figure 3.9, and a comparison using the same uncertainty parameters, but with the original velocities, is shown in Figure S3.9. We find extension across most of the study area except for the Garlock Fault and the northernmost section of the Death Valley Fault. The RMS residual velocity of this model to the GPS data is 0.26 mm/yr in the east component, and 0.25 mm/yr in the north component, and is substantially lower than the misfit produced with the original velocities (Table 3.7). The largest misfit is found at stations along the ECSZ, where velocities increase rapidly. In our preferred model we do not see the systematic, block wide, misfit observed in the original velocity model (Figures S3.10 – S3.11).

Our preferred model estimates higher slip rates across the entirety of the study area compared to the original velocity model, with some of the fastest slip rates found along the fault segments that bound the Las Vegas Valley. These are the Eglington and Decatur faults on the western side of Las Vegas and the Frenchman Mountain Fault to the east. We find the strike slip component on these faults to be particularly low and well below the significance thresholds, but the extensional component is significant. The average extensional slip rate, projected to the east–west component, are

0.31 ± 0.11 mm/yr and 0.27 ± 0.13 mm/yr for the Eglington/Decatur and Frenchman Mountain Fault segments respectively. This reflects a total east–west extension rate across Las Vegas Valley of 0.59 ± 0.12 mm/yr, more than twice that produced by the original velocities. The north–south component of extension is much lower, at a rate of 0.20 ± 0.12 mm/yr.

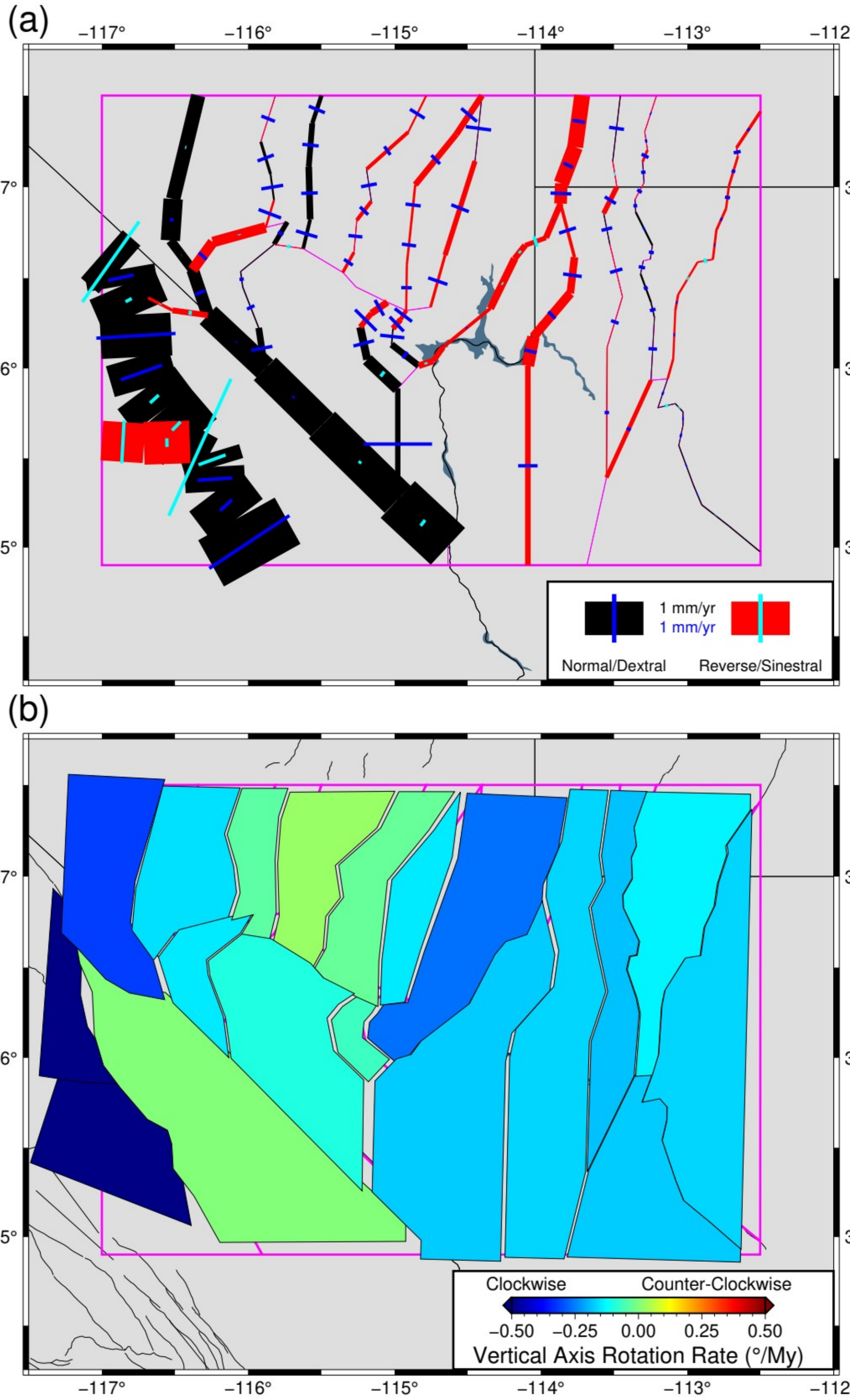
(a)
−117°
−116°
−115°
−114°
−113°
−112°
37°
36°
35°
1 mm/yr
1 mm/yr
Normal/Dextral
Reverse/Sinestral
(b)
Clockwise
Counter-Clockwise
−0.50
−0.25
0.00
0.25
0.50
Vertical Axis Rotation Rate (°/My)

Figure 3.9: Plots of the preferred block model using the final velocities. This model used an a priori uncertainty in the rotation rate of $\beta = 3 \times 10^{-9}$ rad/yr, with an a priori uncertainty in slip rates of $\gamma = 0.2$ mm/yr. **(a)** Fault slip rates. The thickness of the black and red lines represents dextral and sinestral slip rates while the length of the blue and cyan lines represents normal and thrust slip rates. Pink lines represent the bounds of the block model and inactive (non-fault) block edges. **(b)** Rigid block component of motion shown with the strain accumulation near faults to highlight relative block motion. Color scale indicates the vertical axis rotation rate with an exaggeration factor of 1×10^{7}. Pink lines represent the initial block locations.

Table 3.7: Extensional slip rates for Las Vegas Valley faults estimated by block models 1 and 2 (Figures 3.9 and S3.9). Block model 1 used the final velocity data set and block model 2 used the original velocities. Slip rates are projected from the fault segments to east–west and north–south orientations. The Eglington/Decatur fault rates represent the average extensional slip on both fault segments directly west of Las Vegas. Similarly, the Frenchman Mountain rates reflect the average extensional slip on all four fault segments east of Las Vegas. The total Las Vegas extensional slip rates are the sum of these values.

	Block Model 1		**Block Model 2**	
Velocity Data Set	Final		Original	
Component of Extension	**East – West (mm/yr)**	**North – South (mm/yr)**	**East – West (mm/yr)**	**North – South (mm/yr)**
Eglington/Decatur	0.31 ± 0.11	0.08 ± 0.11	0.11 ± 0.11	0.04 ± 0.11
Frenchman Mtn.	0.27 ± 0.13	0.12 ± 0.13	0.10 ± 0.13	0.05 ± 0.13
Total LV Extension Rate	0.59 ± 0.12	0.20 ± 0.12	0.22 ± 0.12	0.08 ± 0.12
GPS RMS Misfit (mm/yr)	0.26	0.25	0.41	0.55

3.7 Discussion

3.7.1 Velocity Field Corrections

The corrections made to the velocity field in this study are substantial, with the postseismic model correcting the magnitudes and orientations of the velocity vectors and common mode filtering greatly reducing their MIDAS uncertainties. Postseismic deformation is pervasive within the central Basin and Range. Inspection of the individual models per GPS station, reveals the primary driving factor of the relaxation field is not the inclusion of specific large events but rather that it is driven by the sum of its parts. We find that no single earthquake dominates the relaxation field across the central Basin and Range and that primary contributors vary across the study area, revealing a dynamic spatio-temporal interplay between positive and negative interference between earthquakes. This is illuminated by Table S3.2, which shows that while both the Ridgecrest and Landers events impart substantial strain rates, their dilatational components are equal and opposite, with Ridgecrest applying contraction to the valley at $-1.26 \text{ x}10^{-9} \text{ yr}^{-1}$ and Landers applying extension at $1.26 \text{ x}10^{-9} \text{ yr}^{-1}$. A similar case can be made for the Wrightwood and El Mayor–Cucapah events, for which Las Vegas lies within the compressional quadrant of the relaxation due to the Wrightwood event, and the extensional quadrant of El Mayor–Cucapah. Higher strain rates are produced when only considering the 11 strongest events compared to our composite model. This shows that the more subtle earthquakes temper the velocity gradients produced by the larger events within the Las Vegas Valley.

Often studies that model postseismic deformation focus on near field events (Dickinson et al., 2016; Guns & Bennett, 2020; Hammond et al., 2009), which for this study, would omit the Cascadia event. This would skew our velocity field within Las Vegas Valley by 0.48 mm/yr in the east component and would also omit a significant velocity gradient across the region as postseismic strain rates associated with the Cascadia event are high (relative to central Basin and Range strain rates), at 0.88 $x10^{-9}$ yr^{-1}. Additionally, we note that for a given station, many of the models produce undetectable levels of displacements and strain rates (i.e., <0.10 mm/yr, <0.25 $x10^{-9}$ yr^{-1}). Individually, these events are inconsequential to the station's velocity and the strain rate field; however, the sum of these trends can be comparable to some of the largest events and alter the velocity gradient of the region. These observations further highlight the necessity to account for all potential sources of postseismic deformation, including lower magnitude (e.g., M_w >6.5 close to the study area and within the GPS timeframe) or fairly distant events (e.g., 1000+ km for M_w 7+ events) when determining an interseismic strain rate field.

The uncertainty analysis reveals variability in the uncertainties by component. We find the east component to exhibit higher uncertainties in both the original and corrected solutions but following filtering it is reversed. We propose that this is likely due to hydrologic loading signals present in the original data which are captured during filtering. Throughout the central Basin and Range, mountain rages generally run north–south, meaning that hydrologic loads within the valleys will as well. As these loads vary, the largest displacements would be oriented in an east–west direction, thus increasing east component variability in the time series. These motions would be correlated across nearby stations allowing them to be captured by Common Mode Component Imaging.

3.7.2 Pahranagat Shear Zone

Kreemer et al. (2010) identified an active Pahranagat Shear Zone, which firmly connected the ECSZ to the southern Wasatch Fault and is strongly spatially correlated to the Southern Nevada Seismic Zone (dePolo & dePolo, 2012). Our results are particularly consistent with this interpretation when we use our original velocity data set (Figure S3.8), which is consistent with Kreemer et al. (2010) not accounting for transient signals in the time-series. Our corrected interseismic velocities reveal a diminished western Pahranagat, with as much as half of the shear originally observed attributed to postseismic relaxation (Figure 3.7). This indicates that rather than being a well-defined consistent structure, the Pahranagat Shear Zone is temporally variable, with the magnitude of its strain rates dependent on the current state of the postseismic relaxation field. These findings do not alter the tectonic importance of the Pahranagat Shear Zone, as it is strongly supported by seismicity, but shed light on its function within the central Basin and Range.

3.7.3 Active Deformation Within the Las Vegas Valley

We see clear evidence, both in the original velocity data set and our final interseismic velocities, that there is active deformation across the Las Vegas Valley. Transect 1 shows that east–west extension between the ECSZ and the Colorado Plateau is extremely coherent, with no significant deviations along its length. The lack of variation in the trend suggests fairly equal accommodation of extension on all faults along the transect, including the Eglington/Decatur and Frenchman Mountain faults. Previous studies found slip on the Frenchman Mountain fault to be less than 0.1 mm/yr (dePolo, 1998; Slemmons, 1998), and while some evidence suggested slip rates for the Eglington fault could be as high as 1.0 mm/yr (dePolo & Ramelli, 1998), the USGS Quaternary Fault and Fold database lists both of these faults at rates under 0.2 mm/yr. While our original velocity block model does estimate rates close to 0.1 mm/yr for these faults, the results corrected for postseismic relaxation, hydrological loading and common mode noise suggest the rates on these faults are substantially higher, at values close to 0.3 mm/yr (Table 7). Totaling 0.5 – 0.6 mm/yr of east–west extension across Las Vegas Valley. These results indicate the presence of substantially higher deformation rates than previously suggested. Further evidence is present in the strain rate solutions. We find average strain rates within the valley to be elevated at $8.5 \pm 2.4 \times 10^{-9}\,\mathrm{yr}^{-1}$. While this value is low in respect to highly seismogenic regions such as the ECSZ and SAFZ, comparison to a more extensional domain is more appropriate. For this we look to the 2008 Wells earthquake in northeastern Nevada, where Hammond et al. (2014) shows strain rates near the event are ~2 $x10^{-9}$ yr^{-1}. Although those rates are particularly low, they are significantly greater than their quoted uncertainties and accumulated stresses were significant enough to produce a M_w 6.0 event which caused considerable damage to buildings in the town of Wells, Nevada (dePolo & Pecoraro, 2011). Considering our preferred strain rates are nearly five times higher (and ~2.5 times higher in the uncorrected data), we find the possibility of a significant event with M_w >6 quite reasonable given the level of deformation observed.

3.8 Conclusions

In this study we provide updated geodetic constraints on the interseismic deformation field within the central Basin and Range. We take advantage of the recent expansion of the GPS network, including 107 semi-continuous MAGNET stations, as well as several recently published processing methods, to obtain the most robust interseismic velocity field for the region to date. We pay careful attention to the removal of transient signals associated by postseismic and hydrologic load deformation and filter out the regional common mode noise. The combined corrections reduce velocity uncertainties dramatically with a total reduction of 62.1% in the east component and 53.8% in the north. These corrections greatly affect the resulting strain rate field and alter the implications of the hazard within the region. We find that strain rates within the Las Vegas Valley are much higher than in previous studies, as well as when compared to the original velocity strain rates, with our preferred value being 8.5 ± 2.4 $x10^{-9}$ yr^{-1}.

Using our final velocities, we produce a GPS velocity budget for the Las Vegas Valley. East to west trends are extremely consistent at a rate of 0.84 ± 0.29 (mm/yr)/100 km, equivalent to 0.52 ± 0.18 mm/yr across the valley. Additionally, we produce a block model which estimates the combined east–west extension on the Eglington/Decatur and Frenchman Mountain faults to be 0.59 ± 0.12 mm/yr. We find that interseismic extension across the valley is more than two times faster after accounting for postseismic transients. The combination of these results clearly supports the interpretation that crustal deformation is active within the Las Vegas urban area, at much higher long-term rates than previously estimated.

3.9 Data And Resources

The Nevada Geodetic Laboratory provides GPS time series (Blewitt et al., 2018), as well as the MIDAS software (Blewitt et al., 2016), at http://geodesy.unr.edu (last accessed July, 2022). The LoadDef software is available at https://www.github.com/hrmartens/LoadDef (Martens et al., 2019) (last accessed May, 2022). The MELD and Haines & Holt software are available upon request. Surface water level data was obtained through the Bureau of Reclamation for Lake Powell at https://www.usbr.gov/rsvrWater/HistoricalApp.html (last accessed February, 2022), and for Lake Mead at https://www.usbr.gov/lc/region/g4000/hourly/mead-elv.html (last accessed February, 2022). Great Salt Lake surface water level data was obtained through the National Water Information System at https://www.maps.waterdata.usgs.gov/mapper/ (last accessed February, 2022). Many of the fault slip models used in this study are available from the SRCMOD database at http://equake-rc.info/srcmod/ (last accessed May, 2022). The PSGRN/PSCMP software is available at https://github.com/pyrocko/fomosto-psgrn-pscmp (Wang et al., 2006) (last accessed May, 2022). All figures were produced using Generic Mapping Tools version 6.0.0 (https://www.soest.hawaii.edu/gmt/; Wessel et al., 2019). The supplemental material contains Tables S3.1 – S3.2 and Figures S3.1 – S3.12.

3.10 Declaration Of Competing Interests

The authors declare no competing interests.

3.11 Acknowledgments

We thank Craig DePolo and Seth Dee for discussions which provided useful insight into the Las Vegas region. This work was funded by USGS NEHRP grants G13AP0018 and G20AP00080, SCEC grant 21176, DOE grant EE0009254, NSF grants EAR-0952166 and EAR-1615253, and NASA grants 80NSSC19K1044 and 80NSSC22K0463. We thank Bret Pecoraro, as well as the many students and colleagues who have aided in GPS data collection. We are grateful for the freely available data provided by UNAVCO (for NOTA GPS stations), the Las Vegas Valley Water District, Leica Smartnet North America, and the Utah TURN network. We thank Jet Propulsion Laboratory, California Institute of Technology, for the GipsyX software and precise orbit and clock products used to generate the GPS time series.

3.12 References

Altamimi, Z., Rebischung, P., Métivier, L., & Collilieux, X. (2016). ITRF2014: A new release of the International Terrestrial Reference Frame modeling nonlinear station motions. *Journal of Geophysical Research: Solid Earth*, *121*(8), 6109–6131. https://doi.org/10.1002/2016JB013098

Amos, C. B., Audet, P., Hammond, W. C., Bürgmann, R., Johanson, I. A., & Blewitt, G. (2014). Uplift and seismicity driven by groundwater depletion in central California. *Nature*, *509*(7501), 483–486. https://doi.org/10.1038/nature13275

Argus, D. F., Landerer, F. W., Wiese, D. N., Martens, H. R., Fu, Y., Famiglietti, J. S., et al. (2017). Sustained Water Loss in California's Mountain Ranges During Severe Drought From 2012 to 2015 Inferred From GPS. *Journal of Geophysical Research: Solid Earth*, *122*(12), 10,559-10,585. https://doi.org/10.1002/2017JB014424

Barrientos, S. E., Stein, R. S., & Ward, S. N. (1987). Comparison of the 1959 Hebgen Lake, Montana and the 1983 Borah Peak, Idaho, earthquakes from geodetic observations. *Bulletin of the Seismological Society of America*, *77*(3), 784–808. https://doi.org/10.1785/BSSA0770030784

Bawden, G. W. (2001). Source parameters for the 1952 Kern County earthquake, California: A joint inversion of leveling and triangulation observations. *Journal of Geophysical Research: Solid Earth*, *106*(B1), 771–785. https://doi.org/10.1029/2000JB900315

Beavan, J., & Haines, J. (2001). Contemporary horizontal velocity and strain rate fields of the Pacific-Australian plate boundary zone through New Zealand. *Journal of Geophysical Research: Solid Earth*, *106*(B1), 741–770. https://doi.org/10.1029/2000JB900302

Bertiger, W., Bar-Sever, Y., Dorsey, A., Haines, B., Harvey, N., Hemberger, D., et al. (2020). GipsyX/RTGx, a new tool set for space geodetic operations and research. *Advances in Space Research*, *66*(3), 469–489. https://doi.org/10.1016/j.asr.2020.04.015

Blewitt, G., Hammond, W. C., & Kreemer, C. (2009). Geodetic observation of contemporary deformation in the northern Walker Lane: 1. Semipermanent GPS strategy. In J. S. Oldow & P. H. Cashman, *Late Cenozoic Structure and Evolution of the Great Basin-Sierra Nevada Transition*. Geological Society of America. https://doi.org/10.1130/2009.2447(01)

Blewitt, G., Kreemer, C., Hammond, W. C., & Gazeaux, J. (2016). MIDAS robust trend estimator for accurate GPS station velocities without step detection. *Journal of Geophysical Research: Solid Earth*, *121*(3), 2054–2068. https://doi.org/10.1002/2015JB012552

Blewitt, G., Hammond, W., & Kreemer, C. (2018). Harnessing the GPS Data Explosion for Interdisciplinary Science. *Eos*, *99*. https://doi.org/10.1029/2018EO104623

Bogusz, J., Gruszczynski, M., Figurski, M., & Klos, A. (2015). Spatio-temporal filtering for determination of common mode error in regional GNSS networks. *Open Geosciences*, *7*(1). https://doi.org/10.1515/geo-2015-0021

Broermann, J., Bennett, R. A., Kreemer, C., Blewitt, G., & Pearthree, P. A. (2021). Geodetic Extension Across the Southern Basin and Range and Colorado Plateau. *Journal of Geophysical Research: Solid Earth*, *126*(6), e2020JB021355. https://doi.org/10.1029/2020JB021355

van Dam, T., Wahr, J., Milly, P. C. D., Shmakin, A. B., Blewitt, G., Lavallée, D., & Larson, K. M. (2001). Crustal displacements due to continental water loading. *Geophysical Research Letters*, *28*(4), 651–654. https://doi.org/10.1029/2000GL012120

van Dam, T., Wahr, J., & Lavallée, D. (2007). A comparison of annual vertical crustal displacements from GPS and Gravity Recovery and Climate Experiment (GRACE) over Europe. *Journal of Geophysical Research*, *112*(B3), B03404. https://doi.org/10.1029/2006JB004335

dePolo, C. (1998). *A reconnaissance technique for estimating the slip rate of normal-slip faults in the Great Basin, and application to faults in Nevada, U.S.A* (unpublished Ph.D. dissertation).

dePolo, C., & Pecoraro, B. (2011). Modified Mercalli Intensity Maps for the February 21, 2008 Wells, Nevada Earthquake. Nevada Bureau of Mines and Geology Special Publication 36.

dePolo, C., & Ramelli, A. R. (1998). Quaternary and suspected Quaternary faults in Nevada south of 37° N. Latitude. Nevada Bureau of Mines and Geology Open-File Report 98-6.

dePolo, D. M., & dePolo, C. M. (2012). Earthquakes in Nevada—1840s to 2010. Nevada Bureau of Mines and Geology.

Dickinson, H., Freed, A. M., & Andronicos, C. (2016). Inference of the viscosity structure and mantle conditions beneath the Central Nevada Seismic Belt from combined postseismic and lake unloading studies. *Geochemistry, Geophysics, Geosystems*, *17*(5), 1740–1757. https://doi.org/10.1002/2015GC006207

Dixon, T., & Xie, S. (2018). A kinematic model for the evolution of the Eastern California Shear Zone and Garlock Fault, Mojave Desert, California | Elsevier Enhanced Reader. https://doi.org/10.1016/j.epsl.2018.04.050

Dziewonski, A. M., & Anderson, D. L. (1981). Preliminary reference Earth model. *Physics of the Earth and Planetary Interiors*, *25*(4), 297–356. https://doi.org/10.1016/0031-9201(81)90046-7

Emolo, A., & Zollo, A. (2005). Kinematic Source Parameters for the 1989 Loma Prieta Earthquake from the Nonlinear Inversion of Accelerograms. *Bulletin of the Seismological Society of America*, *95*(3), 981–994. https://doi.org/10.1785/0120030193

Flesch, L. M., Holt, W. E., Haines, A. J., Wen, L., & Shen-Tu, B. (2007). The dynamics of western North America: stress magnitudes and the relative role of gravitational potential energy, plate interaction at the boundary and basal tractions. *Geophysical Journal International*, *169*(3), 866–896. https://doi.org/10.1111/j.1365-246X.2007.03274.x

Frankel, K., Glazner, A., Kirby, E., Monastero, F., Strane, M., Oskin, M., et al. (2008). Active tectonics of the eastern California shear zone (Vol. 11, pp. 43–81). https://doi.org/10.1130/2008.fld011(03)

Freed, A. M., Ali, S. T., & Bürgmann, R. (2007). Evolution of stress in Southern California for the past 200 years from coseismic, postseismic and interseismic stress changes. *Geophysical Journal International*, *169*(3), 1164–1179. https://doi.org/10.1111/j.1365-246X.2007.03391.x

Freund, L. B., & Barnett, D. M. (1976). A two-dimensional analysis of surface deformation due to dip-slip faulting. *Bulletin of the Seismological Society of America*, *66*(3), 667–675. https://doi.org/10.1785/BSSA0660030667

Fu, Y., Argus, D. F., Freymueller, J. T., & Heflin, M. B. (2013). Horizontal motion in elastic response to seasonal loading of rain water in the Amazon Basin and monsoon water in Southeast Asia observed by GPS and inferred from GRACE: HORIZONTAL SEASONAL MOTIONS BY GPS/GRACE. *Geophysical Research Letters*, *40*(23), 6048–6053. https://doi.org/10.1002/2013GL058093

Gallovič, F. (2015). Modeling Velocity Recordings of the Mw 6.0 South Napa, California, Earthquake: Unilateral Event with Weak High-Frequency Directivity. *Seismological Research Letters*, *87*(1), 2–14. https://doi.org/10.1785/0220150042

Guns, K. A., & Bennett, R. A. (2020). Assessing Long-Term Postseismic Transients From GPS Time Series in Southern California. *Journal of Geophysical Research: Solid Earth*, *125*(4), e2019JB018670. https://doi.org/10.1029/2019JB018670

Haddon, E. K., Amos, C. B., Zielke, O., Jayko, A. S., & Bürgmann, R. (2016). Surface slip during large Owens Valley earthquakes. *Geochemistry, Geophysics, Geosystems*, *17*(6), 2239–2269. https://doi.org/10.1002/2015GC006033

Hammond, W., Kreemer, C., & Blewitt, G. (2009). Geodetic constraints on contemporary deformation in the northern Walker Lane: 3. Central Nevada Seismic Belt postseismic relaxation. *Geol. Soc. Am. Spec. Pap.*, *447*, 33–542447. https://doi.org/10.1130/2009.2447(03)

Hammond, W. C., Kreemer, C., Zaliapin, I., & Blewitt, G. (2019). Drought-Triggered Magmatic Inflation, Crustal Strain, and Seismicity Near the Long Valley Caldera, Central Walker Lane. *Journal of Geophysical Research: Solid Earth*, *124*(6), 6072–6091. https://doi.org/10.1029/2019JB017354

Hammond, William C., & Thatcher, W. (2004). Contemporary tectonic deformation of the Basin and Range province, western United States: 10 years of observation with the Global Positioning System. *Journal of Geophysical Research: Solid Earth*, *109*(B8). https://doi.org/10.1029/2003JB002746

Hammond, William C., Blewitt, G., & Kreemer, C. (2011). Block modeling of crustal deformation of the northern Walker Lane and Basin and Range from GPS velocities. *Journal of Geophysical Research: Solid Earth*, *116*(B4). https://doi.org/10.1029/2010JB007817

Hammond, William C., Blewitt, G., & Kreemer, C. (2014). Steady contemporary deformation of the central Basin and Range Province, western United States. *Journal of Geophysical Research: Solid Earth*, *119*(6), 5235–5253. https://doi.org/10.1002/2014JB011145

Hayes, G. (2009). Preliminary Result of the August 3, 2009 Mw 6.9 Gulf of California Earthquake. NEIC. Retrieved from http://earthquake.usgs.gov/earthquakes/eqinthenews/2009/us2009jwbh/finite_fault.php

He, X., Montillet, J.-P., Fernandes, R., Bos, M., Yu, K., Hua, X., & Jiang, W. (2017). Review of current GPS methodologies for producing accurate time series and their error sources. *Journal of Geodynamics*, *106*, 12–29. https://doi.org/10.1016/j.jog.2017.01.004

Hearn, E. H. (2003). What can GPS data tell us about the dynamics of postseismic deformation, 25.

Hernandez, B., Cotton, F., & Campillo, M. (1999). Contribution of radar interferometry to a two-step inversion of the kinematic process of the 1992 Landers earthquake. *Journal of Geophysical Research: Solid Earth*, *104*(B6), 13083–13099. https://doi.org/10.1029/1999JB900078

Hodgkinson, K., Stein, R., & King, G. (1996). The 1954 Rainbow Mountain-Fairview Peak-Dixie Valley earthquakes: A triggered normal faulting sequence. *Journal of Geophysical Research*, *1012,* 25459–25472. https://doi.org/10.1029/96JB01302

Holt, W. E., & Haines, A. J. (1993). Velocity fields in deforming Asia from the inversion of earthquake-released strains. *Tectonics*, *12*(1), 1–20. https://doi.org/10.1029/92TC00658

Holt, William E., Shen-Tu, B., Haines, J., & Jackson, J. (2000). On the Determination of Self-Consistent Strain Rate Fields Within Zones of Distributed Continental Deformation. In *The History and Dynamics of Global Plate Motions* (pp. 113–141). American Geophysical Union (AGU). https://doi.org/10.1029/GM121p0113

Huber, P. (1981). *Robust statistics*. Wiley, New York.

Ji, C. (2004). Slip history the 2004 (Mw 5.9) Parkfield Earthquake (Single-Plane Model). Source Models of Large Earthquakes. Retrieved from http://www.tectonics.caltech.edu/slip_history/2004_ca/parkfield2.html

Jin, Z., & Fialko, Y. (2020). Finite Slip Models of the 2019 Ridgecrest Earthquake Sequence Constrained by Space Geodetic Data and Aftershock Locations. *Bulletin of the Seismological Society of America*, *110*(4), 1660–1679. https://doi.org/10.1785/0120200060

Johanson, I. A., & Bürgmann, R. (2010). Coseismic and postseismic slip from the 2003 San Simeon earthquake and their effects on backthrust slip and the 2004 Parkfield earthquake. *Journal of Geophysical Research: Solid Earth*, *115*(B7). https://doi.org/10.1029/2009JB006599

Kreemer, C., & Blewitt, G. (2021). Robust estimation of spatially varying common-mode components in GPS time-series. *Journal of Geodesy*, *95*(1), 13. https://doi.org/10.1007/s00190-020-01466-5

Kreemer, C., & Zaliapin, I. (2018). Spatiotemporal Correlation Between Seasonal Variations in Seismicity and Horizontal Dilatational Strain in California. *Geophysical Research Letters*, *45*(18), 9559–9568. https://doi.org/10.1029/2018GL079536

Kreemer, C., Blewitt, G., & Hammond, W. C. (2010). Evidence for an active shear zone in southern Nevada linking the Wasatch fault to the Eastern California shear zone. *Geology*, *38*(5), 475–478. https://doi.org/10.1130/G30477.1

Kreemer, C., Blewitt, G., & Klein, E. C. (2014). A geodetic plate motion and Global Strain Rate Model. *Geochemistry, Geophysics, Geosystems*, *15*(10), 3849–3889. https://doi.org/10.1002/2014GC005407

Kreemer, C., Hammond, W. C., & Blewitt, G. (2018). A Robust Estimation of the 3-D Intraplate Deformation of the North American Plate From GPS. *Journal of Geophysical Research: Solid Earth*, *123*(5), 4388–4412. https://doi.org/10.1029/2017JB015257

Márquez-Azúa, B., & DeMets, C. (2003). Crustal velocity field of Mexico from continuous GPS measurements, 1993 to June 2001: Implications for the neotectonics of Mexico. *Journal of Geophysical Research: Solid Earth*, *108*(B9). https://doi.org/10.1029/2002JB002241

Martens, H. R., Rivera, L., & Simons, M. (2019). LoadDef: A Python-Based Toolkit to Model Elastic Deformation Caused by Surface Mass Loading on Spherically Symmetric Bodies. *Earth and Space Science*, *6*(2), 311–323. https://doi.org/10.1029/2018EA000462

Mccaffrey, R. (2002). Crustal Block Rotations and Plate Coupling. In *Plate Boundary Zones* (pp. 101–122). American Geophysical Union (AGU). https://doi.org/10.1029/GD030p0101

Meade, B. J., & Hager, B. H. (2005). Block models of crustal motion in southern California constrained by GPS measurements. *Journal of Geophysical Research: Solid Earth*, *110*(B3). https://doi.org/10.1029/2004JB003209

Mendoza, C., & Hartzell, S. H. (1988). Inversion for slip distribution using teleseismic P waveforms: North Palm Springs, Borah Peak, and Michoacan earthquakes. *Bulletin of the Seismological Society of America*, *78*(3), 1092–1111. https://doi.org/10.1785/BSSA0780031092

Pollitz, F. F., McCrory, P., Svarc, J., & Murray, J. (2008). Dislocation models of interseismic deformation in the western United States. *Journal of Geophysical Research: Solid Earth*, *113*(B4), B04413-n/a. https://doi.org/10.1029/2007JB005174

Rollins, J. C., & Stein, R. S. (2010). Coulomb stress interactions among $M \geq 5.9$ earthquakes in the Gorda deformation zone and on the Mendocino Fault Zone, Cascadia subduction zone, and northern San Andreas Fault. *Journal of Geophysical Research*, *115*(B12), B12306. https://doi.org/10.1029/2009JB007117

Salichon, J., Lundgren, P., Delouis, B., & Giardini, D. (2004). Slip History of the 16 October 1999 Mw 7.1 Hector Mine Earthquake (California) from the Inversion of InSAR, GPS, and Teleseismic Data. *Bulletin of the Seismological Society of America*, *94*(6), 2015–2027. https://doi.org/10.1785/0120030038

Santamaría-Gómez, A., & Mémin, A. (2015). Geodetic secular velocity errors due to interannual surface loading deformation. *Geophysical Journal International*, *202*(2), 763–767. https://doi.org/10.1093/gji/ggv190

Serpelloni, E., Faccenna, C., Spada, G., Dong, D., & Williams, S. D. P. (2013). Vertical GPS ground motion rates in the Euro-Mediterranean region: New evidence of velocity gradients at different spatial scales along the Nubia-Eurasia plate boundary. *Journal of Geophysical Research: Solid Earth*, *118*(11), 6003–6024. https://doi.org/10.1002/2013JB010102

Shao, G., & Ji, C. (2005). Preliminary Result of the Jun 15, 2005 Mw 7.2 northernca Earthquake. UCSB. Retrieved from http://www.geol.ucsb.edu/faculty/ji/big_earthquakes/2005/06/smooth/northernca.html

Slemmons, D. (1998). Seismotectonic setting for the Las Vegas basin, Nevada. Nevada Bureau of Mines and Geology Open-File Report 98-6.

Smith, B. R., & Sandwell, D. T. (2006). A model of the earthquake cycle along the San Andreas Fault System for the past 1000 years. *Journal of Geophysical Research: Solid Earth*, *111*(B1). https://doi.org/10.1029/2005JB003703

Song, S. G., Beroza, G. C., & Segall, P. (2008). A Unified Source Model for the 1906 San Francisco Earthquake. *Bulletin of the Seismological Society of America*, *98*(2), 823–831. https://doi.org/10.1785/0120060402

Springer, A., Karegar, M., Kusche, J., Keune, J., Kurtz, W., & Kollet, S. (2019). Evidence of daily hydrological loading in GPS time series over Europe. *Journal of Geodesy*, *93*. https://doi.org/10.1007/s00190-019-01295-1

Tian, Y., & Shen, Z.-K. (2016). Extracting the regional common-mode component of GPS station position time series from dense continuous network. *Journal of Geophysical Research: Solid Earth*, *121*(2), 1080–1096. https://doi.org/10.1002/2015JB012253

U.S. Geological Survey, California Geological Survey, Arizona Geological Survey, Nevada Bureau of Mines and Geology, & Utah Geological Survey. (2022). Quaternary fault and fold database for the United States. Retrieved from https://www.usgs.gov/programs/earthquake-hazards/faults

USGS. (2015). M 6.8 - 7 km SSE of Longbranch, Washington Moment Tensor. Retrieved from https://earthquake.usgs.gov/earthquakes/eventpage/uw10530748/moment-tensor

USGS. (2017). M 6.8 - 77 km WNW of Indianola, California Moment Tensor. Retrieved from https://earthquake.usgs.gov/earthquakes/eventpage/nc72182046/moment-tensor

USGS. (2020). M 6.5 - Stanley, Idaho Finite Fault. Retrieved from https://earthquake.usgs.gov/earthquakes/eventpage/us70008jr5/finite-fault

vanDam, T. M., Blewitt, G., & Heflin, M. B. (1994). Atmospheric pressure loading effects on Global Positioning System coordinate determinations. *Journal of Geophysical Research: Solid Earth*, *99*(B12), 23939–23950. https://doi.org/10.1029/94JB02122

Wang, Q., Jackson, D. D., & Kagan, Y. Y. (2009). California Earthquakes, 1800-2007: A Unified Catalog with Moment Magnitudes, Uncertainties, and Focal Mechanisms. *Seismological Research Letters*, *80*(3), 446–457. https://doi.org/10.1785/gssrl.80.3.446

Wang, R., Lorenzo-Martín, F., & Roth, F. (2006). PSGRN/PSCMP—a new code for calculating co- and post-seismic deformation, geoid and gravity changes based on the viscoelastic-gravitational dislocation theory. *Computers & Geosciences*, *32*(4), 527–541. https://doi.org/10.1016/j.cageo.2005.08.006

Wdowinski, S., Bock, Y., Zhang, J., Fang, P., & Genrich, J. (1997). Southern California permanent GPS geodetic array: Spatial filtering of daily positions for estimating coseismic and postseismic displacements induced by the 1992 Landers earthquake. *Journal of Geophysical Research: Solid Earth*, *102*(B8), 18057–18070. https://doi.org/10.1029/97JB01378

Wei, S. (2012). Oct./28/2012 (Mw 7.8), Masset, Canada. Source Models of Large Earthquakes. Retrieved from http://www.tectonics.caltech.edu/slip_history/2012_Masset/index.html

Wei, Shengji, Fielding, E., Leprince, S., Sladen, A., Avouac, J.-P., Helmberger, D., et al. (2011). Superficial simplicity of the 2010 El Mayor-Cucapah earthquake of Baja California in Mexico. *Nature Geoscience*, *4*, 615–618. https://doi.org/10.1038/ngeo1213

Wessel, P., Luis, J. F., Uieda, L., Scharroo, R., Wobbe, F., Smith, W. H. F., & Tian, D. (2019). The Generic Mapping Tools Version 6. *Geochemistry, Geophysics, Geosystems*, *20*(11), 5556–5564. https://doi.org/10.1029/2019GC008515

Young, Z. M., Kreemer, C., & Blewitt, G. (2021). GPS Constraints on Drought-Induced Groundwater Loss Around Great Salt Lake, Utah, With Implications for Seismicity Modulation. *Journal of Geophysical Research: Solid Earth*, *126*(10), e2021JB022020. https://doi.org/10.1029/2021JB022020

Zeng, Y., & Anderson, J. (2000). Evaluation of Numerical Procedures for Simulating Near-Fault Long-Period Ground Motions Using Zeng Method. *Report 2000/01 to the PEER Utilities Program*.

Zheng, A., Chen, X., & Xu, W. (2020). Present-Day Deformation Mechanism of the Northeastern Mina Deflection Revealed by the 2020 Mw 6.5 Monte Cristo Range Earthquake. *Geophysical Research Letters*, *47*(22), e2020GL090142. https://doi.org/10.1029/2020GL090142

3.13 Supplemental Material

3.13.1 Description

The material provided in this file provides additional information to supplement the article listed above and includes Tables S3.1 – S3.2 and Figures S3.1 – S3.12.

3.13.2 Supplemental Tables

Table S3.1: *Fault model parameters used to calculate postseismic deformation at GPS stations. For earthquake type, N = normal, T= thrust, RL = right lateral, and LL = left lateral.*
** Longitude and latitude values are approximate midpoints of individual fault sections.*
† Fault models with high slip resolution. Authors for individual models are listed in Table 3.1.

Event	Section	Longitude*	Latitude*	Length	Strike	Dip	Width	Rake	Type
Borah Peak	†	−113.8600	44.0600	52.0	152	49	26.6	−80	N
Cascadia	1	−125.5624	40.7657	126	358	9	63.9	110	T+RL
	2	−124.9946	40.7855	126	358	9	63.9	110	T+RL
	3	−125.6648	41.9021	126	358	9	63.9	110	T+RL
	4	−125.0970	41.9219	126	358	9	63.9	110	T+RL
	5	−125.7202	43.0018	126	359	9	63.9	110	T+RL
	6	−125.1524	43.0117	126	359	9	63.9	110	T+RL
	7	−125.8166	44.1484	133	359	9	63.9	110	T+RL
	8	−125.2488	44.1583	133	358	10	57.6	110	T+RL
	9	−125.8960	45.3381	137	358	9	63.9	110	T+RL
	10	−125.3282	45.3579	137	358	10	57.6	110	T+RL
	11	−125.9800	46.4954	105	358	9	63.9	110	T+RL
	12	−125.4122	46.5152	115	358	10	57.6	110	T+RL
	13	−126.2030	47.3882	100	337	8	71.9	90	T

	14	−125.5631	47.6382	125	337	10	57.6	90	T
	15	−127.1808	48.7089	255	322	12	48.1	90	T
	16	−126.7577	48.9694	255	322	13	44.5	90	T
Cedar Mountain	1	−117.9100	38.6310	65	344	80	15.2	180	RL
Central Idaho	†	−115.1361	44.4484	62.5	172	74	32	−24	LL+N
Dixie Valley	1	−118.1000	39.8000	24.3	8	49	9	~	N+RL
El Mayor–Cucapah	†	−115.2670	32.3000	168	345	45	21	−156	RL+N
Fairview Peak Complex	1	−118.1170	39.2830	24.16	4	69	17	−61	N+RL
	2	−118.0700	39.3230	13.2	356	64	17	~	N+RL
	3	−118.0900	39.4400	16	0	81	17	~	N+RL
Fort Tejon	1	−119.3000	34.9050	130	315	90	15	180	RL
	2	−118.8150	34.7675	95	290	90	15	180	RL
Gulf of California 1	†	−112.8066	29.4094	108	137.8	74.87	20.8	172	RL
Gulf of California 2	1	−113.7280	29.3100	20	132	80	11	180	RL
Gulf of California 3	1	−113.0270	28.8370	15	311	90	11	178	RL
Gulf of California 4	1	−113.1040	28.6960	110	311	90	15	179	RL
Hebgen Lake	1	−111.2265	44.8238	24.1	114	50	15	−90	N
Hector Mine	†	−116.2700	34.5900	54	330	80	18	178.6	RL
Imperial Valley	1	−115.3820	32.7000	50	315	90	15	180	RL
Kern County	1	−118.8400	35.1320	29.7	51	75	21.7	~	LL+T

	2	−118.7380	35.1985	23.6	51	75	11.9	~	T+LL
Laguna Salada	1	−115.6400	32.4100	20	315	60	14	−139	RL+N
Landers	†	−116.4300	34.2000	80	330	90	15	180	RL
Loma Prieta	†	−121.8830	37.0410	35	130	70	14	140	RL+T
Mendocino Triple Junction 1	1	−124.6180	41.0850	100	51	89	10	27	LL+T
Mendocino Triple Junction 2	1	−125.3970	41.8210	30	46	86	15	28	LL+T
Mendocino Triple Junction 3	1	−124.1970	40.3010	21	350	12	16	94	T+RL
Mendocino Triple Junction 4	1	−125.6800	40.4000	15	274	65	7.5	176	RL+R
Mendocino Triple Junction 5	†	−125.9812	41.2932	102	47	85	35	2.1	LL
Mendocino Triple Junction 6	1	−125.1340	40.8290	20	228	79	15	−2	LL
Masset	†	−131.9270	52.7690	210	319	29	90	112.3	T+RL
Monte Cristo	1	−117.9688	38.1581	17.2	67	83	22	−24	LL+N
	2	−117.8369	38.1801	19.5	77	63	22	−24	LL+N
Napa	†	−122.3130	38.2200	15	155	82	10	−172	RL+N
Nisqually	1	−122.7270	47.1490	25	360	73	15	−91	N
Northridge	†	−118.5370	34.2130	18	122	40	24	97.6	T
Owens Valley	1	−118.1110	36.7255	111	341	80	15	~	RL+N

Parkfield	†	−120.3670	35.8236	40	137	83	14.5	−179	RL
Pleasant Valley	1	−117.6540	40.2580	59	210	45	21.2	−90	N
Ridgecrest 1	†	−117.5040	35.7050	~	225.5	88.85	~	−4	LL
Ridgecrest 2	†	−117.5990	35.7700	~	261.7	82.52	~	179.6	RL
San Francisco 1838	1	−122.0700	37.2700	140	318	90	15	180	RL
San Francisco 1906	†	−122.5100	37.7800	480	325	90	12	180	RL
San Simeon	1†	−121.2062	35.6588	~	295	44.5	~	120	RL+T
	2†	−120.8536	35.6310	~	116	31.7	~	120	RL+T
Sonoran	1	−109.2500	30.7500	108	175	68	18	−90	N
Stillwater	1	−118.5300	39.4200	24.9	25	87	13	~	RL+N
Wrightwood	1	−117.6500	34.3700	85	295	90	15	180	RL

Table S3.2: Individual postseismic model horizontal trends for GPS station UNR1, and model strain rates within the Las Vegas Valley. Station UNR1 is located within Las Vegas. Velocities are calculated with MIDAS and input into MELD to calculate strain rates. Table is sorted based on the magnitude of the second invariant strain rates. Three additional suites of model strain rates are provided. Composite indicates all models were included.

* High trend includes only those models whose trend at UNR1 is greater than 0.10 mm/yr in at least one component. Low trend includes the remainder of the events.

		UNR1 Postseismic Model Trends (mm/yr)		**Postseismic Model Strain Rates within the Las Vegas Valley (1x10^{-9} yr^{-1})**		
Event	**Date**	**V_e**	**V_N**	**2nd Invariant**	**Dilatation**	**Shear**
Fort Tejon*	1857JAN09	1.05	0.28	2.94	−1.81	0.97
Ridgecrest 2*	2019JUL06	0.19	0.01	1.59	−1.26	0.30
Owens Valley*	1872MAR26	0.35	−0.14	1.49	−1.00	0.43
Landers*	1992JUN28	−0.14	−0.37	1.28	1.26	0.07
Hector Mine*	1999OCT16	−0.13	−0.39	1.28	1.38	0.03
San Francisco 1906*	1906APR18	0.64	−0.15	1.21	−0.66	0.46
Wrightwood*	1812DEC08	0.22	0.09	1.03	−0.50	0.44
El Mayor–Cucapah*	2010APR04	0.01	−0.27	0.90	0.56	0.29
Cascadia*	1700JAN26	−0.48	−0.20	0.88	−0.48	0.34
Pleasant Valley	1915OCT03	0.08	−0.08	0.34	−0.06	0.21
Fairview Peak Complex*	1954DEC16	−0.08	0.11	0.33	0.20	0.10
San Francisco 1838*	1838JUN25	0.13	−0.01	0.25	−0.15	0.08
Cedar Mountain	1932OCT21	0.06	−0.04	0.21	−0.10	0.09

Ridgecrest 1	2019JUL04	0.02	0.00	0.19	−0.16	0.03
Kern County	1952JUL21	0.06	0.00	0.18	−0.12	0.05
Monte Cristo	2020MAY15	0.01	−0.01	0.14	−0.06	0.07
Mendocino Triple Junction 3	1992APR25	0.06	−0.02	0.14	−0.04	0.08
Dixie Valley	1954DEC16	0.02	−0.02	0.10	−0.02	0.06
Gulf of California 4	2012APR12	0.00	0.00	0.10	0.05	0.04
Mendocino Triple Junction 1	1980NOV08	0.05	−0.02	0.09	−0.02	0.05
Hebgen Lake	1959AUG18	−0.02	−0.05	0.09	−0.02	0.05
Northridge	1994JAN17	−0.01	−0.02	0.08	0.01	0.05
Loma Prieta	1989OCT18	0.03	0.00	0.07	−0.04	0.03
Gulf of California 1	2009AUG03	0.00	0.00	0.07	0.04	0.02
Imperial Valley	1940MAY18	0.00	−0.02	0.06	0.05	0.01
Mendocino Triple Junction 6	2014MAR10	−0.02	0.01	0.05	0.03	0.02
Mendocino Triple Junction 4	1994SEP01	0.02	0.00	0.05	0.00	0.03
Laguna Salada	1892FEB23	0.00	−0.02	0.05	0.03	0.01
Stillwater	1954AUG24	0.01	−0.01	0.04	−0.02	0.02
Mendocino Triple Junction 2	1991AUG17	0.01	0.00	0.03	−0.01	0.01
Borah Peak	1983OCT28	0.00	0.00	0.02	−0.01	0.00

Sonoran	1887MAY03	−0.01	0.00	0.02	0.01	0.01
Mendocino Triple Junction 5	2005JUN15	−0.01	0.00	0.02	0.00	0.01
San Simeon	2003DEC22	0.00	0.00	0.02	0.00	0.01
Gulf of California 2	2009AUG03	0.00	−0.02	0.02	0.00	0.01
Central Idaho	2020MAR31	0.00	0.00	0.01	−0.01	0.00
Masset	2012OCT28	0.00	0.00	0.01	0.00	0.00
Napa	2014AUG24	0.00	0.00	0.00	0.00	0.00
Nisqually	2001FEB28	0.00	0.00	0.00	0.00	0.00
Parkfield	2004SEP28	0.00	0.00	0.00	0.00	0.00
Gulf of California 3	2012APR12	0.01	−0.04	0.00	0.00	0.00
		Composite		4.36	−1.40	2.24
		High Trend Events		6.25	−2.60	2.91
		Low Trend Events		0.79	−0.51	0.24

3.13.3 Supplemental Figures

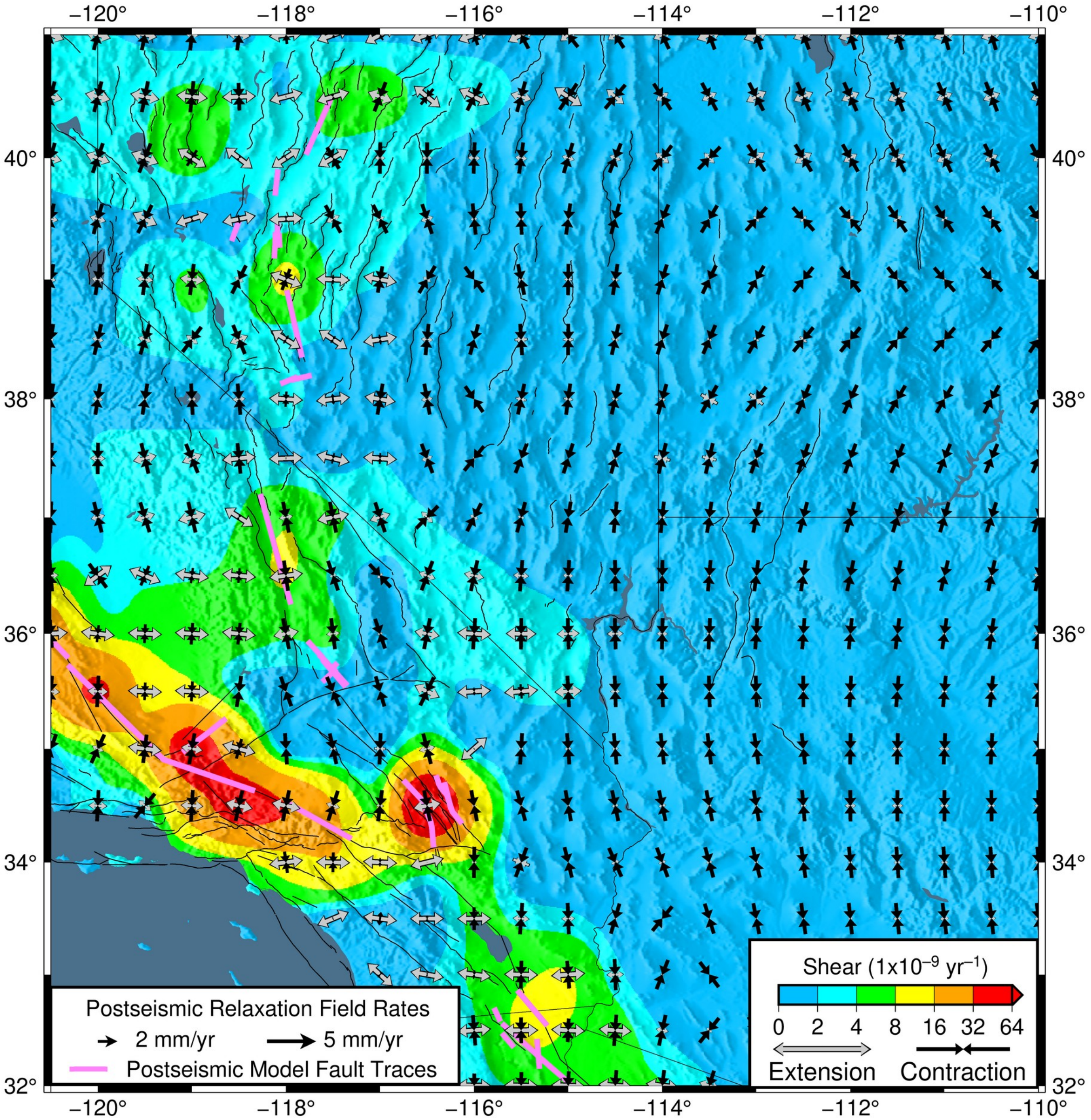

Figure S3.1: Shear strain rate associated with the postseismic relaxation field with normalized strain rate axis. Results are calculated with MELD using the velocities shown in Figure 3.2. Grey arrows indicate extension and black arrows indicate contraction. Pink lines represent the location of fault traces for the earthquake models.

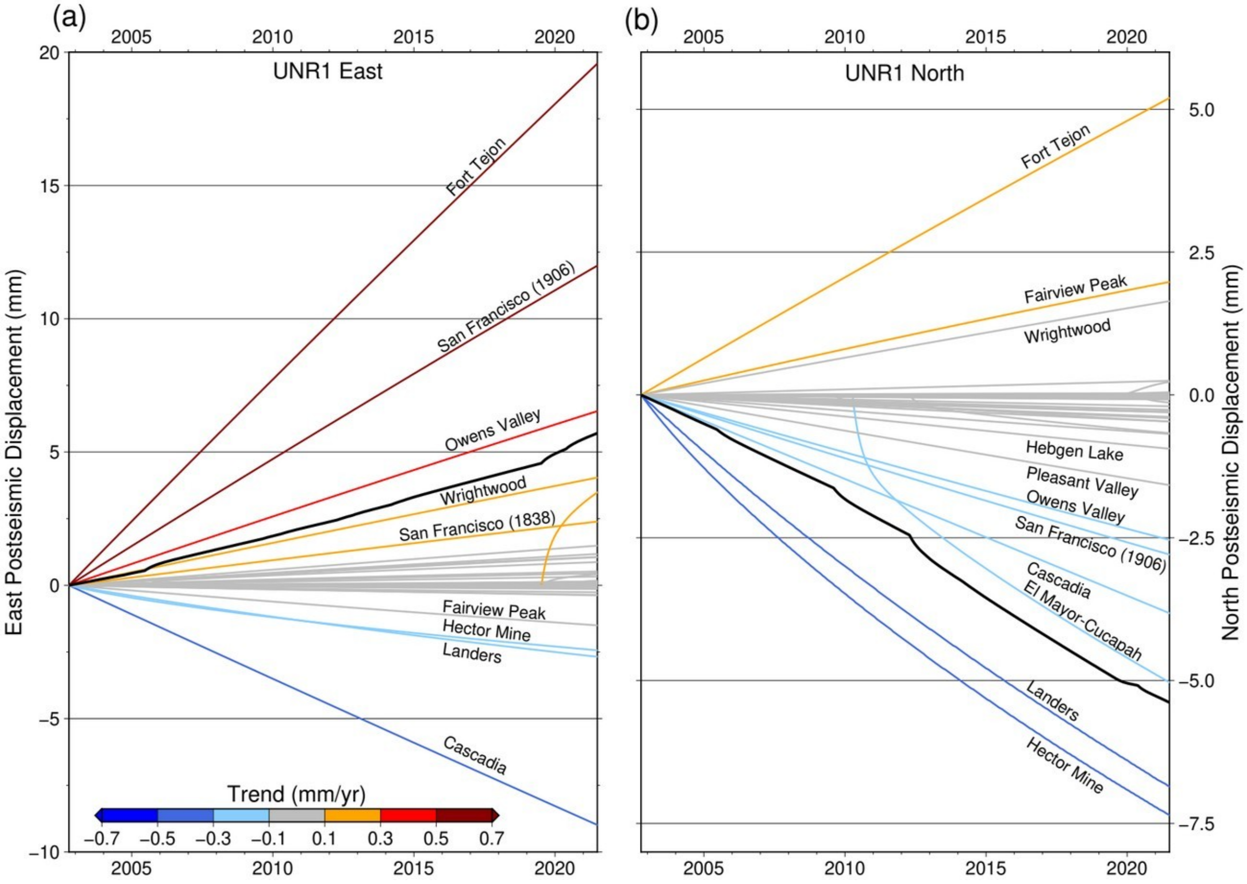

Figure S3.2: Individual postseismic displacement models for GPS station UNR1, located within Las Vegas for the east **(a)** and north **(b)** components. Labels identify individual events and line colors reflect trends across the duration of the station. Solid black lines reflect the cumulative displacements for models whose trends are less than ± 0.10 mm/yr (grey lines). Note the difference in scales between the east and north components.

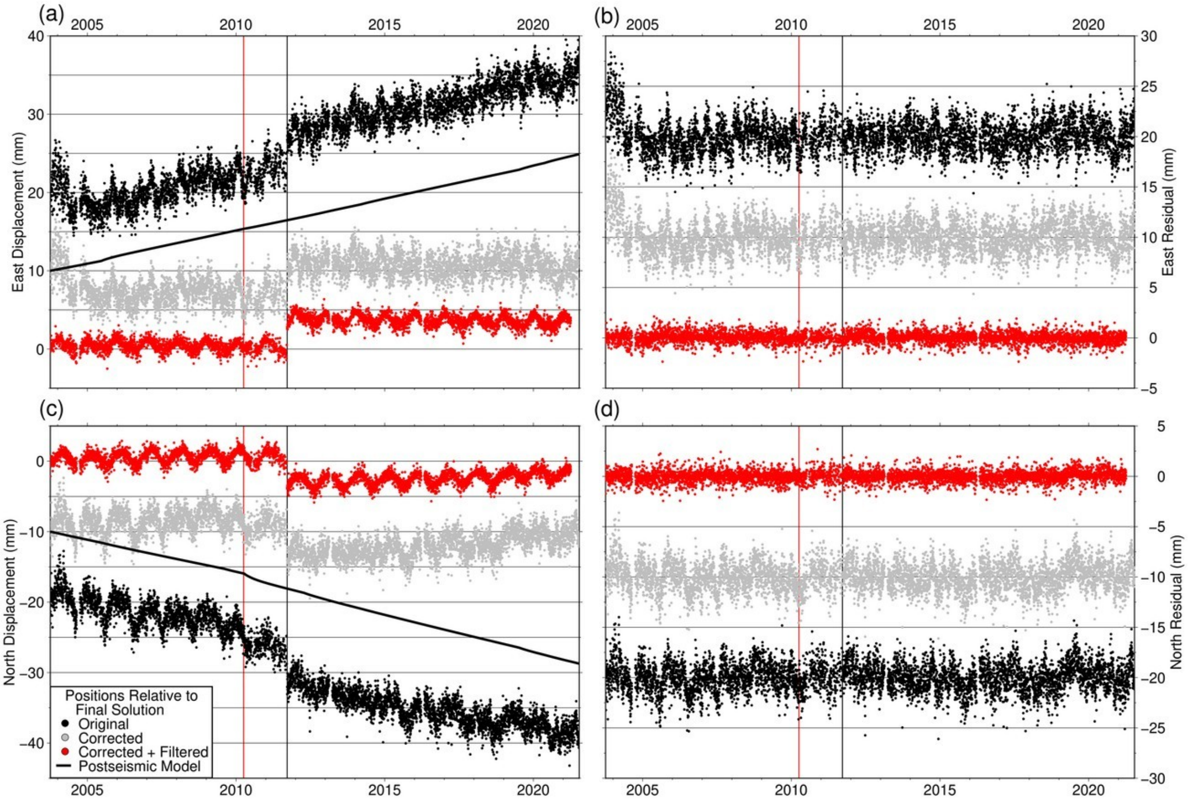

Figure S3.3: Time series comparison for station ECHO, located northeast of Las Vegas within the Pahranagat shear zone. **(a)** East component. Black dots represent original positions. Thick black line is the postseismic deformation model for this station. Grey dots are the position following correcting positions with the postseismic model. Red dots represent the positions after both postseismic correction and common mode filtering. Time series are detrended relative to the corrected and filtered solution. **(b)** East residuals. **(c)** North component. **(d)** North residuals. Vertical black line indicates the time of an equipment related step in the time series and the red vertical line represents the El Mayor–Cucahpah earthquake (2010).

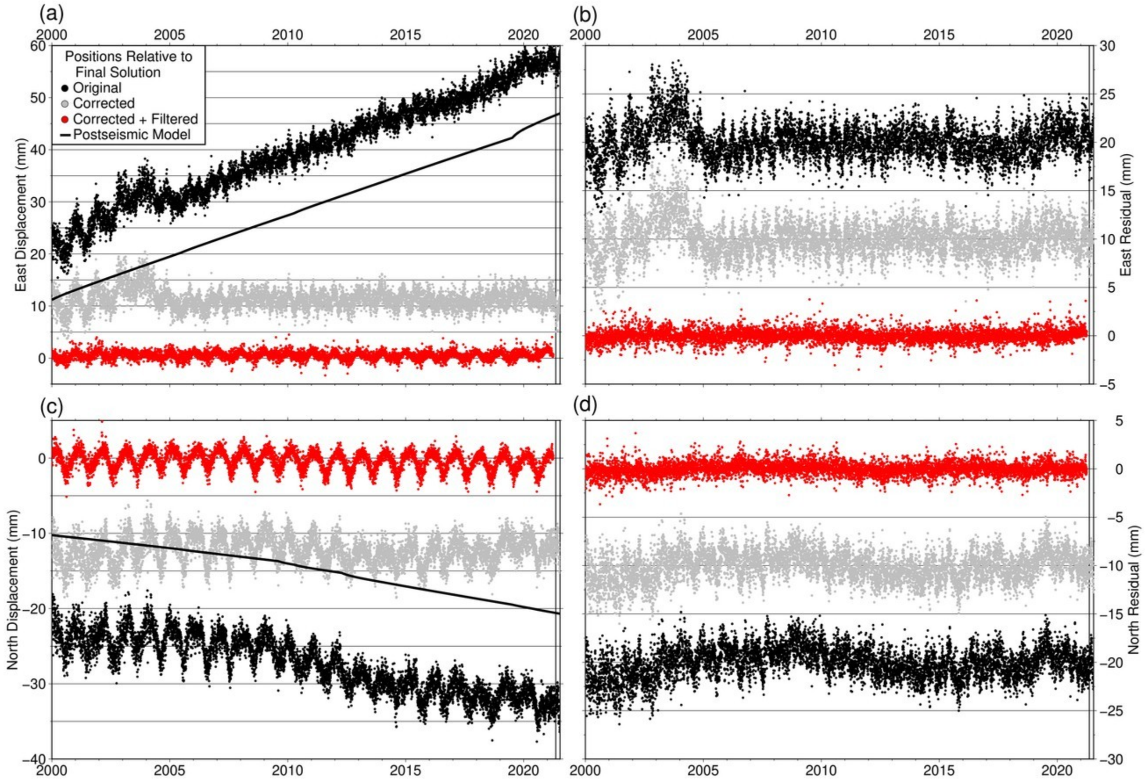

Figure S3.4: Time series comparison for station FERN, located southeast of Las Vegas. Key as described in Figure S3.3. Vertical black line indicates the time of an equipment related step in the time series.

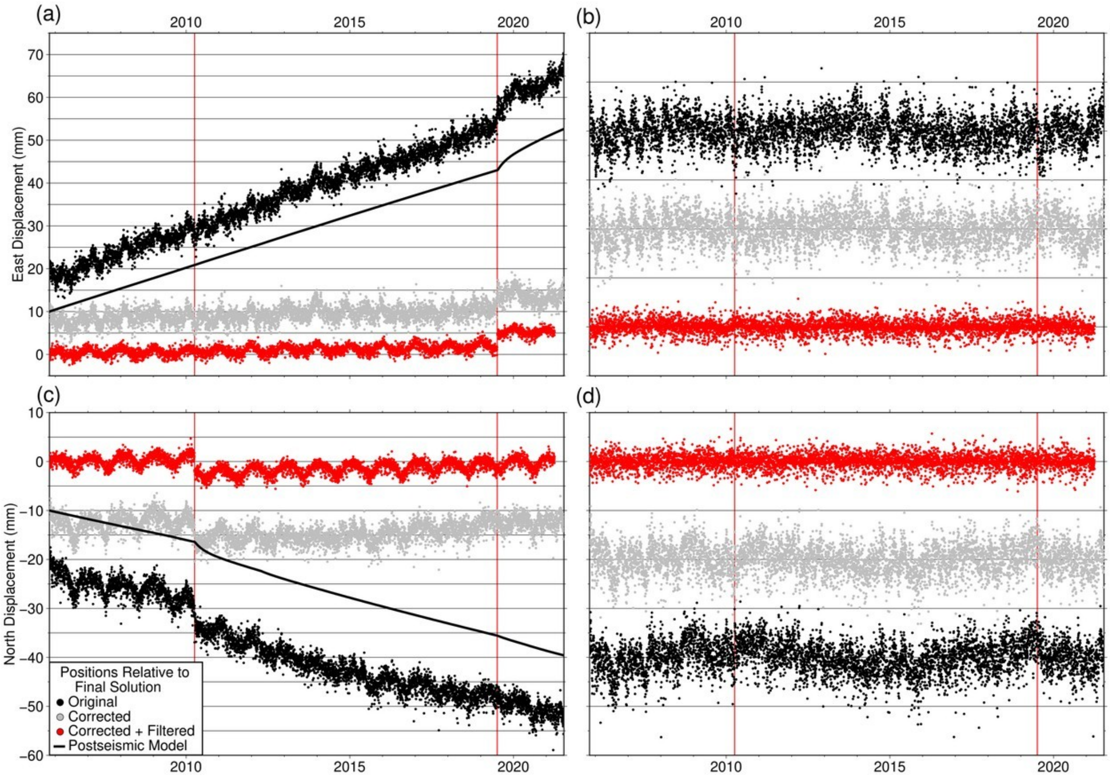

Figure S3.5: Time series comparison for station P626, located southwest of Las Vegas in the Mojave Desert. Key as described in Figure S3.3. Red vertical lines represent the times of the El Mayor–Cucahpah (2010) and Ridgecrest (2019) earthquakes.

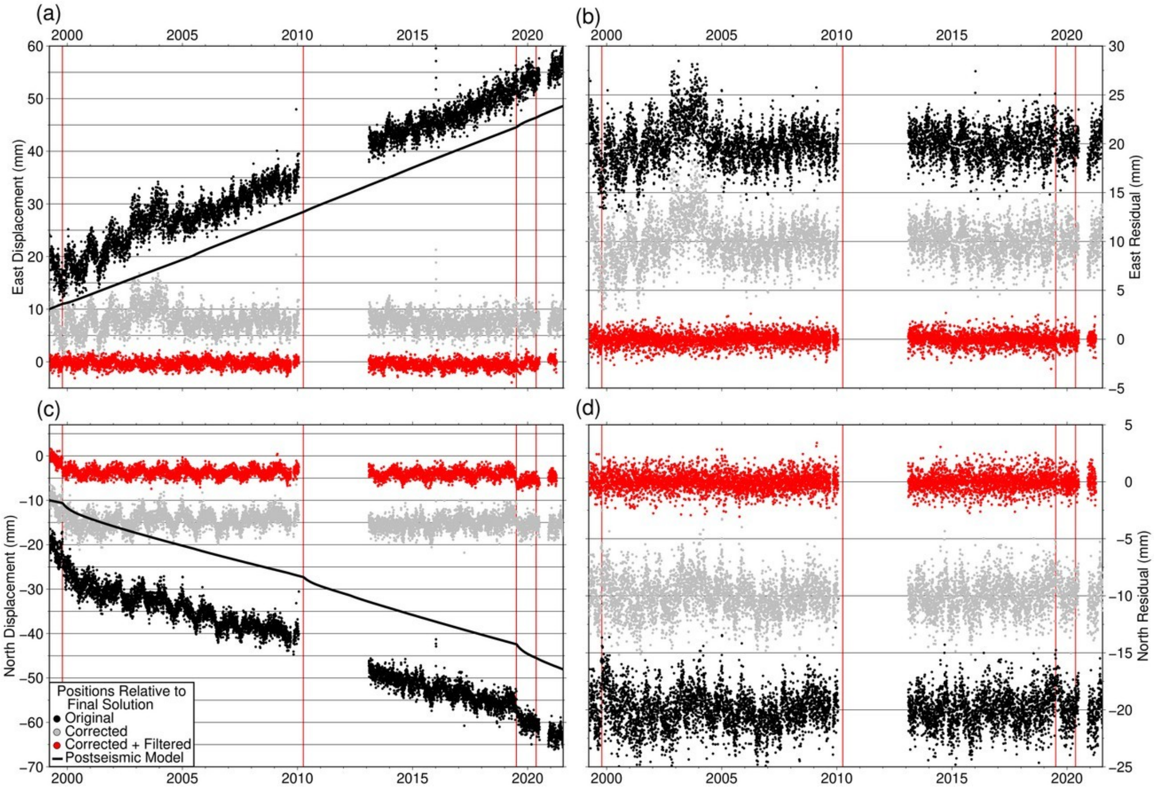

Figure S3.6: Time series comparison for station TIVA, located northwest of Las Vegas near Yucca Mountain. Key as described in Figure S3.3. Red vertical lines represent the times of the Hector Mine (1999), El Mayor–Cucahpah (2010), Ridgecrest (2019), and Monte Cristo (2020) earthquakes.

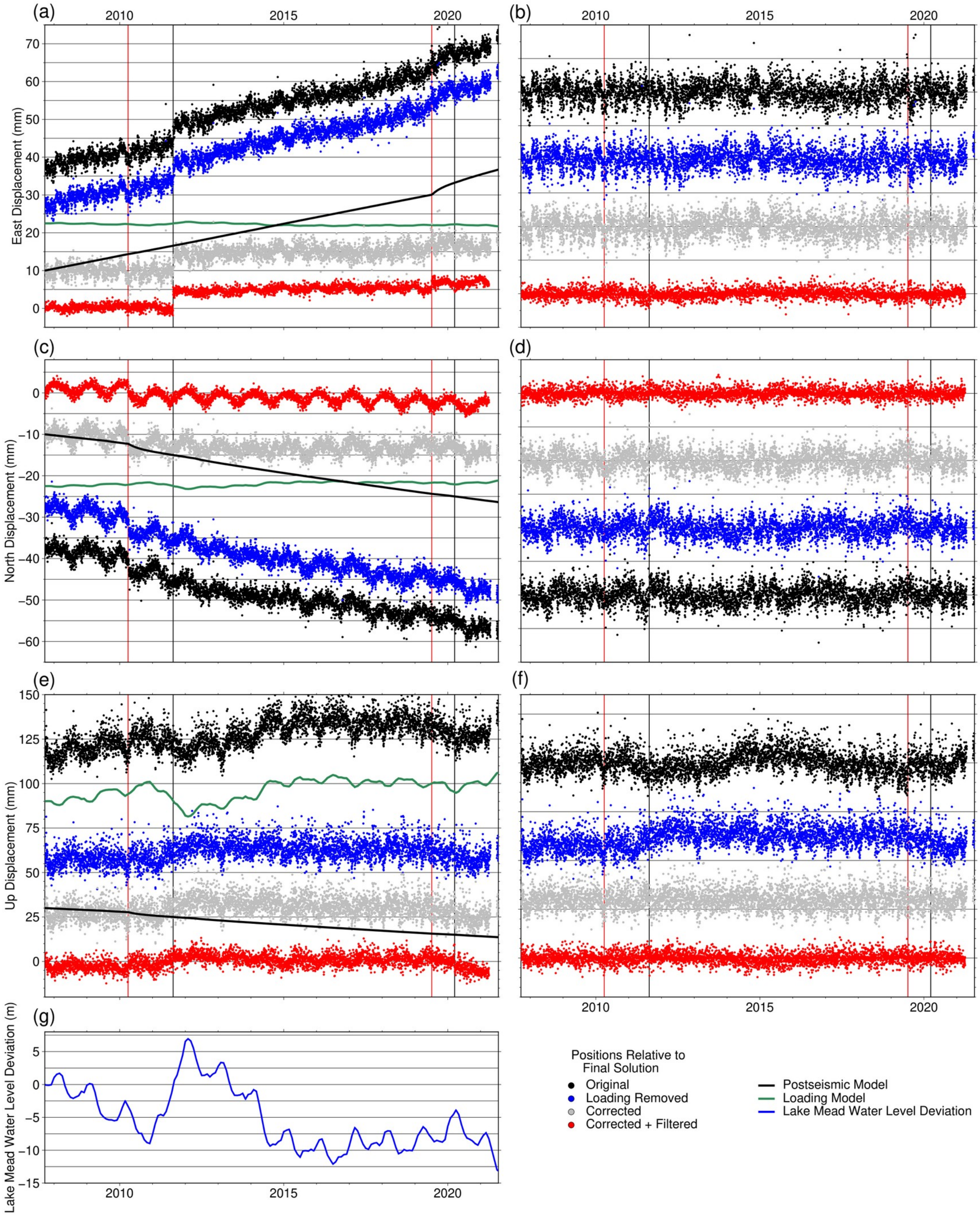
(a)
(b)
(c)
(d)
(e)
(f)
(g)
2010
2015
2020
East Displacement (mm)
East Residual (mm)
North Displacement (mm)
North Residual (mm)
Up Displacement (mm)
Up Residual (mm)
Lake Mead Water Level Deviation (m)
Positions Relative to Final Solution
● Original
● Loading Removed
● Corrected
● Corrected + Filtered
Postseismic Model
Loading Model
Lake Mead Water Level Deviation

Figure S3.7: Time series comparison and hydrologic loading model for station P006, located near Lake Mead. **(a)** East component. Black dots represent original positions. Blue dots show the original positions with the loading model removed. Green line shows the displacements at P006 due to load variation on Lake Mead. Thick black line is the postseismic deformation model for this station. Grey dots are the position following correcting positions with the postseismic model. Red dots represent the positions after corrections and common mode filtering. All time series are detrended relative to the corrected and filtered solution. **(b)** East residuals. **(c)** North component. **(d)** North residuals. **(e)** Up component. **(f)** Up residuals. **(g)** Observed water level deviation for Lake Mead during the time of station P006. Vertical black line indicates the time of an equipment related step in the time series and the red vertical lines represent the El Mayor–Cucahpah (2010) and Ridgecrest (2019) earthquakes.

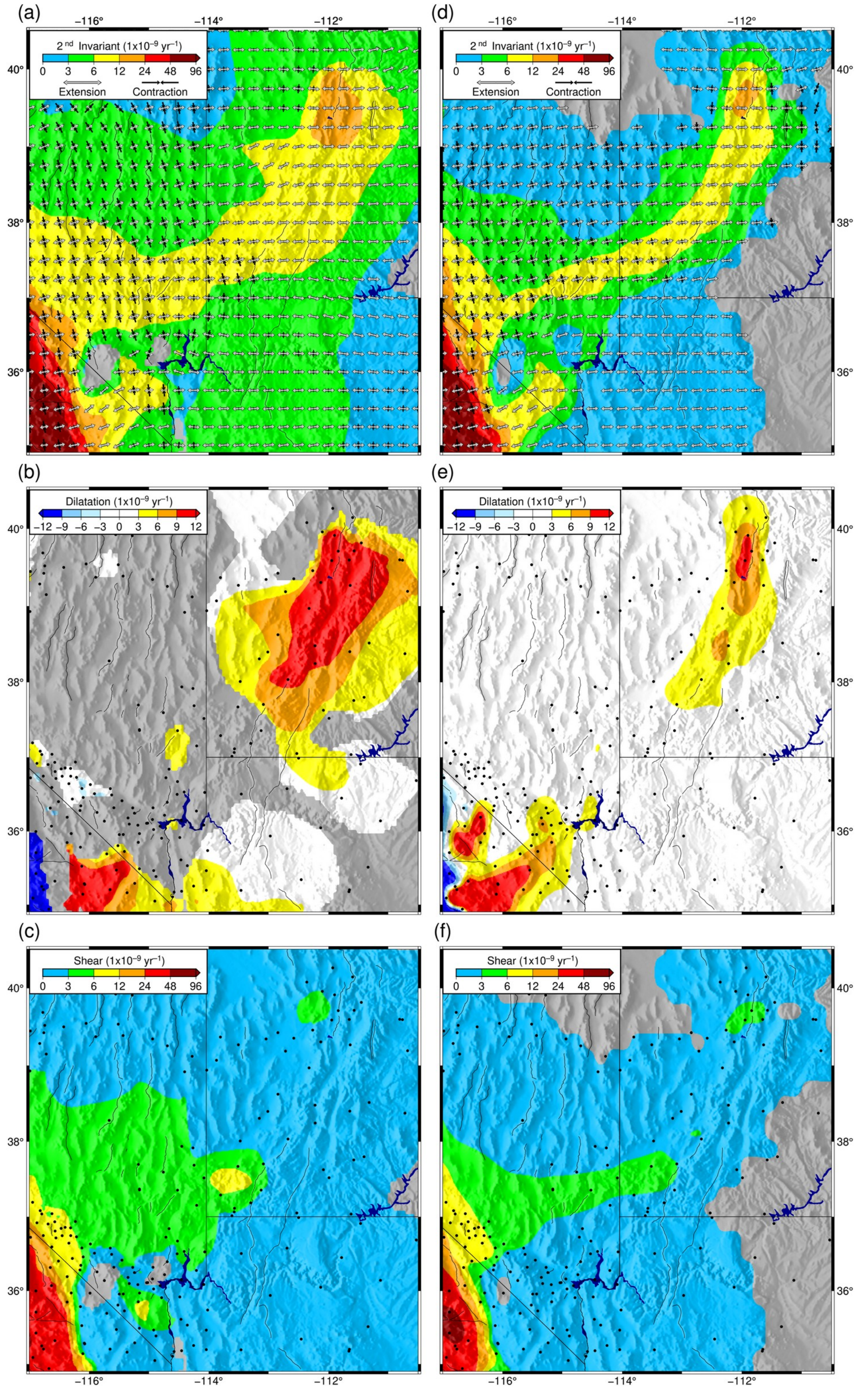
(a)
(d)
(b)
(e)
(c)
(f)
2 nd Invariant (1x10−9 yr−1)
0 3 6 12 24 48 96
Extension
Contraction
Dilatation (1x10−9 yr−1)
−12 −9 −6 −3 0 3 6 9 12
Shear (1x10−9 yr−1)
0 3 6 12 24 48 96
−116°
−114°
−112°
40°
38°
36°

Figure S3.8: Solutions for the MELD **(a – c)** and Haines and Holt **(d – f)** strain rate models for the original velocities. **(a and d)** Plots of second invariant strain rates overlain with normalized strain rate axis. Grey arrows indicate extension and black arrows indicate contraction. **(b and e)** Plots of the dilatational component of the strain rate. **(c and f)** Plot of the shear component of the strain rate. All plots are limited to strain rates greater than one sigma.

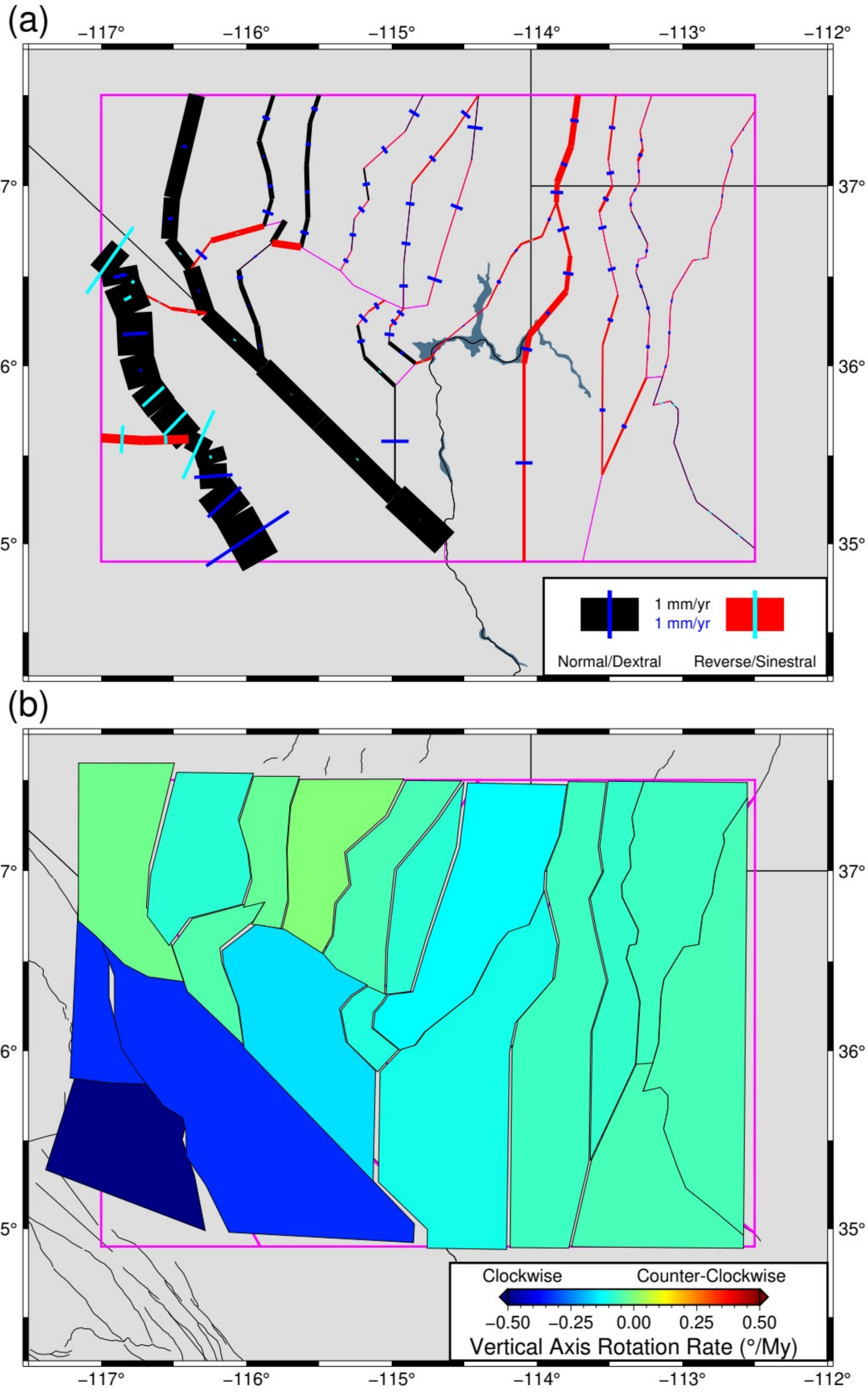
(a)
−117°
−116°
−115°
−114°
−113°
−112°
37°
36°
35°
1 mm/yr
1 mm/yr
Normal/Dextral
Reverse/Sinestral
(b)
37°
36°
35°
Clockwise
Counter-Clockwise
−0.50
−0.25
0.00
0.25
0.50
Vertical Axis Rotation Rate (°/My)
−117°
−116°
−115°
−114°
−113°
−112°

Figure S3.9: Plots of the block model using the original velocities and the same a priori uncertainties in the rotation rate and slip rates as the corrected and filtered velocity block model ($\beta = 3 \times 10^{-9}$ rad/yr, $\gamma = 0.2$ mm/yr). **(a)** Fault slip rates. The thickness of the black and red lines represents dextral and sinestral slip rates while the length of the blue and cyan lines represents normal and thrust slip rates. Pink lines represents the bounds of the block model and inactive (non fault) block edges. **(b)** Rigid block component of motion. Color scale indicates the vertical axis rotation rate with an exaggeration factor of 1 x10^7. Pink lines represent the initial block locations.

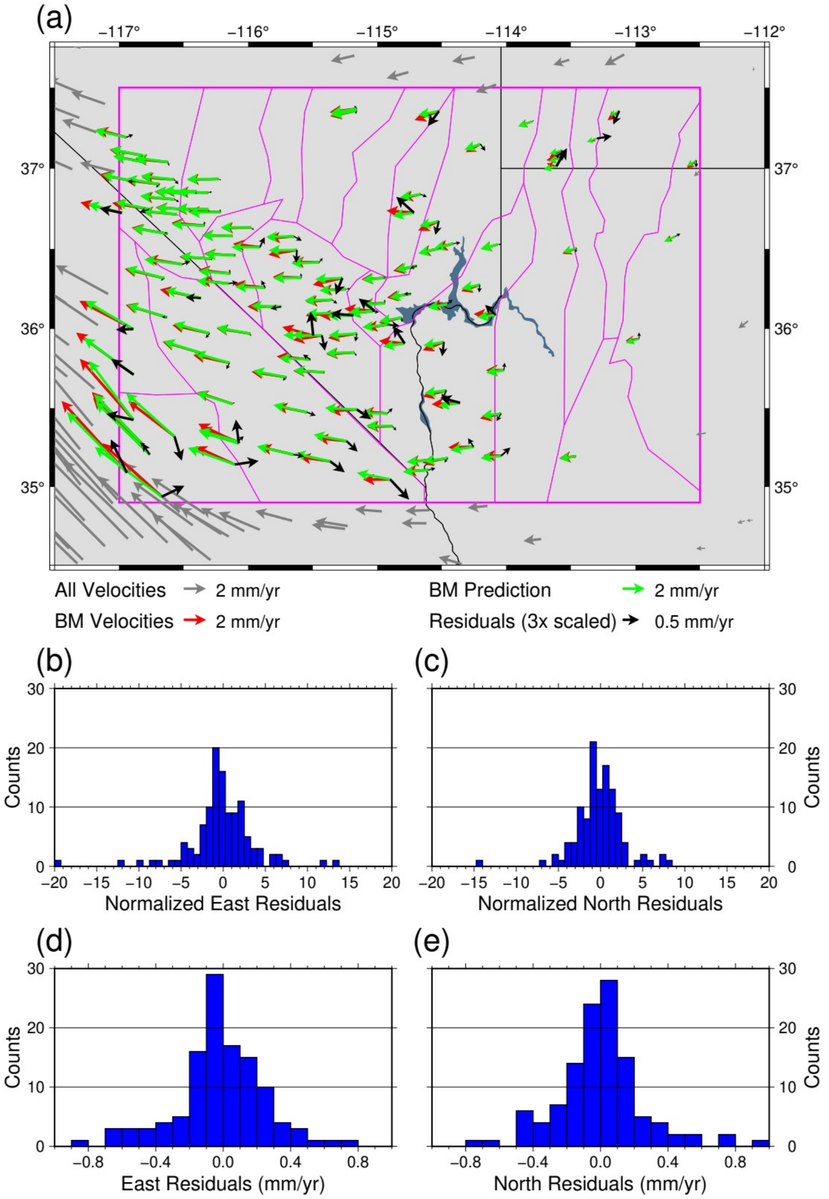

Figure S3.10: Block model fit to the GPS velocities for the corrected and filtered velocity model. **(a)** Velocity vector comparison. Here grey arrows represent velocities not used in the block model. Red arrows represent input GPS velocities and green arrows are the block model prediction. Residuals are shown as black arrows and have been scaled by a factor of 3. Histograms of the east **(b)** and north **(c)** GPS residuals normalized by their uncertainties. Histograms of the east **(d)** and north **(e)** GPS residuals.

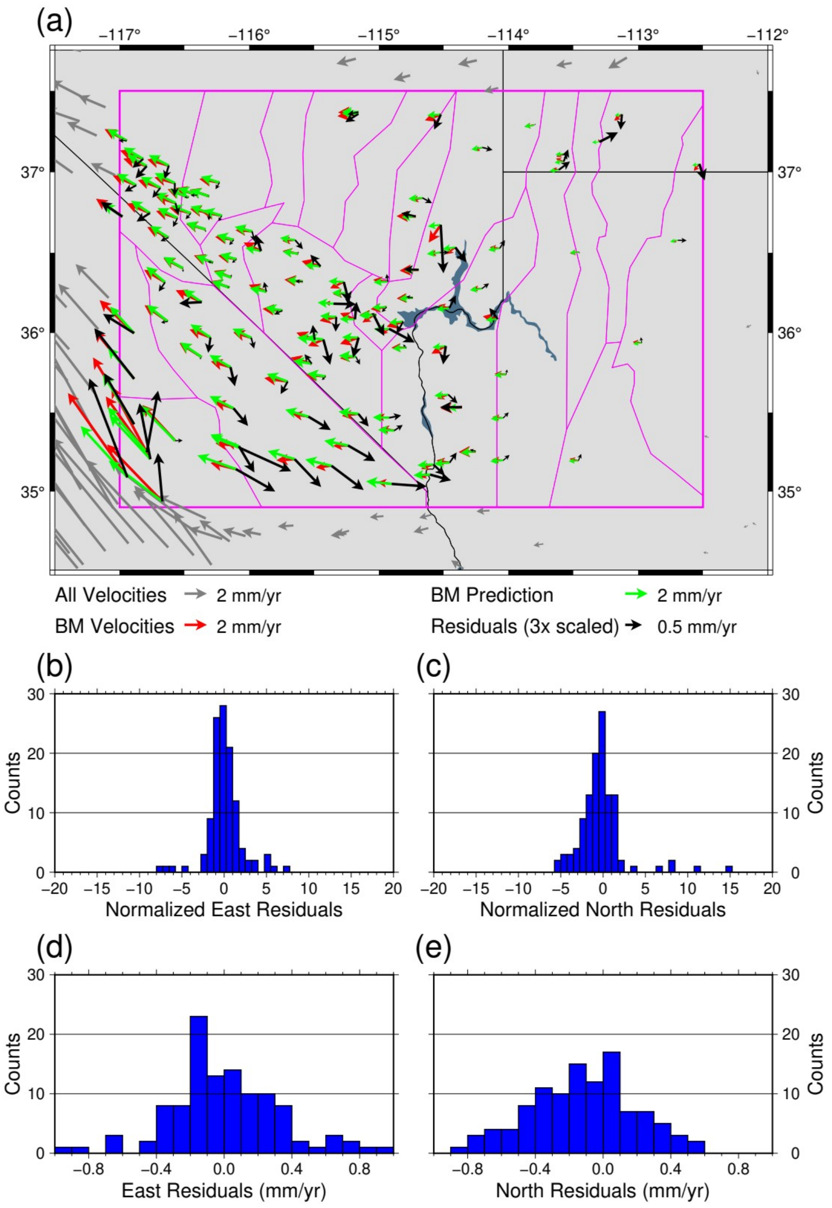

Figure S3.11: Block model fit to the GPS velocities for the original velocity model. Key as described in Figure S3.10.

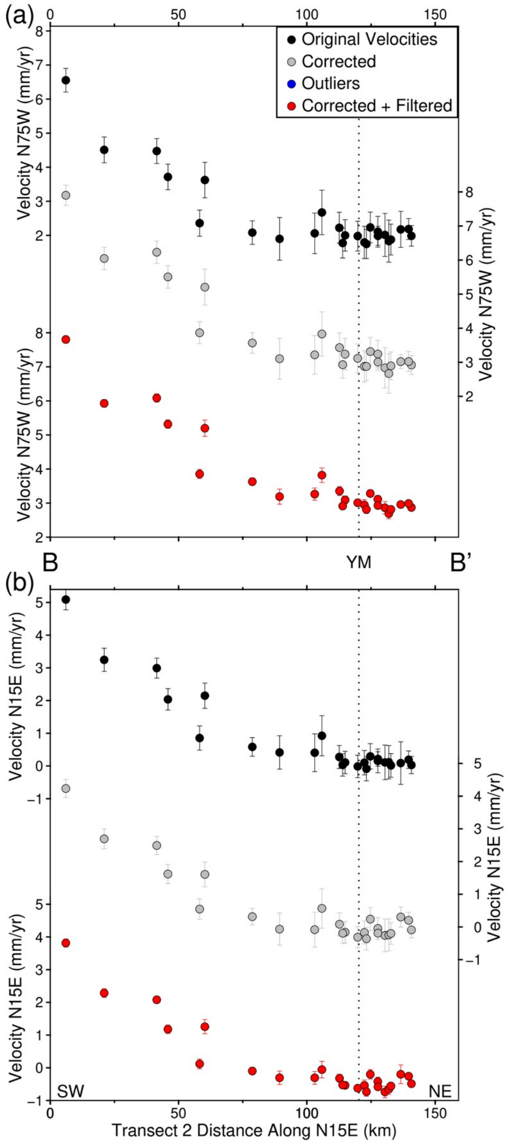

Figure S3.12: GPS velocities along **(a)** and perpendicular **(b)** to Transect S1 (see Figure S3.5), with two sigma error bars. Black dots represent velocities of the original data, grey dots represent corrected velocities, and red dots represent the final velocities following corrections and filtering. No outliers (blue dots) are present along this transect. The dotted line represents the location of Yucca Mountain.

4

Improved GPS Tropospheric Path Delay Estimation Using Variable Random Walk Process Noise

4.1 Publication Status

These results are being prepared for publication with the *Journal of Geodesy* in:

Young, Z. M., G. Blewitt, and C. Kreemer (in prep), Improved GPS Tropospheric Path Delay Estimation Using Variable Random Walk Process Noise.

4.2 Keywords

GPS, tropospheric delay, estimation strategy, random walk, optimization

4.3 Statements and Declarations

- **Authors' contributions.** Young performed the optimization analysis and was the lead author. Blewitt provided guidance, performed the GPS data analysis, and edited the manuscript. Kreemer provided guidance and edited the manuscript.
- **Funding.** NASA Grant Numbers 80NSSC19K1044 and 80NSSC22K0463 funded this work.
- **Conflict of Interest.** The authors declare there is no conflict of interest.
- **Data Availability.** GPS time series generated for this study are available from the Nevada Geodetic Laboratory upon request.

4.4 Abstract

Accurate positioning using the Global Positioning System (GPS) relies on accurate modeling of tropospheric delays. Estimated tropospheric parameters must vary sufficiently to capture true variations in delay, otherwise systematic errors propagate into estimated positions, particularly in the vertical. However, if the allowed tropospheric parameter variation is too large, the propagation of data noise into all parameters is amplified, reducing precision. Here we investigate the optimal choice of tropospheric constraints applied in the GipsyX software, implemented as specified values of random-walk process noise. The commonly adopted default constraint for the zenith wet tropospheric delay (ZWD) is 3 mm/√(hr) (Bar-Sever et al., 1998). Using this default constraint, our investigation reveals spurious wave-like patterns of 5-minute estimates of vertical displacement with amplitudes ~100 m along the California coast, coincident with Winter Storm Ezekiel, November 27, 2019. For this event, loosening the constraint to 24 mm/√(hr) suppresses the spurious vertical waves and greatly reduces the scatter of 5-minute vertical displacements. More globally, looking at various stations through the year, variability of vertical positions is reduced when selecting a constraint of 6 mm/√(hr). Further improvement of 10% over the default constraint is achieved when optimizing the constraint for each station. Best results are achieved, with 24% improvement, when optimizing the constraint with a daily value for each station. Given that applying the current default value of 3 mm/√(hr) produces pervasive positioning

errors in GPS time series, we recommend at least loosening the constraint to 6 mm/√(hr) for ZWD (similarly scaled up for gradient estimation).

4.5 Introduction

Sub-daily Global Positioning System (GPS) estimated station positions have a broad variety of scientific applications, including analyzing early co-/post-seismic mechanisms and earthquake early warning systems (Colombelli et al., 2013; Larson, 2009; Melgar et al., 2012; Twardzik et al., 2019), meteorological applications such as water vapor and total electron content (Fu et al., 2021; Leontiev & Reuveni, 2017; Moore et al., 2015; Rocken et al., 1997; Sun et al., 2021), and real-time volcano monitoring (Escayo et al., 2020; Larson et al., 2010). These applications require quality positions, and consistent repeatability, to distinguish true station motion. The topic of this paper is on improving station coordinate estimation, particularly in the vertical, through improved estimation of time-variable delay in the troposphere. For example, of concern is the ability of the troposphere estimation strategy to capture variations in delay arising from rapidly evolving weather fronts (Gregorius & Blewitt, 1998; Gregorius & Blewitt, 1999; Luddington et al., 2010). Tropospheric delay models are conventionally separated into so-called dry delay (~2 m) and a wet delay (~0.1 m). The wet delay is caused by the interaction of the electromagnetic (EM) waves with the permanent dipole moment of molecules of water vapor. The dry delay is caused by the interaction of EM waves with the induced dipole moments of all gasses in the atmosphere (including a "dry" component from water vapor). In hydrostatic equilibrium, the dry delay relates to air pressure which is typically slowly varying and well modeled (Saastamoinen, 1973). However, the wet component relates to water vapor, which can be highly variable and much more difficult to model (Bar-Sever et al., 1998).

To model tropospheric dry and wet delay, tropospheric mapping functions are used to map zenith dry delay (ZDD) and zenith wet tropospheric delay (ZWD) to the elevation angle of the satellite being observed. Thus, all wet delays can be modeled by estimating a bias in the ZWD. Moreover, the bias in ZWD can be estimated stochastically to allow for time variation (Tralli and Lichten, 1990). More accurate models introduce two additional parameters to account for a 2D gradient in tropospheric delay (Bar Sever et al., 1998). This approach is implemented in the GPS data analysis software "GipsyX" from the Jet Propulsion Laboratory (JPL), which is used for this study (Bertiger et al., 2020).

Note that residual errors in ZDD will be almost entirely absorbed by the estimate of ZWD; therefore, GPS is mostly sensitive to zenith total delay, ZTD = ZDD + ZWD. For purposes of accurate positioning (the objective of this paper), accurate estimation of ZTD is relevant. For purposes of accurate estimation of integrated water vapor (IWV), accurate estimation of ZWD is relevant.

Current models of the zenith dry and wet mapping functions are based on numerical weather models (NWM). For example, the Vienna Mapping Function Model 1 "VMF1" (Boehm et al., 2009), which is implemented in GipsyX, is based on the NWM of the European Center for Medium Range Weather Forecasting (ECMWF). VMF1 mapping functions are produced on a spatial grid in 6-hour intervals, which are then interpolated to the required locations and epochs. Using GipsyX, the ZWD estimate is estimated stochastically (allowed to vary at each 5-min epoch), while being constrained by a random walk parameter. Following Bar-Sever et al., (1998), the default value in GipsyX for this parameter is 3 mm/√(hr) for the zenith delay, and 0.3 mm/√(hr) for the two (east and north) horizontal gradients. Values approximately equivalent to these have often been used by studies (e.g., Geng et al., 2012, 2012; Sun et al., 2021; Xu et al., 2013), and as well as GPS processing centers, e.g., the Nevada Geodetic Laboratory (NGL) (Blewitt et al., 2018), the Automatic Precise Positioning Service (JPL, 2022), and the Geodetic Facility for the Advancement of Geoscience at Central Washington University (Herring et al., 2016). If the real ZTD experiences a significant gradient, however, a strict random walk constraint would limit the ZTD estimate, and the additional displacement will propagate into the position of the GPS station. As weather fronts pass through a region, atmospheric moisture (and to some extent, atmospheric pressure) can vary rapidly, resulting in large, rapid variations in the real ZTD (Gregorius & Blewitt, 1998; Tralli & Lichten, 1990).

For example, preliminary inspection of 5-minute vertical GPS positions across California on November 27, 2019 UTC, reveal significant apparent displacements. During this time, an extratropical cyclone experienced explosive cyclogenesis as it passed through California, as part of Winter Storm Ezekiel. Not only are the displacements large (~100 mm), they are also observed to travel along the coast, starting north of San Francisco, CA at the start of the day, and ending near Los Angeles, CA, by the end of the day (Figure 4.1, Video S4.1). When observed in transect (Figure 4.2), these displacements appear wavelike, with a consistent propagation speed. While studies have linked atmospheric pressure loading to GPS displacements (Martens et al., 2020; Tregoning & Dam, 2005), the atmospheric loading displacements caused by the cyclone are too broad, and of low magnitude (~3 mm over several hours) (GFZ, 2022), to explain the regionally variable displacements. Figure 4.3 shows a comparison between vertical displacement and radar reflectivity on November 27, 2019 at 09:00 UTC (Herzmann, 2022), revealing a strong spatial correlation.

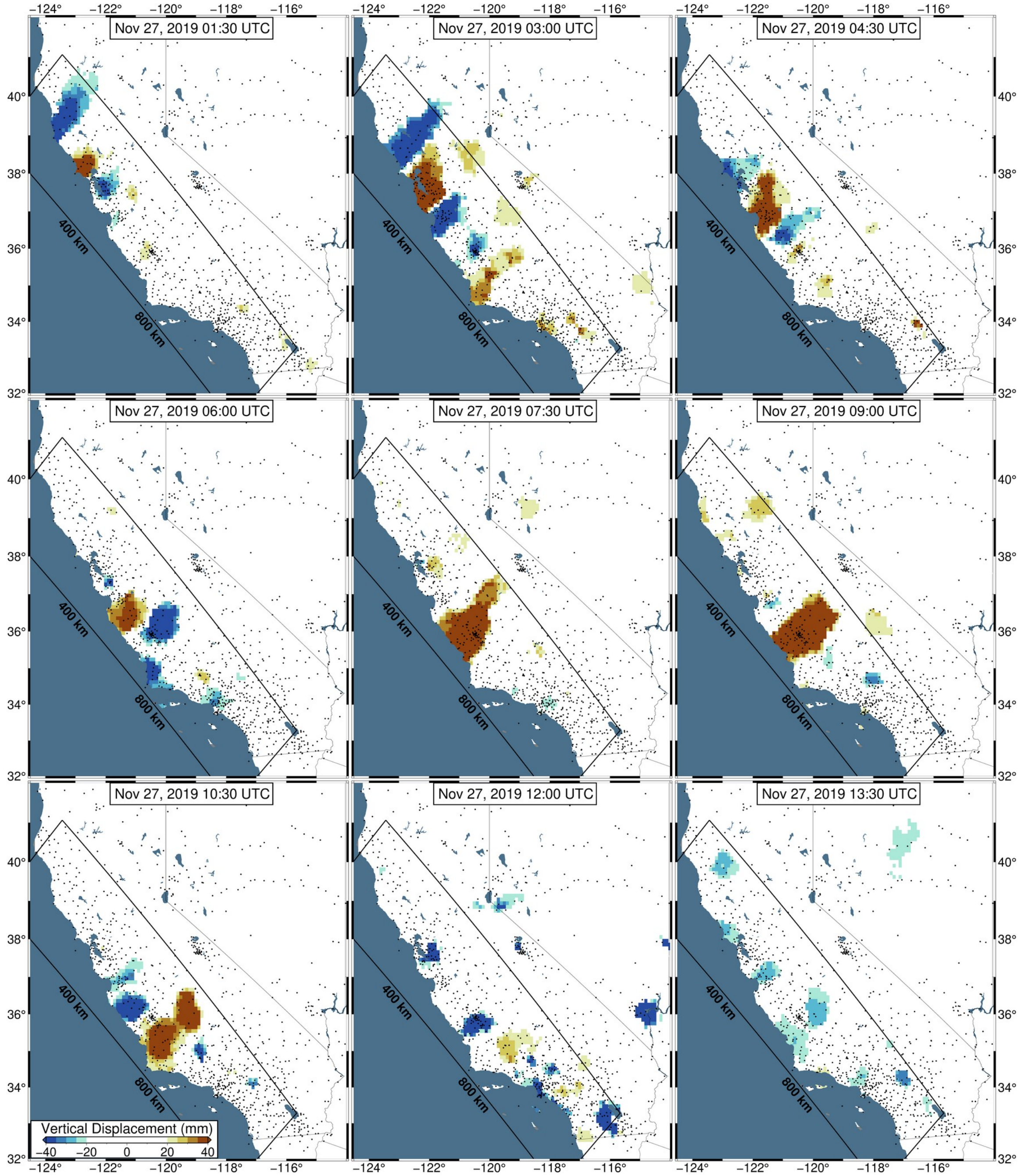

Figure 4.1: Observed 5-minute GPS vertical displacements in 1.5-hour intervals between 01:30 and 13:30 UTC on November 27, 2019. Data have been filtered with Robust Network Imaging (Kreemer et al., 2020), and are produced using current NGL processing standards, with the default ZWD random walk constraint of 3 mm/√(hr). The color bar is set such that colors begin near the average global vertical position uncertainty and

saturate at two sigma. Reds indicate observed uplift and blues reflect observed subsidence. Small black dots indicate GPS station locations, and the black rectangle represents the bounds of the transect shown in Figures 4.2, 4.8, and S4.5.

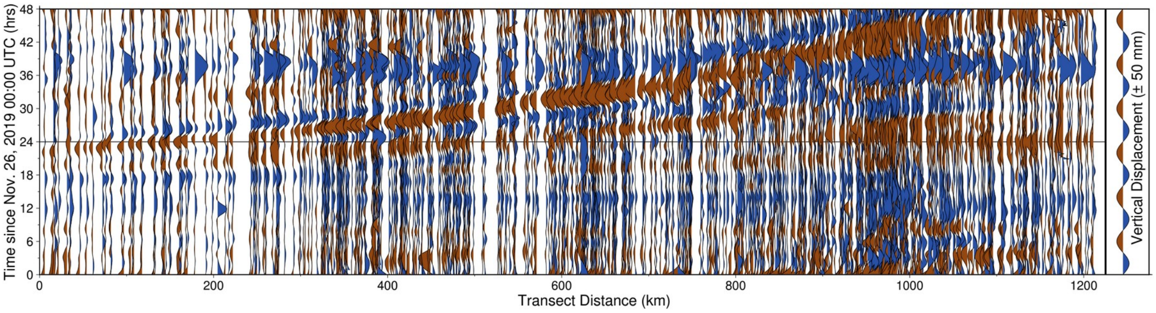

Figure 4.2: Wiggleplot of observed GPS vertical displacements along the transect shown in Figure 4.1 for November 26 – 27, 2019. Data have been smoothed with LOESS local regression, with a smoothing factor of 0.10. Black horizontal bar represents 00:00 UTC on November 27. Note the consistent band of uplift which propagates southward, beginning at the transition to November 27, near the start of the transect, and continues through the entire day.

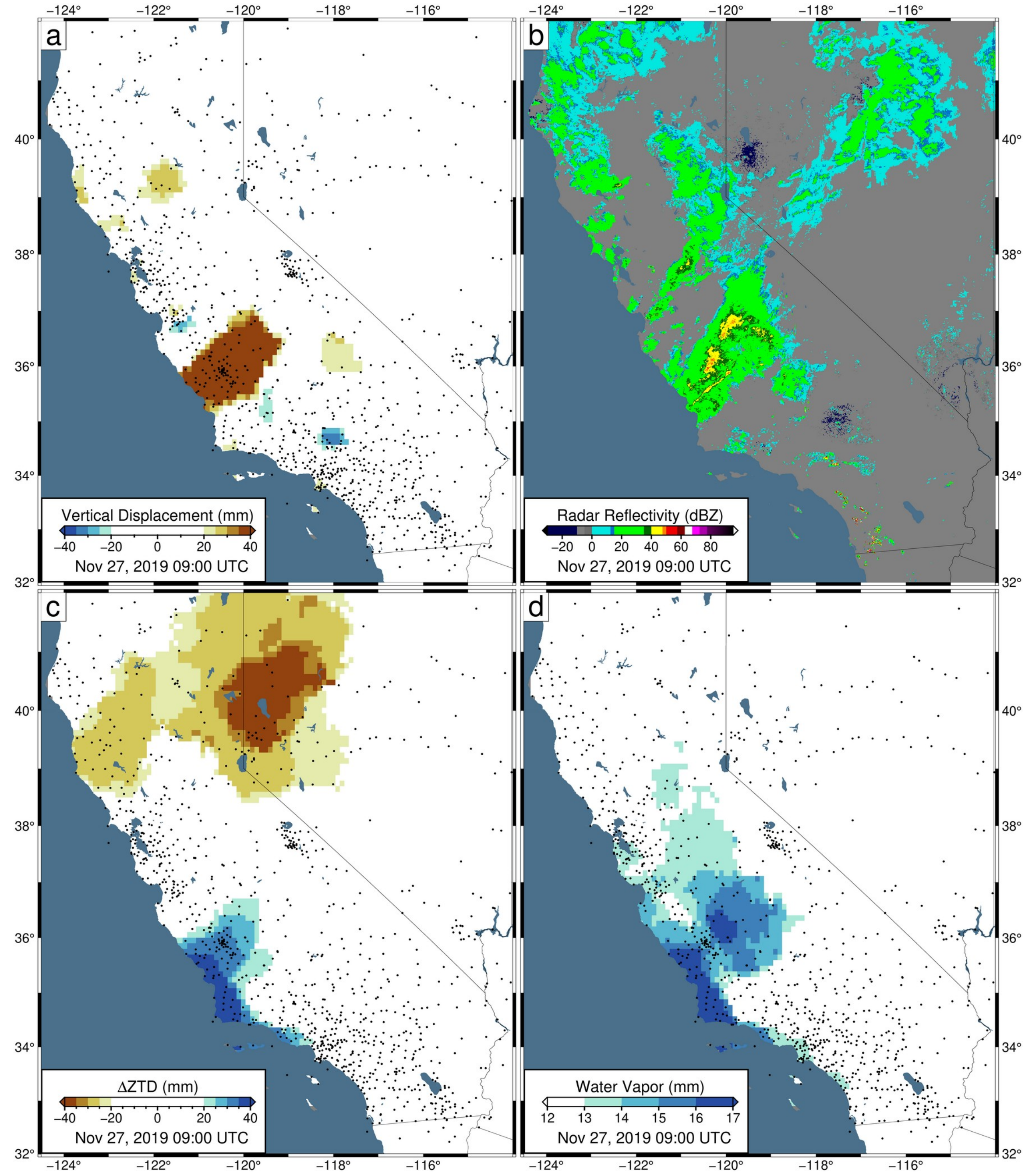

Figure 4.3: Data snapshots on November 27, 2019, at 09:00 UTC for California and Nevada. **(a)** Observed GPS vertical displacements. **(b)** Radar reflectivity. **(c)** Zenith total delay (ZTD) deviation. For each station, the median ZTD across November 26 – 27 is removed. **(d)** Integrated water vapor inferred by GPS. Note the spatial correlation

between vertical uplift and observed radar reflectivity. Data presented in panels a, c, and d have been filtered with Robust Network Imaging.

Additionally, the displacements are spatially correlated with elevated ZTD deviation and water vapor values. While these displacement patterns are fairly localized, Figure S4.1 shows similar displacements, correlated with radar reflectivity along the eastern United States, at the same epoch as shown in Figure 4.3 (Video S4.2). These displacements, however, are coherent over hundreds of kilometers and are of larger magnitude (~150 mm). A primary driver of precipitation is the interaction of cool and warm air masses. As a cool air mass moves under the warm air mass, it pushes moisture higher into the atmosphere allowing it to condense as it cools, forming precipitation. The spatial correlation between the observed vertical displacements and precipitation suggests that they are dominated by errors related to atmospheric variability associated with the weather fronts of the storm.

Gregorius & Blewitt (1999) investigated the impact of weather fronts on vertical GPS positions. Their results revealed that vertical repeatability was significantly improved when considering a random walk constraint of 8 mm/√(hr) on days when fronts passed over the stations. That study, however, was limited to 21 globally distributed stations, preventing substantial investigation into regional and climactic aspects of varying the constraint. In the time since, GPS data processing methods have greatly improved and the global GPS network has experienced significant expansion (Blewitt et al., 2018), improving the ability to distinguish the sensitivity of five-minute GPS positions to the chosen random walk constraint, at both local and global scales. In this study, several suites of 5-minute GPS time series are produced, featuring different levels of ZTD random walk, and we investigate both the impact on positions during the passing of Winter Storm Ezekiel, as well as its effect on global data quality. After which, we provide recommendations for future processing strategies to improve 5-minute GPS positioning quality.

4.6 Methods

4.6.1 Data Analysis Strategy Using GipsyX

Except where noted, this investigation uses JPL's GipsyX software (Bertiger et al., 2020) with NGL's standard production data analysis strategy for kinematic precise point positioning. The strategy is based on the precise point positioning concept by Zumberge et al.(1997) with fixed satellite orbits and clock biases, but with station coordinates estimated freely at every 5-min epoch. GPS satellite positions and clocks are from JPL's "final" product line. Batch solutions are generated for 24-hour GPS days for each station individually using undifferenced carrier phase and pseudorange data every 5-minute epoch from all satellites in view for elevation angles of $e >= 7°$, with observation weights that scale with $\sigma^2=1/\sin(e)$. Station clock biases and station coordinates are estimated with loose constraints so that they are data driven. Ionospheric delay is calibrated using a linear combination of dual-frequency GPS data and is modeled to higher order using a conventional model of the Earth's magnetic field together with JPL data products on ionospheric total electron content. As outlined in the introduction, tropospheric modeling uses VMF1 data products (Boehm et al., 2009) for ZDD and ZWD, and for dry and wet mapping function parameters. Residual ZTD variation is estimated as a random walk in ZWD with a default constraint of 3 mm/√(hr) for the zenith delay, and 0.3 mm/√(hr) for the two horizontal gradients (Bar Sever et al., 1998). The overall level (starting value) of residual ZTD is estimated very loosely with a 0.5 m constraint. Carrier phase bias parameters are introduced for each station-satellite arc and for detected integer discontinuities, some of which may be automatically resolved prior to least-squares estimation (Blewitt et al., 1990). All parameters (typically about 70 per station day) are estimated simultaneously using a square root information filter. GipsyX then constrains real-valued estimates of carrier phase biases with the a priori knowledge that they are linear combinations of integer wavelengths (Bertiger et al., 2010). This improvement is propagated through to all parameters. Finally, for each daily GipsyX batch solution, 24-hour constant coordinates are estimated by computing the weighted mean of the 5-minute coordinate solutions. This final step (outside of GipsyX) allows us to evaluate the impact of estimation strategy on daily coordinate repeatability.

4.6.2 Proxy for Tropospheric Errors

Here we use the 5-minute vertical GPS position variations as a proxy for errors in ZTD estimation. This proxy method assumes that errors in ZTD caused by rapid variation (that exceed the random walk constraints) will generate much larger vertical position errors than real vertical displacement (from atmospheric pressure and surface water loading). More generally, we consider this also a proxy for the more traditionally estimated station positions as constant over each 24-hour GPS day, an assumption that can be tested by investigating the daily mean coordinate solutions. The assumption is that 24-hour position estimates are optimized (have the least error) when 5-minute vertical position estimates have the smallest variation.

4.6.3 Rationale for Loosening Random Walk Constraints

As a preliminary study, we investigated GPS positions along the coast of California on November 26 – 27, 2019 UTC. These days are chosen to facilitate comparison between a day without a passing storm system (November 26), and the atmospheric turbulence produced by Winter Storm Ezekiel on November 27.

If the default random walk constraint of 3 mm/√(hr) is appropriate, and the observed displacements are associated with an un-modeled geophysical signal, then loosening the random walk will amplify the mapping of measurement noise into the 5-min vertical positions (owing to correlations between vertical and ZTD parameters). This would increase station 5-min vertical coordinate root mean square (RMS) scatter while preserving the original signal. However, if the random walk constraint is too tight, loosening its value will allow the ZTD estimate to better account for atmospheric variability, and errors in 5-minute vertical positions should decrease as systematic error is reduced. This would reduce station RMS and suppress the apparent displacements.

To further investigate the random walk constraints under more typical conditions, we then expand our study to the global network and explore the regional and temporal aspects of loosening the constraints. We also look at the effect of loosening constraints on 24-hour constant estimates of vertical coordinates, which is of interest for investigations of slow deformations of the Earth.

4.6.4 Test Tropospheric Estimation Strategies

To address the above goals, daily batches of 5-minute GPS vertical data are produced for November 26 – 27, 2019 UTC, as well as for the first two days of each month of 2021. We adhere to the NGL standard data analysis strategy (Section 2.1) but with a suite of test estimation strategies for which we increase the random walk constraint for ZWD incrementally between the default value of 3 mm/√(hr) and up to 48 mm/√(hr). Table 4.1 shows the constraints used for the specified test estimation strategies. Note that the horizontal gradient constraints are equivalently increased, at a value that is 10% of the zenith constraint.

Table 4.1: Specified test estimation strategies

		Random Walk Constraint [mm/√(hr)]		
Strategy Name	Strategy ID	Zenith Wet Delay	Gradient East	Gradient North
TROPx01*	01	3	0.3	0.3
TROPx02	02	6	0.6	0.6
TROPx04	04	12	1.2	1.2
TROPx08	08	24	2.4	2.4
TROPx12	12	36	3.6	3.6
TROPx16	16	48	4.8	4.8

*Default strategy in GipsyX (Bar Sever et al., 1998).

Henceforth, we will refer to specified strategy either by its full name or identification (ID) number, where ID is the scaling factor of the default strategy. These test strategies generate our "uniform" random walk solutions, in the sense that each strategy is applied to all stations for all days tested without attempt to optimize based on location or time. For the purpose of this study, we focus on the results of the vertical component as our proxy for tropospheric error. Estimation of all other parameters is kept at the default settings (Section 4.6.1), thus isolating the impact of loosening the random walk constraints of the tropospheric parameters.

In addition to the uniform random walk data sets, two data sets are produced in which the random walk is allowed to vary per station. The first, our "station specific" data set, identifies a characteristic station specific random walk constraint, which most frequently minimizes the RMS of 5-min vertical estimates for each station during 2021. The second, our "daily optimal" data set, identifies the solution which minimizes the

RMS 5-minute vertical for each station, on each day, producing a time variable random walk data set. For consistency within the global analysis, we limit stations to those who produced data on all 24 days of our study, resulting in 5819 stations and 139,656 station days.

4.7 Results

4.7.1 Loosening Constraints for Winter Storm Ezekiel

Loosening the random walk constraints clearly improves vertical data quality at stations along the coast of California on November 26 – 27, 2019 UTC. Figure 4.4 shows a comparison of vertical displacements and ZTD estimates for GPS stations P194, CAND, and CBHS. These stations are distributed across California with P194 located north of San Francisco, CAND located near Parkfield, and CBHS located northwest of Los Angeles. On November 26, station positions are consistent; however, on November 27, displacements of up to 105 mm are observed as the storm progresses southward along the coast. Across both days the ZTD estimates are smooth. Upon loosening the random walk constraint to 12 mm/√(hr) (four times looser, strategy TROPx04), the majority of the observed vertical deviations associated with the storm are suppressed and the station ZTD estimate becomes more variable. While the signal from the storm shows slightly more improvement with strategy TROPx08 at 24 mm/√(hr), station scatter begins to increase. This is shown through the 5-minute vertical repeatability values presented in Table 4.2. Repeatability is defined as 1.4826*MAD, where MAD is the median absolute deviation of the time series (Huber, 1981). Here we see that station P194 shows the best repeatability on November 27, with a random walk of 6 mm/√(hr). Stations CAND and CBHS are both most improved at 12 mm/√(hr); however, each of these stations show lower repeatability values up to a random walk of 36 mm/√(hr), compared to the default value. Notably, while these stations do not see improvements in repeatability on November 26, they do not exhibit a significant reduction in data quality until the random walk is eight times looser.

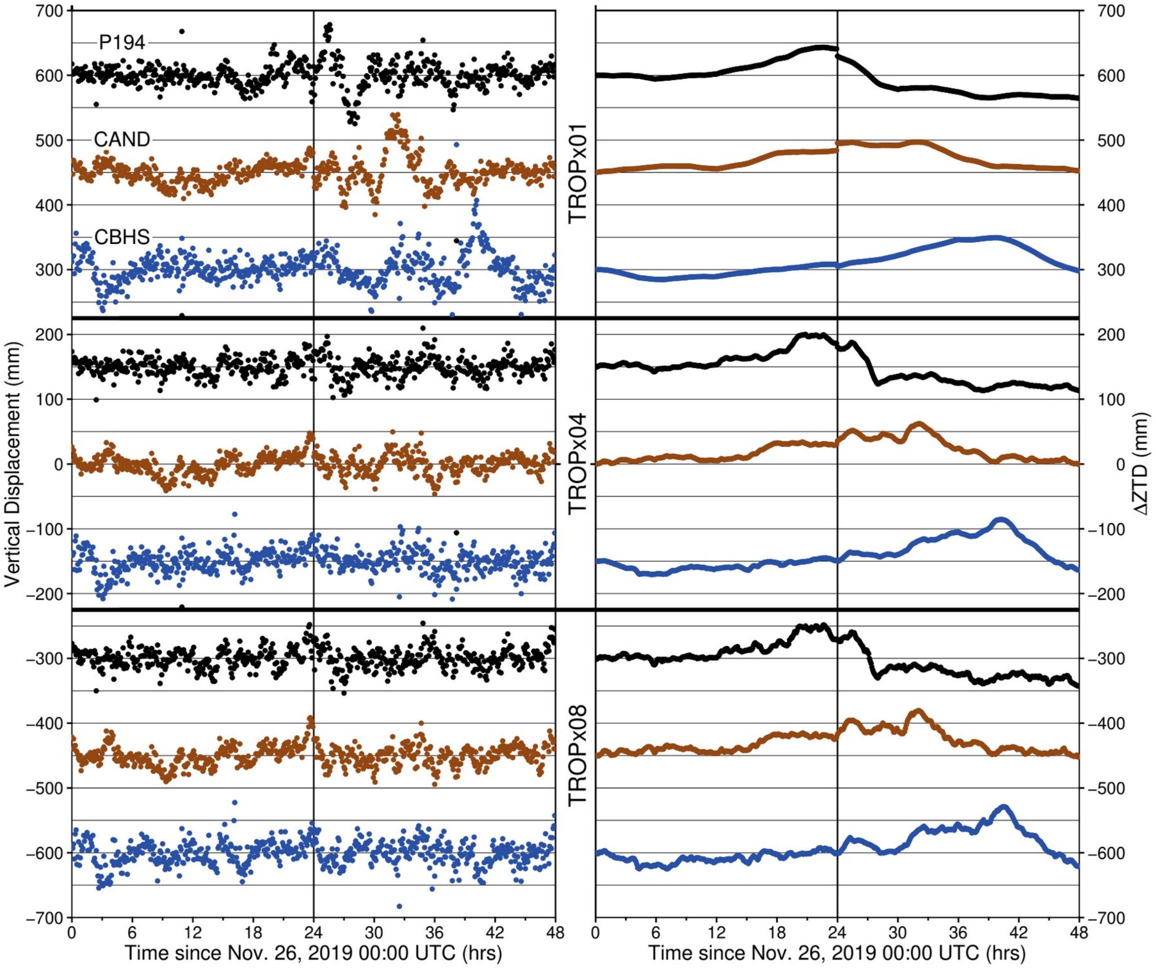

Figure 4.4: Vertical displacement and zenith tropospheric delay comparison for GPS stations P194, CAND, and CBHS. Data are shown for November 26 – 27, 2019 for the default strategy TROPx01, and the TROPx04 and TROPx08 solutions. P194 is located north of San Francisco, CA, CAND is located near Parkfield, CA, and CBHS is located northwest of Los Angeles, CA. Vertical black line identifies the change of day.

Table 4.2: 5-min vertical repeatability for specified strategies.

	Strategy ID					
	01	02	04	08	12	16
Station	Station 5-Min Vertical Repeatability (mm)					
	November 26, 2019					
P194	*12.5	*12.5	12.9	13.5	14.2	15.4
CAND	*14.1	14.6	14.2	15.9	17.3	18.6
CBHS	*15.7	15.8	16.2	18.7	19.9	21.3
	November 27, 2019					
P194	18.2	*14.0	14.5	14.6	14.6	16.2
CAND	17.7	14.9	*13.4	15.6	16.6	18.2
CBHS	26.1	19.0	*14.9	16.5	19.3	19.5

*Optimal solutions for given station and day

The passage of Winter Storm Ezekiel greatly affected regional vertical data quality. Figure 4.5 shows a comparison of station 5-min vertical RMS and repeatability for all stations within the bounds of Figure 4.1, for different processing strategies. Data are separated by date, with red representing the data from the calm November 26, 2019, and blue for the stormy November 27, 2019, with black representing the combination of these dates. During the storm, station RMS values are elevated at 28.2 ± 12.9 mm, compared to 17.6 ± 5.1 mm on the prior day, when using the default random walk constraint (Table S4.1). When loosening its value for the stormy day, results are similar at the TROPx04 and TROPx08 levels. Comparison of the distribution of vertical RMS between the TROPx01 and TROPx08 solutions, shows that for the TROPx08 RMS values become more localized near ~20 mm, rather than being broadly distributed (Figure

S4.2). For both solution sets, RMS and repeatability are substantially improved at ~15% and ~21% respectively. On November 26, the calmer day, the largest data quality improvement is produced using the TROPx02 solution, with RMS and repeatability improved by 5.1% and 11.4% respectively. The combination of these dates sees large improvements in repeatability, at 28.6% for the TROPx08 solution. The majority of the storm can be accounted for with the TROPx04 solution; however, to fully remove the spatial signal, the TROPx08 solution is required (Figure 4.6). At this level, vertical displacements are no longer spatially correlated with the observed radar reflectivity and are now better correlated with deviations in the ZTD estimate and water vapor levels (Figure 4.7). We find that where systematic displacements were previously observed in the vertical displacements (Figure 4.2), no consistent trends are observed at the TROPx08 level (Figure 4.8). The ZTD and water vapor estimates reveal the opposite, with the TROPx08 solution exhibiting increased variability at the times where large vertical displacements were estimated when using the default random walk (Figures 4.9, 4.10, S4.3, S4.4, and S4.5). A comparison of the TROPx01 and TROPx08 solutions, can be viewed in Videos S4.1, S4.3, and S4.4, which provide a time lapse of vertical displacement, ZTD deviation, and water vapor for each solution on November 27, 2019. We observe similar results, with large vertical displacements being suppressed and reallocated to the ZTD estimate by the TROPx08 solution, in the eastern United States (Videos S4.2, S4.5, and S4.6). These findings reveal that 5-minute GPS repeatability can be substantially improved on both stormy and calm days by loosening the random walk constraint. The choice of this value however, is dependent on the complexity of atmosphere on the day in question, and varies from station to station.

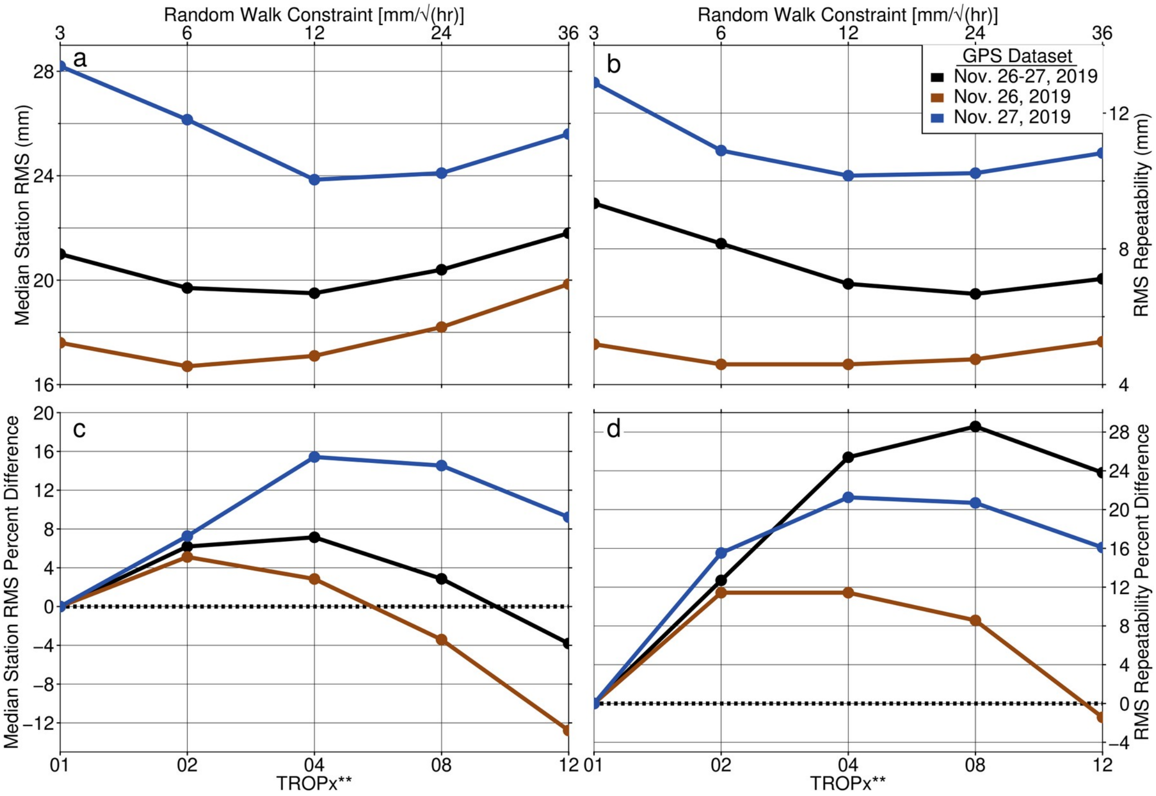

Figure 4.5: Comparison of solutions for GPS stations in California and Nevada on November 26 – 27 for different strategies. **(a)** Median RMS and its **(b)** repeatability by solution. Percent difference for solutions relative to the TROPx01 solution for **(c)** the median station RMS and its **(d)** repeatability. Horizontal dotted black line represents equivalence to the TROPx01 solution. Values are presented in Table S4.1.

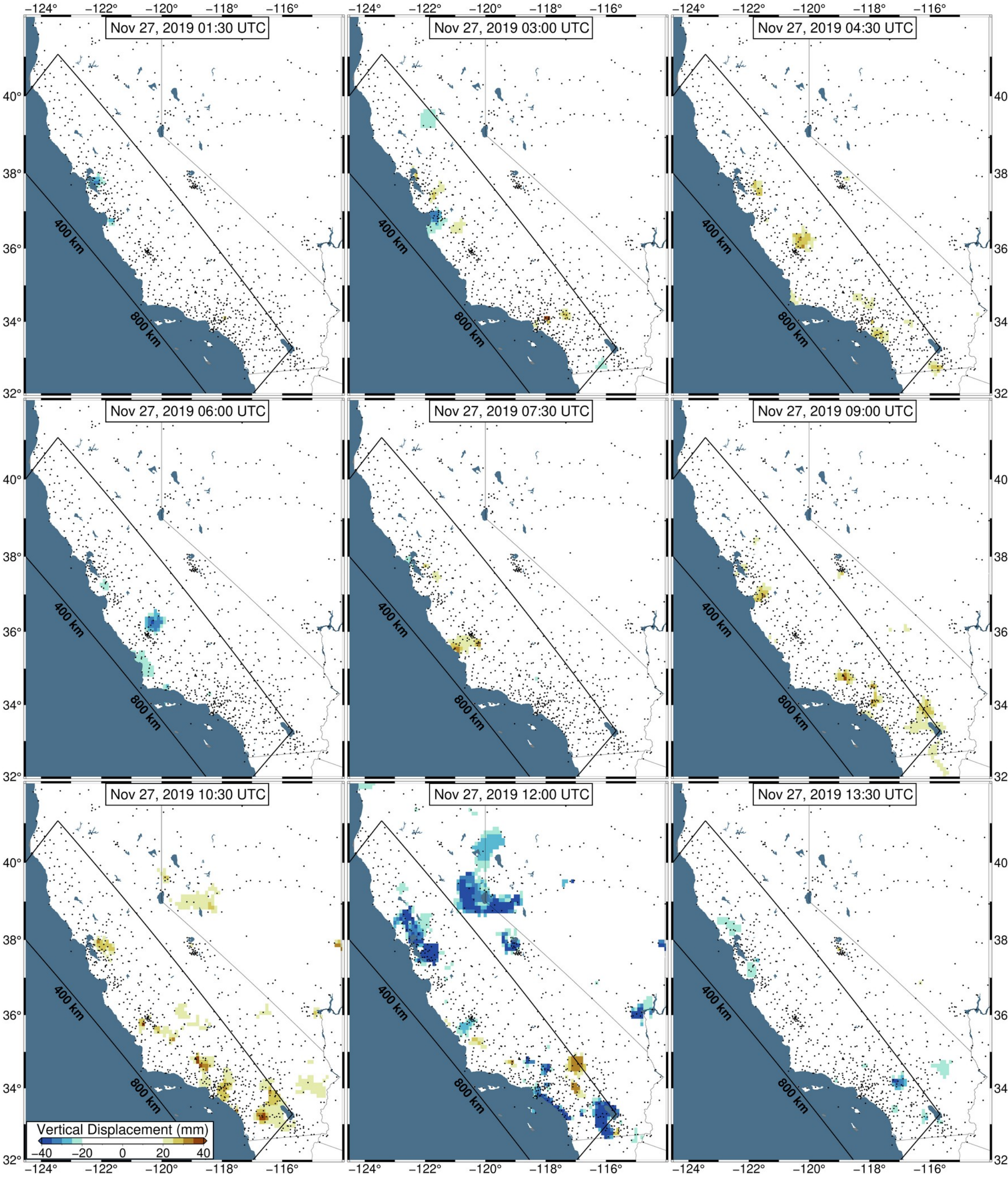

Figure 4.6: Corrected 5-minute GPS vertical displacements in 1.5-hour intervals between 01:30 and 13:30 UTC on November 27, 2019 for the TROPx08 solution. Key as described in Figure 4.1.

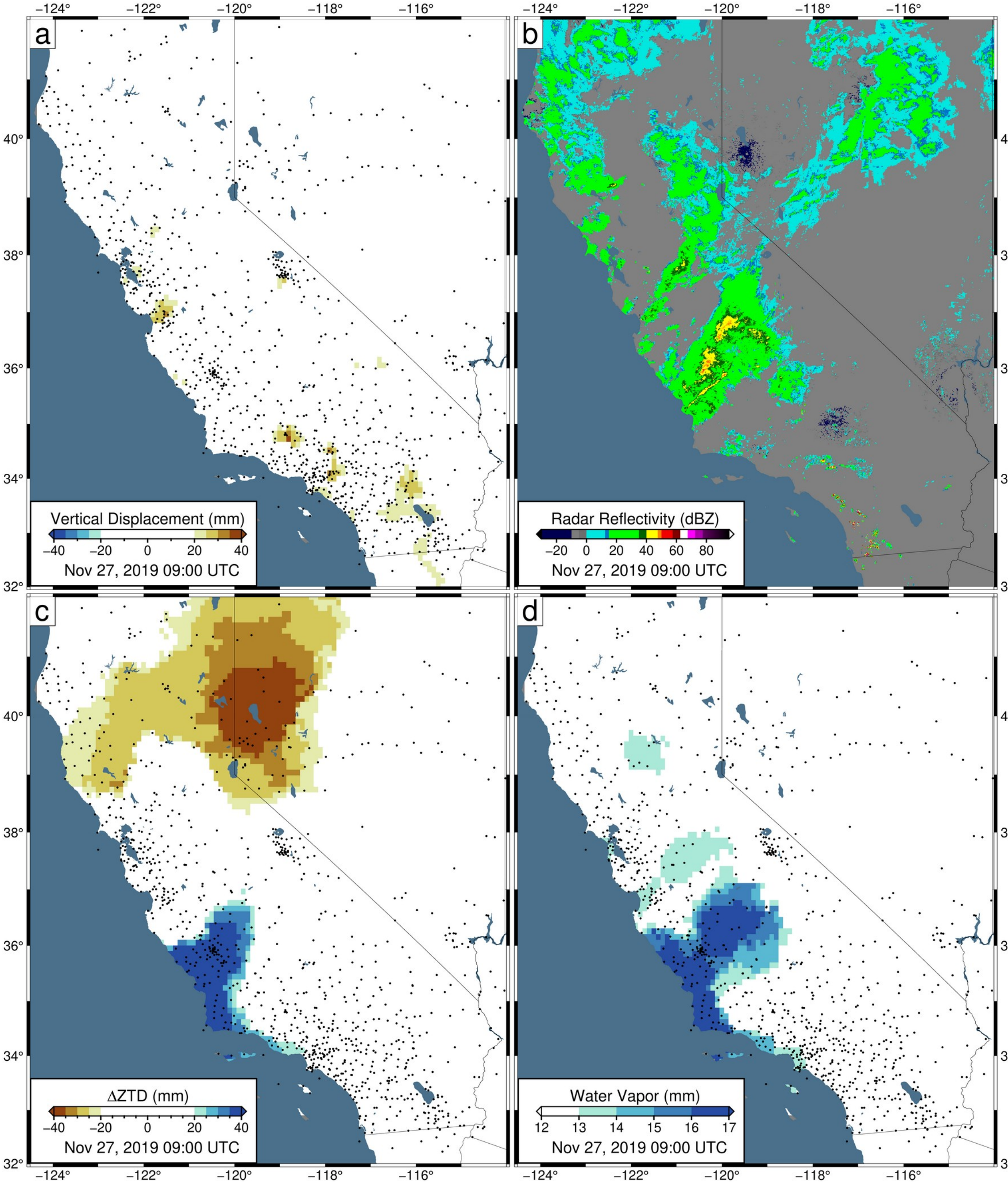

Figure 4.7: Same as Figure 4.3 except for the TROPx08 solution [24 mm/√(hr)]. Note that vertical displacements are now suppressed and the correlation of the ZTD and integrated water vapor estimates, to the radar reflectivity, in increased.

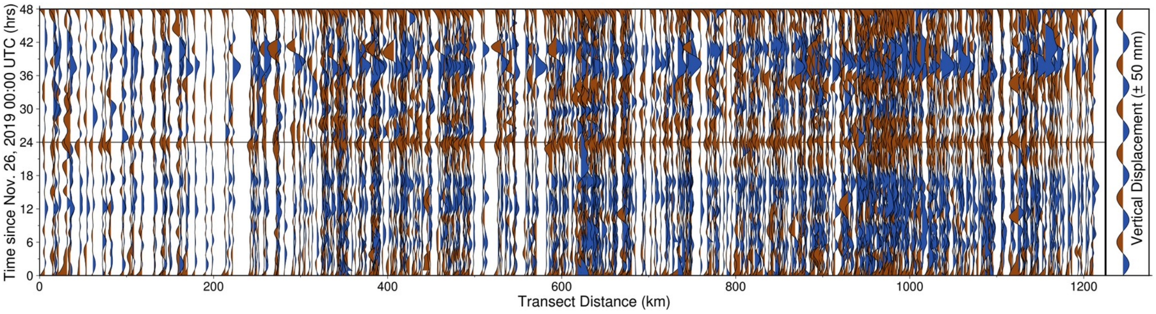

Figure 4.8: Wiggleplot of corrected GPS vertical displacements along the transect identified in Figure 4.1 for November 26 – 27, 2019, for the TROPx08 solution [24 mm/√(hr)]. Data have been smoothed with LOESS local regression, with a smoothing factor of 0.10. Black horizontal bar represents November 27 00:00 UTC. Note that the systematic displacements shown in Figure 4.2 are suppressed.

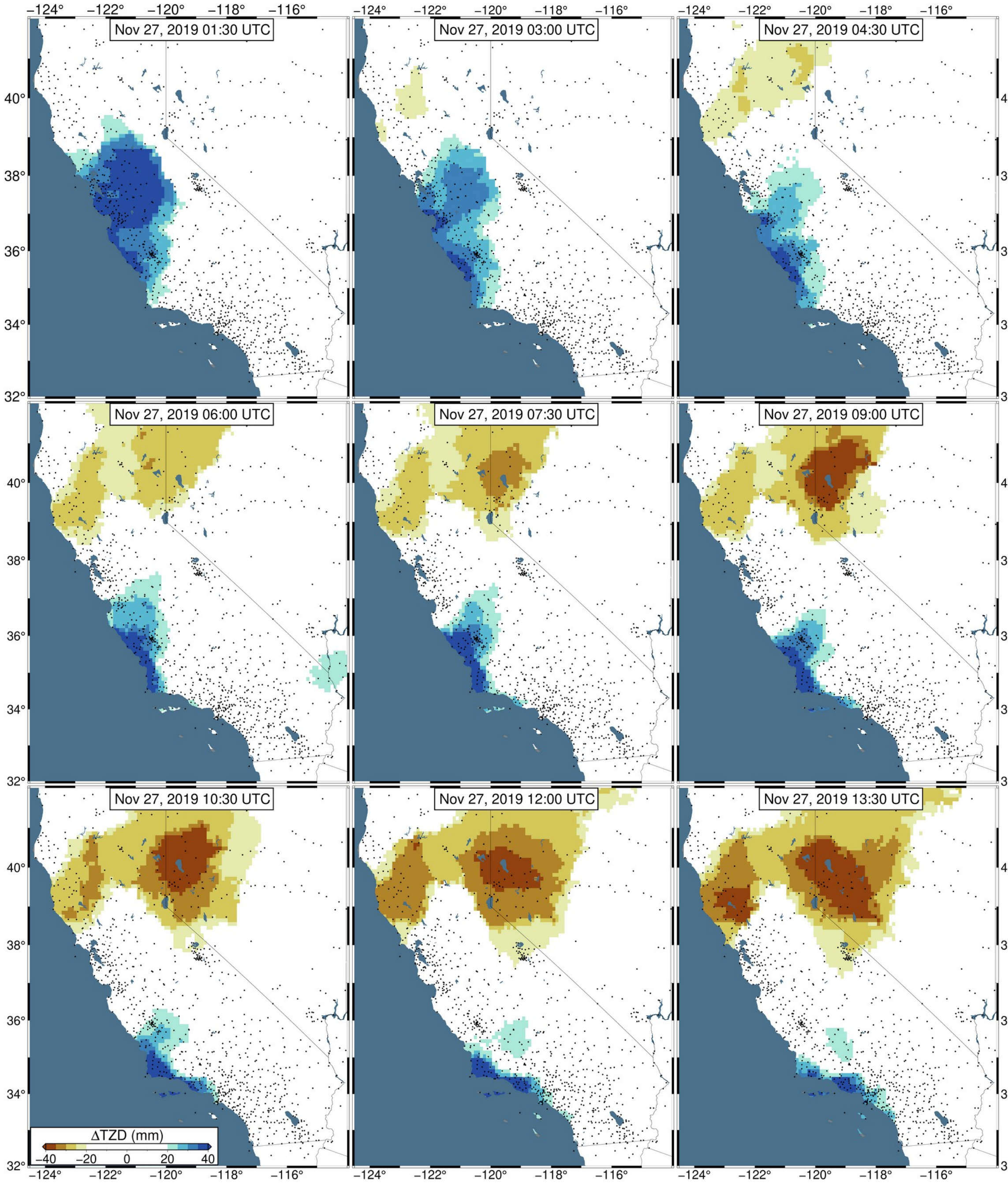

Figure 4.9: Observed zenith tropospheric delay deviation, in 1.5-hour intervals between 01:30 and 13:30 UTC, on November 27, 2019. For each station, the median zenith delay across November 26 – 27 is removed. Data have been filtered with Robust Network Imaging and are produced using a random walk of 3 mm/√(hr). Small black dots indicate GPS station locations.

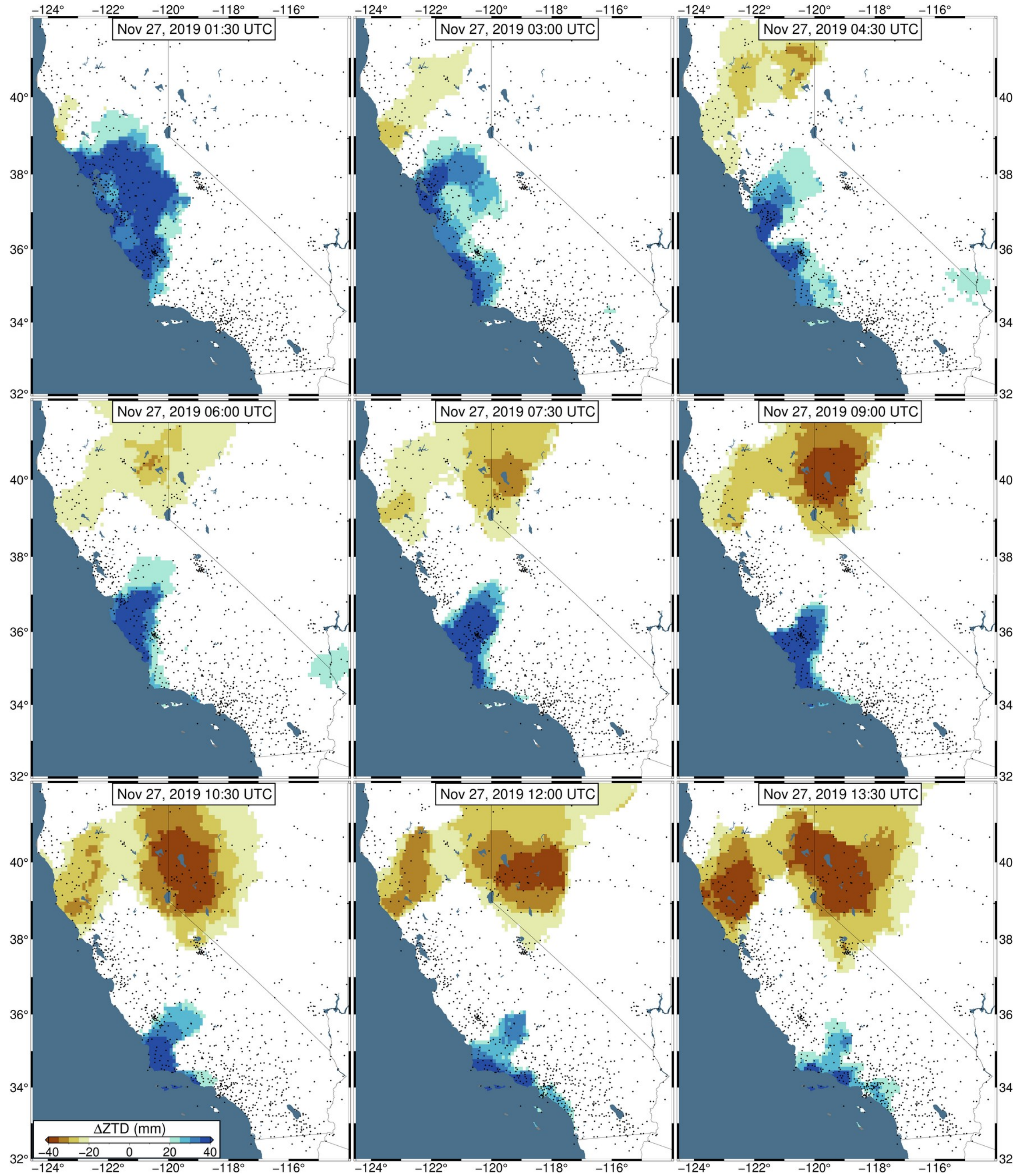

Figure 4.10: Corrected zenith tropospheric delay deviation in 1.5-hour intervals between 01:30 and 13:30 UTC on November 27, 2019, for the TROPx08 solution. For each station, the median zenith delay across November 26 – 27 of the TROPx01 solution is removed. Data have been filtered with Robust Network Imaging and small black dots indicate GPS station locations.

4.7.2 Regional Data Quality

To investigate the effect on the global GPS network of altering the random walk constraint, we first consider its regional impact. Figure 4.11 shows a comparison between median station 5-min vertical RMS and repeatability of the 2021 data for several regions around the globe. Substantial variation is present in the median station RMS, with the lowest values when using the default random walk, produced by stations in New Zealand and the polar region (which we define as stations located at a latitude >|±60°|), at 17.2 mm and 16.6 mm, respectively (Table 4.3). The highest median RMS values are found in Central and South America, with values of 30.8 mm and 25.4 mm, respectively. A similarly large range is observed in station repeatability, with regions exhibiting scatter between 5.2 mm and 10.3 mm. We find that all regions, except for the polar stations, show improvements by loosening the random walk constraint, and that solutions between 6 mm/√(hr) and 24 mm/√(hr), all perform better than the 3 mm/√(hr) solution. The optimal value for most regions is 6 mm/√(hr), however, with respect to repeatability, Central America, Japan, and New Zealand show equivalent improvements with both the 6 mm/√(hr) and 12 mm/√(hr) solutions. Improvements in median RMS range between 4% – 9% with the TROPx02 solution, and Central America improves by 10% with the TROPx04 solution. We find that for station repeatability, most regions improve by 10% – 14% with the TROPx02 solution. Two exceptions are the polar region, which shows no change, and Japan which improves by 21%. Regional data quality is significantly reduced at the 36 mm/√(hr) and 48 mm/√(hr) levels.

When considering the variable random walk data sets, both are found to improve data quality relative to the uniform default value, with the daily optimal solution showing substantial improvements (Table 4.4). Globally, median RMS and repeatability are improved by 4% and 10% when applying a characteristic station specific random walk constraint. For the daily optimal data set, these improvements increase to 10 and 24 percent, with station repeatability in Japan improved by 29%. These results reveal that the global GPS network is particularly sensitive to the level of the applied random walk constraint.

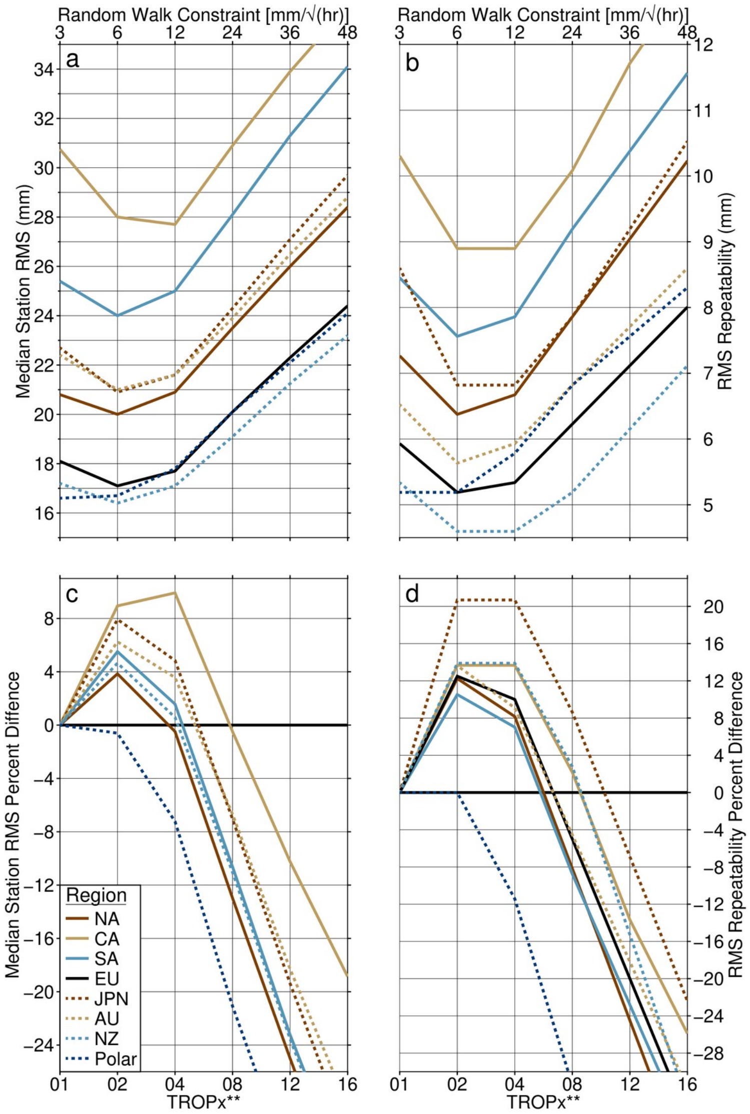

Figure 4.11: Global 2021 data set comparison by region and processing strategy of the **(a)** median station vertical RMS, **(b)** its repeatability, **(c)** the percent difference of the median station vertical RMS relative to the TROPx01 solution, and **(d)** its repeatability relative to the TROPx01 solution . Horizontal black line represents equivalence to the TROPx01 solution. Regions are as follows: NA – North America, CA – Central America, SA – South America, EU – Europe, JPN – Japan, AU – Australia, NZ – New Zealand, and Polar represents stations at latitudes >|±60°|. Note that all except the polar region, exhibit improvements in both RMS and repeatability in the 6 – 12 mm/√(hr) range. Values are presented in Table S4.2.

Table 4.3: Median station 5-min vertical RMS and repeatability by region of the global 2021 data sets, for the current, station specific, and daily optimal processing strategies.

Region	Median RMS ± Repeatability (mm)		
	Current RW	Station Specific RW	Daily Optimal RW
NA	20.8 ± 7.3	20.2 ± 6.7	19.0 ± 5.5
CA	30.8 ± 10.3	27.1 ± 8.5	25.8 ± 7.6
SA	25.4 ± 8.5	24.0 ± 7.6	23.0 ± 7.0
EU	18.1 ± 5.9	17.3 ± 5.3	16.3 ± 4.6
JPN	22.7 ± 8.6	21.1 ± 7.1	19.8 ± 6.1
AU	22.4 ± 6.5	21.1 ± 5.8	20.1 ± 5.0
NZ	17.2 ± 5.3	16.8 ± 5.0	15.7 ± 4.0
Polar	16.6 ± 5.2	16.5 ± 5.0	15.9 ± 4.6
Global	20.7 ± 7.4	19.9 ± 6.7	18.7 ± 5.6

Table 4.4: Median station 5-min vertical RMS and repeatability percent difference relative to the TROPx01 solution, of the station specific and daily optimal results presented in Table 4.3.

Region	Station Specific RW		Daily Optimal RW	
	Median RMS Percent Difference	Repeatability Percent Difference	Median RMS Percent Difference	Repeatability Percent Difference
NA	3	8	9	24
CA	12	18	16	26
SA	6	11	9	18
EU	4	10	10	23
JPN	7	17	13	29
AU	6	11	10	23
NZ	2	6	9	25
Polar	1	3	4	11
Global	4	10	10	24

4.7.3 Regional Variation

Closer inspection of the regional distribution of 5-min vertical RMS values, reveals substantial variation dependent on the local climate. Areas where continental and maritime tropical air masses are typically present, exhibit elevated annual RMS values, while locations where maritime and continental polar air masses are expected, tend to exhibit the lowest RMS values. In North America, this is dramatically present, with much of the southeastern United States exhibiting RMS values >24 mm, while the western and central states exhibit RMS values under 20 mm (Figure 4.12). The sharp gradient between low and elevated RMS values aligns well with the interaction of dry southeastbound continental polar air masses, with moist northeastbound tropical air masses from Mexico and the Gulf of Mexico (Aguado & Burt, 2013). Similar distributions are observed between the Mediterranean region and northern Europe (Figure S4.7), as well as between southern and northern Japan (Figure S4.10), with areas of consistent maritime/tropical air masses exhibiting elevated station RMS.

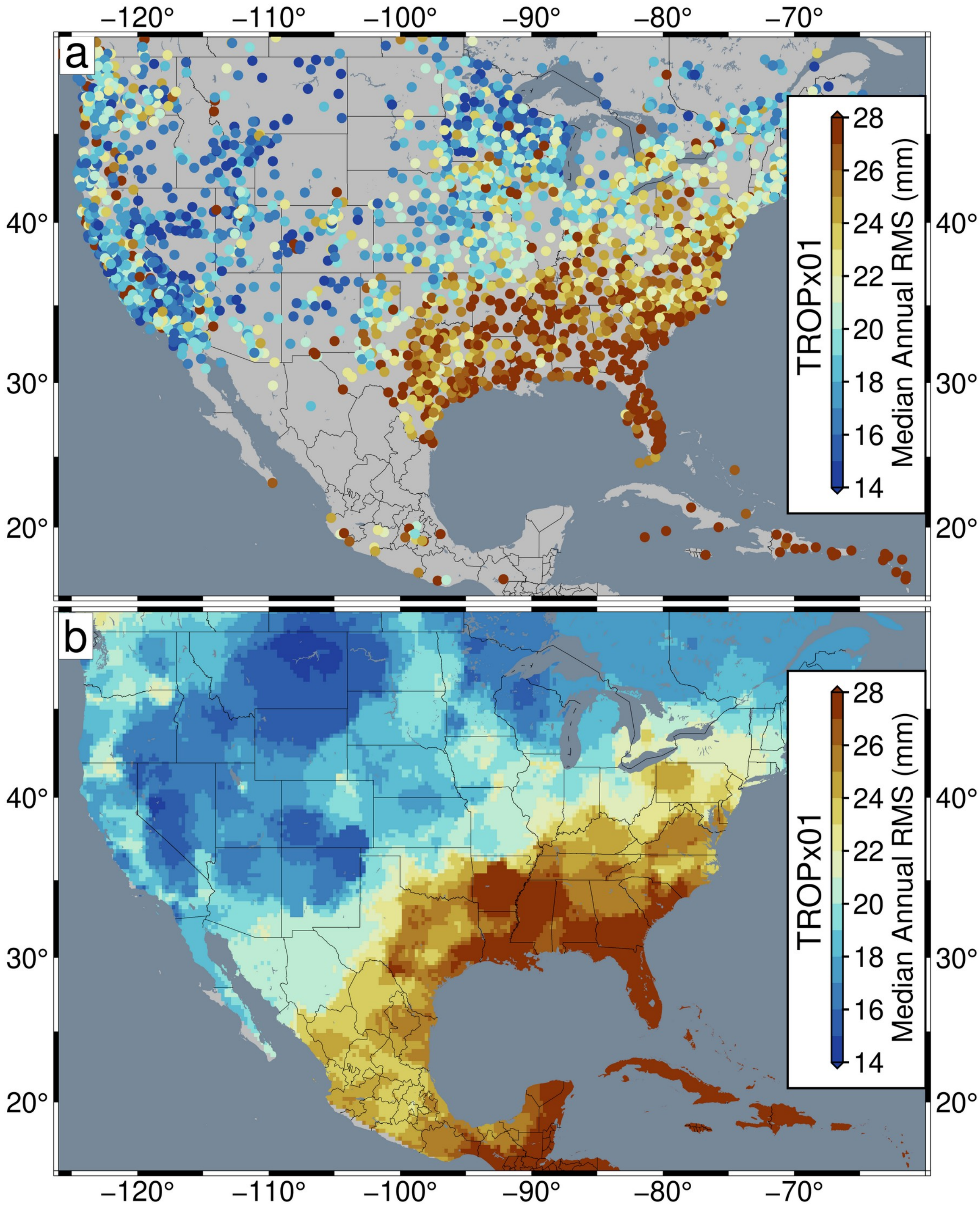

Figure 4.12: (a) Median annual vertical RMS; **(b)** median annual vertical RMS smoothed by Robust Network Imaging, for GPS stations in the United States, Central America, and the Caribbean. Results are for the TROPx01 strategy.

Figure 4.13 shows distributions of Robust Network Imaged median vertical RMS, and it’s percent difference relative to the TROPx01 solution, for the United States, Central America, and the Caribbean, for the TROPx02, TROPx04, station specific, and daily optimal strategies. Results are limited to the 2021 data. The TROPx02 solution shows that most stations show improvements at a random walk of 6 mm/√(hr), with the exception of Utah, Colorado, Arizona, and New Mexico, which exhibit reductions of less than 3%. The largest improvements are observed in the southeastern United States and the Caribbean. At the TROPx04 level, the majority of the western and central United States see reductions in data quality of up to 12%, however, Florida, Georgia, South Carolina, and the Caribbean see larger improvements than the TROPx02 solution.

When considering a station specific random walk, all regions are improved or equivalent to the TROPx01 solution, but the majority is improved by less than three percent. Only the eastern seaboard and the Caribbean exhibit improvements greater than nine percent. The attributed characteristic random walk values, per station, are shown in Figure 4.14. Note that most of the continental interior tends toward the default random walk as optimal, while RMS values in the eastern United States are most frequently minimized at random walk values of 6 and 12 mm/√(hr). In both Europe and Japan, the majority of stations exhibit a characteristic random walk higher than 3 mm/√(hr) (Table 4.5, Figures S4.9 and S4.12). Globally, 47.7% of stations retain 3 mm/√(hr) as their characteristic random walk constraint.

The largest improvements are observed with the daily optimal strategy. Here, all regions exhibit improvements, with most regions greater than 6%, and much of the southeastern United States and the Caribbean improves by more than 18%. Similar levels of improvements are observed with each processing strategy in Europe (Figure S4.8), and Japan (Figure S4.11), with Japan showing significant improvements with the daily optimal strategy, at 29%.

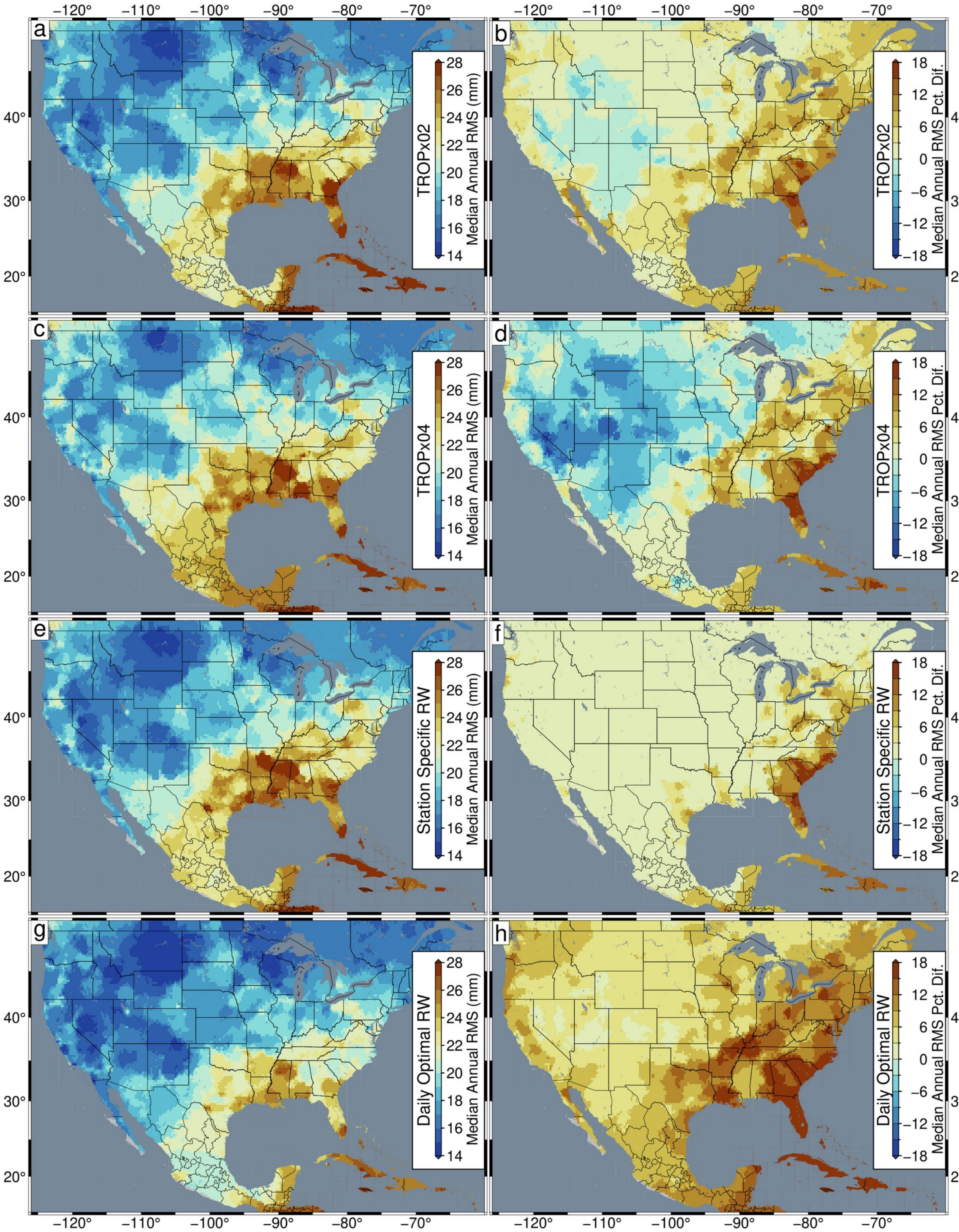
a
b
c
d
e
f
g
h
TROPx02
TROPx04
Station Specific RW
Daily Optimal RW
Median Annual RMS (mm)
14
16
18
20
22
24
26
28
Median Annual RMS Pct. Dif.
−18
−12
−6
0
6
12
18
−120°
−110°
−100°
−90°
−80°
−70°
20°
30°
40°

Figure 4.13: Comparison of **(a, c, e, and g)** Robust Network Imaged median annual vertical RMS and its **(b, d, f, and h)** percent difference relative to the TROPx01 solution for the **(a and b)** TROPx02, **(c and d)** TROPx04, **(e and f)** station specific, and **(g and h)** daily optimal processing strategies for GPS stations in the United States, Central America, and the Caribbean.

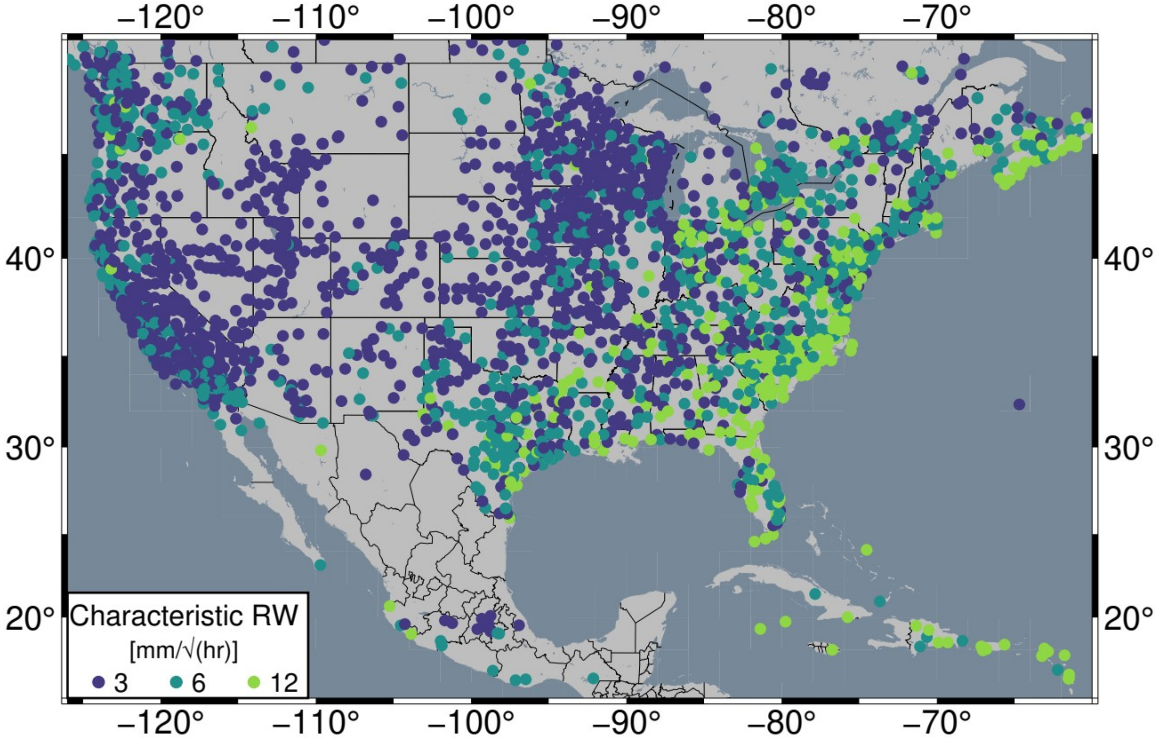

Figure 4.14: Characteristic station random walk constraint for GPS stations in the United States, Central America, and the Caribbean. Values reflect the processing strategy which most frequently minimizes station RMS in 2021.

Table 4.5: Percentage of stations per characteristic random walk constraint, by region. Values indicate the percentage of stations which most frequently exhibit the lowest station RMS per strategy. Distributions are plotted in Figures 4.14, S4.9, and S4.12. Globally, only three stations are characteristic at 24 mm/√(hr).

	Strategy ID			
	01	02	04	
Region	Percentage of Stations			Station Count
NA	56.5	31.8	11.7	3003
EU	42.6	50.3	6.9	923
JPN	27.6	54.0	18.4	976
Global	47.7	40.4	11.8	5819

4.7.4 Annual Variability

A strong annual signal is present in both the station vertical RMS and its repeatability, and substantial variation is present between regions. As expected, the annual signal is opposite between northern hemisphere (Figure 4.15), and southern hemisphere regions (Figure 4.16). These figures reflect the annual component of the fit to daily median vertical RMS and repeatability values, for each region, on the days processed in 2021. Results for each strategy are then compared to the TROPx01 solution. Peak amplitudes are found during the summer months, when the troposphere is thickest (Rieckh et al., 2014). We find that for all cases, the TROPx02 solution performs equivalent to, or better than, the TROPx01 solution. The TROPx04 solution performs better than current processing during the summer months, by hemisphere, but under performs during winter, and the TROPx08 solution rarely performs better than the

TROPx01 solution. The characteristic station specific solution always performs better than the TROPx01 solution, however, it typically under performs during the summer months compared to the TROPx02 solution. The largest improvements to both RMS and repeatability are found in the summer months. In terms of median RMS, the peak improvements for North America, Europe, Japan, South America, and Australia are 12%, 13%, 16%, 11%, and 11% respectively. For station repeatability, peak improvements are 24%, 24%, 29%, 22%, and 25% respectively. Each of which are roughly twice the level of improvement achieved by the TROPx02 and station specific solutions. These results highlight significant annual variability in data quality, dependent on the choice of the random walk constraint.

4.7.5 Daily Position Improvements

Inspection of the daily positions of our 2021 dataset reveals that a majority of stations exhibit improvements at looser random walk values than the default constraint. To determine this, we calculate the annual RMS improvement for each station. This is defined as $\sqrt{(RMS1^2\text{-}RMS0^2)}$, where RMS1 represents the station RMS values of the TROPx01 solution, and RMS0 represents the value which best minimizes the station RMS by strategy. We find that 32% of stations retain the TROPx01 strategy, while the rest of the stations exhibit improvements (Figure S4.13). The median improvement for the global daily positions is 4.5 ± 2.8 mm. These results indicate that the improvements exhibited at the 5-minute processing level by loosening the random walk constraint, propagate into the daily positions.

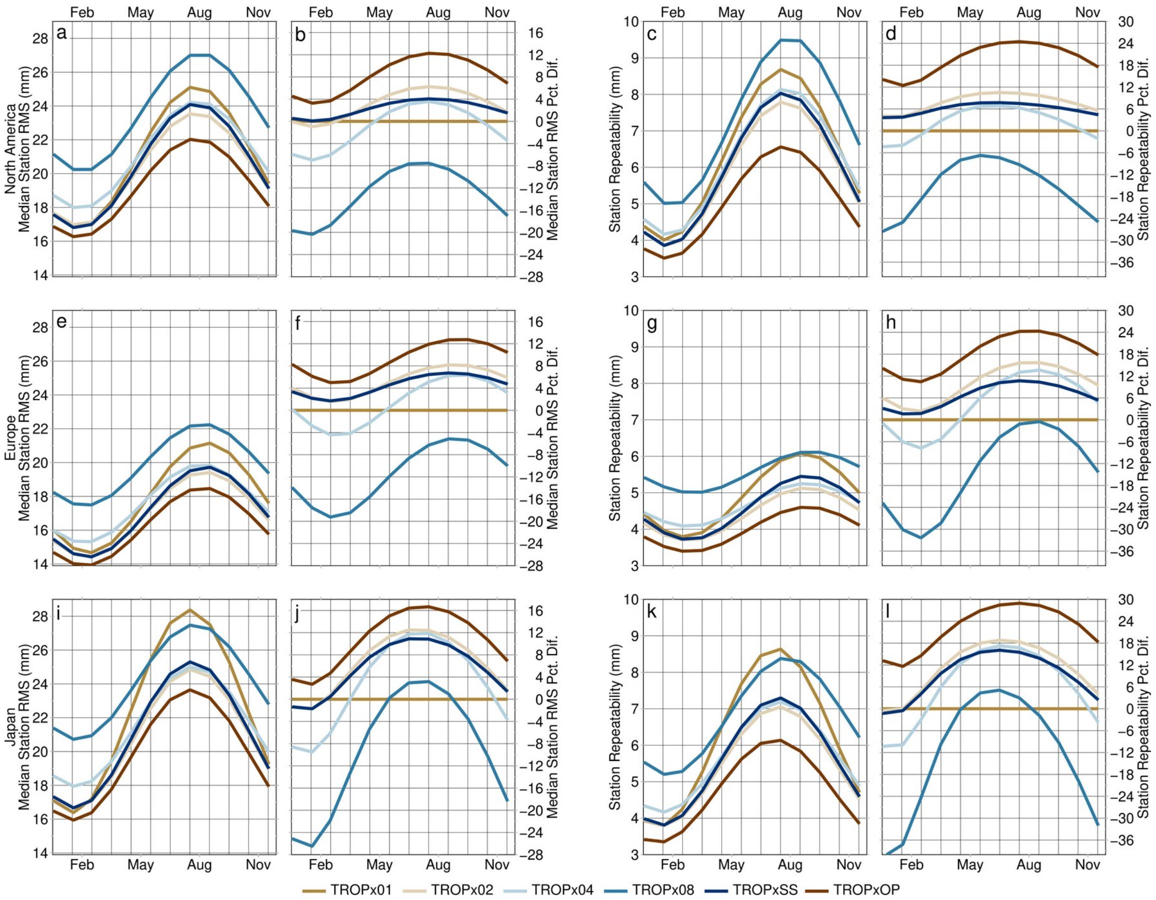

Figure 4.15: Annual component by processing strategy of **(a, e, and i)** the fit to the median station vertical RMS, **(b, f, and j)** it's percent difference relative to the TROPx01 solution, **(c, g, and k)** the fit to the station vertical repeatability, and **(d, h, and l)** it's percent difference relative to the TROPx01 solution, for **(a – d)** North America, **(e – h)** Europe, and **(i – l)** Japan. Here, TROPxSS and TROPxOP reflect the station specific and daily optimal data sets respectively.

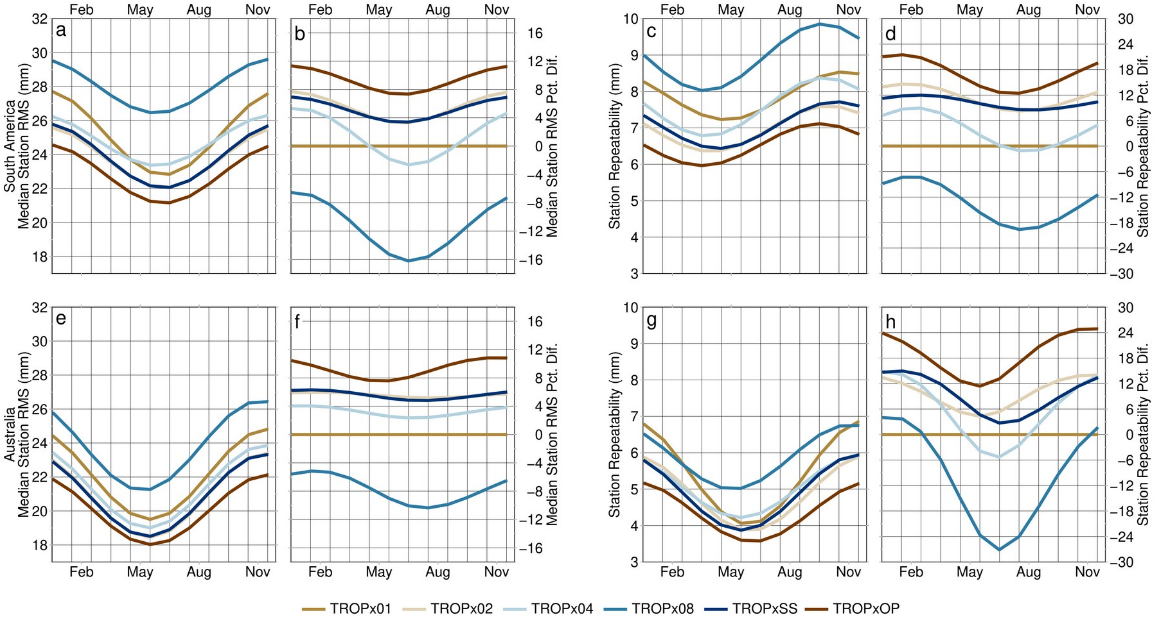

Figure 4.16: Annual component by processing strategy of **(a and e)** the fit to the median station vertical RMS, **(b and f)** it's percent difference relative to the TROPx01 solution, **(c and g)** the fit to the station vertical repeatability, and **(d and h)** it's percent difference relative to the TROPx01 solution, for **(a – d)** South America and **(e – h)** Australia. Here, TROPxSS and TROPxOP reflect the station specific and daily optimal data sets respectively. Note that for median station vertical RMS, the TROPx02 and TROPxSS solutions are nearly identical.

4.8 Discussion

4.8.1 Weather and Sub-daily Positioning

We present clear evidence that the vertical displacements observed by 5-minute GPS time series in California on November 27, 2019, occur due to rapid atmospheric variation caused by the storm. When using the default random walk constraint of 3 mm/√(hr), ZTD estimates are extremely smooth temporally, regardless of atmospheric variation. This can be seen in Figure 4.4, where the TROPx01 solution shows minimal short-term (under two hour) variability on both the calm November 26, and the turbulent November 27, 2019. Relaxing the random walk constraint, allows rapid variation between high- and low-pressure fronts to be better accounted for, resulting in substantially improved position time series, and more dynamic ZTD estimates. While large improvements in data quality during the storm are achieved using random walk constraints of 12 and 24 mm/√(hr), we also find that on the calm day, both the 6 and 12 mm/√(hr) solutions produce improved positions, relative to the default solution. This highlights that, although there wasn't significant weather occurring on November 26, 2019 across California, loosening the random walk during more typical atmospheric conditions, improves data quality. Not only can data improvements be observed along the coast of California, but also regionally across the eastern United States on November 27, showing that limitation on the spatial scale and distribution of potential ZTD estimation improvements, when loosening the random walk, is purely dependent on the scale of the boundary between air masses.

Another factor that sees improvement, is the day-to-day coherency for both station position and ZTD. Often, when combining multiple days of sub-daily time series, there is a step in the data at the day transition. This is driven by differences in the models between days, but we find a large portion can be accounted for by allowing the ZTD more freedom (Figure 4.4). With a looser random walk constraint, the data is able to overcome discrepancies between the model and observations and is more consistent across the day transition. While we focus on improving positioning, the corrected ZTD estimates result in improved water vapor estimates. Indicating that meteorological studies can be improved as well by loosening the random walk constraint.

4.8.2 Implications of Global Network Positioning Improvements

At the global scale, regional and temporal variability in the optimal level of the random walk constraint is substantial for both the uniformly applied, and station variable approaches. We show that for regions which tend to experience polar air masses (i.e., higher latitudes and most of the western and central United States), this value is generally appropriate. However, substantial reduction of station time series scatter is possible for the rest of the global network at values of 6 mm/√(hr) or higher. Coastal regions, where tropical air masses tend to be present, require the loosest random walk constraint, and exhibit improvements often greater than 15%. A spatially variable random walk constraint approach has not been applied to large network analysis in the past, however, the prevalent heterogeneity of characteristic random walk values shown in Figures 4.14, S9, and S12, reveal an excellent opportunity to improve global data repeatability in future reanalysis.

While we focus here on sub-daily GPS positioning, Figure S4.13 clearly shows that these corrections propagate into improved daily positions since they are derived from these sub-daily observations. This raises clear implications for all aspects of GPS analysis, including improved station velocity estimates, reference frame identification, and satellite orbit determination.

4.8.3 Recommended Processing Strategies

In this study, we explored three types of random walk constraint applications, the uniform value, characteristic station specific, and daily variable applications. Using a uniform value is the default approach for GPS processing. We show that while for some regions data quality improves dramatically as the random walk is loosened (i.e., the southeastern United States, the Mediterranean, and southern Japan, see Figures 4.13, S4.8, S4.11), other areas see large reductions (i.e., the western/central United States). This trade off may be acceptable for localized studies which produce their own data, however, for global network processing, increasing the random walk constraint >12 mm/√(hr) uniformly, is not advised. Nevertheless, global data quality is improved by a random walk of 6 mm/√(hr), with only a few regions showing minor reductions, and is our recommended threshold for uniform application.

Applying characteristic station specific random walk constraints is of course better than the uniform method, as it allows for regional climatic variability to be accounted for. Additionally, in terms of global network processing, it would be a simple adjustment to the current processing flow since it would only require defining a suite of values for the network. The characteristic random walk values could then be interpolated to the position of newly installed stations until enough data is present to define the station. With this approach, 52% of stations globally can be improved with this simple adjustment.

The daily variable approach produced superior results compared to the other data sets. This is because it is able to account for, not just regional climate variability, but temporal variability associated with both annual fluctuations and passing weather systems. For small scale studies producing their own data, it is highly recommended to test and identify daily station specific random walk values, regardless of the study area, as we find that even in polar regions (which showed no improvement by loosening the random walk), repeatability is substantially improved (Table 4.5). In terms of global network processing, identifying daily optimal random walk constraints using the methods applied here, would scale poorly and would need to be identified during the processing flow.

An alternative, which would not be as computationally expensive, would be to define an annual random walk per station. As shown in Figures 4.15 and 4.16, annual variation is significant, and peak improvements are obtained during the summer by looser solutions. Often with the TROPx04 strategy performing better than the TROPx02 and characteristic strategies. Thus, a time variable random walk per station could range from the TROPx01 strategy, for winter months and the TROPx04 strategy for summer, by determining a seasonal amplitude and phase term per station. We leave determination of an efficient identification method to future studies, but note that for the 2021 data set, 63.8% of station days exhibited RMS reductions by allowing the random walk to vary each day, per station.

4.9 Conclusions

In this study, we present a sensitivity analysis of the ZTD random walk constraint on 5-minute GPS positions at local and global scales. We show that station RMS and repeatability can be improved by loosening the random walk constraint from the GipsyX default value of 3 mm/√(hr) to 6 – 24 mm/√(hr). The choice of the optimal threshold, however, is strongly dependent on the atmospheric, regional, temporal, and climatic conditions of the station. We find that during Winter Storm Ezekiel of November 2019, using a random walk constraint of 24 mm/√(hr) more adequately accounts for variations in the ZTD, improving station repeatability by 21%. Additionally, on the calmer day prior to the storm, November 26, 2019, station repeatability is improved by 11% when loosening the random walk to 6 mm/√(hr). Showing that during more typical atmospheric conditions, station data quality can be improved by loosening its value as well.

In the global analysis, we find that there is substantial opportunity to improve data quality by loosening the random walk, with the largest impact on station repeatability exhibited by stations in Japan. Median vertical RMS and station repeatability are most improved when using a random walk of 6 – 12 mm/√(hr), and (with the exception of polar stations which do not typically improve), improve by 4% – 9% and 10% – 21% respectively. Additionally, we show that that the improvements observed in the 5-minute timeseries, propagate into the daily station vertical position. Regional heterogeneity in the optimal level of the random walk constraint is substantial, indicating a variable approach is more appropriate. Tests of two variable random walk methods each show significant improvements relative to the default random walk. When defining characteristic random walks for individual stations, we find global repeatability to improve by 10%, alternatively, when applying daily optimal station specific random walks, global station repeatability is improved by 24% and in Japan by 29%. While the daily optimal random walk method is preferred, it is difficult to scale to global network analysis and will be addressed in future studies. Defining characteristic random walk values would be a simple adjustment in the data flow and could be implemented rapidly, resulting in significant improvements in station repeatability for global GPS network processing. At minimum, for uniform application within the GipsyX software, increasing the default value of the random walk constraint to 6 mm/√(hr) is recommended.

4.10 References

Aguado, E., & Burt, J. (2013). Chapter 9 Air Masses and Fronts. In *Understanding weather and climate* (6th ed., pp. 258–277). Pearson.

Bar-Sever, Y. E., Kroger, P. M., & Borjesson, J. A. (1998). Estimating horizontal gradients of tropospheric path delay with a single GPS receiver. *Journal of Geophysical Research: Solid Earth*, *103*(B3), 5019–5035. https://doi.org/10.1029/97JB03534

Bertiger, W., Desai, S.D., Haines, B., Harvey, N., Moore, A. W., Owen, S., Weiss, J. P. (2010). Single receiver phase ambiguity resolution with GPS data. Journal of Geodesy, 84: 327-337. https://doi.org/10.1007/s00190-010-0371-9

Bertiger, W., Bar-Sever, Y., Dorsey, A., Haines, B., Harvey, N., Hemberger, D., et al. (2020). GipsyX/RTGx, a new tool set for space geodetic operations and research. *Advances in Space Research*, *66*(3), 469–489. https://doi.org/10.1016/j.asr.2020.04.015

Blewitt, G. (1990). An automatic editing algorithm for GPS data. Geophysical Research Letters, 17(3) 199-202. https://doi.org/10.1029/GL017i003p00199

Blewitt, G., Hammond, W., & Kreemer, C. (2018). Harnessing the GPS Data Explosion for Interdisciplinary Science. *Eos*, *99*. https://doi.org/10.1029/2018EO104623

Boehm, J., Kouba, J., & Schuh, H. (2009). Forecast Vienna Mapping Functions 1 for real-time analysis of space geodetic observations. *Journal of Geodesy*, *83*(5), 397–401. https://doi.org/10.1007/s00190-008-0216-y

Colombelli, S., Allen, R. M., & Zollo, A. (2013). Application of real-time GPS to earthquake early warning in subduction and strike-slip environments. *Journal of Geophysical Research: Solid Earth*, *118*(7), 3448–3461. https://doi.org/10.1002/jgrb.50242

Escayo, J., Fernández, J., Prieto, J. F., Camacho, A. G., Palano, M., Aparicio, A., et al. (2020). Geodetic Study of the 2006–2010 Ground Deformation in La Palma (Canary Islands): Observational Results. *Remote Sensing*, *12*(16), 2566. https://doi.org/10.3390/rs12162566

Fu, W., Ma, G., Lu, W., Maruyama, T., Li, J., Wan, Q., et al. (2021). Improvement of Global Ionospheric TEC Derivation with Multi-Source Data in Modip Latitude. *Atmosphere*, *12*(4), 434. https://doi.org/10.3390/atmos12040434

Geng, J., Williams, S. D. P., Teferle, F. N., & Dodson, A. H. (2012). Detecting storm surge loading deformations around the southern North Sea using subdaily GPS. *Geophysical Journal International*, *191*(2), 569–578. https://doi.org/10.1111/j.1365-246X.2012.05656.x

GFZ. (2022). ESMGFZ Product Repository - NTAL. Retrieved June 21, 2022, from http://rz-vm115.gfz-potsdam.de:8080/repository/entry/show?entryid=80daee1b-ff73-481f-b0f3-18026282c03e

Gregorius, T., & Blewitt, G. (1998). Weather Fronts on GPS Measurements, 8.

Gregorius, T. L. H., & Blewitt, G. (1999). Modeling weather fronts to improve GPS heights: A new tool for GPS meteorology? *Journal of Geophysical Research: Solid Earth*, *104*(B7), 15261–15279. https://doi.org/10.1029/1998JB900067

Herring, T. A., Melbourne, T. I., Murray, M. H., Floyd, M. A., Szeliga, W. M., King, R. W., et al. (2016). Plate Boundary Observatory and related networks: GPS data analysis methods and geodetic products: PBO Data Analysis Methods and Products. *Reviews of Geophysics*, *54*(4), 759–808. https://doi.org/10.1002/2016RG000529

Herzmann, D. (2022). IEM :: Current & Historical IEM NEXRAD Mosaic Loop. Retrieved July 12, 2022, from https://mesonet.agron.iastate.edu/current/mcview.phtml?prod=usrad&java=script&mode=archive&frames=1&interval=60&year=2019&month=11&day=27&hour=3&minute=0

Huber, P. (1981). *Robust statistics*. Wiley, New York.

Jet Propulsion Laboratory. (2022). Automatic Precise Positioning Service - APPS. Retrieved June 24, 2022, from https://apps.gdgps.net/apps_underhood.php

Kreemer, C., Blewitt, G., & Davis, P. M. (2020). Geodetic evidence for a buoyant mantle plume beneath the Eifel volcanic area, NW Europe. *Geophysical Journal International*, *222*(2), 1316–1332. https://doi.org/10.1093/gji/ggaa227

Landskron, D., & Böhm, J. (2018). VMF3/GPT3: refined discrete and empirical troposphere mapping functions. *Journal of Geodesy*, *92*(4), 349–360. https://doi.org/10.1007/s00190-017-1066-2

Larson, K. M. (2009). GPS seismology. *Journal of Geodesy*, *83*(3–4), 227–233. https://doi.org/10.1007/s00190-008-0233-x

Larson, K. M., Poland, M., & Miklius, A. (2010). Volcano monitoring using GPS: Developing data analysis strategies based on the June 2007 Kīlauea Volcano intrusion and eruption. *Journal of Geophysical Research: Solid Earth*, *115*(B7). https://doi.org/10.1029/2009JB007022

Leontiev, A., & Reuveni, Y. (2017). Combining Meteosat-10 satellite image data with GPS tropospheric path delays to estimate regional integrated water vapor (IWV) distribution. *Atmospheric Measurement Techniques*, *10*(2), 537–548. https://doi.org/10.5194/amt-10-537-2017

Luddington, T., Santos, M. C., & Nievinski, F. G. (2010). Neutral Atmosphere Induced GPS Errors Caused by The 2004 Halifax Weather Bomb. *GEOMATICA*, *64*(3), 303–311. https://doi.org/10.5623/geomat-2010-0031

Martens, H. R., Argus, D. F., Norberg, C., Blewitt, G., Herring, T. A., Moore, A. W., et al. (2020). Atmospheric pressure loading in GPS positions: dependency on GPS processing methods and effect on assessment of seasonal deformation in the contiguous USA and Alaska. *Journal of Geodesy*, *94*(12), 115. https://doi.org/10.1007/s00190-020-01445-w

Melgar, D., Bock, Y., & Crowell, B. W. (2012). Real-time centroid moment tensor determination for large earthquakes from local and regional displacement records. *Geophysical Journal International*, *188*(2), 703–718. https://doi.org/10.1111/j.1365-246X.2011.05297.x

Moore, A. W., Small, I. J., Gutman, S. I., Bock, Y., Dumas, J. L., Fang, P., et al. (2015). National Weather Service Forecasters Use GPS Precipitable Water Vapor for Enhanced Situational Awareness during the Southern California Summer Monsoon. *Bulletin of the American Meteorological Society*, *96*(11), 1867–1877. https://doi.org/10.1175/BAMS-D-14-00095.1

Rieckh, T., Scherllin-Pirscher, B., Ladstädter, F., & Foelsche, U. (2014). Characteristics of tropopause parameters as observed with GPS radio occultation. *Atmospheric*

Measurement Techniques, 7(11), 3947–3958. https://doi.org/10.5194/amt-7-3947-2014

Rocken, C., Van Hove, T., & Ware, R. (1997). Near real-time GPS sensing of atmospheric water vapor. *Geophysical Research Letters*, *24*(24), 3221–3224. https://doi.org/10.1029/97GL03312

Saastamoinen, J. (1973). Contributions to the theory of atmospheric refraction, 22.

Sun, P., Zhang, K., Wu, S., Wan, M., & Lin, Y. (2021). Retrieving Precipitable Water Vapor from Real-Time Precise Point Positioning Using VMF1/VMF3 Forecasting Products. *Remote Sensing*, *13*(16), 3245. https://doi.org/10.3390/rs13163245

Tralli, D. M., & Lichten, S. M. (1990). Stochastic estimation of tropospheric path delays in global positioning system geodetic measurements. *Bulletin Géodésique, 64*(2), 127–159. https://doi.org/10.1007/BF02520642

Tregoning, P., & Dam, T. van. (2005). Atmospheric pressure loading corrections applied to GPS data at the observation level. *Geophysical Research Letters, 32*(22). https://doi.org/10.1029/2005GL024104

Twardzik, C., Vergnolle, M., Sladen, A., & Avallone, A. (2019). Unravelling the contribution of early postseismic deformation using sub-daily GNSS positioning. *Scientific Reports*, *9*(1), 1–12. https://doi.org/10.1038/s41598-019-39038-z

Xu, A., Xu, Z., Ge, M., Xu, X., Zhu, H., & Sui, X. (2013). Estimating Zenith Tropospheric Delays from BeiDou Navigation Satellite System Observations. *Sensors (Basel, Switzerland), 13*(4), 4514–4526. https://doi.org/10.3390/s130404514

Zumberge, J. F., Heflin, M. B., Jefferson, D. C., Watkins, M. M., & Webb, F. H. (1997). Precise point positioning for the efficient and robust analysis of GPS data from large networks. *Journal of Geophysical Research: Solid Earth*, *102*(B3), 5005–5017. https://doi.org/10.1029/96JB03860

4.11 Supplemental Material

4.11.1 Description

This material consists of Tables S4.1-S4.2, Figures S4.1-S4.11, and Videos S4.1-S4.6.

4.11.2 Supplemental Tables

Table S4.1: Median station vertical RMS, its repeatability, and their percent differences relative to current processing, for GPS stations in California and Nevada on November 26 – 27 at different processing levels. Data are plotted on Figure 4.5.

TROPx**	Median RMS ± Repeatability (mm)	RMS Percent Difference	Station Repeatability Percent Difference
Nov. 26-27, 2019			
01	21 ± 9.3	~	~
02	19.7 ± 8.2	6.2	12.7
04	19.5 ± 7.0	7.1	25.4
08	20.4 ± 6.7	2.9	28.6
12	21.8 ± 7.1	-3.8	23.8
Nov 26, 2019			
01	17.6 ± 5.2	~	~
02	16.7 ± 4.6	5.1	11.4
04	17.1 ± 4.6	2.8	11.4
08	18.2 ± 4.7	-3.4	8.6
12	19.85 ± 5.3	-12.8	-1.4
Nov. 27, 2019			
01	28.2 ± 12.9	~	~
02	26.15 ± 10.9	7.3	15.5
04	23.85 ± 10.1	15.4	21.3
08	24.1 ± 10.2	14.5	20.7
12	25.6 ± 10.8	9.2	16.1

Table S4.2: Global median vertical RMS, its repeatability, and their percent difference relative to the TROPx01 solution, by region and processing strategy.

TROPx**	**Median RMS ± Repeatability (mm)**	**RMS Percent Difference**	**Repeatability Percent Difference**
Region - Station Days			
North America – 70,320			
01	20.8 ± 7.3	~	~
02	20.0 ± 6.4	4	12
04	20.9 ± 6.7	0	8
08	23.5 ± 7.9	-13	-8
12	26.0 ± 9.0	-25	-24
16	28.4 ± 10.2	-37	-41
Central America – 1,344			
01	30.8 ± 10.3	~	~
02	28.0 ± 8.9	9	14
04	27.7 ± 8.9	10	14
08	30.9 ± 10.1	0	2
12	33.9 ± 11.7	-10	-14
16	36.6 ± 13.0	-19	-26
South America – 4,560			
01	25.4 ± 8.5	~	~
02	24.0 ± 7.6	6	11
04	25.0 ± 7.9	2	7
08	28.1 ± 9.2	-11	-9
12	31.3 ± 10.4	-23	-23
16	34.1 ± 11.6	-34	-37
Europe – 20,688			
01	18.1 ± 5.9	~	~
02	17.1 ± 5.2	6	13

04	17.7 ± 5.3	2	10
08	20.1 ± 6.2	-11	-5
12	22.3 ± 7.1	-23	-20
16	24.4 ± 8.0	-35	-35
Japan – 24,192			
01	22.7 ± 8.6	~	~
02	20.9 ± 6.8	8	21
04	21.6 ± 6.8	5	21
08	24.3 ± 7.9	-7	9
12	27.1 ± 9.2	-19	-7
16	29.7 ± 10.5	-31	-22
Australia – 5,184			
01	22.4 ± 6.5	~	~
02	21.0 ± 5.6	6	14
04	21.6 ± 5.9	4	9
08	23.9 ± 6.8	-7	-5
12	26.5 ± 7.7	-18	-18
16	28.8 ± 8.6	-29	-32
New Zealand – 3,312			
01	17.2 ± 5.3	~	~
02	16.4 ± 4.6	5	14
04	17.1 ± 4.6	1	14
08	19.1 ± 5.2	-11	3
12	21.3 ± 6.2	-24	-15
16	23.2 ± 7.1	-35	-33
Polar – 4,656			
01	16.6 ± 5.2	~	~
02	16.7 ± 5.2	-1	0
04	17.8 ± 5.8	-7	-11

08	20.1 ± 6.8	-21	-31
12	22.1 ± 7.6	-33	-46
16	24.1 ± 8.3	-45	-60
Global – 138,656			
01	20.7 ± 7.4	~	~
02	19.7 ± 6.5	5	12
04	20.5 ± 6.7	1	10
08	23.1 ± 7.9	-12	-6
12	25.7 ± 9.0	-24	-22
16	28.0 ± 10.1	-35	-36

4.11.3 Supplemental Figures

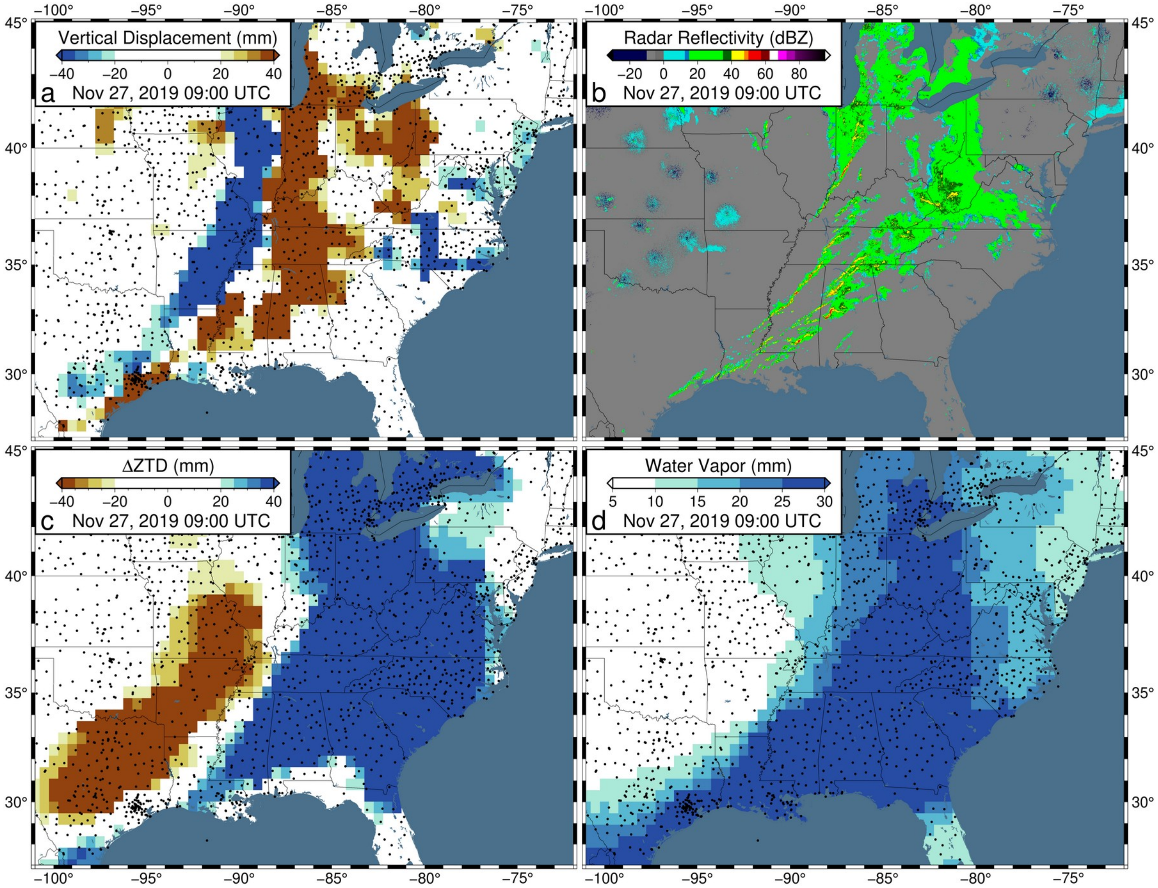

Figure S4.1: Data snapshots on November 27, 2019 at 09:00 UTC for the eastern United States. **(a)** Observed GPS vertical displacements. **(b)** Radar reflectivity. **(c)** Zenith tropospheric delay (ZTD) deviation. For each station, the median ZTD across November 26 – 27 is removed. **(d)** Observed water vapor. Note the spatial correlation between vertical uplift and observed radar reflectivity. Data presented in panels a, c, and d have been filtered with Robust Network Imaging.

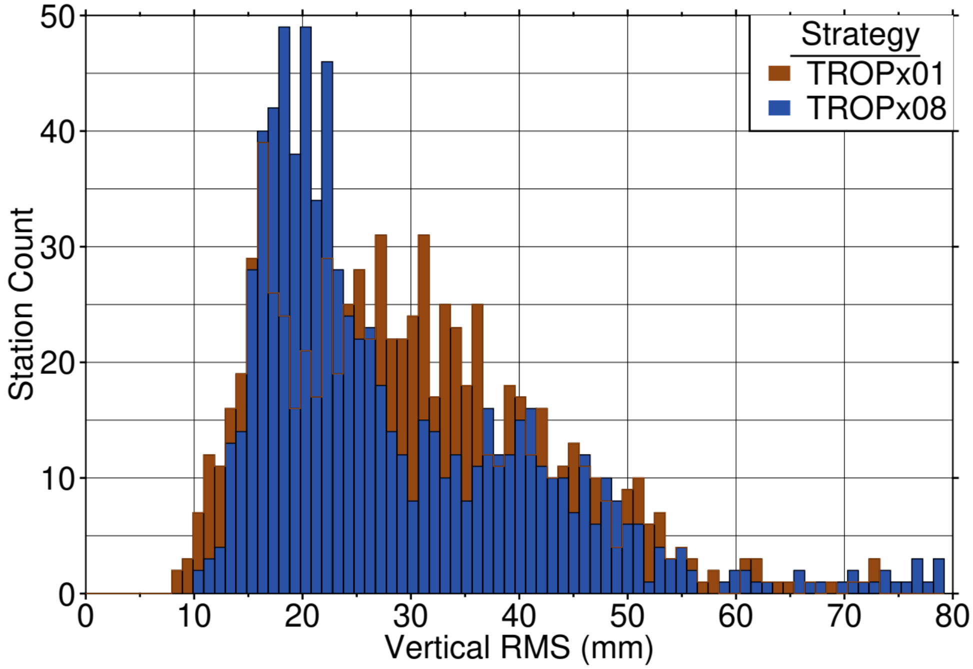

Figure S4.2: Histograms of station 5-min vertical RMS for GPS stations in California and Nevada on November 26 – 27. Red represents the TROPx01 [default, 3 mm/√(hr)] solution and blue represents the TROPx08 [24 mm/√(hr)] solution.

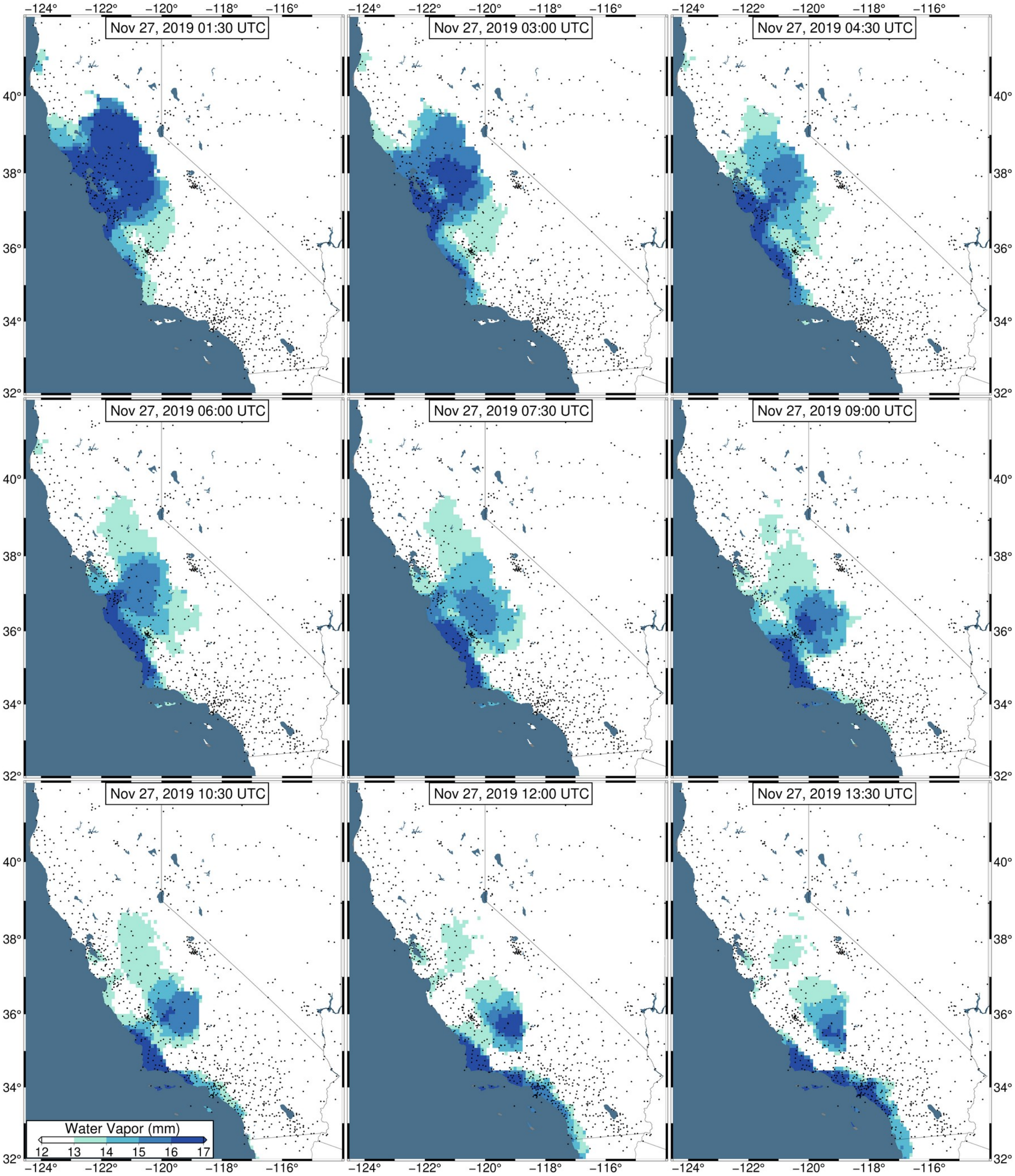

Figure S4.3: Observed GPS derived water vapor in 1.5-hour intervals between 01:30 and 13:30 UTC on November 27, 2019. Data have been filtered with Robust Network Imaging and are produced using a random walk of 3 mm/√(hr). Small black dots indicate GPS station locations.

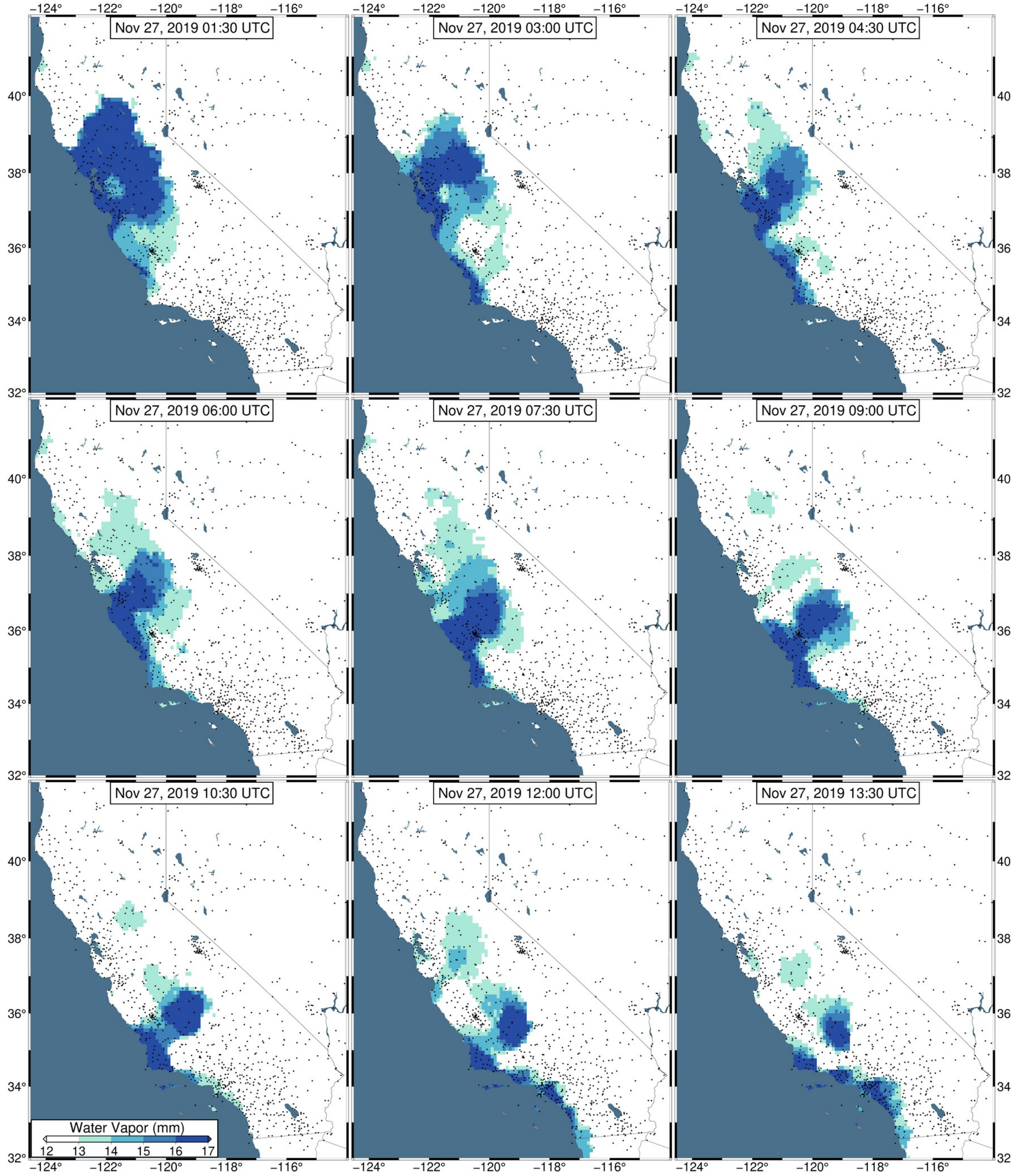

Figure S4.4: Corrected GPS derived water vapor in 1.5-hour intervals between 01:30 and 13:30 UTC on November 27, 2019, for the TROPx08 solution. Data have been filtered with Robust Network Imaging and small black dots indicate GPS station locations.

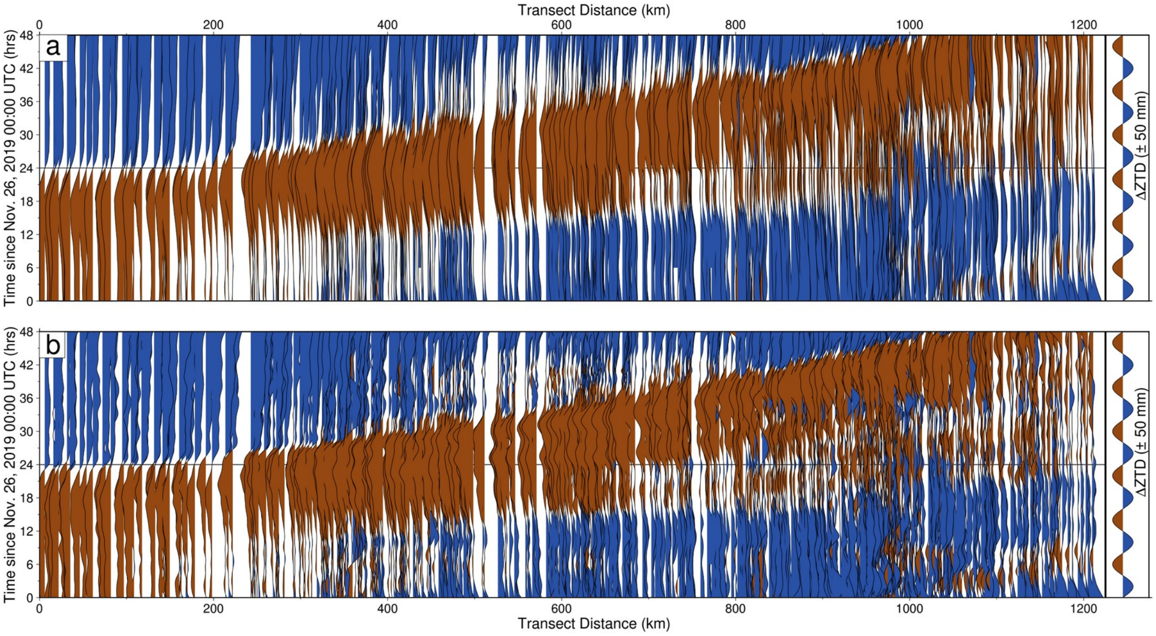

Figure S4.5: Wiggleplots of zenith tropospheric delay (ZTD) deviations along the transect identified in Figure 4.1 for November 26 – 27, 2019, for **(a)** current processing and **(b)** the TROPx08 solution. For the TROPx08 versions, deviations are relative to the median station value across November 26 – 27 for the TROPx01 solution. Data have been smoothed with loess local regression with a smoothing factor of 0.10. Black horizontal bar represents the start of November 27. Note that the ZTD estimates of the TROPx08 solution exhibit more variability.

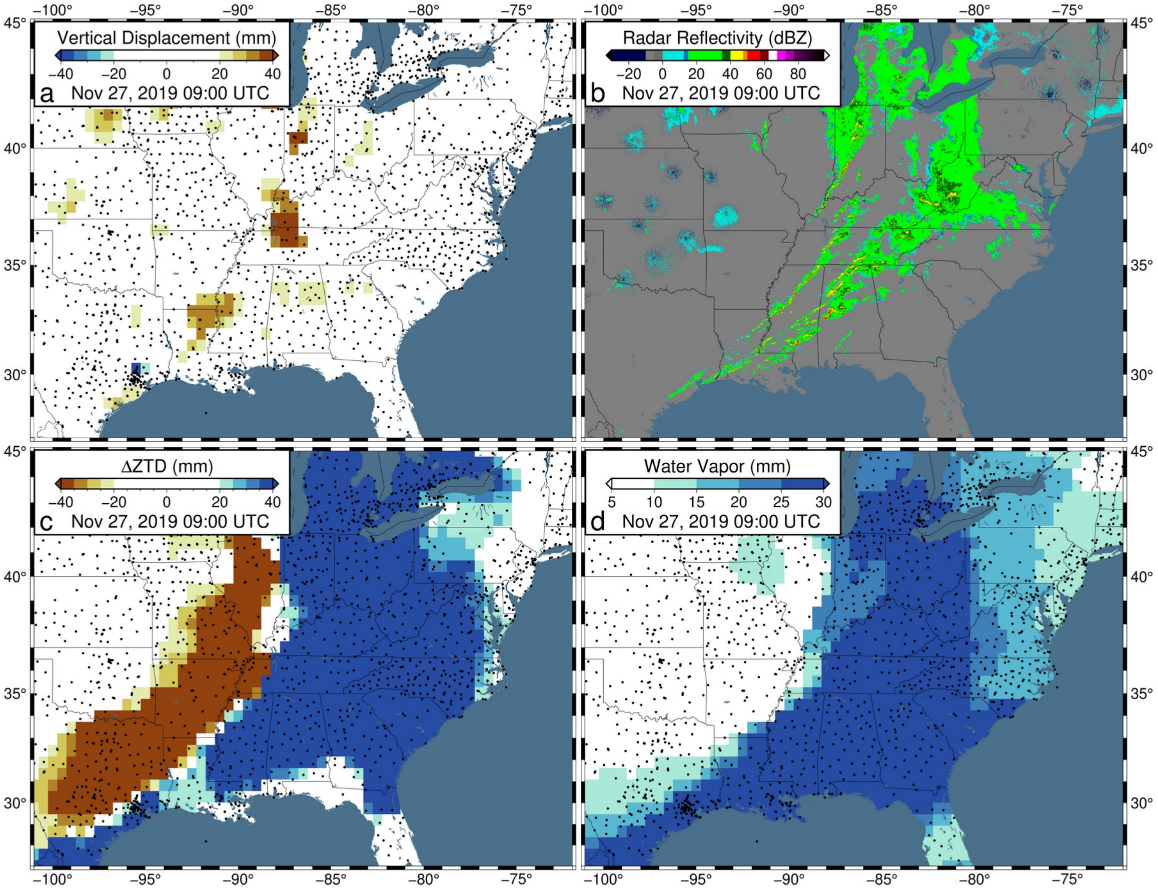

Figure S4.6: Same as Figure S4.1 except for the TROPx08 Solution. Note that the vertical displacements are corrected and the gradient of water vapor between air masses is much sharper.

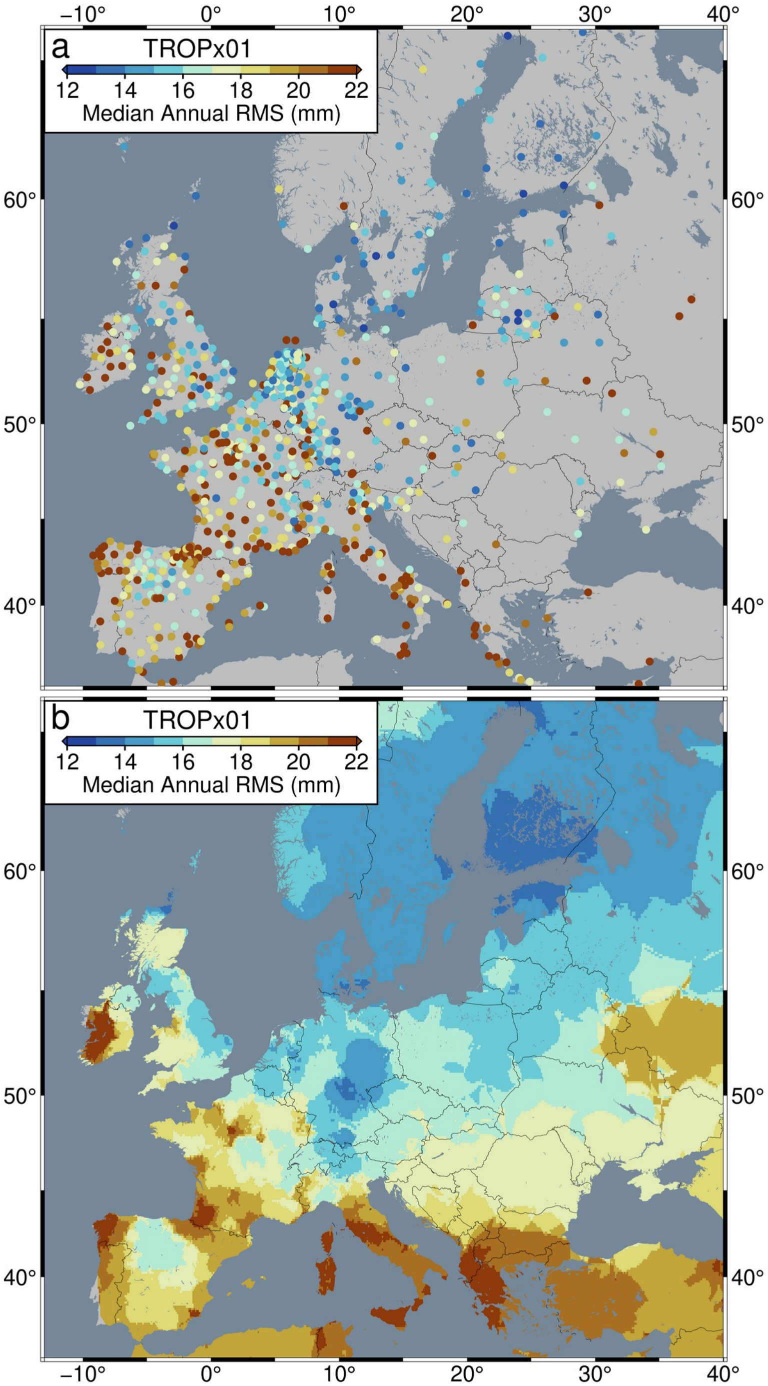

Figure S4.7: (a) Median annual RMS and **(b)** Robust Network Imaged median annual RMS, for GPS stations across Europe. Results are for the TROPx01 solution.

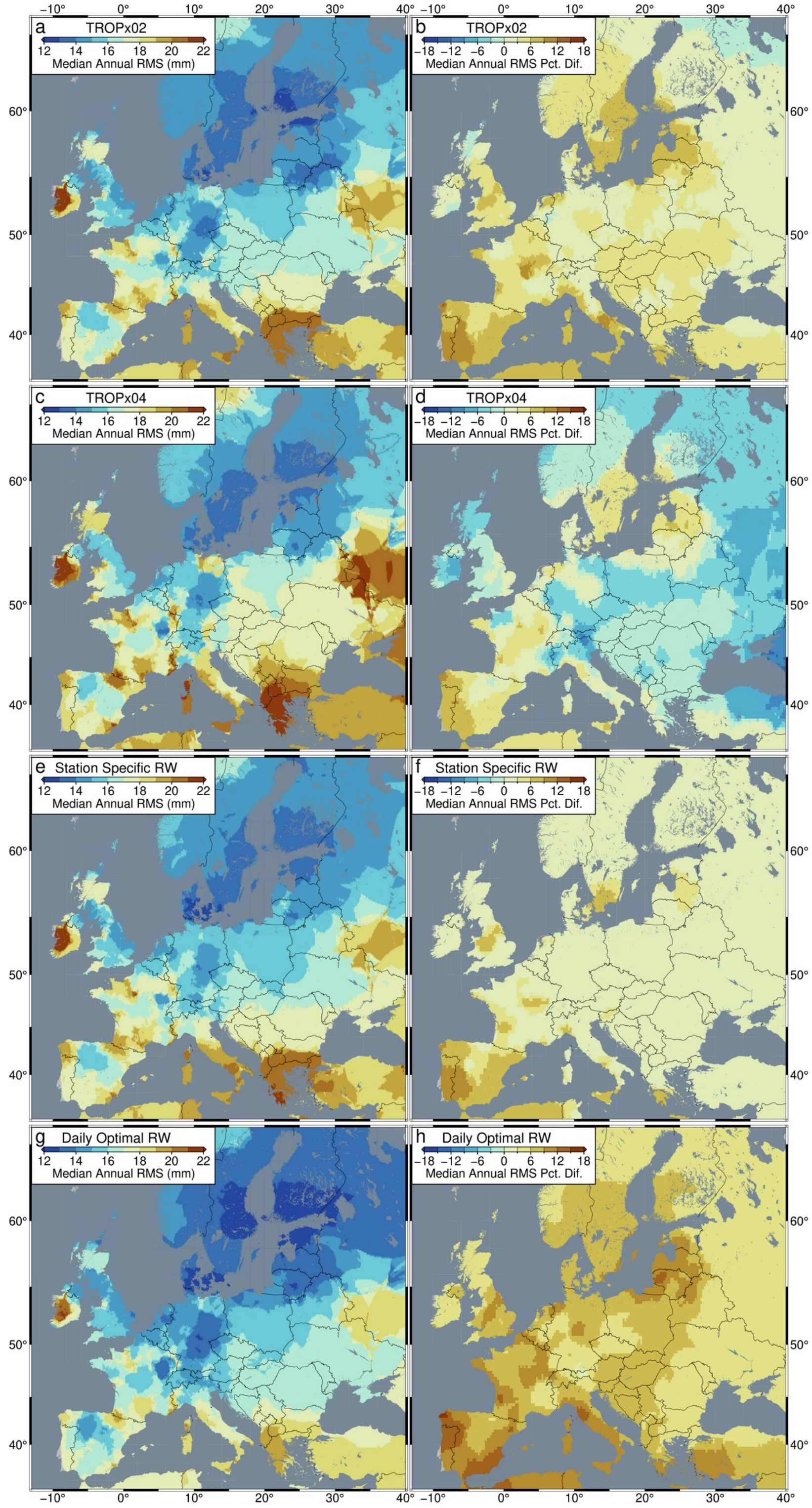
a TROPx02
12 14 16 18 20 22
Median Annual RMS (mm)
b TROPx02
−18 −12 −6 0 6 12 18
Median Annual RMS Pct. Dif.
c TROPx04
12 14 16 18 20 22
Median Annual RMS (mm)
d TROPx04
−18 −12 −6 0 6 12 18
Median Annual RMS Pct. Dif.
e Station Specific RW
12 14 16 18 20 22
Median Annual RMS (mm)
f Station Specific RW
−18 −12 −6 0 6 12 18
Median Annual RMS Pct. Dif.
g Daily Optimal RW
12 14 16 18 20 22
Median Annual RMS (mm)
h Daily Optimal RW
−18 −12 −6 0 6 12 18
Median Annual RMS Pct. Dif.
−10° 0° 10° 20° 30° 40°
60° 50° 40°

Figure S4.8: Comparison of **(a, c, e, and g)** Robust Network Imaged median annual RMS and its **(b, d, f, and h)** percent difference relative to the TROPx01 solution for the **(a and b)** TROPx02, **(c and d)** TROPx04, **(e and f)** Station specific, and **(g and h)** daily optimal processing strategies for GPS stations across Europe.

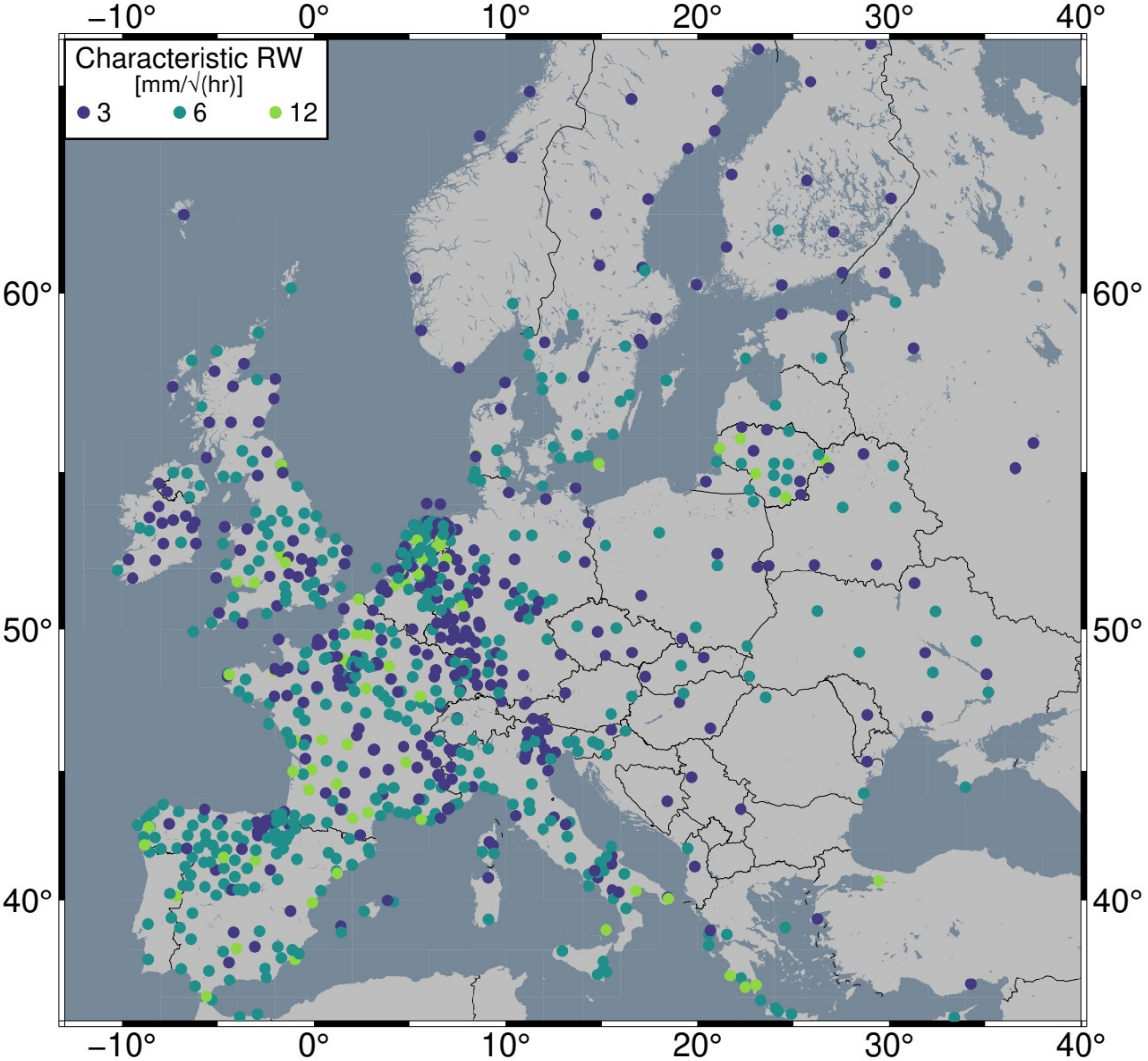

Figure S4.9: Characteristic station random walk constraint for GPS stations across Europe. Values reflect the processing strategy which most frequently minimizes station RMS.

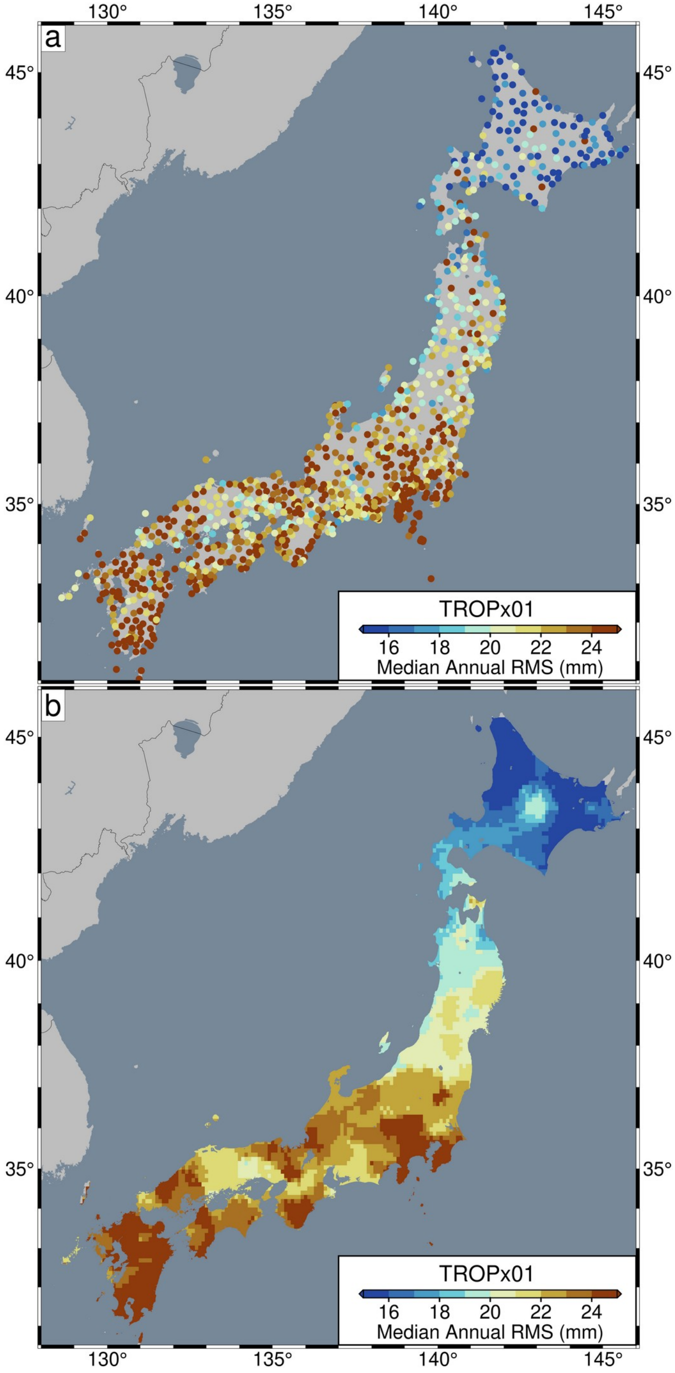

Figure S4.10: (a) Median annual RMS and **(b)** Robust Network Imaged median annual RMS, for GPS stations in Japan. Results are for the TROPx01 solution.

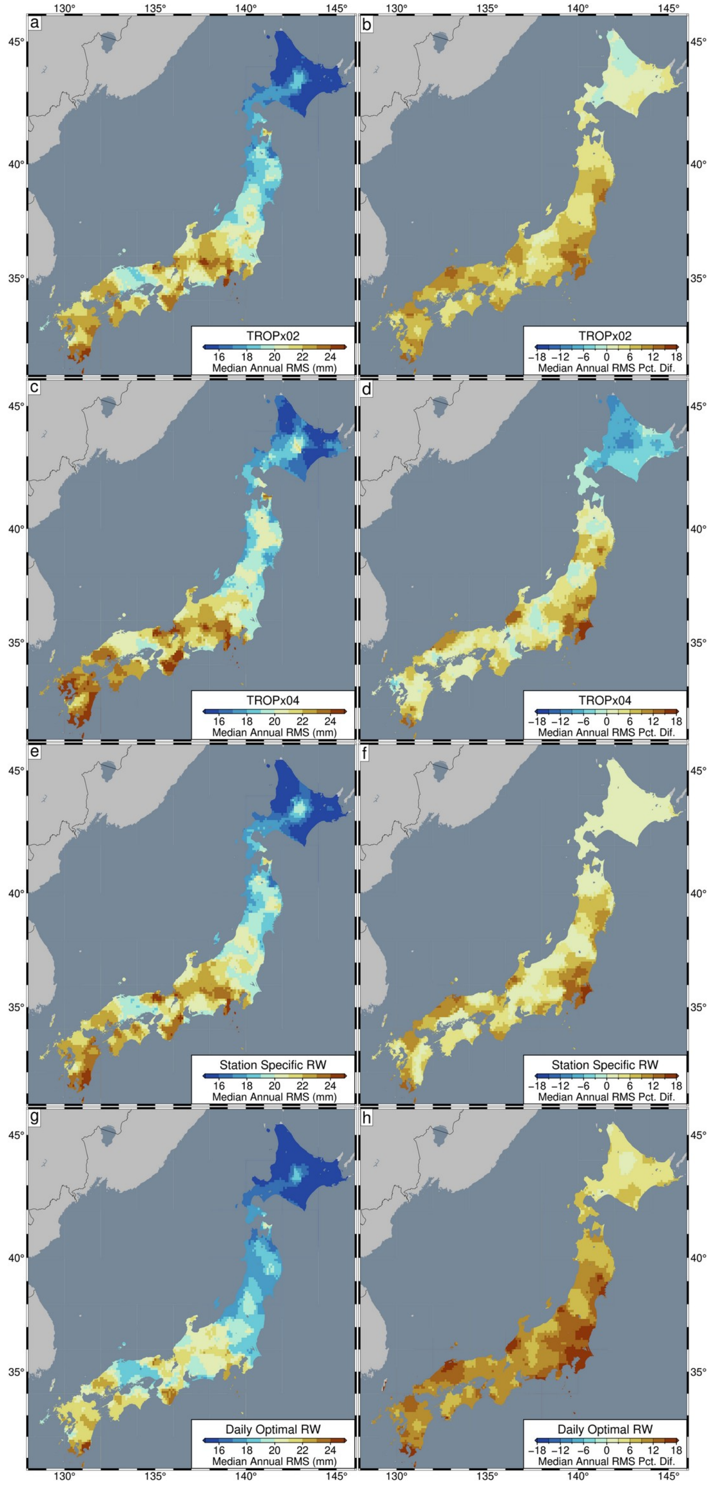
a
b
c
d
e
f
g
h
130°
135°
140°
145°
45°
40°
35°
TROPx02
TROPx04
Station Specific RW
Daily Optimal RW
16 18 20 22 24
Median Annual RMS (mm)
−18 −12 −6 0 6 12 18
Median Annual RMS Pct. Dif.

Figure S4.11: Comparison of **(a, c, e, and g)** Robust Network Imaged median annual RMS and its **(b, d, f, and h)** percent difference relative to current processing for the **(a and b)** TROPx02, **(c and d)** TROPx04, **(e and f)** Station specific, and **(g and h)** daily optimal processing strategies for GPS stations in Japan.

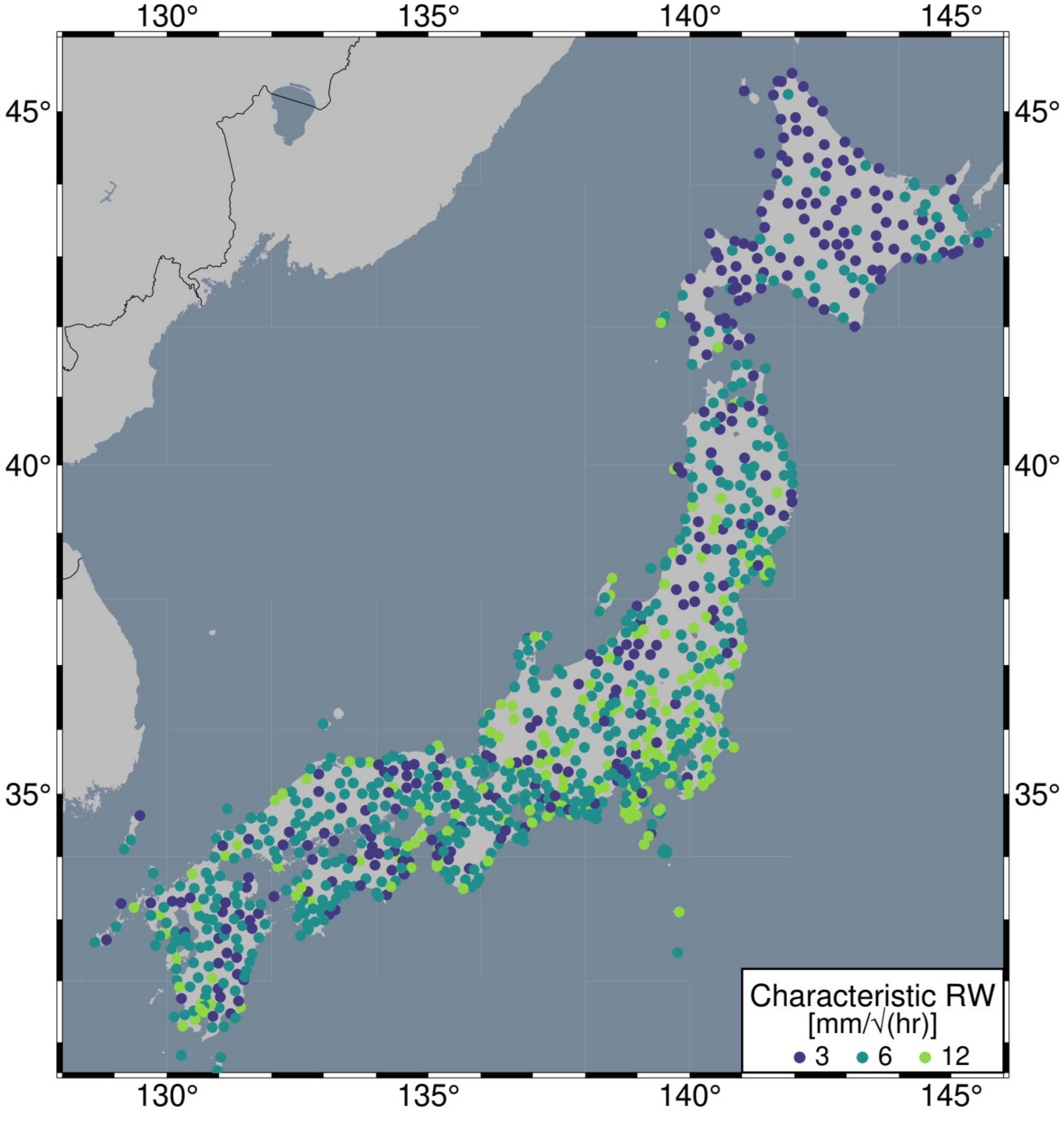

Figure S4.12: Characteristic station random walk constraint for GPS stations in Japan. Values reflect the processing strategy which most frequently minimizes station RMS.

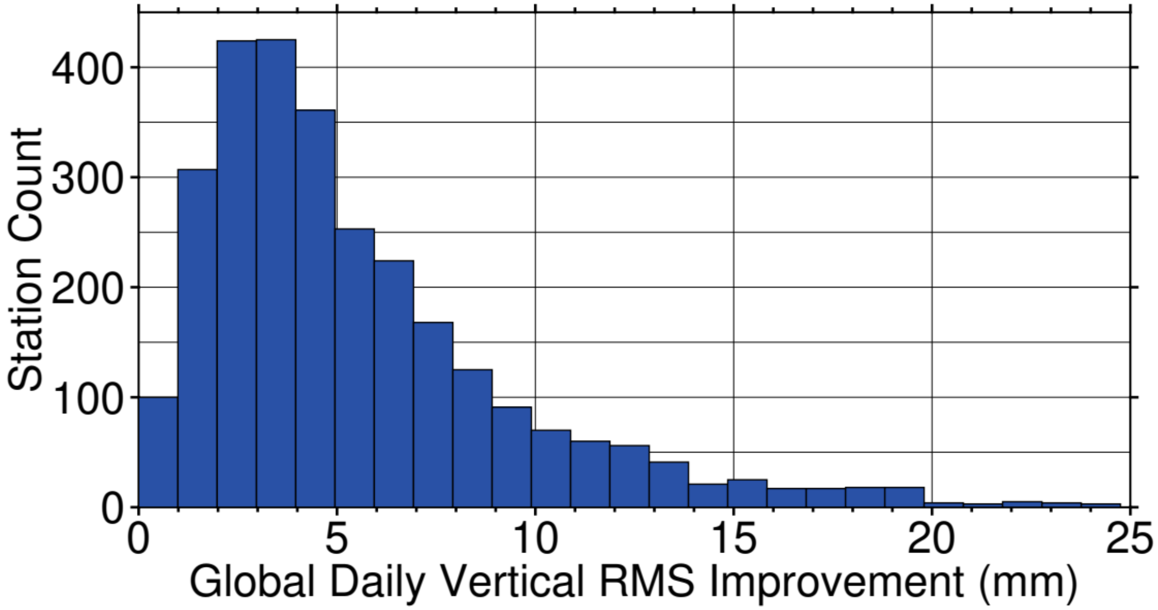

Figure S4.13: Global daily position vertical RMS improvement for the 2021 data set. Values are defined following √(RMS1^2-RMS0^2). Here, RMS1 represents the station RMS values of the TROPx01 solution, and RMS0 represents the value which best minimizes the station RMS by strategy. Note that solutions which maintain the TROPx01 solution as optimal, and thus show no difference, are not plotted here. There are 1356 stations (32%), which retain the TROPx01 strategy.

4.11.4 Supplemental Videos

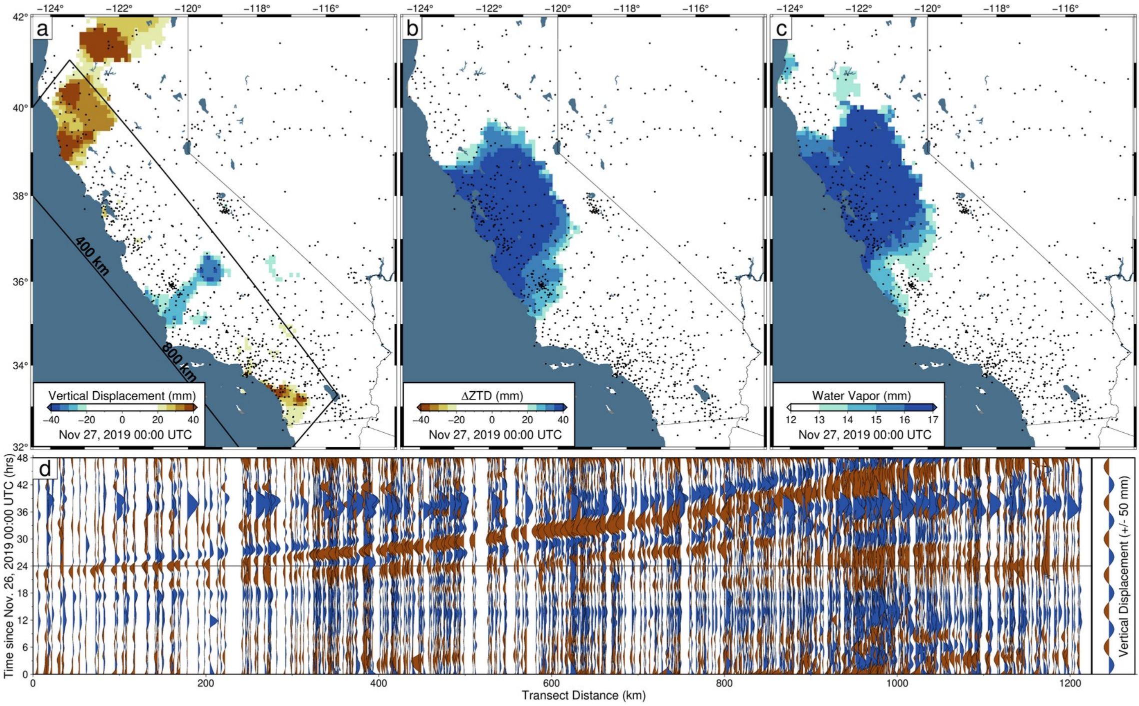

Video S4.1: Observed **(a)** GPS vertical displacement, **(b)** zenith tropospheric delay (ZTD) deviation, and **(c)** GPS derived water vapor, in five minute increments beginning on November 27, 2019 00:00 UTC. Data have been smoothed with Robust Network Imaging and were produced using a random walk of 3 mm/√(hr). Black dots represent GPS station locations. **(d)** Wiggle plot of observed vertical displacements for November 26 – 27, 2019. The bounds of the transect are shown by the black rectangle in panel a. Horizontal black line represents the current epoch shown in panels a – c.

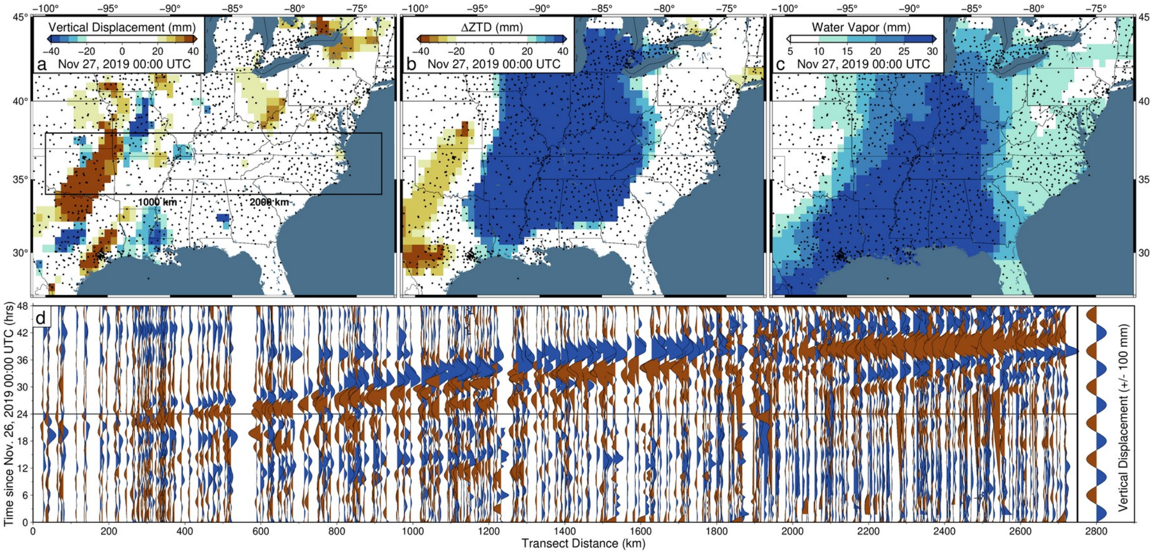

Video S4.2: Same as Video S4.1, except for the eastern United States during the same timeframe, for current processing.

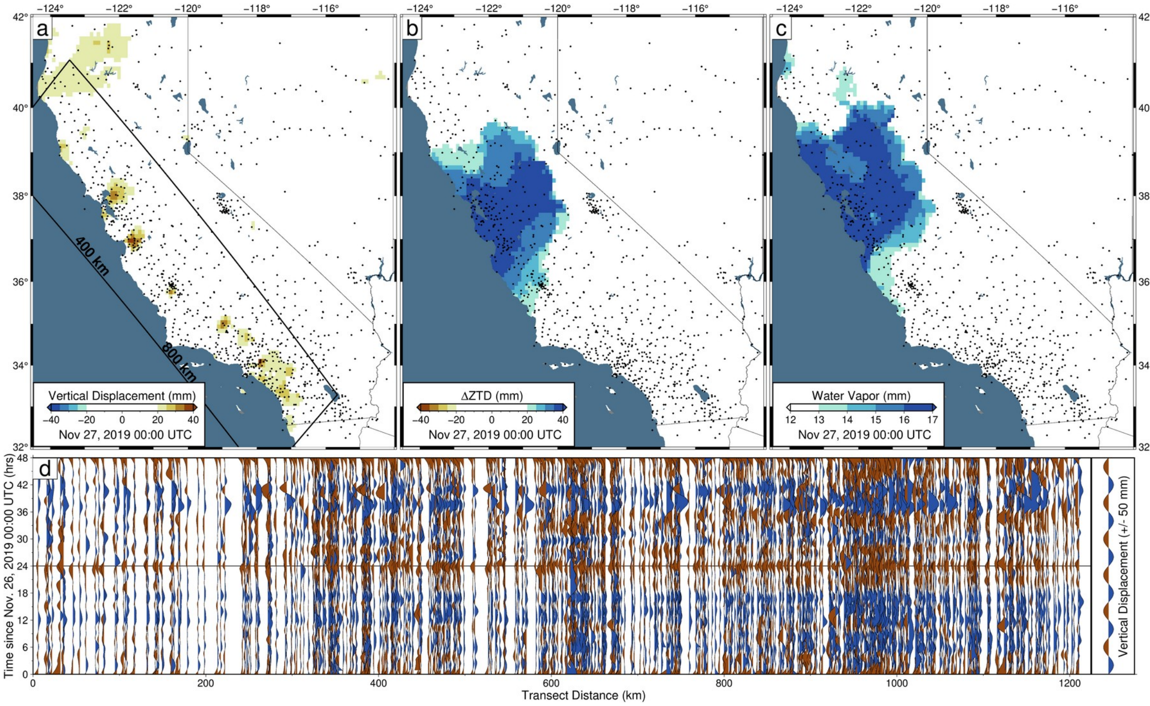

Video S4.3: Corrected **(a)** GPS vertical displacement, **(b)** zenith tropospheric delay (ZTD) deviation, and **(c)** GPS derived water vapor, in five minute increments beginning on November 27, 2019 00:00 UTC. Data have been smoothed with Robust Network Imaging and are for the TROPx08 solution. Black dots represent GPS station locations. **(d)** Wiggle plot of observed vertical displacements for November 26 – 27, 2019. The bounds of the transect are shown by the black rectangle in panel a. Horizontal black line represents the current epoch shown in panels a-c.

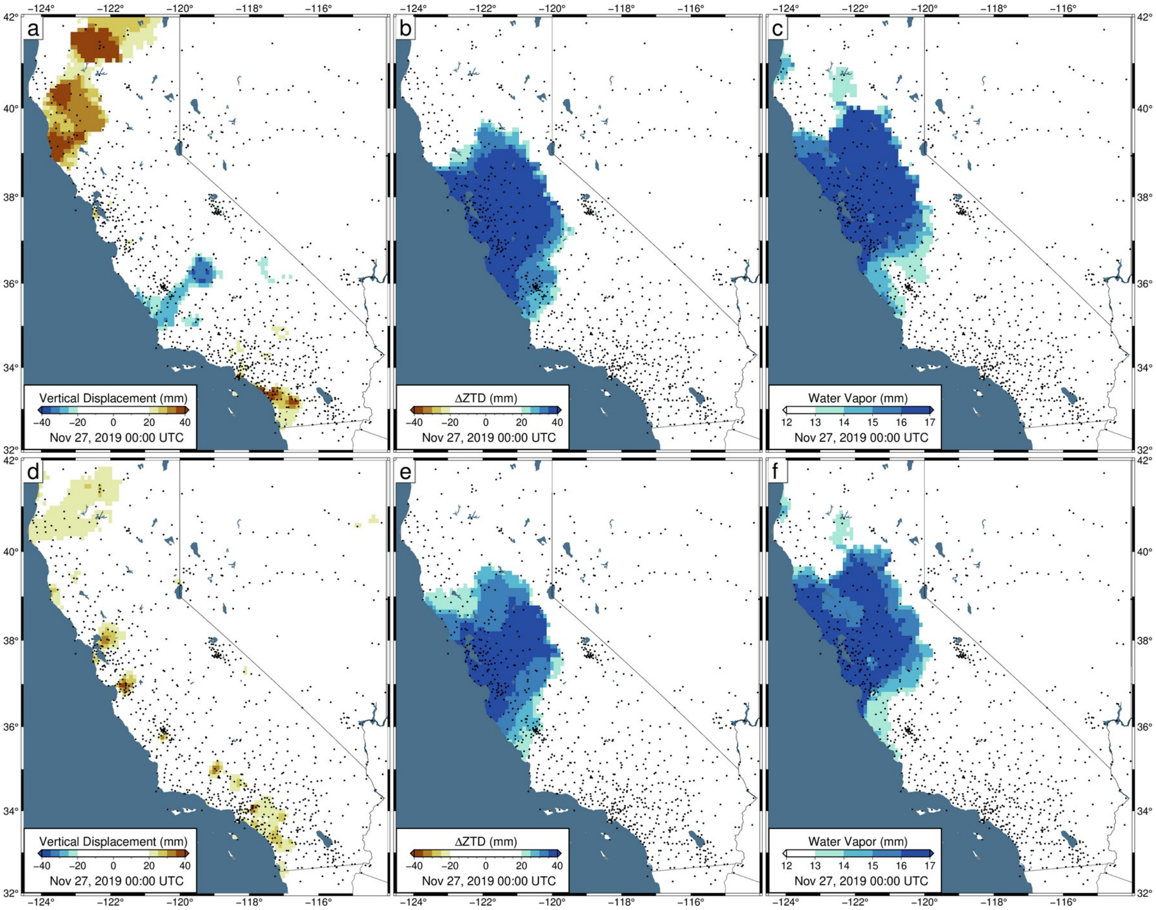

Video S4.4: Comparison of the **(a-c)** TROPx01 solution to the **(d-f)** TROPx08 solution for **(a,d)** GPS vertical displacement, **(b,e)** zenith tropospheric delay (ZTD) deviation, and **(c,d)** GPS derived water vapor.

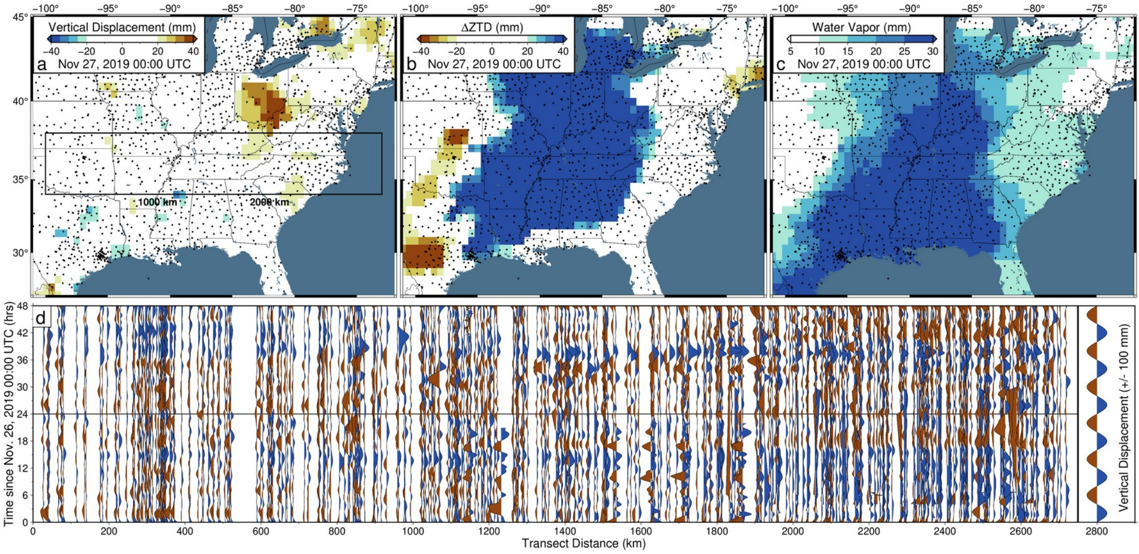

Video S4.5: Same as Video S4.2, except for the TROPx08 solution.

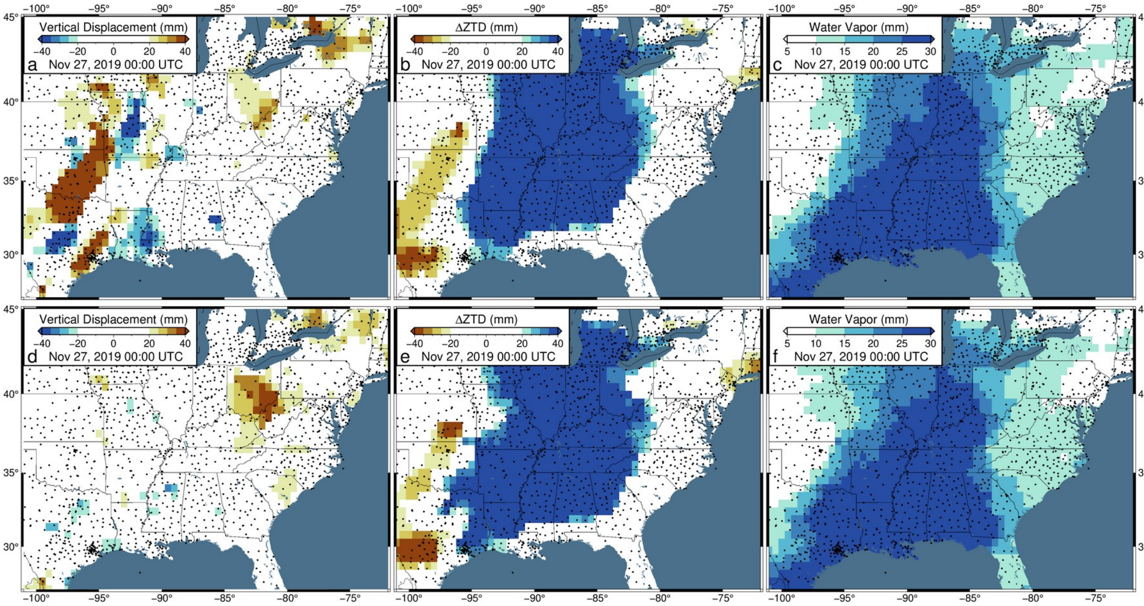

Video S4.6: Same as Video S4.4, except for the eastern United States during the same timeframe. Comparison between the TROPx01 and TROPx08 solutions.

5

Discussion and Conclusions

The findings presented in these studies highlight the prevalence, and impact, of subtle deformation signals observed by GPS time series in the western United States. Within each chapter, we present methods to identify and/or correct unique signals at daily, sub-daily, and multi-year time frames. We show how, when left unaccounted for, these signals can modify velocity fields, increase station uncertainties, and can lead to altered interpretations of the results. A range of deformation sources are investigated and we rely on recently published robust analysis methods, as well as the rapid expansion of the GPS network over the last fifteen years, to distinguish them. While these studies are focused on deformation within the western United States, their impact is broad, as they highlight the sensitivity of GPS positions to subtle signals and the necessity to account for all transient signals to produce robust analyses. The main conclusions for each chapter and their broader impacts are presented in the following paragraphs.

In the first chapter, we investigate the sensitivity of GPS stations to drought at small spatial scales. Many studies have used GPS data, in conjunction with Gravity Recovery and Climate Experiment (GRACE) data, to quantify hydrologic load variation at regional and continental scales. These studies typically only rely on the vertical GPS component and do not explore load variation below the spatial resolution of GRACE. Considering many water resources are stored in areas smaller than what can be resolved by GRACE, it is important to identify methods with which to quantify this variation. To address this, we focus on Great Salt Lake (GSL), in Utah, which lost 1.89 m of water during the 2012 – 2016 drought. The GPS stations near the lake show a clear three-dimensional change in trend during this period, however, we find that these displacements cannot be explained solely by the unloading of the lake. Following a sensitivity analysis of groundwater load distributions, we find that three-dimensional GPS is able to quantify both the unloading of the lake and nearby groundwater. This is achieved by considering radial rings of groundwater around the lake and the inferred groundwater loss is substantial (10.9 ± 2.8 km^3), at twice the volume observed on the lake (5.58 ± 0.11 km^3). While the the choice of using rings is a simple model to represent the true complex distribution of groundwater, we find that well observations within the loaded region support our distribution. These findings identify substantial mass loss during the drought and reveal that three-dimensional GPS data is useful to quantify small scale hydrologic variation. Such usage of GPS data would be quite beneficial to water resource managers, particularly when considering water resources which are difficult to quantify such as aquifers. In our analysis, we assess the limitations of the current GPS network around GSL and find that a denser network is required to improve the resolution of the load distribution. Future studies near GSL, would greatly benefit from an expanded GPS network to better understand groundwater variation. An option to address areas with sparse data would be to install a semi-continuous network. Such a network could be applied across a variety of scales (i.e., around GSL or smaller aquifers), to efficiently increase the resolution of the network and quantify multi-year hydrologic variation.

The inclusion of the horizontal components in this study better constrains our results and reveal variability in station horizontal velocities dependent on the hydrologic cycle. This factor is of particular interest for studies inspecting regional velocity fields since short duration or semi-continuous stations will exhibit bias depending on the time in which they recorded data. Since our study, a few stations near GSL have been installed or re-occupied, and the lake entered another period of decline beginning in 2020. Data for these stations show similar displacements to those presented in this study, however, velocities of new stations will be heavily biased by the new drought signal. Our findings highlight the necessity to account for hydrologic variation in order to robustly investigate GPS velocity fields near large water storages.

Further support of our load distribution is found in the seismicity analysis which finds that within the load region, seismicity is modulated by the hydrologic cycle. We find that as stresses on faults under the load are reduced during dry periods, earthquakes occur ~20% more frequently while seismicity outside of the load shows no such relationship. These findings indicate that near GSL, hydrologic unloading plays a larger long term role than hydrologic processes acting upon the faults themselves, which would reveal the opposite trend. This is of particular interest considering that since this study was prepared, the surface elevation of GSL has continued to decline to the lowest level on record and the lake is as risk of drying up completely. The findings presented in this study would suggest that, in the event of a fully emptied GSL, seismicity near GSL would then be less affected by the hydrologic cycle, resulting in more consistent earthquake rates.

The most robust interseismic velocity field produced to date for the central Basin and Range is presented in the second chapter. Since deformation rates are particularly low here, it is crucial to account for any subtle transient signals present in the timeseries. To address this, corrections for postseismic deformation, hydrologic loading, and regional common mode error are produced. We find that postseismic deformation substantially alters the velocity field, and that the common mode correction greatly reduces station uncertainties. Our final velocity field exhibits median velocity uncertainties which are 62.1% and 53.8% lower, in the east and north components, relative to the original velocity uncertainties. Strain rates within the Las Vegas Valley are high, at 8.5 ± 2.4 $\mathrm{x}10^{-9}\mathrm{yr}^{-1}$, and our velocity budget for the valley finds 0.52 ± 0.18 mm/yr of east–west extension.

Our revised geodetic constraints on deformation within the central Basin and Range are important for revising future seismic hazard models within the region. Particularly with respect to the hazard near Las Vegas, for which our results clearly support that deformation is active within the valley. We show that the long term interseismic trends within Las Vegas are substantially higher than previously estimated due to postseismic deformation. The relaxation field is oriented such that our original dataset, and that of previous studies of the region, reflect slower extension across the valley. This shows that although the Eglington/Decatur and Frenchman Mountain faults are not particularly known for their modern seismicity rates, the combination of their long term extension rates and the elevated strain rates within the valley, suggest seismic hazard is higher than previously suggested.

Accurate modeling of zenith tropospheric delays (ZTD) plays a key role in producing quality GPS positions. When the delay estimate is too strict (or too loose), however, systematic errors (increased data noise) propagate into the position. In the final chapter, we present a sensitivity analysis of the tropospheric random walk constraint, at both local and global scales, in 5-minute GPS positioning. We find that spurious vertical displacements observed during Winter Storm Ezekiel on November 27, 2019 along the coast of California, are suppressed when using a random walk constraint of 24 mm/√(hr) (eight times looser than the default value), improving station timeseries RMS and repeatability by 15% and 21% respectively. The loosened constraint allows the ZTD estimate to better account for rapid variation of atmospheric conditions, preventing additional displacements from propagating into the position of the station.

When the random walk constraint is chosen correctly, 5-minute GPS time series become substantially straighter. This is of particular importance for any sub-daily analysis of co-seismic displacements and early postseismic relaxation. In the event that an earthquake occurs during the passing of a weather front, which is not an unlikely occurrence, additional displacements when the random walk constraint is too strict could lead to incorrect estimation of the displacement field. This raises concern for the application of GPS based earthquake early warning systems which are dependent on accurate displacement fields. An overly strict random walk constraint could result in either over or under estimating the magnitude of the event, of which minimizing both aspects are of key concern for proper early warning systems. A similar case can be made for assessing early postseismic deformation, in which additional displacements associated with ZTD underestimation could lead to altered estimates of postseismic parameters, and for any studies investigating crustal deformation over hourly time frames. Each of these aspects can be improved by ensuring proper ZTD estimation.

We find that global GPS network vertical RMS and repeatability is improved by 4% – 9% and 10% – 21% respectively by region, when using a random walk of 6 mm/√(hr). While these errors can produce substantial spurious displacements within the 5-minute GPS time series, they propagate subtly into the daily positions, revealing a significant source of vertical station scatter which is readily correctable. The vertical component exhibits generally 2 – 3 times higher uncertainties than the horizontals and we find that by identifying the optimal random walk per station, we can improve station daily vertical position RMS values for 68% of the global network. This raises clear implications for improving our understanding of vertical displacement fields. As described in Chapter 2, many studies have relied on vertical displacements to better understand hydrologic variations, and reduced vertical scatter due to properly identified random walk constraints will improve model accuracy. This pertains to any modeling which relies on vertical displacement fields as a constraint (e.g., volcanic, seismic, or pressure loading).

The results of this study clearly show that adjustments to the ZTD random walk constraint are necessary in future re-analysis of the global GPS network. We find that a variable constraint yields greater improvements due to regional heterogeneity of optimal station random walk values, compared to the default uniform value approach. This is driven by climactic, temporal, and geographic factors. When applying a characteristic random walk constrain to each station, global station vertical repeatability can be improved by 10%, however, the improvement is substantially larger when identifying the daily optimal random walk per station at 24%. While the characteristic approach would be simple to apply, this method is unable to account for annual variability. The daily optimal approach, while clearly the best choice, would scale poorly to global GPS analysis. Thus, in order to account for both regional and temporal variability, defining an annual sinusoidal random walk constraint per station would be the optimal approach for improving station repeatability while also being able to scale to global network analysis. Such an approach would capture most of the improvements observed by the daily optimal method and is expected to attain ~20% global improvement in station repeatability. At minimum, it is strongly recommended to loosen the uniform random walk to 6 mm/√(hr).